

LIFE PROJECT

“Participatory and multi-level governance process to design a transformational climate change adaptation project at Cala Millor beach from an integrated and multidisciplinary science-based approach”.

DELIVERABLE NUMBER 3.4: *Integrated multidisciplinary methodology for the assessment of impacts and associated risks of different progressive global change projections at urban beaches: Application at Cala Millor beach.*

PROJECT ACRONYM	LIFE AdaptCalaMillor
GRANT AGREEMENT NUMBER	LIFE21/GIC/ES/101074227
CALL AND TOPIC	LIFE-2021-SAP-CLIMA-GOV
FUNDING BODY	CINEA
PROJECT DATES	1 st of January 2021 – 30 th of April 2027
COORDINATOR BENEFICIARY	Directorate General of Energy and Climate Change (DGECC)
WEBSITE	

DELIVERABLE NUMBER	D3.4
DELIVERABLE TITLE	<i>Integrated multidisciplinary methodology for the assessment of impacts and associated risks of different progressive global change projections at urban beaches: Application at Cala Millor beach.</i>
WORK PACKAGE AND TASK NUMBER	WP3; Task T3.4.
LEAD PARTICIPANT PARTNER	IMEDEA-CSIC
DISSEMINATION LEVEL	public
DELIVERY DUE DATE	31/01/2025
LAST MODIFIED DATE	30/01/2025
AUTHORS (alphabetical order)	Àngels Fernàndez-Mora, Daniel García Veira, Lluís Gómez-Pujol, Nuria Marbà, Marta Marcos, Alejandro Orfila, Bartolomé Pascual Fuster, Jaume Rosselló Nadal, Elena Sánchez-García.

This project has received funding from the European Union's LIFE programme under grant agreement N° LIFE21/GIC/ES/101074227

Disclaimer: The information and views set out in this report are those of the author(s) and do not necessarily reflect the official opinion of the European Union. Neither the European Union institutions and bodies nor any person acting on their behalf may be held responsible for the use which may be made of the information contained therein.

Project partners:



Authors contribution:

Physical Dimension:	Àngels Fernàndez-Mora, Elena Sánchez-García, Lluís Gómez-Pujol, Alejandro Orfila, Marta Marcos
Environmental Dimension:	Daniel García Veira, Alejandro Orfila, Lluís Gómez-Pujol, Nuria Marbà
Socio-economic Dimension:	Bartolomé Pascual Fuster, Jaume Rosselló Nadal, Lluís Gómez-Pujol, Elena Sánchez-García
Urban Dimension:	Àngels Fernàndez-Mora, Elena Sánchez-García
Impact maps:	Elena Sánchez-García, Daniel García Veira

Cita: Fernàndez-Mora, A., García-Veira, D., Gómez-Pujol, L., Marbà, N., Marcos, M., Orfila, A., Pascual-Fuster, B., Rosselló-Nadal, J., Sánchez-García, E. (2025). DELIVERABLE NUMBER 3.4: *Integrated multidisciplinary methodology for the assessment of impacts and associated risks of different progressive global change projections at urban beaches: Application at Cala Millor beach.* <http://doi.org/10.25704/PSWX-X018>

EXECUTIVE SUMMARY

This document provides a summary of the findings from the study on the historical evolution and current status of the urban beach of Cala Millor (Mallorca, Balearic Islands, Western Mediterranean), with a focus on its physical, environmental, and socio-economic dimensions. The study examines the elements exposed to various risk factors associated with global change, primarily rising sea levels, the impact of storms, increasing atmospheric temperatures, and rising water temperatures. Based on an assessment of the current situation, the exposure, risk, and impact linked to the effects of global change have been modelled according to two climate scenarios (RCP-4.5 and RCP-8.5) and three time horizons (2030, 2050, and 2100), using downscaled IPCC data and marine climate models.

The key conclusions of this work are presented below, categorised according to the physical, environmental, and socio-economic dimensions:

PHYSICAL DIMENSION

- In terms of sediment balance, a slight overall sediment deficit is observed ($-0.14 \text{ m}^3/\text{m}^2$) within the context of topo-bathymetric three-dimensional changes. However, considering the limitations of the topo-bathymetric surveys, along with the recorded episodes of positive sediment balance, it is reasonable to infer that much of the sediment exiting the monitored area is not lost, but rather remains in adjacent regions. Depending on wave characteristics and direction, this sediment may eventually return to the study area.
- Shoreline and dry beach width variability at Cala Millor are important, because of the sand bars dynamics and changes in sediment mass budgets related to energetic storms. Changes backwards and seaward around 20 m, also on a daily basis, are not unusual.
- On a longtime scale, the historic beach width still remains above the reference natural conditions exhibited in aerial photographs from 1956. Long time scale shoreline analyses show that the system prograded in comparison to 1956 because of beach nourishment. Nevertheless, the average life and efficiency of historical beach nourishments at Cala Millor has not exceeded 15 years in the best of cases.
- High spatio-temporal resolution data collected from the Cala Millor beach monitoring station from 2011 to 2023 reveal that there is a general decreasing trend in dry beach width along the time of study. Although it can be observed some positive variations representing an increase in mean beach width. Spatially, the central area of the beach remains wider than the rest of the areas. The southern area that presents rock outcrops, has a smaller width and it is controlled by rocks. The northern area presents higher variability, with width varying over time, and particularly from 2018 to 2023. Spatio-temporal analyses highlight that this variability is mainly controlled by the annual sea-level cycle, the seasonal wave climate, specific storms, and there is a peak of lower frequencies (2.5 yr) that could be related to climatic cycles.

- The hazard assessment of coastal flooding has been developed through modelling different scenarios and time-horizons, taking into account factors such as sea-level rise, storm surge, wave action, and *Posidonia oceanica* meadow evolution to predict the extent of flooding:
 - For the IPCC scenario RCP-4.5 in 2030 the area affected by permanent sea level flooding will range from $\sim 2,800 \text{ m}^2$ to $8,075 \text{ m}^2$, and the area affected by temporary storm flooding from $\sim 72,000 \text{ m}^2$ to $83,500 \text{ m}^2$; in 2050 the area affected by permanent sea level flooding will range from $\sim 4,025 \text{ m}^2$ to $14,700 \text{ m}^2$, and the area affected by temporary storm flooding from $\sim 78,200 \text{ m}^2$ to $101,900 \text{ m}^2$, and for the 2100 scenario the area affected by permanent sea level flooding will range from $\sim 8,975 \text{ m}^2$ to $31,700 \text{ m}^2$, and the area affected by temporary storm flooding from $\sim 86,800 \text{ m}^2$ to $240,500 \text{ m}^2$.
 - For the IPCC scenario RCP-8.5 in 2030 the area affected by permanent sea level flooding will range from $\sim 2,925 \text{ m}^2$ to $8,075 \text{ m}^2$, and the area affected by temporary storm flooding from $\sim 69,800 \text{ m}^2$ to $82,400 \text{ m}^2$; in 2050 the area affected by permanent sea level flooding will range from $\sim 4,550 \text{ m}^2$ to $15,750 \text{ m}^2$, and the area affected by temporary storm flooding from $\sim 79,400 \text{ m}^2$ to $98,400 \text{ m}^2$, and for the 2100 scenario the area affected by permanent sea level flooding will range from $\sim 15,750 \text{ m}^2$ to $43,900 \text{ m}^2$, and the area affected by temporary storm flooding from $\sim 100,800 \text{ m}^2$ to $723,600 \text{ m}^2$.
- Considering the ecosystemic services of the beach, especially those related to recreation, beach mean width is expected to be reduced:
 - For the IPCC scenario RCP-4.5 in 2030 by $\sim 20.32\%$ in average compared to its current state, and an average reduction of $\sim 27\%$ and $\sim 48.57\%$ in 2050 and 2100 respectively.
 - In relative terms and considering now the less favourable scenario (RCP-8.5), this represents a dry beach loss between 16.05% and 26.47% in 2030, between 19.59% and 41.69% in 2050, and between 41.69% and the 94.84% in 2100.

ENVIRONMENTAL DIMENSION

- The current coastal dune system of Cala Millor has lost over 99% of its original extent since 1956, now reduced to a small fraction of its initial size.
- *Posidonia oceanica* upper limit shows moderate fluctuations in the position of the upper boundary of the meadow over time. Although the changes between years are not drastic, a certain trend of retreat can be identified between 1956 and 1989. Upper limit comparison between 1956 and 2024 (398 m and 409 m respectively) shows that the upper limit has not undergone a substantial change over the last 70 years indicating stability in the system, albeit presenting periods with some fluctuations.
- For both RCP-4.5 and RCP-8.5 scenarios, *P. oceanica* density presents a large decline for 2050 with respect to the current state. This decline is notably higher at lower depths changing from the current 600 plants/m^2 to densities around 200 plants/m^2 . In 2100 for both RCP-4.5 and RCP-8.5, due to the sea water temperature increase, *P. oceanica* will totally disappear in Cala Millor.

SOCIOECONOMIC DIMENSION

- Global tourism demand models do not allow us to predict a substantial change in tourism demand that would affect the Cala Millor area. Local factors linked to rising temperatures and the loss of beach surface are what can determine the economic impact of climate change on Cala Millor.
- The total economic value of the Cala Millor area has been estimated at 2.673 billion euros. Rising temperatures, but especially the loss of beach surface area due to climate change, will lead to a loss in value of the area of between 25% and 83% depending on the scenario considered:
 - For the IPCC RCP-4.5 scenario in 2030 the lost value of the area ranges between 25% and 33%, in 2050 between 28% and 43% , and in 2100 between 35% and 67%.
 - For the IPCC RCP-8.5 scenario in 2030 the lost value of the area ranges between 26% and 42%, in 2050 between 29% and 48% , and in 2100 between 44% and 83%.

INDEX

EXECUTIVE SUMMARY.....	3
INTRODUCTION.....	8
1. DEFINITION OF FORCING SCENARIOS.....	10
1.1. Sea-level rise projections.....	10
1.2. Wave forcing: mean conditions and extreme conditions.....	11
1.2.1. Data Sources and validation.....	11
1.2.2. Characterization of extreme storm wave events for modeling.....	14
1.3. Sea water temperature projections.....	17
1.4. Atmospheric temperature projections.....	19
2. HAZARD ASSESSMENT: Application at Cala Millor.....	21
2.1. Physical Dimension.....	21
2.1.1. Data sources, quality control and numerical methods.....	21
2.1.1.1. Data sources and quality control.....	21
2.1.1.2. Numerical modelling.....	22
2.1.2. Conceptual Model of Cala Millor beach morphodynamics.....	24
2.1.2.1. Geomorphological context.....	24
2.1.2.2. Marine Climate.....	32
2.1.2.3. Sediment balance.....	37
2.1.2.4. Shoreline Evolution.....	50
2.1.2.5. Morphodynamic behavior of Cala Millor beach.....	53
2.1.2.6. Conceptual model.....	71
2.1.3. Hazard Assessment Physical Dimension.....	73
2.1.3.1. Model setup.....	73
2.1.3.2. Sea-level Scenarios and time-horizons.....	73
2.1.3.3. Wave forcing.....	75
2.1.3.4. Posidonia oceanica meadow conditions.....	75
2.2. Environmental Dimension.....	80
2.2.1 Coastal dune system.....	80
2.2.1.1 Historical changes of the Dune.....	81
2.2.1.2 Current state of the coastal dune.....	84
2.2.2 Posidonia oceanica meadow.....	87
2.2.2.1 Upper limit.....	87
2.2.2.2 Levels of burial and growth.....	89
2.2.2.3 Current status.....	91
2.2.2.4 Future projections for Posidonia oceanica meadows.....	93
2.3. Socio-Economic Dimension.....	99
2.3.1. The Worldwide context.....	99
2.3.2. Characterization of the economic activities of Cala Millor by cadastral parcels.....	100
2.3.3. Valuation of cadastral parcels.....	101

2.3.3.1. Hotels and other tourism accommodations.....	102
2.3.3.2. Commerce.....	103
2.3.3.3. Market value of the economic activity.....	104
2.3.4. Risk Assessment.....	106
2.4. Urban Dimension: Compound flooding.....	111
2.4.1. Rationale.....	111
2.4.2. Compound Coastal And Rainfall Flooding Impacts On Drainage Systems.....	112
2.4.2.1. Data and methods.....	112
2.4.2.2. Modelling StormWater Systems Functioning.....	114
2.4.3. Analysis of drainage system across different scenarios.....	116
2.4.3.1. Current State wo/w T100 wave storm.....	116
2.4.3.2. Future Projections for 2030.....	117
2.4.3.3. Future projections for 2100.....	119
2.4.4. Hazard assessment of compound flooding.....	120
3. IMPACT MAPS.....	123
3.1. Flooding maps.....	123
3.2. Posidonia oceanica meadow shoot density impact maps.....	134
3.3. Coastal dune impact maps.....	144
3.4. Compound flooding impact maps.....	145
BIBLIOGRAPHY.....	150
ANNEX 1. Historical photographs.....	156
ANNEX 2. Impact maps.....	161

INTRODUCTION

This document presents the implementation of an ad-hoc integrated multidisciplinary methodology for the assessment of impacts and associated risks of different progressive global change projections at Cala Millor (Mallorca, Balearic Islands) urban beach.

The methods implemented and the obtained results consigned in this deliverable respond to the following specific and main objectives of the LIFE ADAPT CALA MILLOR project Work Package 3 (WP3):

- Identification of the extent and implications of global change -namely sea level rise and sea climate- on the full beach system (beach and backshore dynamics, environment, urban and socio-economic systems);
- Assessing potential impacts and associated risks of different climate change scenarios at the beach site embracing physical, environmental and the socio-economic dimensions individually and as a whole;
- Developing a systematic, replicable and integrated methodology to assess climate change hazards and risks at urban beaches.

The content of each section is in line with the tasks described in the Action Description of Grant Agreement-101074227-LIFE21-GIC-ES-LIFE AdaptCalaMillor (p. 83 to 88), as set out in the following table:

Deliverable D3.4 Section	Task description at Grant Agreement	Major products
1. Definition of forcing scenarios	T.3.2.1. Physical dimension T.3.2.2. Environmental dimension T.3.2.3. Socio economic dimension	<ul style="list-style-type: none"> • Sea-level rise projections • Wave forcing: mean and extreme conditions • Sea water temperature projections • Atmospheric temperature projections
2.1. Hazard assessment: physical dimension	T.3.2.1 Physical dimension Hazard assessment T.3.3.1 Physical dimension exposed elements and historical impacts at Cala Millor	<ul style="list-style-type: none"> • Beach context description • Marine climate analysis • Storms and extreme events characterization • Mean and storm/extreme conditions waves and currents modelling • Sediment budget analysis • Shoreline analysis at decadal, interannual and seasonal time-scale. • Beach conceptual morphodynamic model • Permanent marine flooding maps under RCP-4.5 and RCP-8.5 sea-level scenarios and time horizons, and different contorn conditions. • Temporal marine flooding maps related to wave storms and extremes under RCP-4.5 and RCP-8.5 sea-level scenarios and time horizons, and different contorn conditions.

2.2. Hazard assessment: environmental dimension	T.3.2.2 Environmental dimension Hazard assessment T.3.3.2 Environmental dimension exposed elements and historical impacts at Cala Millor	<ul style="list-style-type: none"> · Evolution and current state of the coastal dune system at Cala Millor. · Evolution and current state of <i>Posidonia oceanica</i> meadow at Cala Millor. · Maps of <i>P. oceanica</i> extensions and density under RCP-4.5 and RCP-8.5 sea-water temperature scenarios
2.3. Hazard assessment: socio-economic dimension	T.3.2.2 Socio-economic dimension Hazard assessment T.3.3.3 Socio-economic dimension exposed elements and historical impacts at Cala Millor	<ul style="list-style-type: none"> · Characterization of the economic activities of Cala Millor by cadastral parcels. · Direct and indirect valuation of cadastral parcels. · Analysis of Cala Millor economic valuation under RCP-4.5 and RCP-8.5 coastal flooding and air temperature scenarios.
2.3. Hazard assessment: urban dimension	T.3.2.4 Urban dimension Hazard assessment T.3.3.4 Urban dimension exposed elements and historical impacts at Cala Millor	<ul style="list-style-type: none"> · Characterization of compound coastal and rainfall flooding impacts on urban drainage systems. · Analysis of urban drainage systems under RCP-4.5 and RCP-8.5 scenarios.
3. Hazard maps	T.3.4.1 Physical dimension risk assessment T.3.4.2 Environment dimension risk assessment T.3.4.3 Socio Economic dimension T.3.4.4 Urban dimension	<ul style="list-style-type: none"> · Permanent marine flooding maps under RCP-4.5 and RCP-8.5 sea-level scenarios and time horizons, and different contorn conditions. · Temporal marine flooding maps related to wave storms and extremes under RCP-4.5 and RCP-8.5 sea-level scenarios and time horizons, and different contorn conditions. · Maps of <i>P. oceanica</i> extension and density decrease under RCP-4.5 and RCP-8.5 sea-water temperature scenarios. · Maps of urban drainage compound flooding and urban elements affected by permanent and extreme coastal flooding under RCP-4.5 and RCP-8.5 sea-level scenarios and time horizons, and different contorn conditions.

Please note that tasks T.3.2.4, T.3.3.4 and T.3.4.4 were not previously considered in action descriptions and the contract agreement, but they have been incorporated to improve the risk assessment, and as a basis to test the contribution of the different possible adaptation solutions to the risk mitigation.

1. DEFINITION OF FORCING SCENARIOS

In climate research, socio-economic and emission scenarios offer plausible projections of how the future might unfold across various factors, such as socio-economic developments, technological advancements, energy and land use changes, and emissions of greenhouse gases and air pollutants. These scenarios serve as inputs for climate model simulations and form the basis for evaluating potential climate impacts, mitigation strategies, and associated costs.

In this report we used the Representative Concentration Pathways (RCPs) scenarios, named based on their radiative forcing target levels for 2100. Radiative forcing estimates account for the impact of greenhouse gases and other influencing agents. These were adopted in the IPCC 5th Assessment Report to evaluate policy and socio-economic impacts from climate change. In this Project in particular, we will use two of the available RCPs (see van Vuuren *et al.*, 2011): the RCP-4.5, which represents a medium stabilization scenario, and the RCP-8.5, also known as “business as usual”, which corresponds to a high baseline emission scenario.

1.1. Sea-level rise projections

Following the regional study by Luque *et al.* (2021), the climate scenarios RCP-4.5 and RCP-8.5 are used. Projections of regional sea level rise are obtained using the methodology developed by Kopp *et al.* (2014) (Fig. 1). The factors contributing to global mean sea-level rise (MSLR) include ocean thermal expansion from ocean heat uptake and water mass addition from the melting of mountain glaciers and ice sheets. Regional sea level changes deviate from the global mean due to regional climate processes, such as differential heat uptake, ocean circulation and atmospheric pressure and wind changes. Also gravity variations due to land surface mass changes, mostly from continental land-ice melting induce patterns of sea level change. All these processes are accounted for in the methodology used here to estimate regional mean sea level projections.

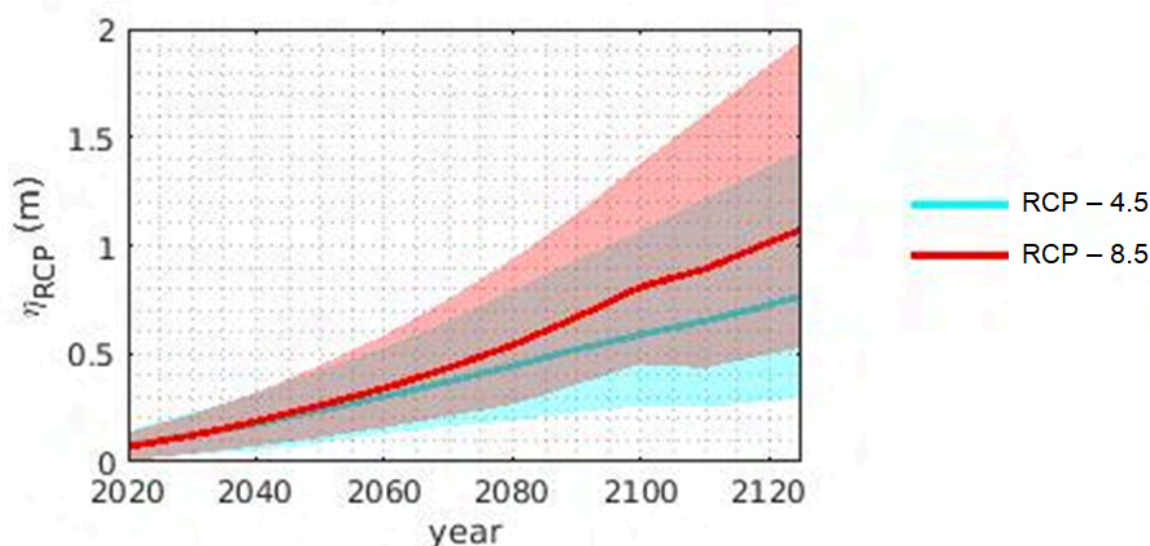


Figure 1. MSLR projections under RCP-4.5 (blue) and RCP-8.5 (red) climate scenarios. Solid lines indicate the multi-model ensemble median and shadowed regions indicate the 5–95% probability intervals.

1.2. Wave forcing: mean conditions and extreme conditions

1.2.1. Data Sources and validation

To compute the synthetic wave forcing, sufficiently long-term data of local wave conditions and sea level is necessary. Considering the in-situ data available from the SOCIB Beach Monitoring system, which has been operating since 2011, the duration is not long enough to provide a reliable synthetic extreme storm for a 100-year return period. Therefore, we have relied on the available hindcast data to calculate the reference storms (Fig. 2). The available hindcasts are:

i) ERA5

ERA5 is the fifth generation ECMWF atmospheric reanalysis of the global climate covering the period from January 1940 to present. ERA5 is produced by the Copernicus Climate Change Service (C3S) at ECMWF. ERA5 provides hourly estimates of a large number of atmospheric, land and oceanic climate variables. ERA5 includes information about uncertainties for all variables at reduced spatial and temporal resolutions. The ERA5 dataset contains one (hourly, 31 km) high resolution realization (referred to as "reanalysis" or "HRES") and a reduced resolution ten member ensemble (referred to as "ensemble" or "EDA"). The ensemble is required for the data assimilation procedure, but as a by-product also provides an estimate of the relative, random uncertainty. Generally, the data are available at a sub-daily and monthly frequency and consist of analyses and short (18 hour) forecasts, initialized twice daily from analyses at 06 and 18 UTC. Most analyzed parameters are also available from the forecasts. However, there are a number of forecast parameters, e.g. mean rates/fluxes and accumulations, that are not available from the analyses.

The data are archived in the ECMWF data archive (MARS) and a pertinent sub-set of the data, interpolated to a regular latitude/longitude grid, has been copied to the C3S Climate Data Store (CDS) disks. On the CDS disks, where single level and pressure level data are available, analyses are provided rather than forecasts, unless the parameter is only available from the forecasts. The interpolation software (MIR) was updated when the ERA5 production was moved to the new ATOS HPC on 24 October 2022. Details can be found at <https://www.ecmwf.int/en/forecasts/dataset/ecmwf-reanalysis-v5>.

ii) CoExMed

This dataset developed at IMEDEA was created from the fully-coupled hydrodynamic and wave model SCHISM (Zhang *et al.*, 2016), an upgraded version of the original SELFE model (Zhang and Baptista, 2008), which was designed to perform the generation and propagation of storm surges and wind-waves in the Mediterranean Sea (Toomey *et al.*, 2022). The model allows to perform simulations with its 2DH barotropic mode alone (hydrodynamic simulation) and fully coupled (hydrodynamic-wave coupled simulation) with the spectral wave model WWM-III (Roland *et al.*, 2012). Both modules share the same unstructured grid covering the whole Mediterranean basin, with an open boundary defined as a 15° semi-circle extending west from the Strait of Gibraltar. The strait plays a key role in water exchanges between the Mediterranean Sea (e.g. tidal flows, along-strait wind setup) and the Atlantic Ocean, and accounting for these processes is important to accurately simulate variations in sea surface elevation within the basin, especially for long periods of time. The model domain includes the western side of the Strait of Gibraltar to account for the region where

alongshore winds induce Atlantic-Mediterranean wind driven sea level differences (Menemenlis *et al.*, 2007). At the open boundary, the sea surface elevation is forced with the hydrostatic equilibrium formulation (the so-called inverted barometer effect), since atmospheric pressure is a major driver of barotropic sea level variability in the open ocean. Over the entire domain, the SCHISM model is forced with 10 m above sea level hourly wind fields and mean sea level pressure ($1/4^\circ$ spatial resolution) that are obtained from the ERA5 reanalysis dataset for the 1950-2022 period (Hersbach *et al.*, 2020). The grid size varies between 20 km in the deep ocean down to 200 m at the coast. Tides were not considered and the total wave spectral energy was distributed over 24 frequencies and 36 directions ranging from 0.04 to 1 Hz and $0-360^\circ$, respectively.

From the CoExMed hindcast data we selected a node located inside Cala Millor beach at 30 m depth that includes significant wave height, wave period and storm surge at hourly output since 1940. Astronomical tides were computed using UTide software (Codiga *et al.*, 2011) to reconstruct the time series of the nearest tide gauge.

iii) Wave historical runs and projections

With a similar model setup as described in Toomey *et al.*, (2022) and above, SCHISM is implemented with surface wind fields from twelve Euro-CORDEX GCM-RCMs for historical periods (1979-2005) and future projections (2034-2060 and 2074-2100) under the climate scenarios RCP-4.5 and RCP-8.5. These additional wind fields have temporal resolutions of 6-h (5 models) and 3-h (7 models), along with a 0.11° spatial resolution. The generation and propagation of wind-waves are performed using an unstructured mesh with a horizontal grid resolution ranging from ~ 10 km in the open ocean down to ~ 2 km at the coast. This setup provides output wave bulk parameters at hourly temporal resolutions over the Mediterranean Sea. A grid point close to Cala Millor has been selected.

iv) IHCantabria DOW Dataset (Downscaling Ocean Waves)

The provided wave data is part of the DOW (Downscaling Ocean Waves) dataset, developed by IHCantabria. The DOW database offers high-resolution coastal wave information and hourly wave parameter series over historical periods (hindcast products) of more than 30 years, ensuring a robust characterization of the maritime climate. The initial hindcast coastal wave data for DOW has been generated within the framework of the CoCliCo ("Coastal Climate Core Services") project, (H2020-LC-CLA-2020-2).

The hindcasts have undergone comprehensive evaluation, considering both total and extreme analyses of the main variables, to determine the most accurate match with the data. This selected hindcast will serve as the basis for constructing extreme reference storms. Table 1 summarizes the absolute error of H_s for each dataset with respect to observations considering all the data (total error) and also different ranges of wave heights.

To determine the best fit of the provided datasets, the return period of the maximum annual wave height has been computed for each set, considering only the common time period with the in-situ observations (Fig. 3).

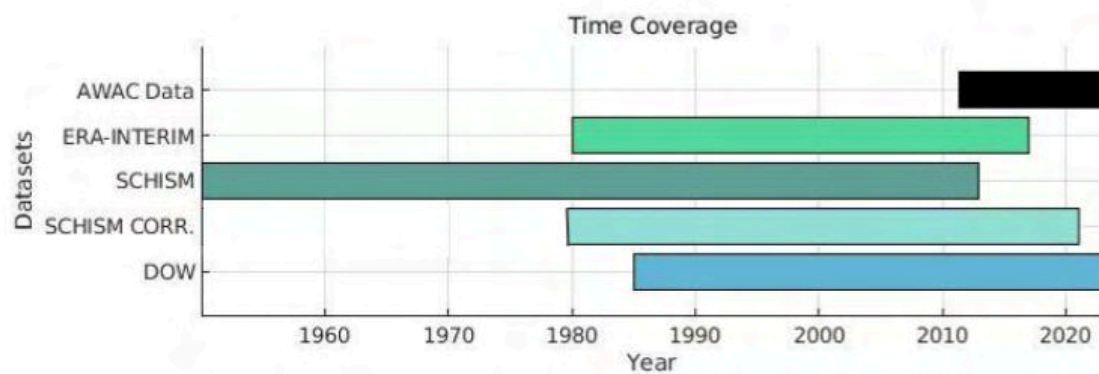


Figure 2. Time coverage of the available wave height, wave period and wave direction datasets.

	Total error ε_t	H_s ranges				
		0 - 0.5 m	0.5 - 1 m	1 - 1.5 m	1.5 - 2 m	> 2 m
ERA5	0.51	0.16	0.21	0.30	0.34	0.56
CoExMed	0.49	0.08	0.14	0.21	0.44	0.68
SCHISM-CORRd	0.13	0.08	0.15	0.21	0.37	0.50
DOW	0.19	0.16	0.21	0.27	0.34	0.45

Table 3. Absolute mean error of the assessed wave hindcast data.

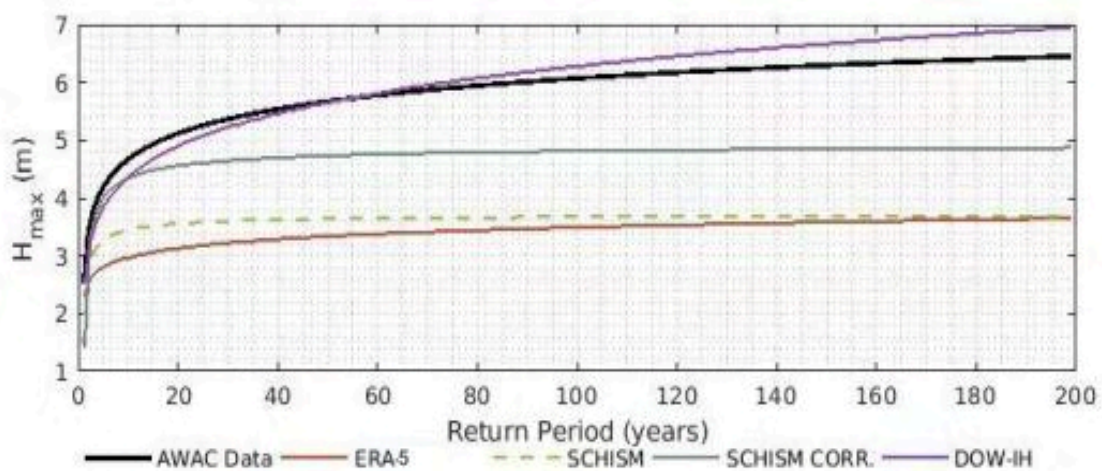


Figure 3. Maximum wave height return period for each data set.

1.2.2. Characterization of extreme storm wave events for modeling

The design or reference extreme storm is estimated following the methodology of Fernández-Mora *et al.* (2022), using a multivariate probabilistic analysis of the variables in the storm definition tuple, along with the simulation of values for individual and bivariate variables beyond the range of extreme event data. The methodology for each step is described in the following sections.

a) Variables dependence

The main variable considered is the significant wave height H_s , as it defines storm events. Before performing the multivariate analysis, it must be ensured that the variables exhibit at least a minimal dependency or semi-dependency relationship. This analysis is conducted using Kendall's τ_K parameter (Kendall, 1938), which represents the statistical dependence between two variables, with a threshold set at 0.2 (Lin-Ye *et al.*, 2016). This preliminary analysis has been performed for the pairs $[H_s, T_p]$, $[H_s, M]$, and $[H_s, S_s]$ where T_p is the peak period, M the storm magnitude and S_s the storm surge. The dependency or lack thereof for the pair $[H_s, S_s]$ is crucial for characterizing the reference storm.

b) Marginal characterization

To characterize the T_{100} reference storm, it is necessary to analyze the extreme climatology and the relationships between variables beyond the data range. First, the marginal probability functions of the variables must be evaluated and fitted separately to simulate random variables (Fig. 4). The newly developed set of variables will serve as the basis for evaluating the multivariate characterization of the storms. Drawing on previous work in the marginal and bivariate characterization of surge storms (Goda *et al.*, 1992, de Michele *et al.*, 2007, Bernardino *et al.*, 2008, Soldevilla *et al.*, 2015, Ministerio de Fomento, (2009), Lin-Ye *et al.*, 2016, Lira-Loarca *et al.*, 2020) and after a preliminary analysis, different theoretical distributions (Sadegh *et al.*, 2017; Sadegh *et al.*, 2018) are considered for H_s , T_p , and M . Among these, the primary distributions to be considered are Weibull (WEI), Gumbel's de minimis (GEV), and Lognormal (LGN) distributions (Martin-Hidalgo *et al.*, 2014). Since the storm magnitude M intrinsically includes the storm duration D , M is used as the base variable for determining the storm duration.

The extremal characterization of storm surges (S_s) has been conducted using the maximum S_s of the storm. To ensure the goodness-of-fit for the marginal distribution of extreme events, various preliminary analyses have been performed to identify the best-fitting theoretical distributions (Walton, 2000; Gaufres & Sabatier, 2005; Calafat & Marcos, 2020; Caruso & Marani, 2021).

The statistical analysis of the storm peak direction θ_p is a special case because it is a variable in circular coordinates. Many studies related to the multivariate characterization of storm phenomena do not consider θ_p , as it is not a relevant variable for their analysis purposes. Its characterization has been carried out using the Von Mises distribution (Berens, 2009). Similar to the previous variables, the distribution is fitted to the peak direction sampling. This analysis allows for determining the θ_p with the highest probability of occurrence during the storm state, and it is assumed to remain constant throughout.

The goodness-of-fit has been estimated using the EKS parameters, the p -value of the Kolmogorov-Smirnov test, and h_0 of the null hypothesis (Martin-Hidalgo, 2015). The smaller the EKS, the better the fit for p -value > 0.05 (fit likelihood). It should be noted that the Kolmogorov-Smirnov

test on a given fit can be positive even if the null hypothesis is rejected ($h_0=1$). If the null hypothesis fails for the considered distributions, a parametric fit distribution is used.

A marginal analysis has been conducted for each variable defining the storms $\{H_s, T_p, M, S_s\}$ at each point. For each variable, 5000 values have been simulated following the best-fitting marginal distribution to obtain variable values beyond the initial data ranges. These simulated values form the core of the multivariate characterization

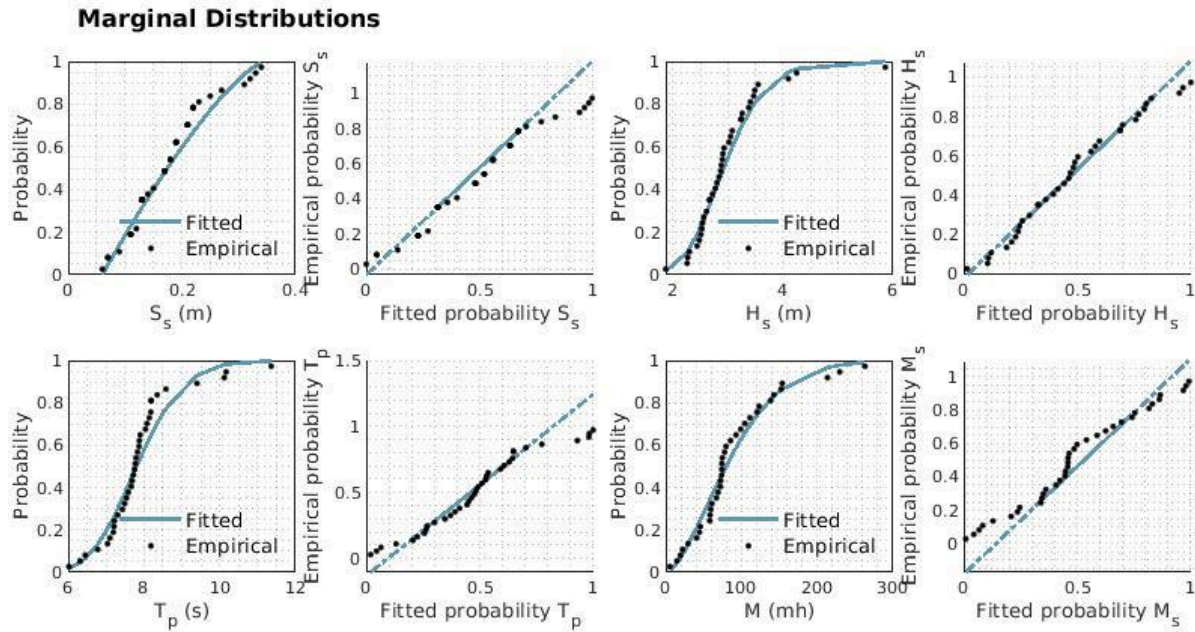


Figure 4. Marginal characterization for the variables H_s , T_p , M and S_s .

c) Join characterization

Previous studies on determining reference storms through multivariate analysis have focused on the joint characterization of the variables H_s , T_p , and M (de Michele et al., 2007, Soldevilla et al., 2015, Martin-Soldevilla et al., 2015, Lira-Loarca et al., 2020). In the present study, S_s is also considered in the joint characterization if it shows dependence on H_s . The multivariate analysis is based on fitting joint probability distribution functions, or copulas, of two or more variables. Thus, considering H_s as the main variable, extreme events are analyzed bidimensional by pairs of variables: $[H_s, S_s]$, $[H_s, T_p]$, and $[H_s, M]$, through the fitting of copulas to the simulated values in the marginal characterization. This involves fitting a surface to the bivariate distribution defined by each pair of variables using different theoretical bivariate distributions (Fig. 5). A preliminary compatibility analysis of bivariate distributions for the variables under study has been conducted (Martin-Soldevilla et al., 2015, Lira-Loarca et al., 2020). The goodness-of-fit of the copulas is assessed using the EKS and p-value parameters for bivariate functions, the χ^2 parameter, and the normalized mean square error (NMSE).

A corresponding multivariate analysis has been conducted for each pair of variables, and 5000 pairs have been simulated following the best-fitting copula distribution to obtain values beyond the ranges of the original data. These simulated pairs are used to characterize the reference storm.

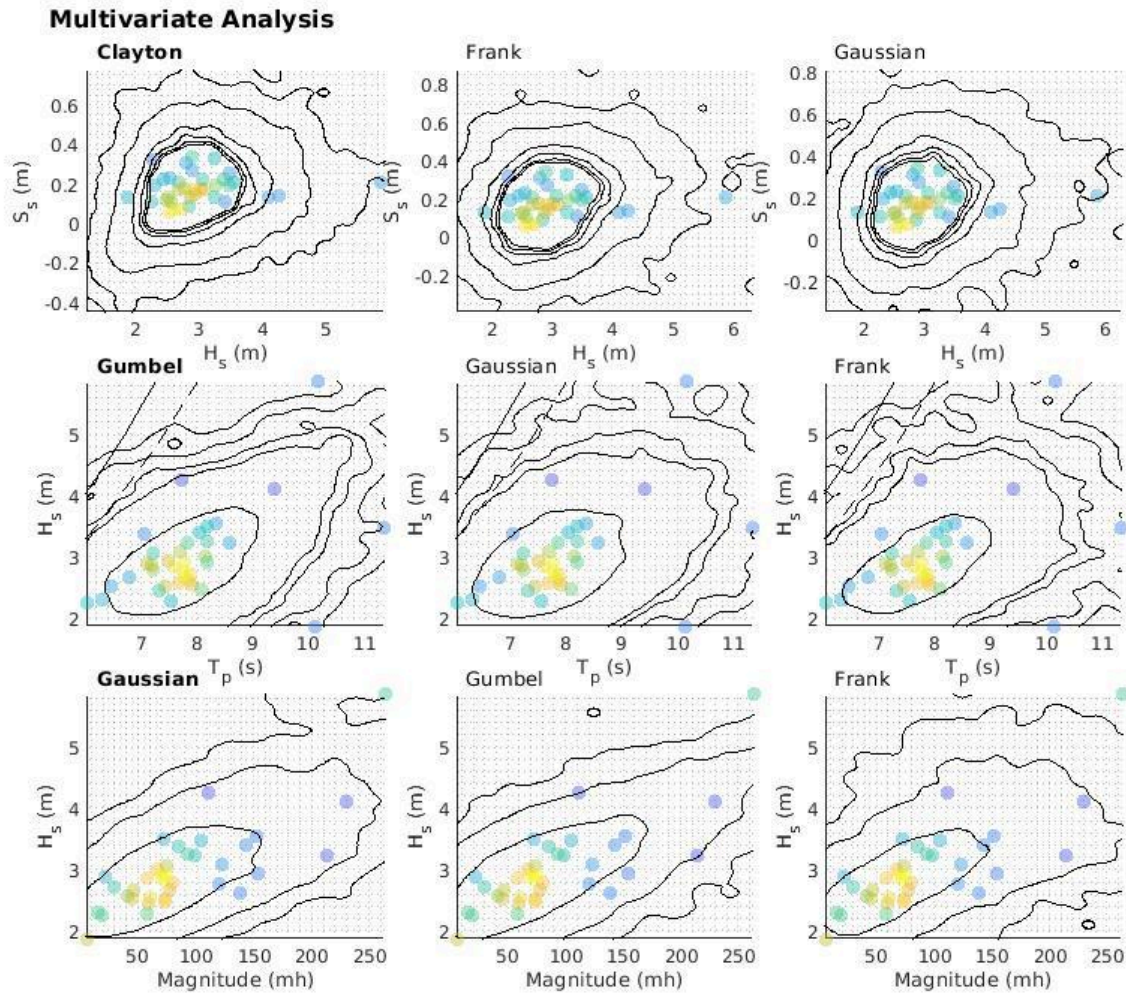


Figure 5. Multivariate Analysis results for the bivariate analysis [H_s - S_s], [T_p - H_s] and [Mag - H_s]. First column stands for winning copula for each pair and second and third columns stand for the second and third position of winning copulas, considering the goodness-of-fitting criteria.

d) Storm evolution

The variables of H_s , T_p , and S_s evolve throughout a storm, delineating a curve or storm shape. This shape is determined by its geometric form and the storm model, which defines the time series of the model's forcing variables. [Ministerio de Fomento \(2009\)](#) categorizes storms as triangular if they last less than 3 hours or trapezoidal if they are longer, without specifying the method for parameterizing the storm shape.

While adopting a centered triangular scheme for the storm is a common practice ([as seen in Luque et al., 2021](#)), for the sea level evolution during a storm), this analysis employs the trapezoidal shape. Its formulation allows for other shapes (isosceles, triangular, or trapezoidal) based on the average shape of storms used in its calculation ([Martin-Hidalgo et al., 2015](#); [Duo et al., 2020](#)).

To obtain the storm pattern, the n storms are initially normalized in both duration (t_i/D_i) and wave height through the normalization of the equivalent wave height, defined as $H_{eq} = H_i - H_{s,thres}$ as

$H_{eq}/H_{sp,i}$, where i represents each storm in the initial time series data. This yields a set of normalized storms for each point, with a range of [0, 1] in time and [0, 1] in wave height (Fig. 6).

For each normalized storm i , we search for the normalized coordinates $(x_{1,i}, y_{1,i})$ and $(x_{2,i}, y_{2,i})$ of the two major peaks. Thus, the peaks defining the reference normalized storm are determined by $\bar{x}_1 = \frac{1}{n} \sum_i x_{1,i}$, $\bar{y}_1 = \frac{1}{n} \sum_i y_{1,i}$ and $\bar{x}_2 = \frac{1}{n} \sum_i x_{2,i}$, $\bar{y}_2 = \frac{1}{n} \sum_i y_{2,i}$, where n equals the number of analyzed storms.

The storm model relates the storm magnitude and wave height with its duration. In the present analysis, the Equivalent Storm Magnitude (EMS) model (Martin-Hidalgo et al., 2015) is considered, in which the storm duration is determined such that its magnitude M equals that of the corresponding storm:

$$M_R = \frac{1}{2} H_{eq} D_{tr} (\bar{x}_1 \bar{y}_1 + (\bar{y}_1 + \bar{y}_2)(\bar{x}_2 - \bar{x}_1) + \bar{y}_2(1 - \bar{x}_2))$$

The reference magnitude, M_R , will be the one with the highest probability derived from the joint analysis $[H_s, M]$ for the reference wave height, H_d , of T_{100} .

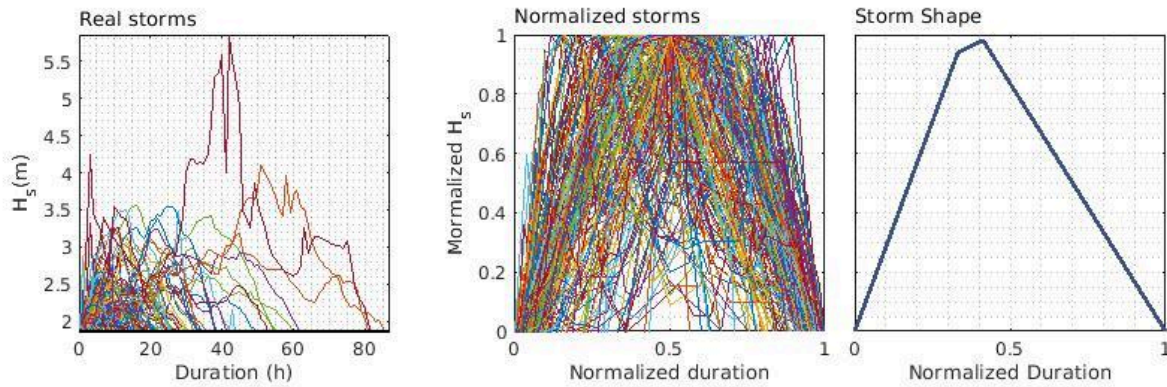


Figure 6. a) Storm duration respect to wave height from the analysis. b) Normalized storms; c) Normalized storm shape.

1.3. Sea water temperature projections

Global climate projections are simulations of the global climate system using general circulation models. These models are crucial for decision-making in climate change mitigation, adaptation, and impact assessment (Tebaldi et al., 2021).

The Coupled Model Intercomparison Project (CMIP) coordinates simulations of multiple coupled global climate models developed by research institutes around the world. This set of simulations is essential for the Intergovernmental Panel on Climate Change (IPCC) Assessment Reports (World Climate Research Programme, 2020).

The sixth phase of the CMIP (CMIP6), the most recent and central to the IPCC Sixth Assessment Report, includes advanced Earth system models (ESMs) and comprehensive climate experiments (Eyring *et al.*, 2016). It contains data from historical simulations spanning from 1850 to 2014 (Eyring *et al.*, 2016), projections for a set of eight new 21st-century scenarios based on Shared Socioeconomic Pathways (SSPs), and projections for different future emissions scenarios (RCPs). These provide different scenarios of future climate forcing, covering the period from 2015 to 2100 (O'Neill *et al.*, 2016).

CMIP6 simulations facilitate a better understanding of the past and present climate system, provide estimates of future climate change and its uncertainties, supply data for climate change adaptation, examine climate predictability, and assess the accuracy of models in simulating recent climate (World Climate Research Programme, 2020).

To obtain the climate projections of sea surface temperature, data from the Copernicus Climate Data Store platform¹ have been used. This catalog provides global daily and monthly climate data generated from computational models developed within the framework of CMIP6. The obtained climate projection data cover both two-dimensional and three-dimensional formats, allowing the application of spatial and/or temporal subsampling in the data request. These data are produced in NetCDF4 format and follow the Climate and Forecast Metadata Convention (CF-1.7 CMIP-6.2).

The CMIP6 climate models require adjustment to mitigate differences in the initial conditions of their projections, enabling all simulations to start from a common baseline and facilitating comparisons between models. To perform this adjustment, the average annual maximum temperature over the historical period 1980–2014 was calculated for each CMIP6 model using the simulated data corresponding to that interval. Additionally, the average annual maximum temperature observed by satellite during the same period was obtained and used as a standard derived from observational data.

The adjustment of the projections was performed using the following formula for every model independently:

$$Tmax_A = Tmax_p - Tmax_H + Tmax_{HSA}$$

where, $Tmax_A$ represents the maximum temperature adjusted for each projection year, $Tmax_p$ is the maximum temperature projected by the model for a given year, $Tmax_H$ corresponds to the average of the maximum temperatures simulated by the model between 1980 and 2014, and $Tmax_{HSA}$ is the average of the maximum temperatures observed by satellite during the same period.

This procedure corrects systematic deviations between model simulations and satellite observations, ensuring that the projections are better aligned with empirical data and providing a more robust foundation for comparative analysis of climate projections.

Output data were downloaded from 29 sea surface temperature models (Table 2) for the period 2024 to 2100 under two emission scenarios, RCP-4.5 and RCP-8.5. The spatial window to be analyzed was from 39° to 40° N and from 2°E to 3°E. These data allow us to perform a detailed analysis of the evolution of water surface temperature in this specific area during the time interval of interest.

¹ <https://cds.climate.copernicus.eu/cdsapp#!/dataset/projections-cmip6?tab=form>

Model	Country	Resolution
ACCESS-CM2	Australia	1.875° × 1.25°
CAMS-CSM1-0	China	1.1250° × 1.1215°
CanESM5-CanOE	Canada	2.81° × 2.81°
CESM2	USA	1.25° × 0.9424°
CIESM	China	1° × 1°
CMCC-CM2-SR5	Italy	1.3° × 0.9°
CMCC-ESM2	Italy	1.3° × 0.9°
CNRM-CM6-1	France	1.40625° × 1.40625°
CNRM-CM6-1-HR	France	0.5° × 0.5°
CNRM-ESM2-1	France	1.40625° × 1.40625°
EC-Earth3-CC	Europe	0.7° × 0.7°
EC-Earth3-Veg-LR	Europe	0.7031° × 0.7018°
FGOALS-f3-L	China	1° × 1°
FGOALS-g3	China	2° × 2.0253°
FIO-ESM-2-0	China	1.875° × 0.625°
HadGEM3-GC31-LL	UK	1.9° × 1.3°
IITM-ESM	India	1.875° × 1.904°
INM-CM4-8	Russia	2° × 1.5°
INM-CM5-0	Russia	2° × 1.5°
IPSL-CM6A-LR	France	2.5° × 1.2676°
KIOST-ESM	South Korea	1.88° × 1.88°
MCM-UA-1-0	USA	3.750° × 2.250°
MIROC6	Japan	1.406° × 1.4°
MIROC-ES2L	Japan	2.813° × 2.813°
MPI-ESM1-2-LR	Germany	0.9375° × 0.9375°
NESM3	China	1.875° × 1.865°
NorESM2-LM	Norway	2.5° × 1.9°
NorESM2-MM	Norway	1.25° × 0.9°
UKESM1-0-LL	UK	1.875° × 1.250°

Table 2. Information about the CMIP6 models in this study, including model name, originating group/country, and spatial resolution.

1.4. Atmospheric temperature projections

For the analysis of average summer temperatures in the years 2030, 2050, and 2100, the same methodology described in Section 1.3 was applied. Data from the Copernicus Climate Data Store platform were utilized, specifically the Near-Surface Air Temperature variable, which represents the air temperature at 2 meters above the surface of the land, sea, or inland waters.

For each of the selected years, daily average temperatures for the months of June, July, and August were calculated using atmospheric data simulated by the models. Additionally, historical average temperatures for the period 1980–2014, derived from both model simulations and satellite observations, were incorporated as a standard derived from observational data.

The atmospheric projections were adjusted using the formula:

$$T_A = T_p - T_H + T_{HSA}$$

where, T_A represents the adjusted average temperature for the months of June, July, and August in the projected years (2030, 2050, and 2100), T_p is the projected average temperature for each of these years, T_H corresponds to the average temperature simulated by the model between 1980 and 2014, and T_{HSA} is the satellite-observed average over the same interval. This procedure adjusts for systematic deviations between simulations and observations, ensuring better alignment with empirical data and providing a more robust foundation for comparisons between models and emission scenarios.

Output data were obtained from 24 near-surface air temperature models (Table 3) for the period 2024–2100 under two emission scenarios, RCP-4.5 and RCP-8.5. The spatial window analyzed spans from 39° to 40° N and from 2° to 3° E. These data enable a detailed analysis of the evolution of near-surface air temperature in this specific area over the time period of interest.

RCP-4.5				RCP-8.5			
YEAR	P25	P50	P75	YEAR	P25	P50	P75
2024	24.1°C	24.9°C	25.8°C	2024	24.1°C	24.8°C	25.2°C
2030	24.3°C	24.8°C	25.6°C	2030	23.4°C	25.0°C	25.8°C
2050	25.5°C	25.8°C	26.4°C	2050	24.9°C	26.1°C	26.6°C
2100	25.3°C	26.8°C	27.5°C	2100	28.6°C	29.4°C	29.9°C

Table 3. Daily summer averaged near-surface air temperature (June, July and August) for the period 2024–2100 under two emission scenarios, RCP-4.5 and RCP-8.5.

2. HAZARD ASSESSMENT: Application at Cala Millor

2.1. Physical Dimension

The hazard assessment for the physical dimension of Cala Millor beach has been developed following the methodology outlined in D3.1. To estimate coastal flooding and beach erosion under different RCP scenarios and time horizons, the following analyses have been conducted:

1. Conceptual model of Cala Millor beach morphodynamics
 - a. Geomorphological context
 - b. Wave climate
 - c. Shoreline evolution
 - d. Sediment balance
 - e. Morphodynamic behavior
 - f. Conceptual model
2. Hazard assessment
 - a. Coastal flooding
 - b. Potential beach erosion

The methodology applied in each analysis is detailed in the following sections, along with the respective results. Please note that the final outcomes of the hazard assessment, including coastal flooding and potential beach erosion maps, are provided in D3.5.

2.1.1. Data sources, quality control and numerical methods

2.1.1.1. Data sources and quality control

The data source used to analyze the marine climate corresponds to the Acoustic Wave and Current (AWAC) sensor located at 17.65 m depth and 1 km from the shoreline of Cala Millor beach (Fernández-Mora et al., 2023). This instrument provides precise and high-resolution hourly measurements of wave characteristics, essential for understanding the local wave climate (Figure 7). The wave and water depth dataset spans from 2011/05/20 up to the present day, except for a gap from 2019/05/20 to 2019/10/29 due to an instrument failure. The AWAC data records also account for the corresponding instrument error codes. These error codes enable the determination of data reliability². Data records that do not meet the determined quality standards are disregarded.

² Further details on the definition of AWAC error codes can be found at <https://www.nortekgroup.com/>.

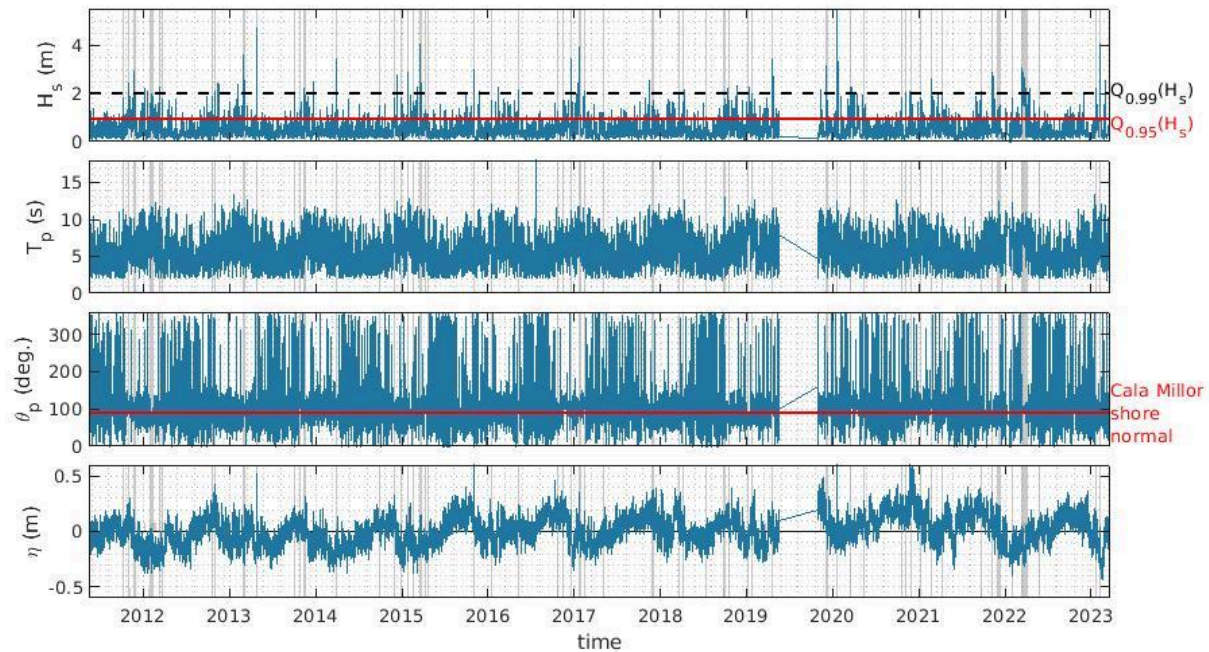


Figure 7. In-situ wave conditions measurements at Cala Millor (2011-2023). From up to down: Significant wave height (H_s); Peak period (T_p); Direction of the peak of the spectrum; and sea surface elevation.

Since 2011, regular topographic surveys at Cala Millor have been conducted twice a year: early summer (to capture winter storm effects) and mid-autumn (to capture summer wave conditions). A 6 m pneumatic boat with sonar and GNSS antenna surveys the shoreface from 1 m to 15 m depth. From 2011 to 2015, a single-beam echo-sounder was used; since 2015, a multi-beam echo-sounder has been employed. An RTK-GPS system measures sand levels in shallow waters and the dry beach. This system covers from 1.4 m depth to the upper beach edge, with paths spaced 10-15 m apart. All points are measured in ETRS89 with EGM08-IGN as the vertical reference. Until 2018, summer campaigns covered the entire beach, while winter campaigns only took profile measurements. Since autumn 2018, complete bathymetries are performed in all campaigns. Raw 3D point clouds are post-processed to remove outliers, resulting in high-resolution 1x1 m Digital Elevation Models (DEMs). Further details of measurement and postprocessing can be found at [Fernandez-Mora et al. \(2023\)](#).

Shoreline positions have been extracted from the georeferenced composite plan views of the 5 cameras of the SIRENA video-monitoring system located in the hotel “Castell de Mar” (39°59’N and 3°38’E WGS84 and at ~46m height) in Cala Millor beach, from 2012 to 2023, with a regular cadence of 15 days and around 10h UTC. The coastline data prior to 2012 were obtained by digitising the relevant information from available aerial orthophotography, corresponding to various years between 1950 and 2010.

2.1.1.2. Numerical modelling

The XBEACH model ([Roelvink et al., 2009](#)) is nowadays confirmed as a reference numerical model for coastal flooding and beach erosion. Its capabilities in simulating wave and hydrodynamic processes, sediment transport, and morphological changes allow for a comprehensive understanding of coastal

dynamics. By providing valuable insights into beach behavior under varying conditions, XBEACH supports decision-making, coastal management, and the development of strategies to mitigate coastal hazards and protect coastal environments.

a) Computational domain and grid

The computational domain covers 3.27 x 2.8 km, from Punta de n'Amer in the south to Cala Bona pocket beach in the north, and from 0.5 km inland from the promenade to 2.3 km offshore to a depth of ~25 m (Fig. 8, right panel).

The coordinate system used for modeling is a local coordinate system (x' , y') whose axis is located at the upper-right corner of the georeferenced computational domain and rotated 180°, as shown in (Fig. 8, left panel)

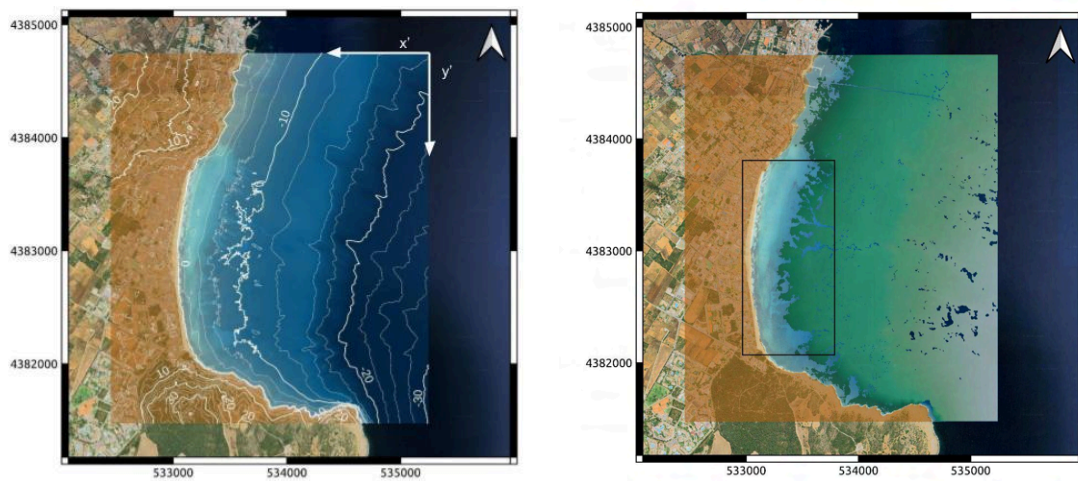


Figure 8. Computational domain for wave propagation at Cala Millor: a) topobathymetry and model coordinate system (x' , y'); b) *Posidonia oceanica* meadow extent. Black square stands for the high resolution topobathymetries area and sediment balance analysis domain.

b) Boundary conditions

i) Bottom conditions

The topo-bathymetry is a composition of high resolution topographies and bathymetries from different sources. The Digital Elevation Model (DEM) from the Spanish National Geographic Institute (IGN, 2019), with a resolution of 2.5 x 2.5 m, has been used to extend inland the topo-bathymetry beyond the regular area of regular topo-bathymetric bathymetric surveys. Bathymetry has been extended offshore considering the SideScan data from former habitats survey (2019-2020) developed by the oceanographic consultant Tecnoambiente.

ii) Lateral conditions

Lateral Neumann boundary conditions are applied. To prevent the creation of numerical shadow zones and to ensure more realistic wave group propagation, the gradient of wave energy along the crests is set to zero. Previous analyses have demonstrated the significance of considering Punta de

n'Amer in circulation patterns. To mitigate boundary effects in the nearshore area, the computational domain has been sufficiently extended to the north and south.

iii) *Posidonia oceanica* meadow conditions

To account for the effects of *Posidonia oceanica* in the XBEACH model, the parameters must be carefully considered. Key parameters include: N , the density of *P. oceanica* (number of plants per square meter), stem diameter b_v and leaf length α_h . Physical characteristics of the seagrass, such as stem diameter, leaf length, and leaf flexibility, influence the drag coefficient and the resulting energy dissipation. XBEACH can incorporate these through vegetation drag formulations that account for these morphological traits.

iv) Forcing

The model is forced from the offshore left boundary with the corresponding time-series of hourly wave and sea-level conditions of the related analysis (detailed in the following sections).

v) Model Calibration

The model has been calibrated in terms of sandbar migration, shoreline evolution and beach flooding considering the real case of the Gloria storm during 19-26 January 2020 (Fernández-Mora et al., 2025, in prep.), which were captured through extraordinary field campaigns during and immediately after the storm as well from the video-monitoring system at Cala Millor.

2.1.2. Conceptual Model of Cala Millor beach morphodynamics

2.1.2.1. Geomorphological context

The Bay of Cala Millor, situated in the eastern coast of Mallorca, is a coastal embayment measuring over 6 km in width and 2.7 km in depth. Its major axis extends from the northeast (NE) to the southwest (SW), with a predominant orientation towards the east-southeast (E-SE). Geomorphologically, the embayment is located at the confluence of two distinct physiographic units: the Marina de Llevant and the reliefs of the Serres de Llevant. The bay is delineated to the north by the Cap des Pinar headland, which is an extension of the Jurassic formations of the Son Jordi mountains (part of the Serres de Llevant), and to the south by Punta de n'Amer, marking the terminal outcrops of the Late Miocene platform along the eastern coast of the island (Marina de Llevant). In the outer area of the bay, depths of between 20 and 25 metres are reached (Fig. 9).

Within the bay, two primary beaches can be found: Cala Millor, which extends nearly 2 km, and Sa Marjal beach, which measures slightly over 500 m. Both beaches are associated with small coastal basins. The northernmost basin, related to Sa Marjal beach, is drained by the torrents of Xiclatí and Son Jordi, the latter of which has been modified near the coast, draining a former marshland. Inland, the basin is flanked by the rounded topography of the Serra de Pula and na Jordana to the northeast, and by Puig de Son Corb to the west (Fig. 9).

The southernmost basin, associated with Cala Millor beach, encompasses an area of 1,898.5 ha and is classified as a secondary basin (Fig. 10). In contrast to the adjacent basins, it exhibits a notable scarcity of significant river systems. It is important to highlight that Cala Millor beach marks the

coastal terminus of an alluvial plain, characterised primarily by an ambiguous drainage system, particularly in its central and southern sectors.



Figure 9. Location and physiographic context of Cala Millor. Image from the ICGIB orthophoto collection.

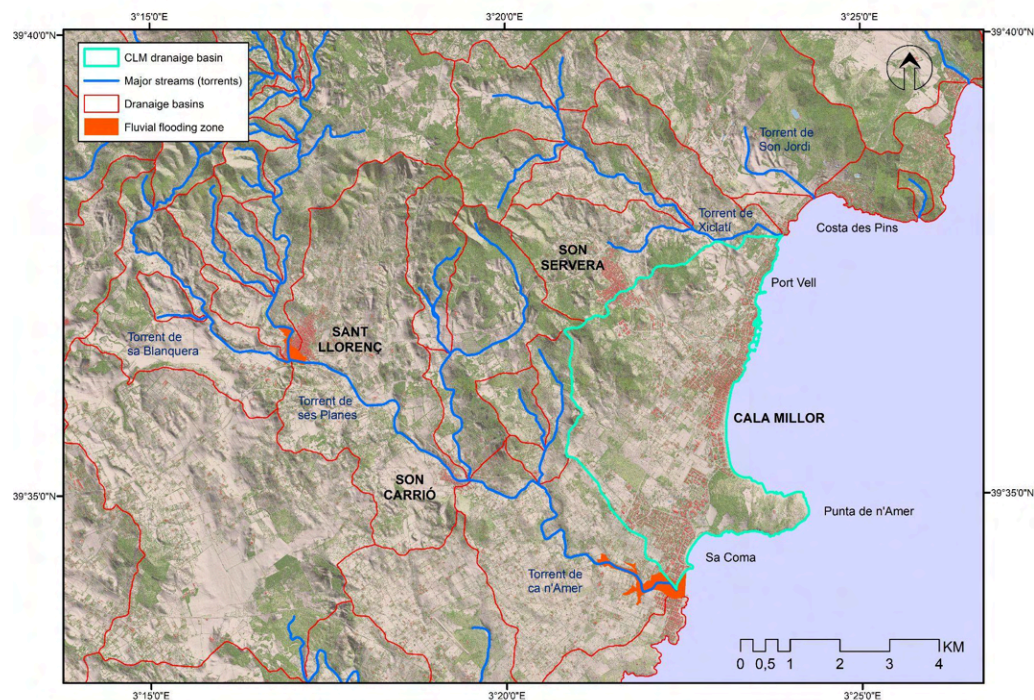


Figure 10. Drainage basins and fluvial flooding areas around Cala Millor.. Mapa base from the ICGIB.

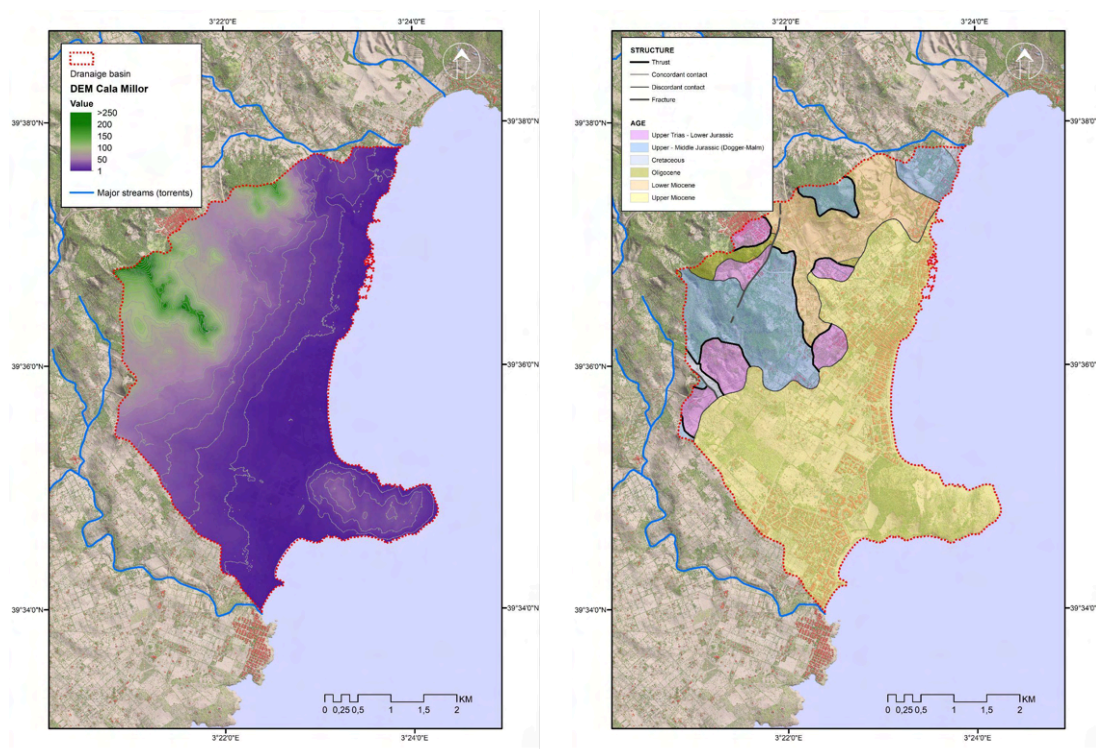


Figure 11. Cala Millor digital elevation model (left) and geological simplified map (right). Mapa base from the ICGIB.

In the Cala Millor basin, the highest elevations, which reach 271 m at Puig de sa Font, 200 m at Penyes Roges, and 181 m at Puig de Son Corb, correspond to the outcrops of Jurassic, Triassic, and Cretaceous materials associated with the folded reliefs of the Serra de Llevant (Fig. 11 left panel). In contrast, from 50 m above sea level down to the coastline, one encounters a gentler topography, which, although underpinned by calcarenitic materials from the Upper Miocene, is predominantly covered by Plio-Quaternary colluvial and alluvial deposits (Fig. 11 right panel).

From a geomorphological perspective, the transitions from gentle relief to alluvial glacia are characterised by the presence of minimally developed alluvial fans (Fig. 12). Distinct sectors of the alluvial plain can be identified, numbering three to four, extending from north to south. In the northern region, specifically in the vicinity of Es Port Vell, the proximity of the Serres de Llevant rock outcrops is indicative of a paleochannel that discharges into Port Nou. Historically, prior to 1956, this channel drained the lands of Son Corb until its course was redirected to flow through the Torrent Nou, located at the inlet of ses Bassetes. This area features a relatively flat ravine bottom, which was previously utilised for agricultural purposes; however, it has since undergone urbanisation in its coastal sector. This development carries a certain risk of flooding, as, despite being disconnected from its source area, the channel continues to facilitate and organise river flow during episodes of intense rainfall (Fig.12).

A second sector, situated between Port Vell and Cala Bona, is distinguished by a consistent glacia, within which the Torrent de Cala Millor is carved. In its final stretch, and within the Son Servera sector of Cala Millor, this watercourse has been artificially redirected to facilitate underground drainage at the tip of Ses Savines (Fig. 12).

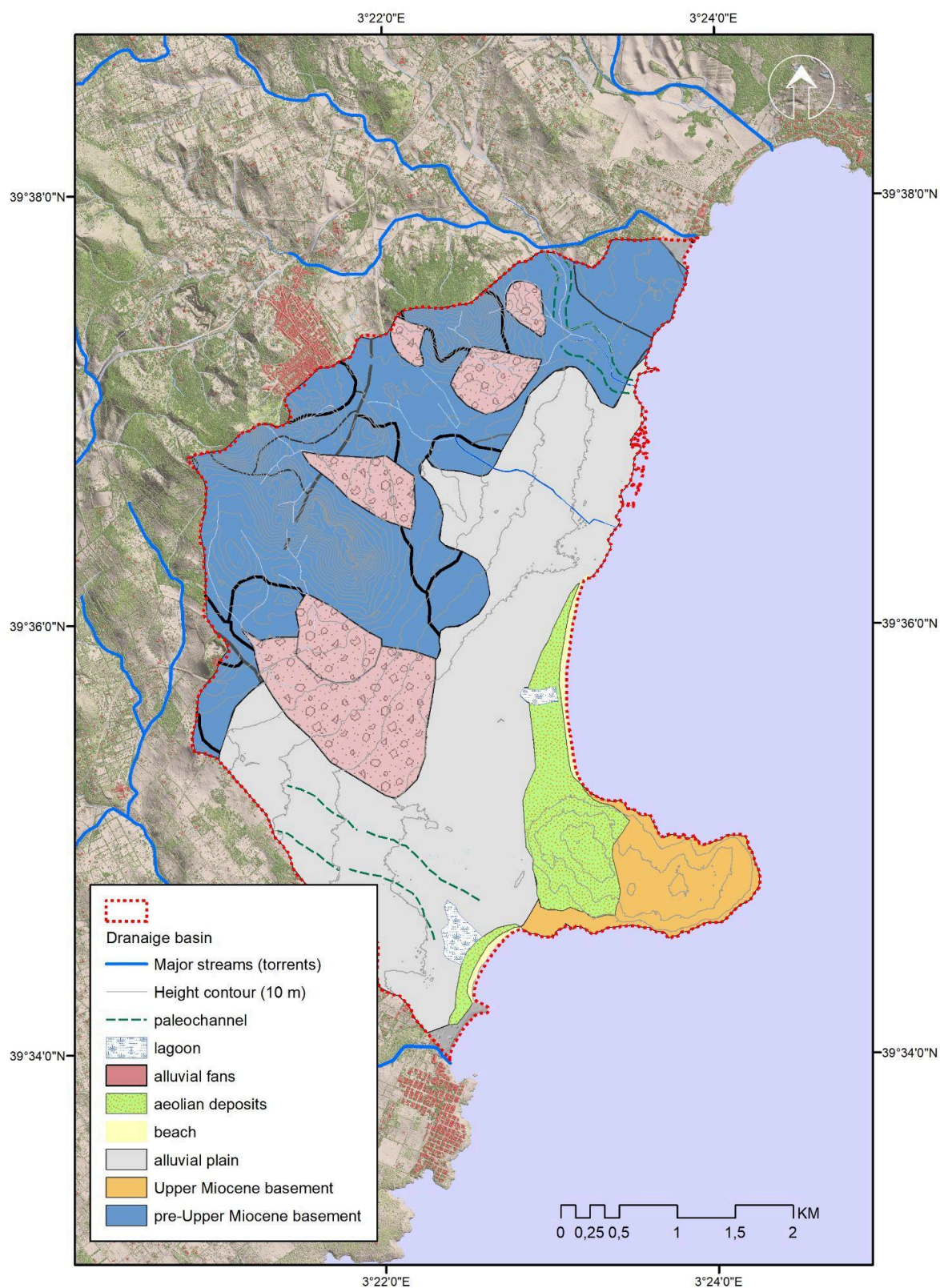


Figure 12. Cala Millor geomorphological sketch. Mapa base from the ICGIB.

The largest alluvial plain in terms of area is situated behind Cala Millor beach and is characterised by an arheic domain, lacking defined courses or preferred pathways for the circulation of surface water flows. This phenomenon is likely influenced by the calcarenite composition of the Upper Miocene basement, as well as the scattered Pliocene and Holocene dune formations that create a subtle crest, delineating the boundary between Pla de Son Moro and sa Coma. To the south of this subtle ridge, a paleochannel is evident, manifesting as a flat-bottomed ravine. This channel appears to be disconnected from the Son Amer torrent, to which it was seemingly once connected, as suggested by the surrounding topography (Fig. 12). The channel terminates at the beach of Sa Coma. Aerial photographs from 1956, predating urbanisation, reveal the presence of a dune system in the form of a sand barrier ridge -foredune-, which separates the beach from a modest wetland area.

Historically, a significant portion of the Holocene dune system associated with Cala Millor beach extended across this plain, enveloping and surpassing Punta de n'Amer, and approaching Sa Coma beach. However, much of this dune system has been considerably disrupted by human activity (Fig. 13). Today, only remnants can be found at the southern end of Cala Millor beach, where they create a transition zone between the beach and the elevated terrain of Punta de n'Amer. Additionally, stabilised and vegetated remnants of this dune system continue to exist on the surface of the Punta de n'Amer peninsula, where they are observable as an aeolian mantle (Fig. 14).



Figure 13. Views of Cala Millor beach and the dune barrier prior to its dismantling at the end of the 1960s. Left image: View to the south, highlighting the scale of the barrier system (approximately 4 m in height). Right image: View to the north, with notably low sea level. On the beach face, remnants of *Posidonia oceanica* necromass are visible (indicating temporary swash marks). Behind the woman, the remains of military defensive structures can be seen.

Although the coastal system is now highly anthropized, historical evidence from 1956 (Fig. 14) indicates that Cala Millor once formed part of a coastal barrier system that enclosed a lagoon and marshland. Aerial photographs from 1956 reveal the persistence of a barrier dune system, particularly in the southern sectors where dunes reached over 4 m in height. At that time, the lagoon had been drained for agricultural use, though the area still retains the toponym "s'Estanyol" (that means coastal lagoon in Catalan). Remnants of wetland vegetation and traces of former marsh channels remain as evidence of the previous landscape configuration (Fig. 14).

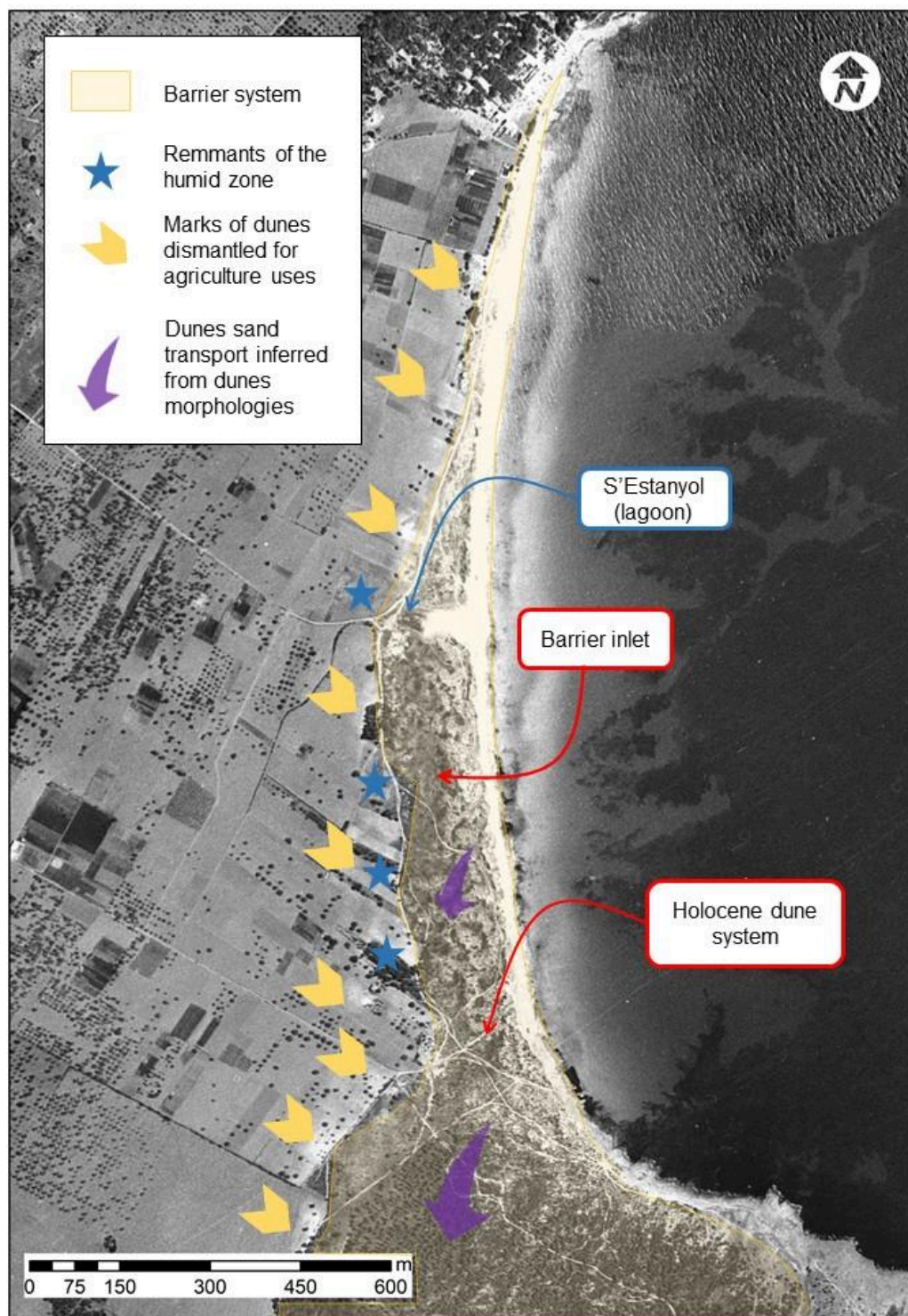


Figure 14. Remnants of Cala Millor barrier system in 1956. Image from the ICGIB orthophoto collection.

From a morphodynamic point of view, Cala Millor is a microtidal, carbonate sandy beach, extending over 2 km in length, with a concave shape and bordered by boulevard walls (Fig. 15). It is an intermediate beach, exhibiting a configuration of transverse and crescentic bars, along with notable

alongshore variability and the presence of rip channels (Gómez-Pujol *et al.*, 2007; Álvarez-Ellacuría *et al.*, 2011). The beach sediments at Cala Millor consist of medium carbonate bioclastic marine sands with a median diameter of approximately 1.8 phi (Gómez-Pujol *et al.*, 2011). These sediments correspond to a mid-Holocene attached regressive barrier that prograded landward through a foredune and a field of parabolic dunes.

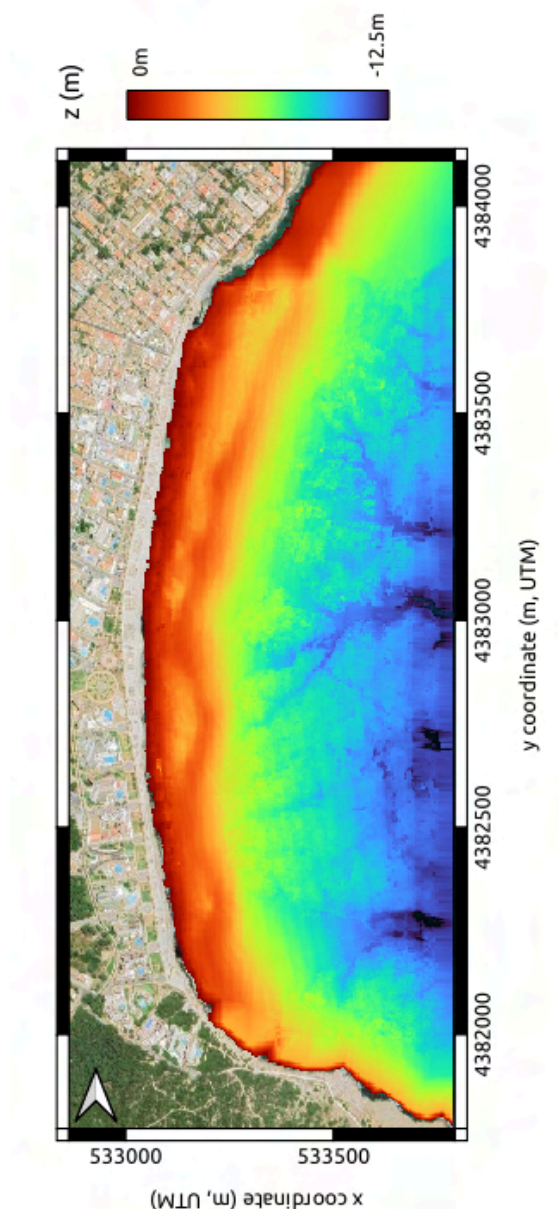


Figure 15. High resolution Cala Millor bathymetry (October 2019).

The seafloor is characterised by the exposure of rocky reefs (Fig. 16), especially in front of sa Màniga and Cala Nau sectors, and at depths ranging from 6 to 35 metres, paleochannels are present alongside a seagrass meadow dominated by the endemic *Posidonia oceanica* (Tintoré *et al.*, 2009). The nearshore bathymetry is further defined by a dendritic network of paleochannels, which fragment the seagrass meadows, observable from depths of 5 m to deeper areas. The principal

channel varies in width between 25 and 40 metres and disrupts the seagrass meadow continuously for more than 500 m in a crossshore direction (Fig. 16).

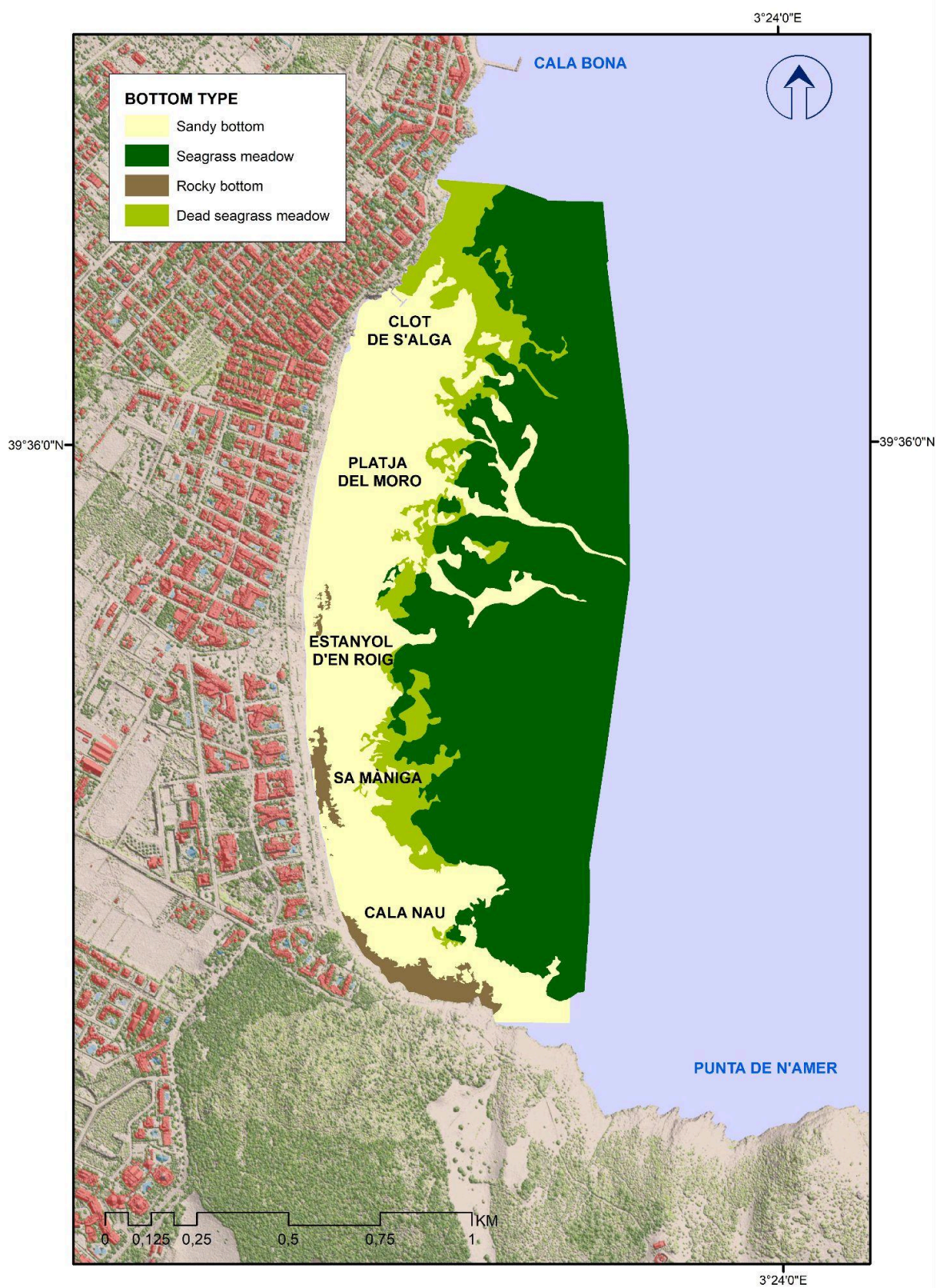


Figure 16. Bottom typology at Cala Millor bay.

2.1.2.2. Marine Climate

a) Sea-surface elevation

Sea-surface elevation $\eta(t)$ is computed by considering the time-averaged water column depth above the AWAC sensor provided by the instrument and the real depth of the instrument deployment assuming and hydrostatic pressure state. To extract the storm surges contribution $S_s(t)$ from $\eta(t)$ (Fig. 17a), two signals are analyzed from the original $\eta(t)$: the corresponding tidal oscillations $\eta_{tide}(t)$ and the inter-annual sea-level variation $\eta_i(t)$ due to inter-annual fluctuations of sea-temperature, internal oscillations in the Mediterranean basin, and the interaction of internal currents in the Western Mediterranean sea (Haddad *et al.*, 2013).

To assess long-term sea-level oscillations in the study area using in-situ measurements, a low-pass filter with a frequency of $2.3 \times 10^{-3} \text{ h}^{-1}$ is applied to the observed data (Fig. 17b). This filter effectively isolates the mid-term trends, allowing for a clearer analysis of sea-level changes over several years. By focusing on this specific frequency range, we can remove high-frequency fluctuations, such as daily or tidal oscillations, and focus on longer-term patterns.

Interannual oscillations are analyzed by applying a low-pass filter with a frequency of $2.7 \times 10^{-3} \text{ h}^{-1}$ (Fig. 17c). This filter enables the visualization of interannual variations, providing insights into sea-level changes that occur on a yearly basis. The choice of this specific frequency helps to distinguish between seasonal effects and the interannual variability of sea-level changes, offering a more detailed understanding of the factors contributing to the observed variability.

To further refine the analysis, the T_tide model is applied to the filtered signal to extract tidal oscillations (Pawlowicz *et al.*, 2002). The T_tide model is a well-established method for isolating tidal components, ensuring that the remaining signal accurately reflects non-tidal influences on sea level.

After removing both the tidal and interannual components, the remaining signal represents the residual sea-level η_{res} , isolating shorter-term processes such as surges (Fig. 17d).

b) Mean wave climate

Mean wave climate analysis involves the study of the average wave conditions in a particular region over an extended period. It includes the assessment of key wave parameters, such as wave height, wave period, and direction, which help define the long-term characteristics of wave climate in the area.

The mean wave climate has been studied both on an interannual and seasonal basis to better understand the variability of wave conditions over different time scales. Interannual studies focus on variations in wave parameters from year to year, often influenced by large-scale climate patterns. Seasonal studies, on the other hand, analyze how these wave characteristics change throughout the year, revealing patterns linked to shifts in atmospheric and oceanic conditions. This dual approach provides valuable insights into both long-term trends and short-term fluctuations in wave behavior.

The average wave climate at Cala Millor displays pronounced seasonality (Fig. 18). During autumn and winter, wave significant heights typically range from 0.5 to 0.7 m, gradually diminishing through spring and reaching an average height of 0.3 m in summer. This seasonal pattern is also observed in sea level fluctuations, as previously noted (Fig. 17 and Fig. 19). In addition, wave periods tend to be longer during winter months, transitioning to very short waves in summer, reflecting calmer sea conditions.

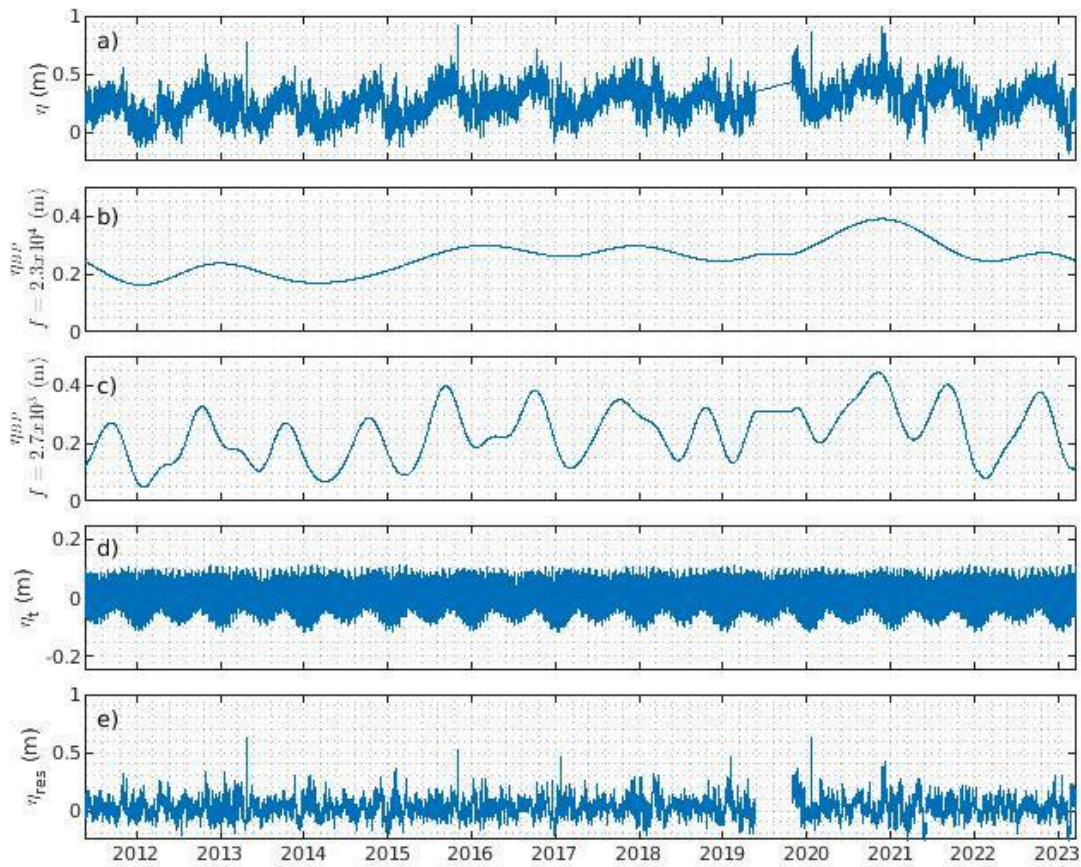


Figure 17. Sea surface elevation at Cala Millor. a) Sea-surface elevation from AWAC; b) BandPass filter at $f=2.3 \times 10^{-4}$ related to sea-level interannual variations; c) BandPass filter at $f=2.7 \times 10^{-3}$ related to seasonal sea-level fluctuations; d) tide fitting (astronomical tides); e) residual sea-level (surges).

The predominant wave direction varies slightly seasonally, generally shifting between E-ENE and E-ESE, which may influence local sediment transport and coastal morphology throughout the year.

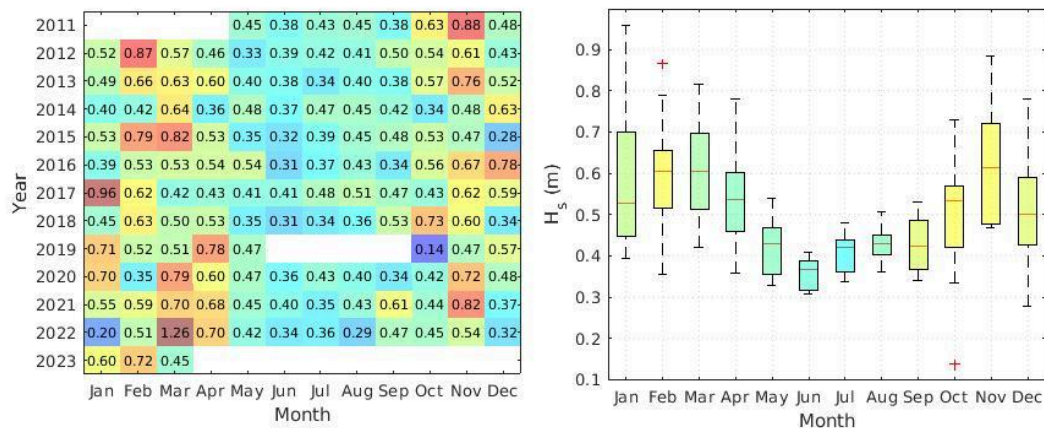


Figure 18. Cala Millor mean wave climate. Left: Monthly mean wave height (H_s) per year. Right: Mean, interquartile range, standard deviation and outliers of H_s per month.

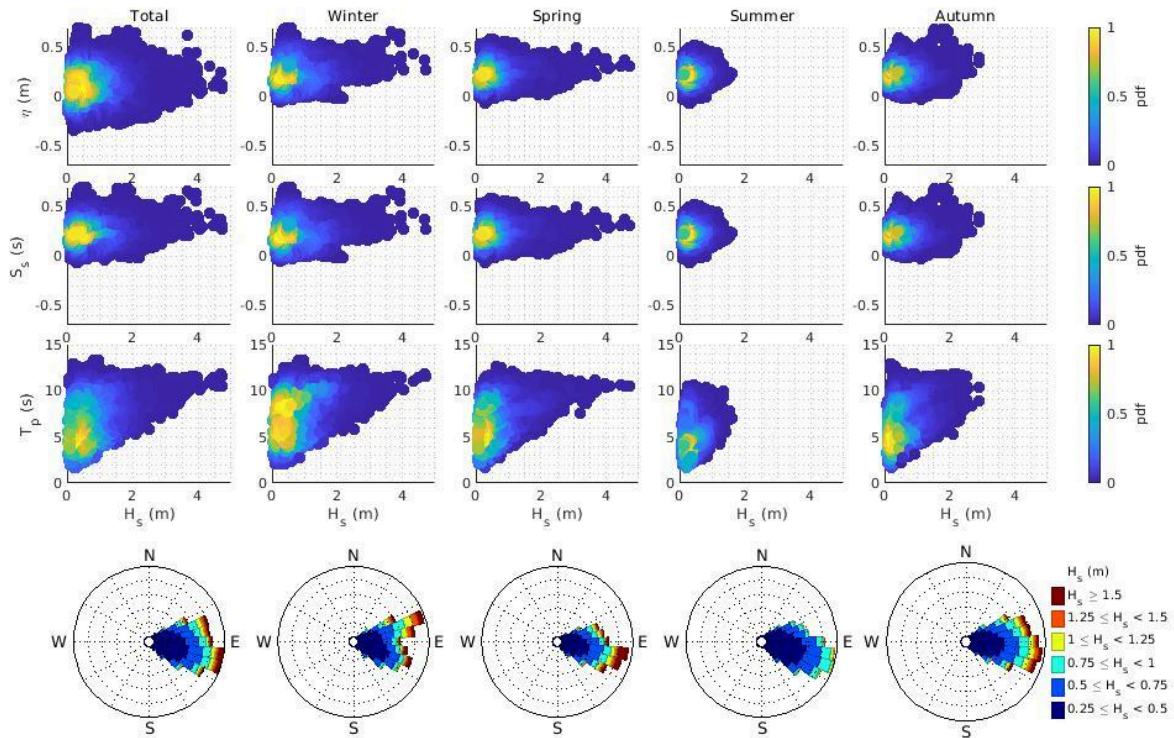


Figure 19. Annual and seasonal wave climate conditions. Upper panel: sea surface elevation (η_t) respect wave significant height (H_s); Middle upper panel) Surge (S_s) react to wave significant height (H_s); Lower Upper panel) Wave period (T_p) respect to wave significant height (H_s); Lower panel: Wave direction roses.

c) Storm and Extreme wave climate analysis

The identification of wave storms from a wave time-series uses the peak-over-threshold (POT) method, a robust approach from extreme data analysis to estimate the return period of environmental variables. In this method, data exceeding a defined threshold, corresponding to storm wave events, are extracted. The storm threshold $H_{s\text{ thres}}$ distinguishes storm events from regular ones, and storm duration D is the time from exceeding the $H_{s\text{ thres}}$ to the first instance where $H_s < H_{s\text{ thres}}$. A minimum storm duration D_{\min} is defined to account for rapid fluctuations around $H_{s\text{ thres}}$. To ensure independence between storm events (t_{ist}), a minimum time t_{\min} between events is set. There is no standard method for determining these parameters as local effects and climate conditions must be considered. The 95th percentile of the H_s time-series is commonly used as $H_{s\text{ thres}}$ in wave-dominated coasts (see Fig. 20).

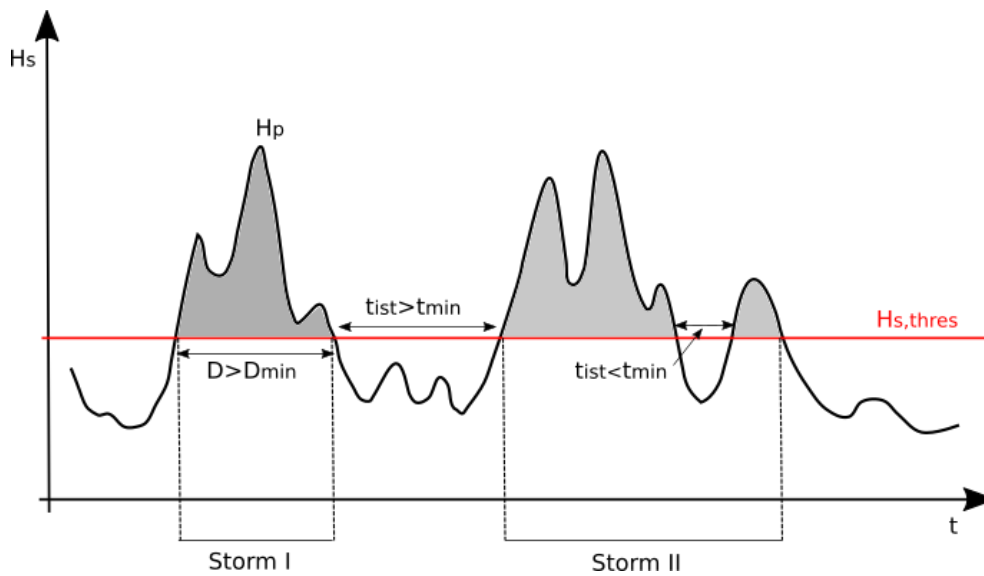


Figure 20. Definition of wave storm event.

In the current case, following previous works of wave climate and storminess patterns at the Balearic Islands (Cañellas *et al.*, 2007) and analyzing the AWAC data from 2012/01 until 2023/01, a wave **storm event** is defined considering the following conditions:

1. Wave height storm threshold ($H_{s,thres}$), as the quantile 95 of the H_s time-series at each reference point.
2. Minimum storm duration D_{min} , set to 6 hours over $H_{s,Q95}$.
3. The minimum distance between storms (calm duration) t_{min} , set to 72 h (Luceño *et al.*, 2006, Mendoza *et al.*, 2011), with consecutive events within this interval considered a single storm event.
4. Initiation/End $H_{s,Q75}$ (Masselink *et al.*, 2014).

Following this definition, a storm will be considered as **extreme** if additionally the second condition satisfies that the event lasts 6h over $H_{s,Q95}$ with 3h over $H_{s,Q99}$.

Average storm conditions in Cala Millor by year and month, along with annual statistics for the in-situ data are provided in Fig. 21. Energetic wave periods at Cala Millor are observed predominantly during the winter and autumn months, when both maximum and extreme values occur. Storm events are rare during the summer period. When analyzing extreme events (Fig. 21), defined by the 99th percentile of wave height, these are most frequently observed in mid-autumn and late winter. While sea level does not exhibit a clear seasonal pattern during storm events (Fig. 22 and 23), wave period and direction do show seasonality. Longer wave periods are associated with winter storms, while shorter periods are more common in other seasons. In terms of wave direction, winter storms display a distinct E-NE component, whereas spring storms are more variable, with a mix of E-NE and E-SE directions, the latter being predominant. Autumn storms, on the other hand, show a broader range of directions.

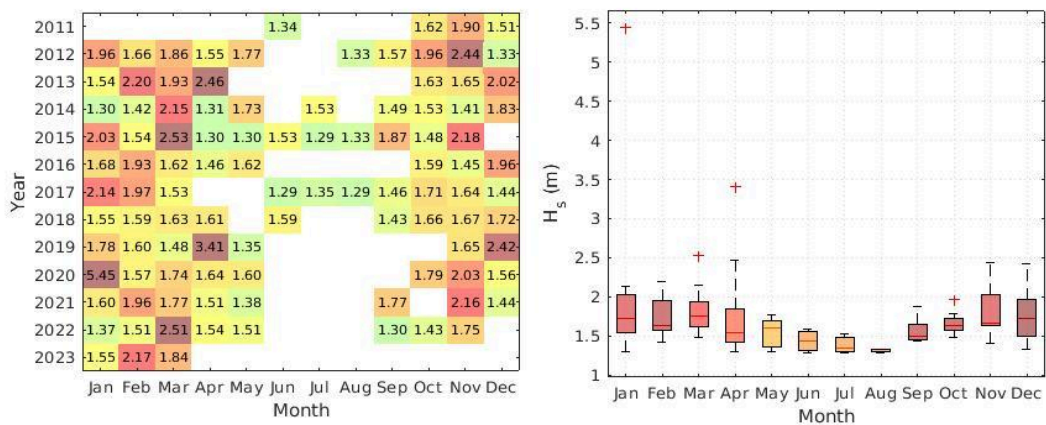


Figure 21. Cala Millor storm wave climate. Left: Matrix showing the temporal distribution of storm event wave significant heights (H_s) by month and year, with higher values represented in warmer tones. Right: Box and Whisker plot of wave significant height (H_s) from all years (2012 to 2023) by month.

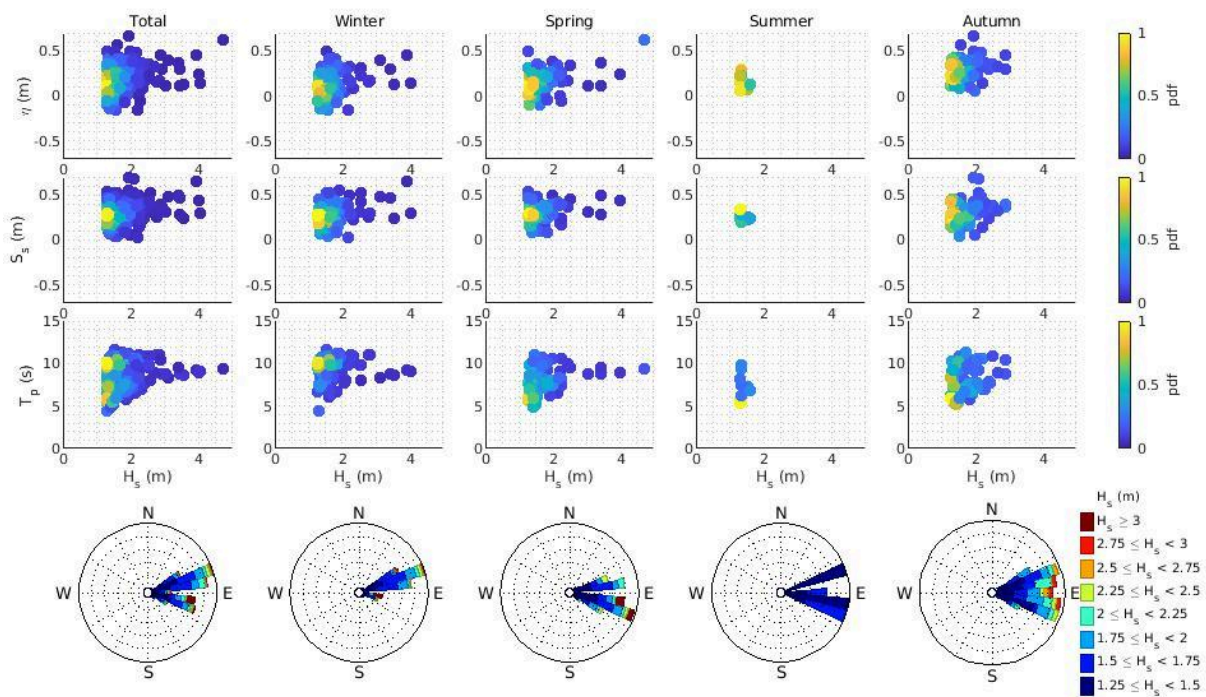


Figure 22. Annual and seasonal storm and wave climate conditions at Cala Millor: Upper panel: sea surface elevation (η_t) respect wave significant height (H_s); Middle upper panel: Surge (S_s) react to wave significant height (H_s); Lower Upper panel: Wave period (T_p) respect to wave significant height (H_s); Lower panel: Wave direction roses.

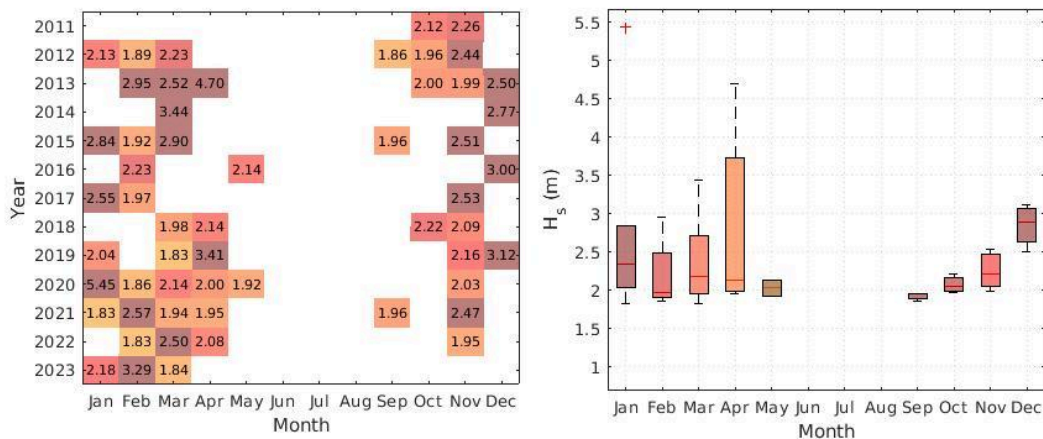


Figure 23. Cala Millor extreme wave climate. Left: Matrix showing the temporal distribution of extreme storm event significant wave heights (H_s) by month and year, with higher values represented in warmer tones. Right: Box and Whisker plot of significant wave height (H_s) from all years (2012 to 2023) by month.

Storms in Cala Millor follow a typical Mediterranean climate with more extreme events during winter and autumn reaching minima during summer season (Fig. 24). There is no clear signal of the frequency and duration of storms in the long term although longer series are necessary to analyze this in more detail (Fig. 24).

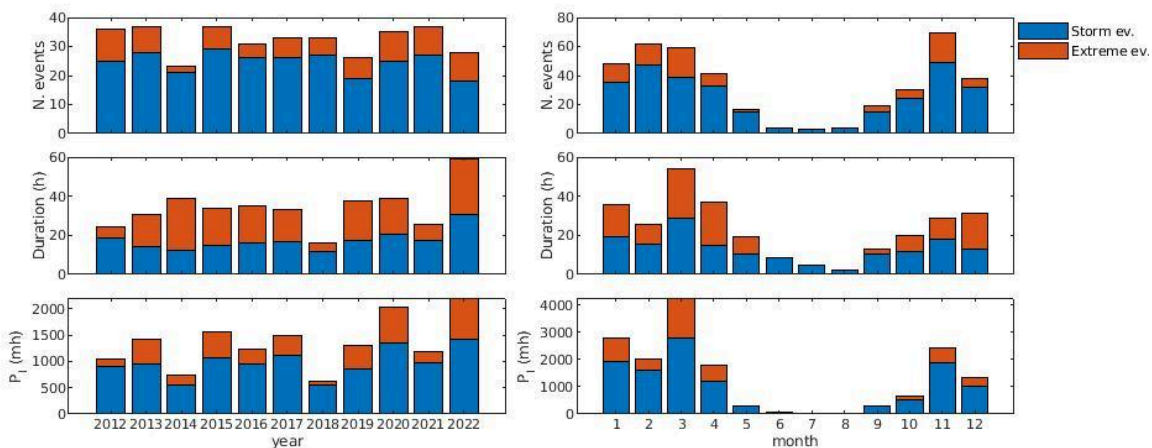


Figure 24. Average Number, Duration and Power index (maximum significant wave height multiplied by the storm duration; Dolan and Davis, 1992) of the occurred storms and extreme events per year in Cala Millor. Data from 2012/01 until 2023/01, SOCIB AWAC.

2.1.2.3. Sediment balance

Analyzing sediment balance using in-situ data is essential for understanding near-shore dynamics, as it provides precise insights into sediment transport processes, coastal erosion, and deposition patterns. The dataset described in Section 2.1.1.1 encompasses the frontal zone of the study area, extending to approximately 15 m depth. However, based on preliminary data analysis, the current

study considers sediment balance up to 10 m depth, corresponding to the depth-of-closure in this region. It should be noted that the surveyed area does not extend laterally toward the Cap de n'Amer or northward to the Cala Bona area. Nevertheless, it comprehensively captures the dynamics of the submerged sandbar, submerged canyons, and the entire dry beach.

In addition to analyzing the beach as a whole, the sediment balance has been divided into dynamic areas for each bathymetry, each representing distinct wave, current, and sediment transport processes -extending [Gómez-Pujol et al. \(2011\)](#) analysis from their eight-month 2004 experiment at Cala Millor-. The dynamic areas are defined as follows: the *dry beach*, corresponding to elevations above 0 m (emerged beach); the *surf and inner surf zones*, encompassing elevations between -4 m and 0 m, which include the breaking zone and the wave reforming zone (bore advection area); the *shoaling zone*, covering elevations between -6 m and -4 m; and the *outer zone*, comprising elevations below -6 m.

Several previous analyses have been conducted to assess the morphodynamics from topo bathymetries. To ensure that certain dynamics are not masked by the use of averages, the annual analysis has been adjusted to use bathymetries corresponding to the summer profile. Thus, the inter-annual sediment balance Δz_b is calculated as the difference between the summer bathymetries of consecutive years, while the intra-annual sediment balance focuses on variations within a single year (summer-winter profiles). In addition, the unitary balance ϵ_{zb} has been calculated as the balance divided by the corresponding area, providing an estimate of changes per square meter. Note that dynamic areas evolve on time. Given the intrinsic error of elevation measurements with the echosounder, estimated at approximately 0.05 m, any $\Delta z_b(x,y)$ values smaller than this threshold have been disregarded.

a) Inter-annual sediment balance: 2011-2022

As aforementioned, from 2011 to 2014, bathymetric surveys were carried out using a single-beam echosounder. Starting in 2015, these surveys have been conducted with a multi-beam echosounder. Consequently, interpolation of single-beam surveys may introduce errors when analyzing sediment balances. To minimize potential inaccuracies, the detailed analysis presented here focuses exclusively on complete bathymetric data from 2015 to 2022, although a brief description of morphodynamic changes is provided for all bathymetries. It is important to note that the 2016 bathymetry is truncated at -5 m, and no summer bathymetry data is available for 2018.

[Figs. 25, 26 and 27](#) show the analyzed bathymetries with the corresponding bottom changes. Table 5 summarizes Δz_b and ϵ_{zb} for each dynamic zone and years. In the following the annual changes are described:

2011-2012: While existing morphodynamic patterns cannot be clearly identified, during this period, accretion occurred in the surf zone and inner-surf zone. This was likely due to erosion in the dry beach area and, partially, sediment transport from the shoaling zone to these areas. The erosion observed in the outer zone is considered an artifact of using single-beam equipment for the survey. This area is dominated by the presence of *Posidonia oceanica* meadows, which generally exhibit very low bottom-change values, as identified in the analysis using high-resolution data.

2013-2012: Similar to the previous period, although the data do not allow for a detailed analysis of bedforms, accretion is again observed in the deeper part of the surf zone, while erosion occurs in its inner section. This suggests the formation or deepening of the trough and the formation or

growth of a sandbar, predominantly in the northern part of the beach. In contrast, the southern area exhibits erosive behavior across its dynamic zones.

2014-2013: Observing the 2014 bathymetry, a crescentic bar is evident along the beach, likely corresponding to the bedform changes identified in the previous period. The bottom-change pattern once again, particularly between the central and northern sections, shows bar growth in the outer part of the surf zone and erosion in the trough. Given the position of the bar, some offshore displacement is inferred, though this cannot be quantified clearly without data from earlier periods. Additionally, accretion is observed in the inner-surf zone, near the coastline. The southern zone continues displaying a clear erosive behavior, along with the dry zone, which exhibits localized accretion areas.

2015-2014: The crescentic bar remains evident in the 2015 bathymetry, now captured with high-resolution multibeam sounding. The erosion-accretion patterns suggest offshore migration of the bar, particularly in the southern area, accompanied by an increase in the crescentic form and the height of the bar lobes, as well as deepening of the bar troughs. Notably, the dry beach exhibits accretion across the entire stretch during this period.

2016-2015: The erosion-accretion patterns suggest the onshore migration of the sandbar during this period and in the central area it is almost attached to the dry beach. The inner-surf zone became stretched with sand losses of around 2,000 m³. An overall accretion is observed along the dry beach (unitary balance of +0.03 m), except at the southern/central area. Since 2016 bathymetry is truncated, no patterns can be identified at the shoaling and outer zones.

2017-2016: The dry zone appears to be experiencing an erosive episode with an average sand loss of 3,000 m³, particularly in the southern and central areas where these erosive patterns extend to the surf zone. However, this pattern differs with the northern area where accretion predominates, resulting in a positive balance in this surf zone of around 40,000 m³. In addition, an off-shore migration of the sandbar is observed.

2019-2017: Despite the period spanning more than two years between the selected bathymetries, it is interesting to observe that in the 2019 bathymetry, the crescentic sandbar is clearly identifiable. Patterns of accretion and erosion highlight the increased depth of the troughs and the height of the sandbar crest, with a slight offshore migration. The northern section of the dry beach shows evidence of erosion (a general loss of 8,000 m³ in the dry zone), accompanied by the widening of the inner-surf zone and the possible detachment of a secondary shallow sandbar in this area. However, a general erosion pattern is observed along the whole zone with sand losses up to 105,000 m³.

2020-2019: The 2020 bathymetry still shows evidence of the sandbar, although it appears more dispersed, with a deepening of the main rip channels. While there is a decrease in the height of the sandbar crest, particularly in the northern area, accretion in the shoaling zone (a positive balance of 25,000 m³) together with significant erosion in the surf zone (-51,000 m³) suggests the breakdown of the sandbar toward deeper areas. Additionally, during this period, both the dry beach (with a unitary balance of around +0.08 m) and the inner-surf zone in the southern and northern areas show accretion, while erosion is observed near the central part of the beach.

2021-2020: The 2021 bathymetry does not reveal a distinct sandbar but instead shows an enlarged inner-surf zone (positive sediment balance of 37,000 m³). Based on the erosion and

deposition patterns, the sandbar likely migrated onshore and merged with the inner-surf zone and shoreline. Additionally, the dry beach exhibits a clear accretion pattern during this period with a unitary balance of +0.03 m. Noteworthy, the shoaling and the outer zones analysis show a negative balance up to -51,000 m³ and -24,000 m³ respectively for both areas. Part of this erosive pattern in the shoaling zone can be attributed to the onshore migration of the sandbar.

2022-2021: In this period the offshore migration of the sandbar is again evidenced by both morphodynamic patterns analysis and sediment balance, resulting in a wider surf zone ($\Delta z_b \sim 34,000$ m³, $\epsilon_{zb} \sim 0.13$ m), an accretion pattern in shoaling and outer zones, but a detriment of the dry beach showing an overall erosion of $\sim 3,000$ m³ (-0.07 m).

Overall, it can be stated that Cala Millor beach, despite experiencing moderate wave energy, is a highly dynamic system characterised by significant changes in its topo-bathymetry. A comparison of bathymetric surveys with higher spatial resolution reveals that, in terms of sediment balance, a slight overall sediment deficit is observed (-0.14 m³/m²) within the context of three-dimensional changes. However, considering the limitations of the topo-bathymetric surveys, along with the recorded episodes of positive sediment balance, it is reasonable to infer that much of the sediment exiting the monitored area is not lost, but rather remains in adjacent regions (either near Punta de n'Amer or in front of Cala Bona). Depending on wave characteristics and direction, this sediment may eventually return to the study area. Notably, between 2021 and 2022, the final sediment balance indicated an influx of 52,000 m³ of sediment into the control area.

As illustrated in [Fig. 28](#), which presents the temporal results, there is a sequence of positive and negative sediment balance episodes. Although this time series is arguably one of the most comprehensive for any beach in the western Mediterranean, it does not yet allow us to draw definitive conclusions about the existence of significant temporal patterns or the specific forces responsible for these changes. However, it is evident that sediment balance dynamics involve transfers between different hydrodynamic zones of the beach. When the dry beach experiences sediment loss, accumulation tends to occur in the surf and shoaling zones, whereas when sediment is lost from these zones, the dry beach tends to recover. This cross-shore dynamic, highlighted by [Gómez-Pujol *et al.* \(2011\)](#) and further elaborated by [Morales-Márquez *et al.* \(2018\)](#) and [IH Cantabria \(2017\)](#), reflects an uneven response to the impacts of extreme events, which typically transport large volumes of sediment to depths greater than 2 m in a short time frame. For sediment to be transported back to shore, however, less energetic and more persistent forces are required, which are not always present in the study area.

Additionally, [Figs. 25 to 27](#) demonstrate that the system of paleochannels beneath the beach plays a role in its dynamics. In successive bathymetric surveys, the geometry of these paleochannels appears more or less pronounced, depending on the sediment covering them, further influencing the beach's morphodynamics.

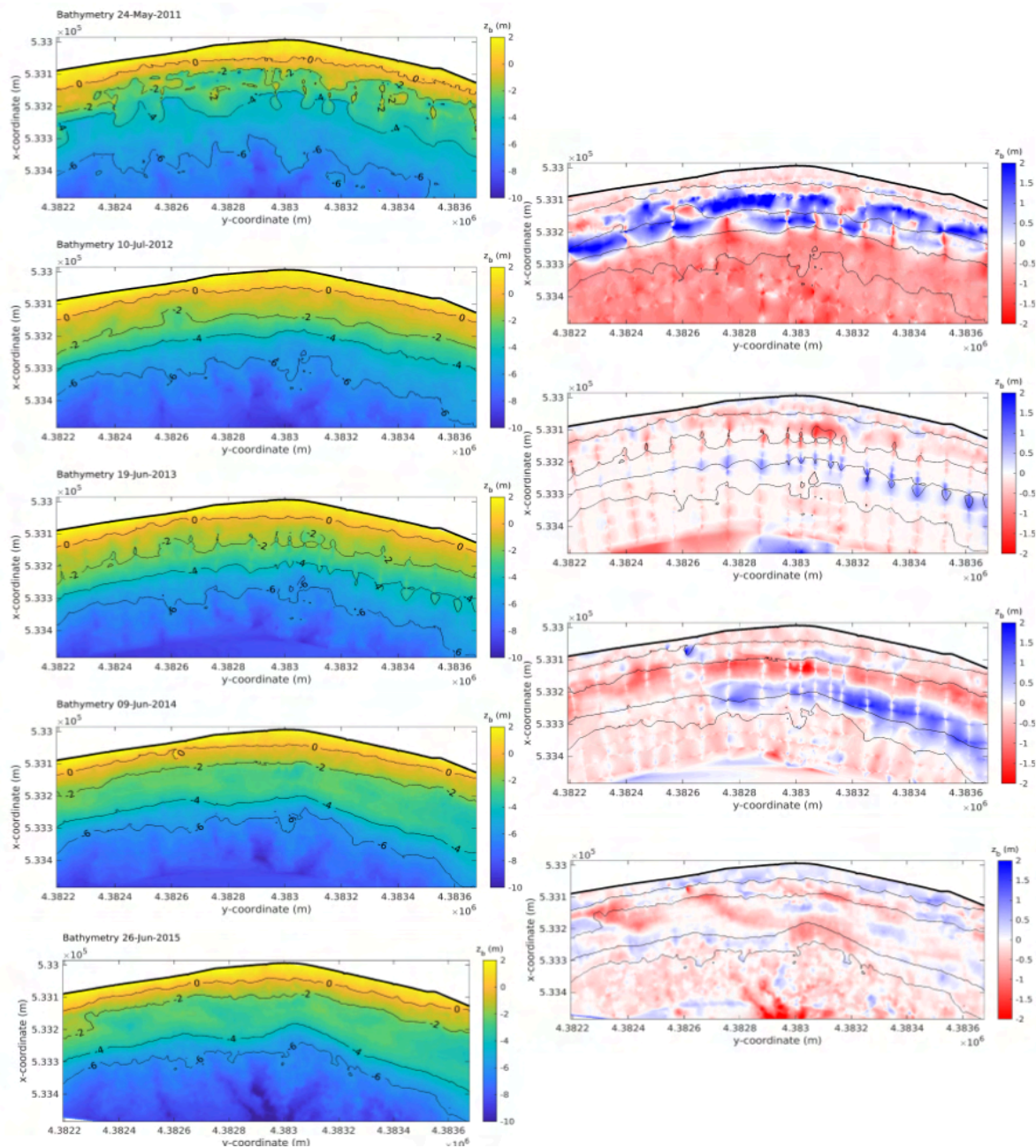


Figure 25. Interannual bottom changes 2011-2015 at Cala Millor: left panels, summer bathymetries; right panels, interannual bottom changes between bathymetries.

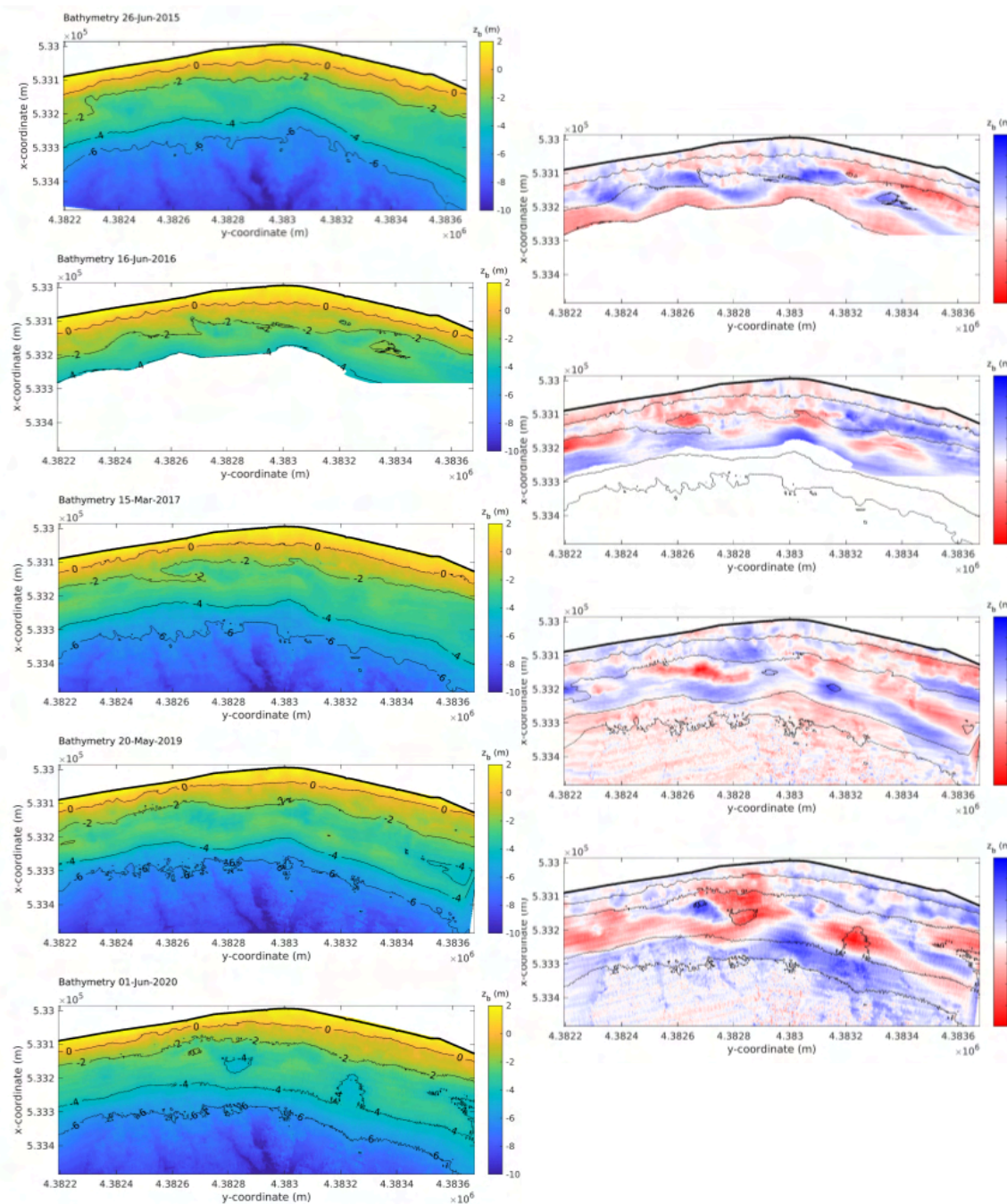


Figure 26. Interannual bottom changes 2015-2020 at Cala Millor: left panels, summer bathymetries; right panels, interannual bottom changes between bathymetries.

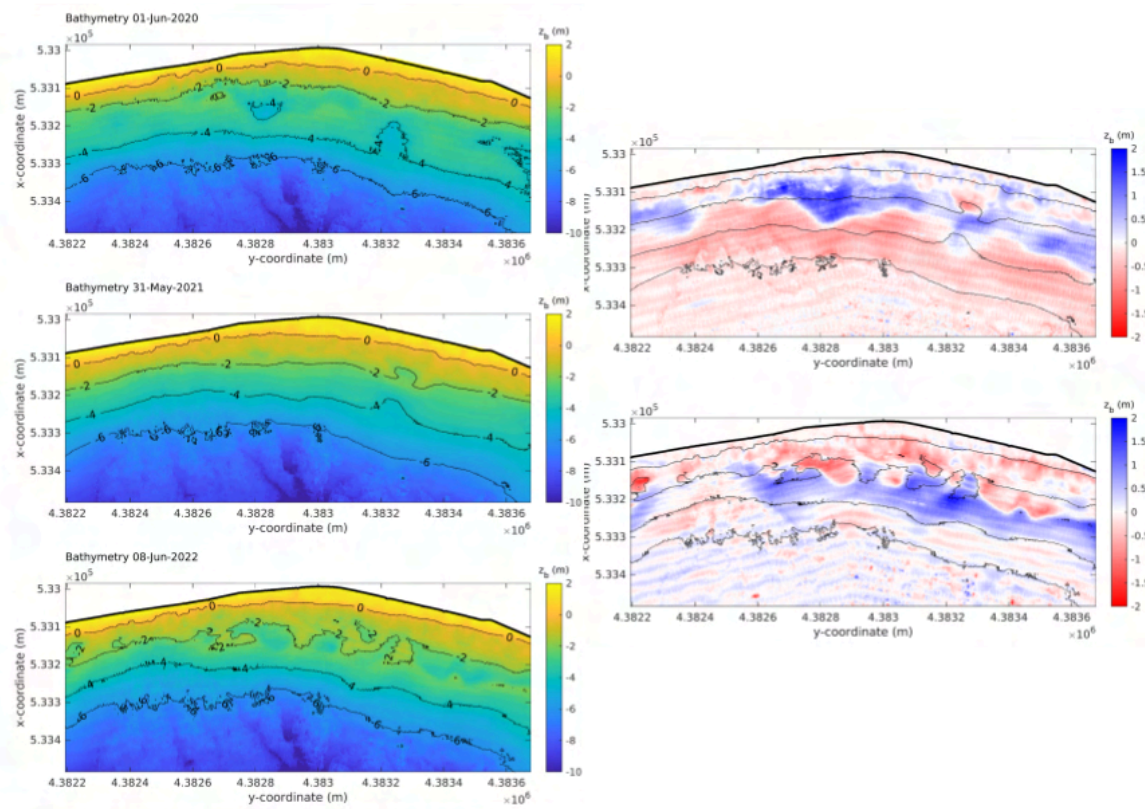


Figure 27. Interannual bottom changes 2020-2022 at Cala Millor: left panels, summer bathymetries; right panels, interannual bottom changes between bathymetries.

	Dry Zone $Z \geq 0$ m	Surf Zone $-4 \leq Z < 0$ m	Shoaling Zone $-6 \leq Z < -4$ m	Outer Zone $Z < -6$ m	Full beach
2012-2011	-4,000 (-0.07)	97,000 (0.44)	-97,000 (-0.65)	-180,000 (-0.79)	-183,000 (0.28)
2013-2012	-4,000 (-0.07)	-14,000 (-0.06)	9,000 (0.07)	-25,000 (-0.11)	-34,000 (-0.05)
2014-2013	-6,000 (-0.10)	-28,000 (-0.10)	12,000 (0.12)	-25,000 (-0.10)	-46,000 (0.07)
2015-2014	10,000 (0.16)	-23,000 (-0.09)	-7,000 (-0.07)	-45,000 (-0.18)	-65,000 (-0.10)
2016-2015 ³	2,000 (0.03)	-2,000 (~0.00)	—	—	~0.0 (~0.00)
2017-2016 ⁴	-3,000 (-0.05)	40,000 (0.16)	—	—	37,000 (0.11)
2019-2017 ⁵	-8,000 (-0.07)	-21,000 (-0.07)	-23,000 (-0.23)	-53,000 (-0.23)	-105,000 (-0.15)
2020-2019	10,000 (0.08)	-51,000 (-0.19)	25,000 (0.20)	11,000 (0.05)	-5,000 (~0.00)
2021-2020	2,000 (0.03)	37,000 (0.15)	-51,000 (-0.36)	-24,000 (-0.11)	-36,000 (-0.06)
2022-2021	-3,000 (-0.07)	34,000 (0.13)	4,000 (0.03)	17,000 (0.07)	52,000 (0.08)
2022-2017 ⁶	-5,000 (-0.15)	-19,000 (-0.08)	-30,000 (-0.30)	-40,000 (-0.24)	-94,000 (-0.14)

Table 4. Interannual volumetric balances (m^3) at the different beach zones analyzed at Cala Millor Data inside the parentheses refers to the unitary balance, expressed in m^3/m^2 .

³ Sediment balance is analyzed only considering the dry beach and the inner-surf zone, since 2016 topo bathymetries is truncated at 5 m depth.

⁴ Sediment balance is analyzed only considering the dry beach and the inner-surf zone, since 2016 topo bathymetries is truncated at 5 m depth.

⁵ Note that this is a two-years sediment balance (2017-2018 and 2018-2019), since no data is available for 2018.

⁶ Overall changes are computed for the period 2017-2022.

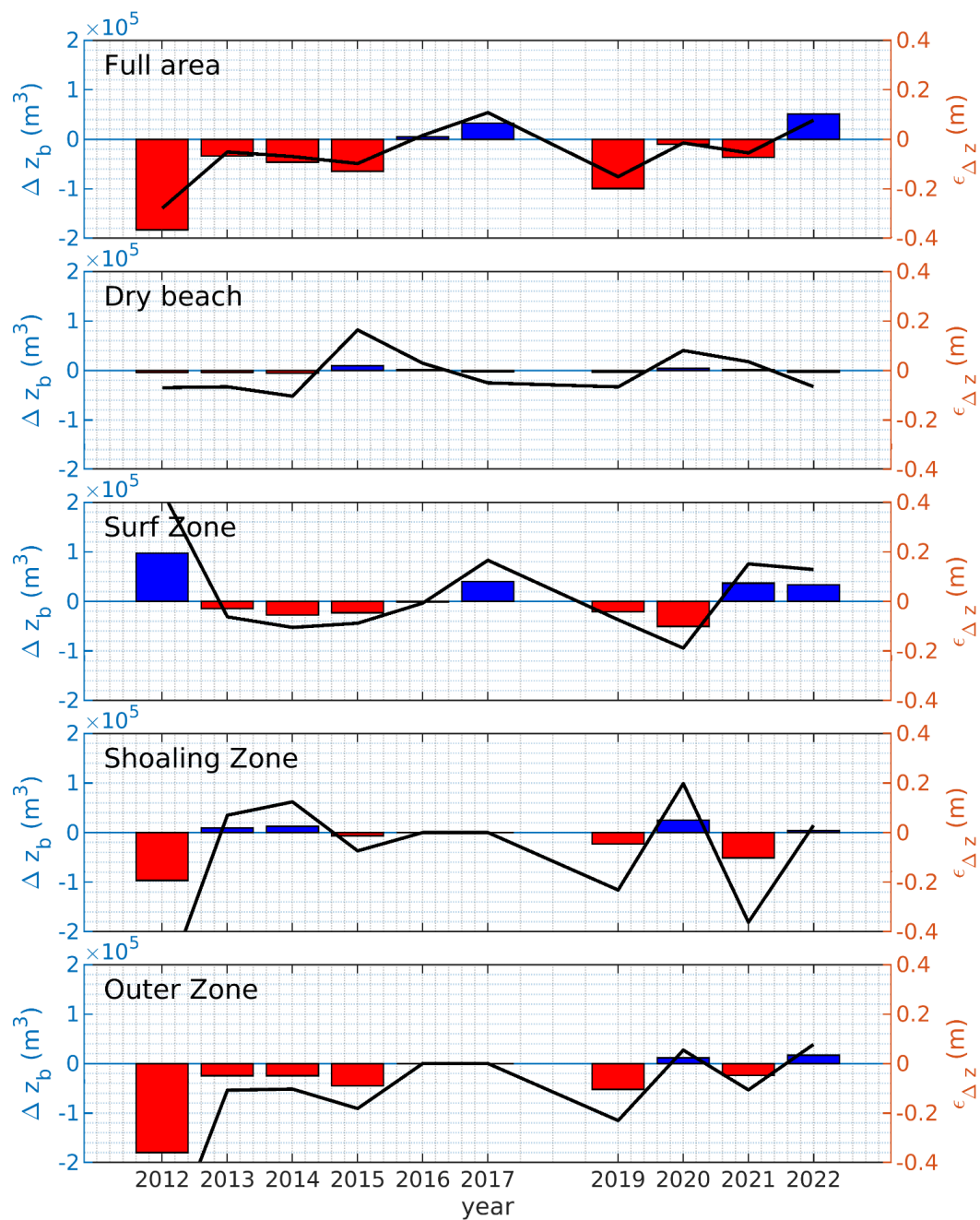


Figure 28. Interannual Sediment balances at Cala Millor: bar plots stand for total volume changes (m^3); line plots stand for unitary changes (m/m^2).

b) Seasonal sediment balance

Similar to the previous section, the sediment balance has been analyzed on a seasonal basis. It is important to note the absence of data for November 2014 and June 2018. Since June 2016 bathymetric measurements have been truncated at a depth of -5 m, analysis related to shoaling and outer areas have been excluded for the corresponding period. However, from 2011 to 2017, the echo-sounding surveys conducted in October–November were limited to profile surveys rather than full bathymetries. This limitation may introduce interpolation errors and distort the results. Therefore, an in-depth analysis will focus exclusively on bathymetries from 2018 onward.

Figure 29 illustrates the intra-annual sediment balance (Δz_b) and the unitary balance (ϵz_b). A consistent pattern is observed throughout the study period, reflecting the seasonal shift between summer and winter profiles. Accretion is evident during the June–November periods, characterized by milder wave conditions. Conversely, erosive patterns are apparent in June bathymetries, which are conducted after the winter season when wave energy is higher.

On focusing on the 2018-2022 period (Fig. 29, 30 and 31), the following morphodynamic behaviour is observed:

2018/10 – 2019/05: During this period, the crescentic sandbar, initially located at a depth of ~1 m, underwent significant offshore migration (~80 m), reaching a depth of ~2.65 m. Simultaneously, the dry beach experienced notable erosion. This evolution can be attributed to the major storm event that struck the beach in April 2019. This storm caused substantial erosion of the shoreline and dry beach, particularly at the southern area, and that likely resulted in the offshore migration of the sandbar.

2019/05 – 2019/10: This period was characterized by accretion, marked by a modest offshore migration of the sandbar (~20 m) and notable accretion, especially in the northern sector of the dry beach. Changes in the shoaling and outer zones during this timeframe were minimal, indicating limited sediment transport or redistribution in these areas.

2019/10 – 2020/06: The sandbar exhibited slight offshore migration, accompanied by a widening of the inner-surf zone. The dry beach remained relatively stable, with minimal changes observed. However, significant bottom changes were detected in the shoaling and outer zones. A critical event during this period was the extreme Gloria storm in January 2020. This storm caused the sandbar to migrate further offshore, reaching depths of ~5 m, and led to the formation of megarip patterns within the crescentic sandbar (Fernández-Mora *et al.*, 2025, in preparation). Despite the offshore migration, accretion was observed on the dry beach. Additionally, sediment replenishment was evident in the shoaling zone and the submerged channels.

2020/06 – 2020/10: This period showed minimal bottom changes as the beach began recovering from the disruptions caused by the Gloria storm. While recovery was incomplete, some accretionary patterns emerged in the inner-surf zone, and there was a slight onshore migration of the sandbar.

2020/10 – 2021/06: An accretionary state was observed in both the dry beach and inner-surf zone during this phase. The sandbar showed a notable attachment to the shoreline, indicating a

stabilization process. Meanwhile, no significant changes occurred in the shoaling and outer zones, suggesting a period of relative calm and limited sediment transport in these areas.

2021/06 – 2021/11: This period is characterised by relatively minor changes, although a negative trend is observed across the entire surf and shoaling zone. The wave time series (Fig. 7) reveals no extreme storms of the magnitude seen in the previous two years, although several storms of lesser intensity are recorded. From the central section of the beach to its northernmost part, significant accretion areas are evident, once again forming the crescentic bars typical of the region, and even sand waves extending to the dry beach. In the mid-section, less pronounced but still notable, slightly transverse bars are observed between the shoreline and a depth of 2 m.

2021/11 – 2022/06: During this period, the crescentic sandbars, initially located at a depth of ~1 m, underwent again offshore migration, reaching a depth of ~3 m. Simultaneously, the dry beach experienced and shallow waters experienced erosion because of the impact of January 2022 extreme event.

The results of the sediment balance on a seasonal scale do not show substantial differences from those observed in the annual analysis, as described in the previous section. However, they do highlight the impact of specific extreme events and underscore the fact that significant volumes of sand are transported from the dry beach and surf zone to deeper areas in a short period of time. These sediments then require much longer periods of calm conditions to return to the shore. Spatially, it is common for a sedimentary prism to form between the upper limit of *Posidonia oceanica* and a depth of 3 m in the sector between Es Clot de s'Alga and Platja del Moro, as well as another between Sa Mániga and Cala Nau.

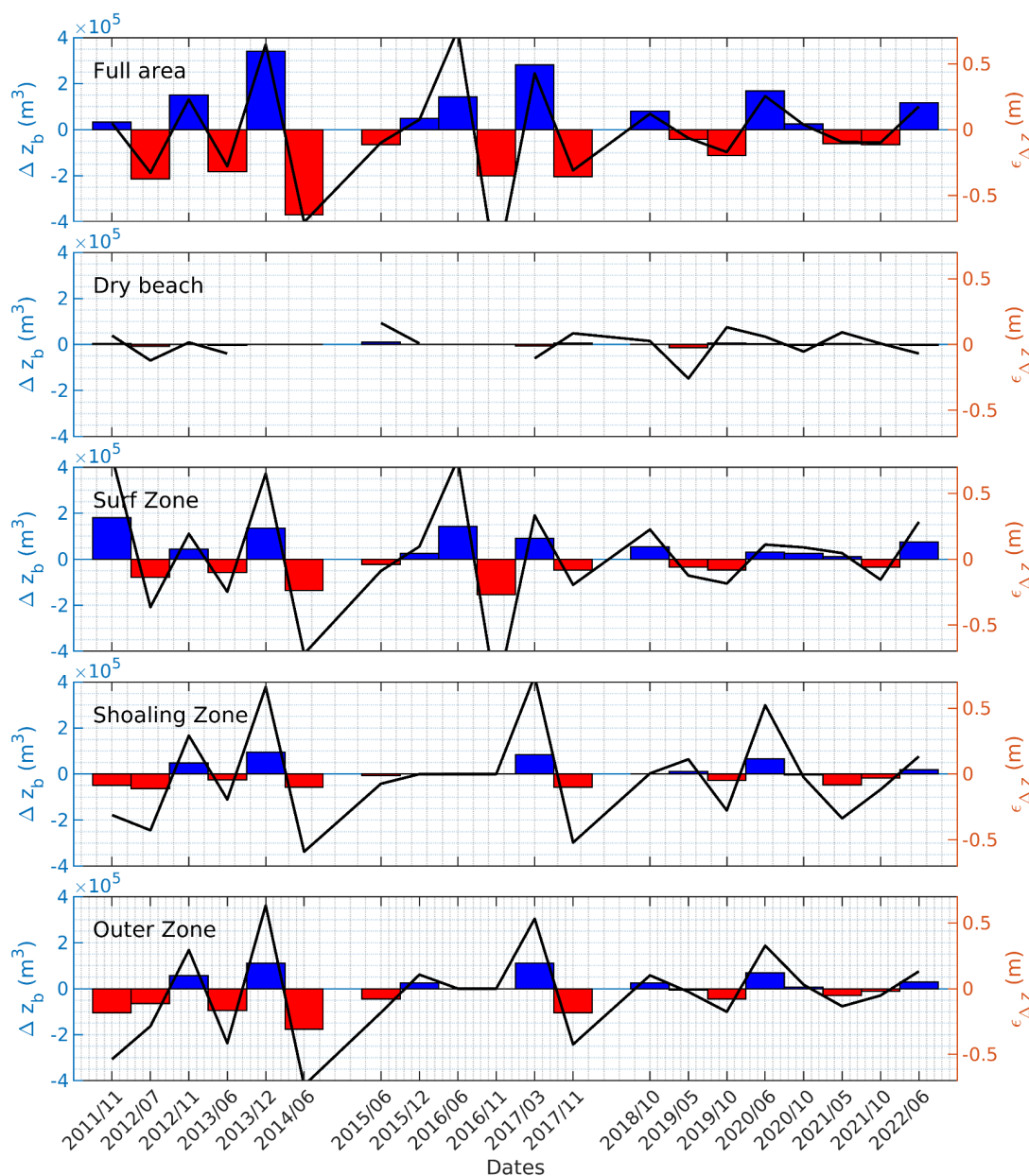


Figure 29. Seasonal sediment balances for the period 2011 to 2022. Bar plots stand for total volume changes (m^3); line plots stand for unitary changes (m/m^2 per square meter).

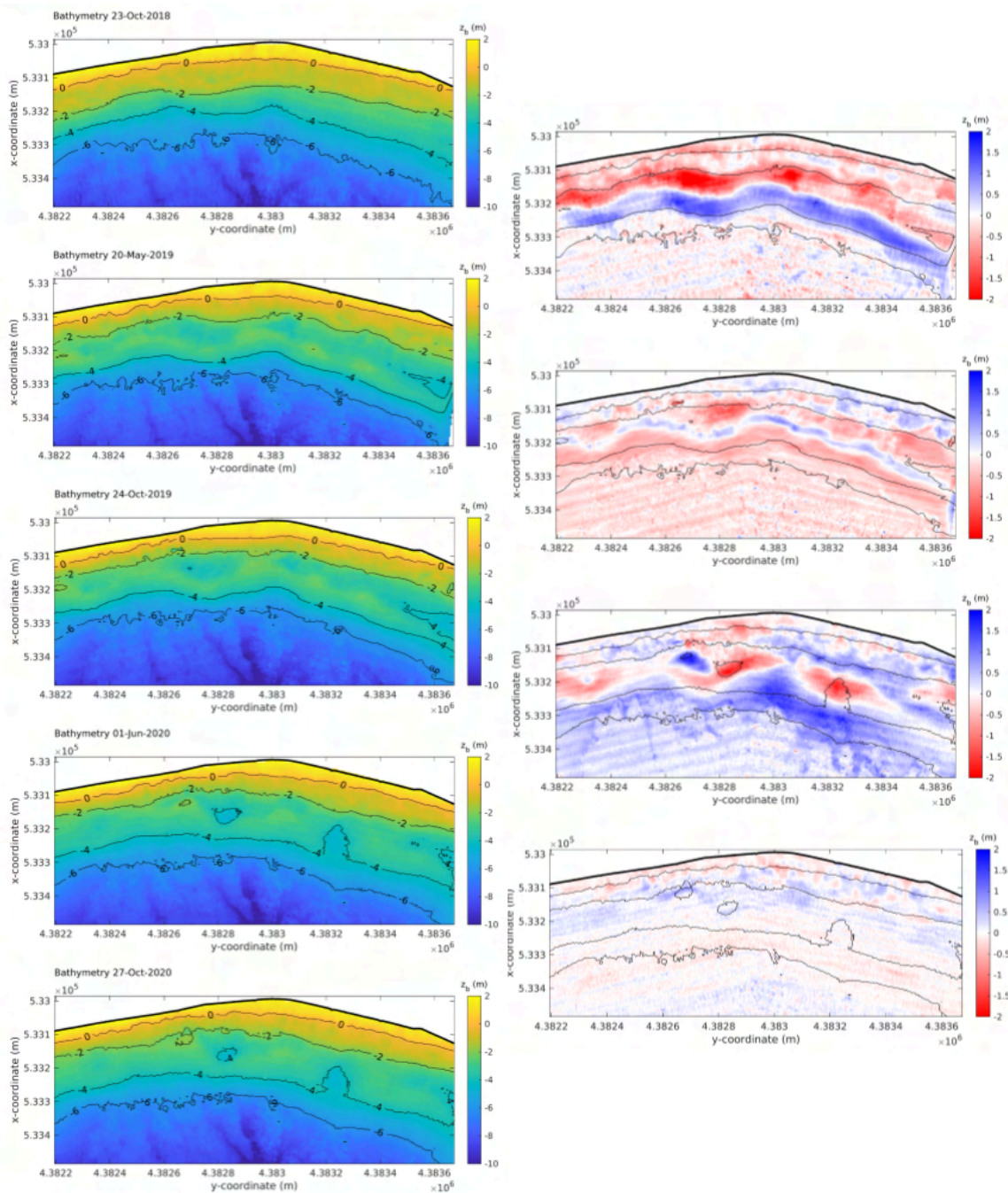


Figure 30. Intra-annual balances for the period 2018 to 2020 at Cala Millor: left panels, summer bathymetries; right panels, interannual bottom changes between bathymetries

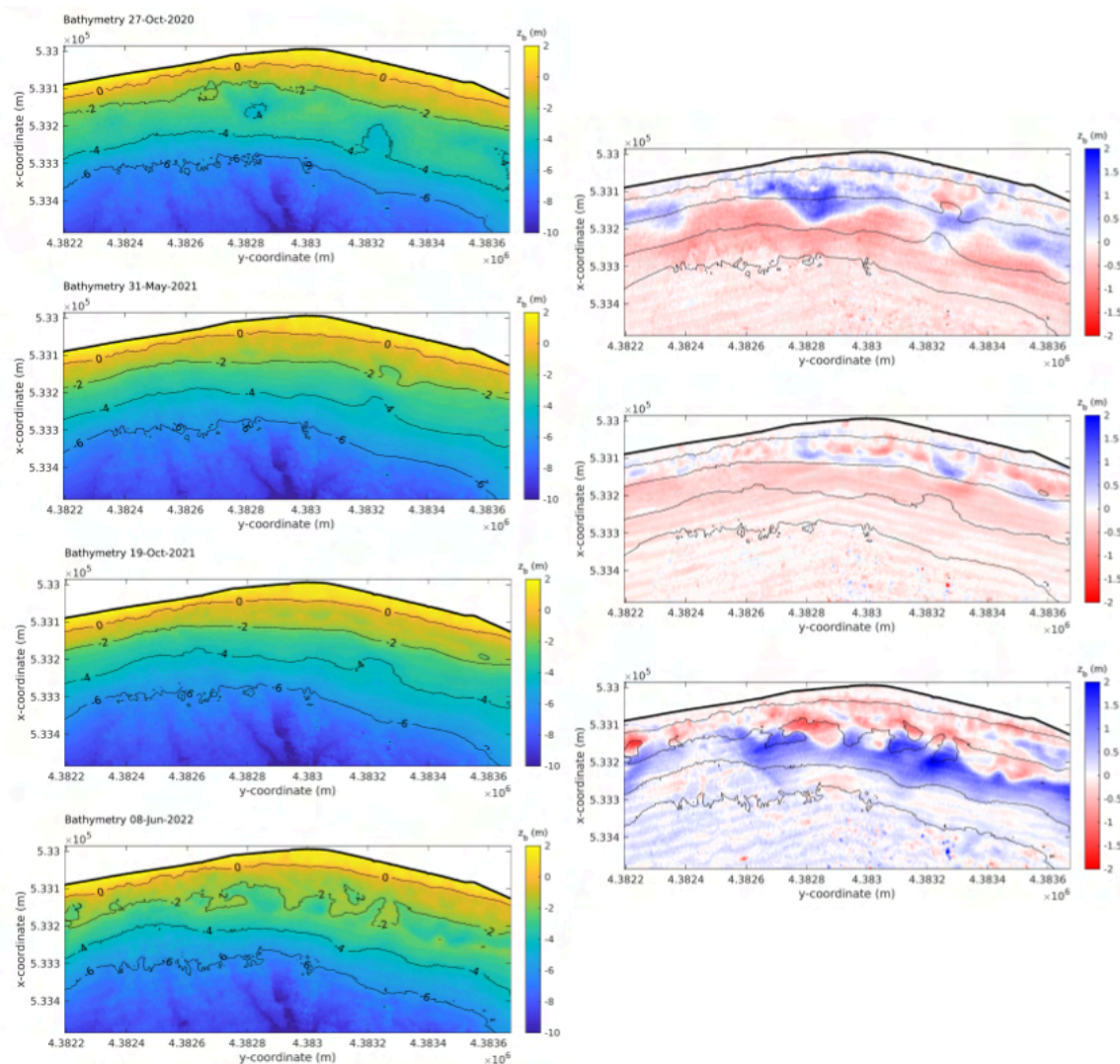


Figure 31. Intra-annual balances for the period 2020 to 2022 at Cala Millor: left panels, summer and winter bathymetries; right panels, intra-annual bottom changes between bathymetries.

2.1.2.4. Shoreline Evolution

To understand the transformation of Cala Millor from a natural beach to an urbanized one, we need to look at the period between the late 1950s and the early 1960s, around the time when the tourism boom began in 1956 (Fig. 32). The urbanistic project covered an area of 5 km², including the entire beach-dune system. In 1968, the construction of the promenade led to the dismantling of the entire dune system, primarily the foredune. During the 1980s, the area continued to expand, disrupting the natural balance of the beach-dune system. Despite the additional sand brought to the beach due to the destruction of the dune system, the beach gradually returned to its natural width. However, without the sand reservoirs provided by the foredune, the beach could not maintain its natural equilibrium. In response to this issue, various interventions began to be implemented.

According to the regeneration records of the General Directorate of Coasts (Balearic Coastline Demarcation), Cala Millor has undergone artificial regenerations from 1989 to 1996 (General Directorate of Coasts). The first sand deposition (in 1989) was carried out by the Sant Llorenç Town Hall in the southern area of the beach, and the amount of sand added is unknown. After this regeneration, three more were conducted during the 1990s, with recorded volumes of less than 10,000 m³ each according to the General Directorate of Coasts (Table 5). Finally, in 2002, an estimated volume of over 40,000 m³ of sediment was deposited.

It is worth noting that although the individual volumes are relatively small, the total amount deposited is comparable to the existing dry beach volume, estimated to be between 60,000 and 90,000 m³ (refer to GOIB and IMEDEA, 2004 and Annex 1).

Cala Millor reported sand nourishments	
Year	Volume (m ³)
1968	?; but Promenade construction and dismantling of the dune ridge of >65,400 m ²
1989	?
1990	8,000
1993	5,400
1996	4,759
2002	> 40,000
Total	> 58,149

Table 5. Nourishments carried out in Cala Millor according to the General Directorate of Coasts (cf. Tintoré et al., 2009).

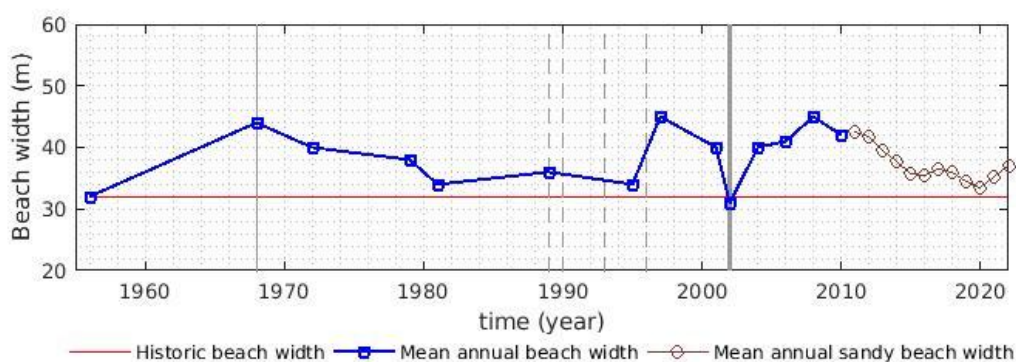


Figure 32. Annual mean beach width. Gray-dashed lines stand for the minor beach nourishments listed in Table 7. Gray thin solid line stands for the dismantling of the dune area during the 60's. Gray thick line stands for the nourishment held in 2002.

On a large time scale, the historic beach width still remains above the reference natural conditions exhibited in aerial photographs from 1956 (Fig. 32). When the beach still has a healthy coastal dune ridge to compensate for the erosive action of the most energetic storms. Historically the dry beach has experienced 6 sand nourishments. The last one in 2002 in order to compensate

for the impact of the 2001 extreme event, that receded the beach to lower value in terms of mean beach width, slightly below the 1956 reference. From 2008 and taking into account the maximum width attended after the last nourishment, the dry mean beach width is receding, specially in the southern sector of the beach where rock reefs crops out because the combined action of storm wave impact, urban pluvials draining on the beach and the interactions with the promenade wall that don't follow the natural plan view geometry of the beach (Tintoré et al., 2009).

High spatio-temporal resolution data collected from the Cala Millor beach monitoring station from 2011 to 2023 (Fig. 33) reveal that shoreline and dry beach width variability at Cala Millor are important, because the sand bars dynamics and changes in sediment mass budgets related to energetic storms. Changes backwards and seaward around 20 m, also on a daily basis, are not unusual (Fig. 33b). Nevertheless there is a general decreasing trend in dry beach width along the time of study. Although the dry beach width still is larger than the 1956 natural conditions references, and in the time series it can be observed some positive variations representing an increase in mean beach width. The central area of the beach remains wider than the rest of the areas. The southern area that presents rock outcrops, has a smaller width and it is controlled by rocks (vid. Fig. 16). The northern area presents higher variability, with B_w varying along the time, and particularly from 2018 to 2023.

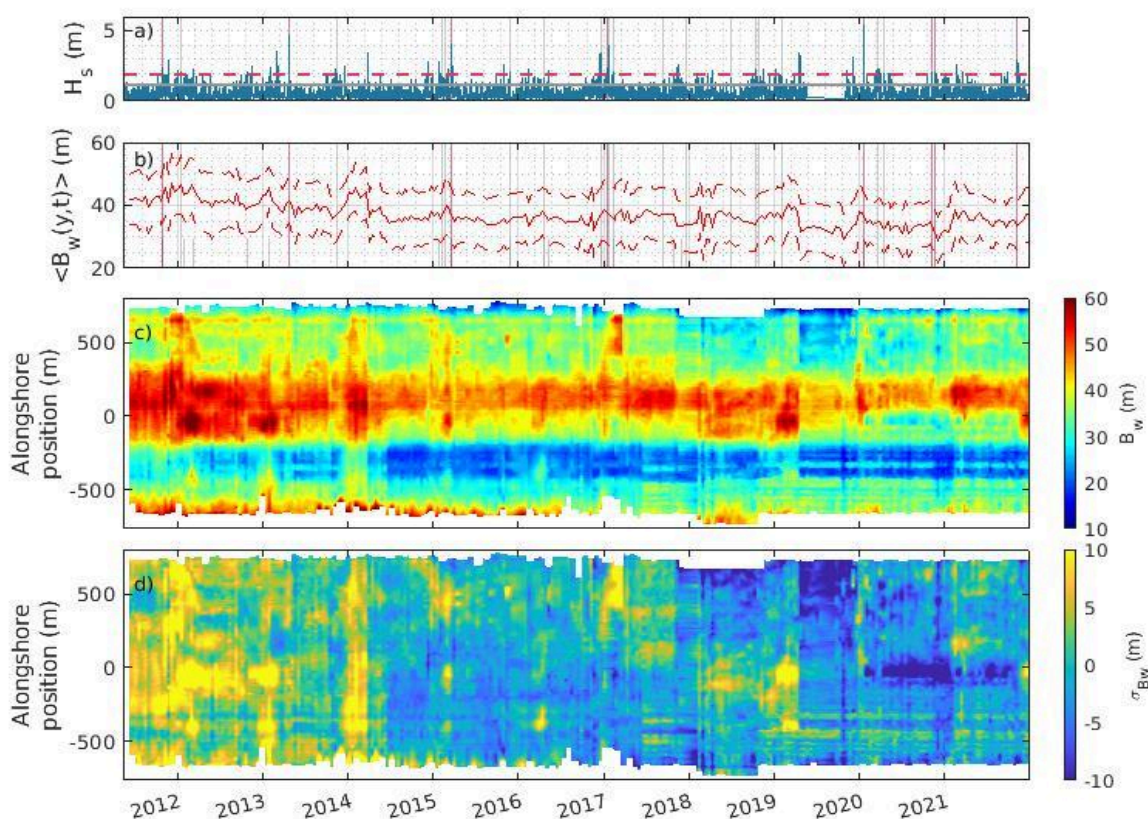


Figure 33. Shoreline and dry beach width variability at Cala Millor. a) hourly significant wave height H_s (m) along time; b) Alongshore averaged Beach width, B_w (m); c) B_w along the beach (from positive to negative values on the y-axis, moving from North to South of Cala Millor beach); d) Beach width variation (σ_{Bw}).

To gain more insights into the spatio-temporal patterns of shoreline beach width, a spectral analysis of the B_w signal was conducted (Fig. 34). Regarding the alongshore-averaged B_w , a significant peak in the spectrum at a frequency of 1 year is evident, likely related to the annual sea-level cycle. A secondary relevant peak is found at a frequency of 2, which can be associated with the seasonal variability of wave conditions. Noisy peaks at higher frequencies are related to storms. A notable peak at lower frequencies (2.5 years) could indicate the same cycle observed in morphological analysis, most probably related to climatic cycles. In analyzing the spectrum of B_w along the beach, the 1-year peak is evident along the beach, as well as the higher frequency peaks. Notably, the low-frequency peaks are particularly present in the central part of the beach.

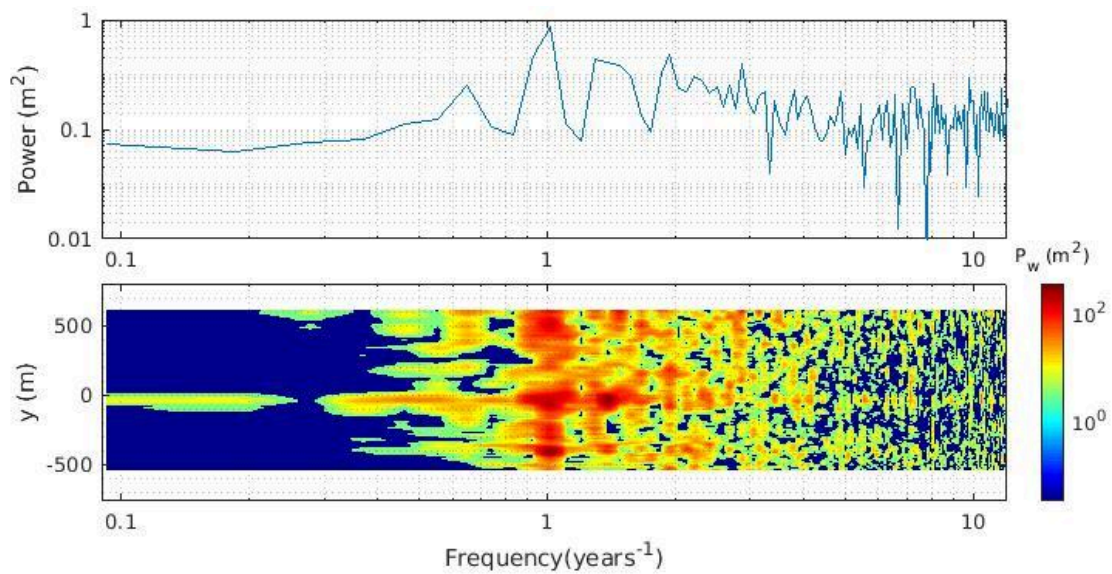


Figure 34. Cala Millor beach width power spectrum: upper panel, mean B_w ; lower panel; space dependent B_w .

2.1.2.5. Morphodynamic behavior of Cala Millor beach

From the wave climate analysis in terms of mean, storm and extreme conditions in Section 2.1.1.2, the following wave and sea-level conditions have been considered on modelling beach morphodynamics (Table 6 and 7; Fig. 35 to 50):

	MEAN MARINE CLIMATE	WINTER CONDITIONS	SPRING CONDITIONS	SUMMER CONDITIONS	AUTUMN CONDITIONS
H_s (m)	0.5	0.54	0.55	0.36	0.53
T_p (s)	6.2	7.17	6.43	4.92	6.1
θ (deg)	100.3	96.5	102	105.8	96.2
η_t (m)	0.39	0.34	0.34	0.4	0.5

Table 6. Mean Climate conditions at Cala Millor: Annual and seasonal.

	MEAN STORM CLIMATE			WINTER CONDITIONS	SPRING CONDITIONS			SUMMER CONDITIONS			AUTUMN CONDITIONS
	Ave.	N	S		Ave.	N	S	Ave.	N	S	
H_s (m)	1.47	1.34	1.67	1.76	1.63	1.32	1.68	1.38	1.3	1.53	1.7
T_p (s)	8.47	6.8	10.6	9.42	7.8	8.0	7.7	7.15	5.4	7.2	8.04
θ (deg)	86.9	75	105	77.9	95.8	85	110	92.6	75	105	89
η_t (m)	0.44	0.34	0.44	0.42	0.45	0.42	0.46	0.42	0.35	0.45	0.58

Table 7. Mean Storm conditions at Cala Millor: Annual and seasonal

a) Morphodynamics under mean wave conditions
i) ANNUAL WAVE CONDITIONS

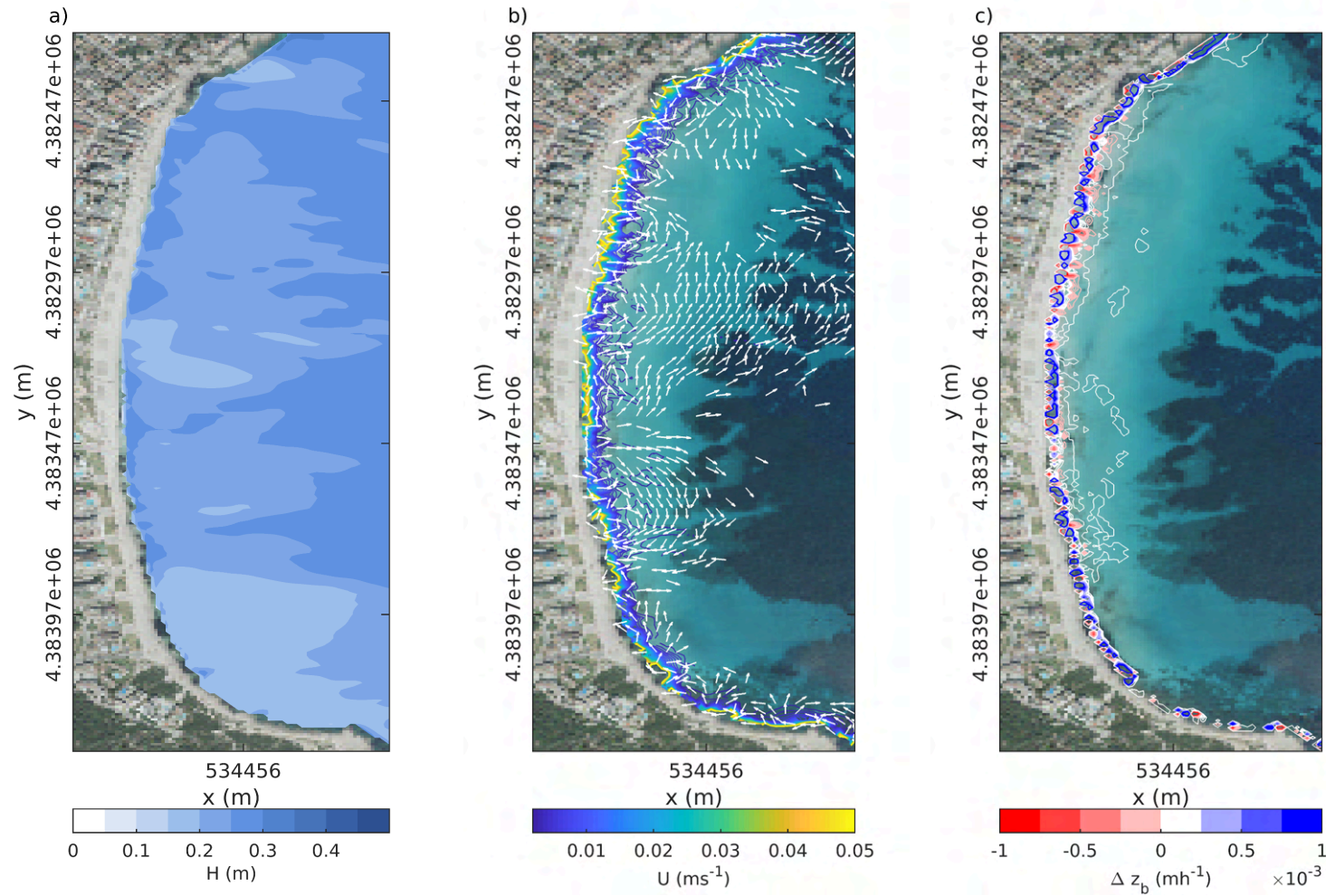


Figure 35. Annual wave conditions at Cala Millor. a) Time averaged significant wave height H_s (m); b) Mean current field U (ms^{-1}) (arrows show the mean circulation patterns related to $U > 0.01 ms^{-1}$); c) time-averaged bottom changes Δz_b (mh^{-1}).

ii) MEAN CLIMATE WINTER

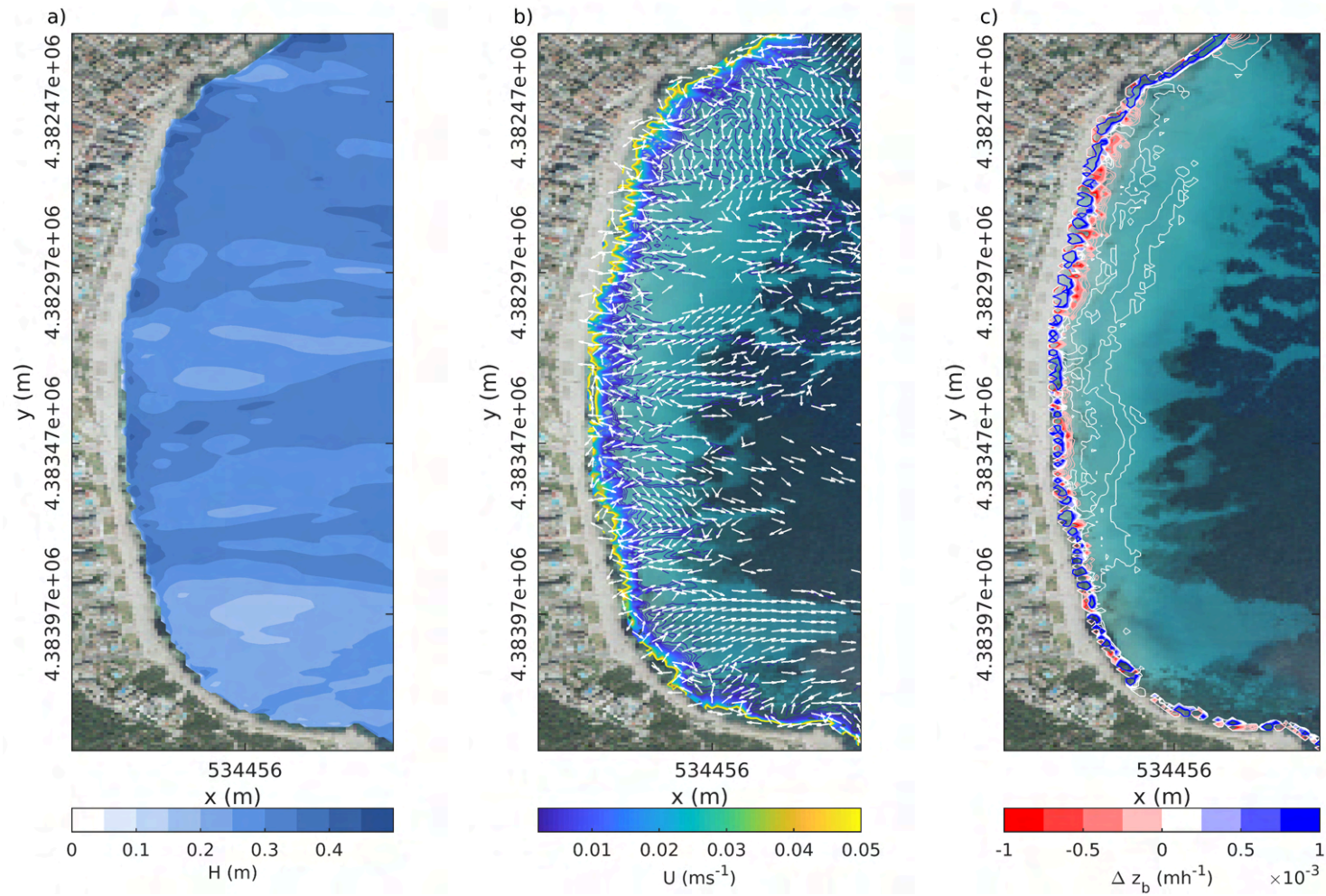


Figure 36. Mean winter wave conditions at Cala Millor. a) Time averaged significant wave height H_s (m); b) Mean current field U (ms^{-1}) (arrows show the mean circulation patterns related to $U > 0.01 ms^{-1}$); c) time-averaged bottom changes Δz_b (mh^{-1}).

iii) MEAN CLIMATE SPRING

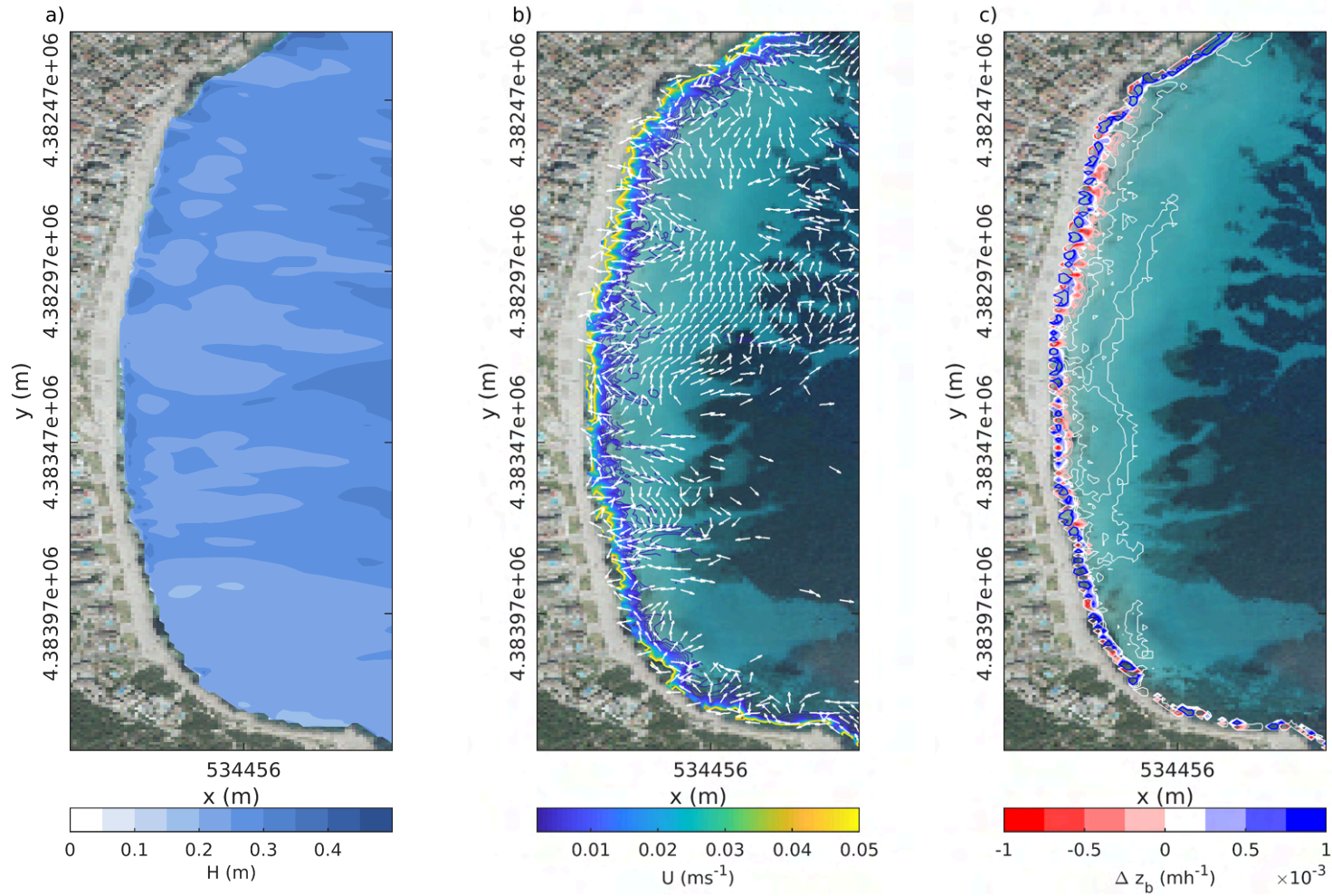


Figure 37. Mean spring wave conditions at Cala Millor. a) Time averaged significant wave height H_s (m); b) Mean current field U (ms^{-1}) (arrows show the mean circulation patterns related to $U > 0.01 \text{ ms}^{-1}$); c) time-averaged bottom changes Δz_b (mh^{-1}).

iv) MEAN CLIMATE SUMMER

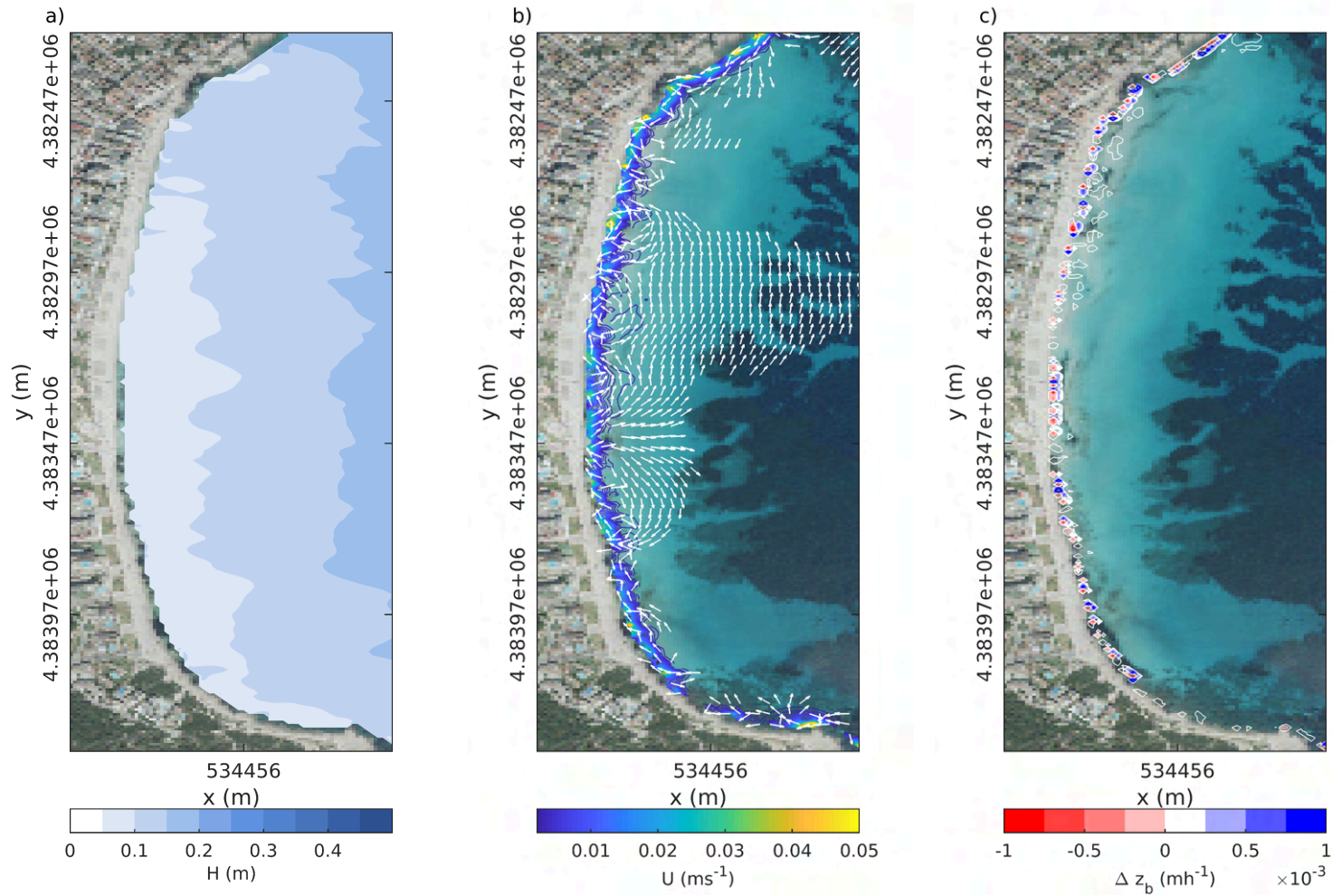


Figure 38. Mean summer wave conditions. a) Time averaged significant wave height H_s (m); b) Mean current field U (ms^{-1}) (arrows show the mean circulation patterns related to $U > 0.01 ms^{-1}$); c) time-averaged bottom changes z_b (mh^{-1}).

v) MEAN CLIMATE AUTUMN

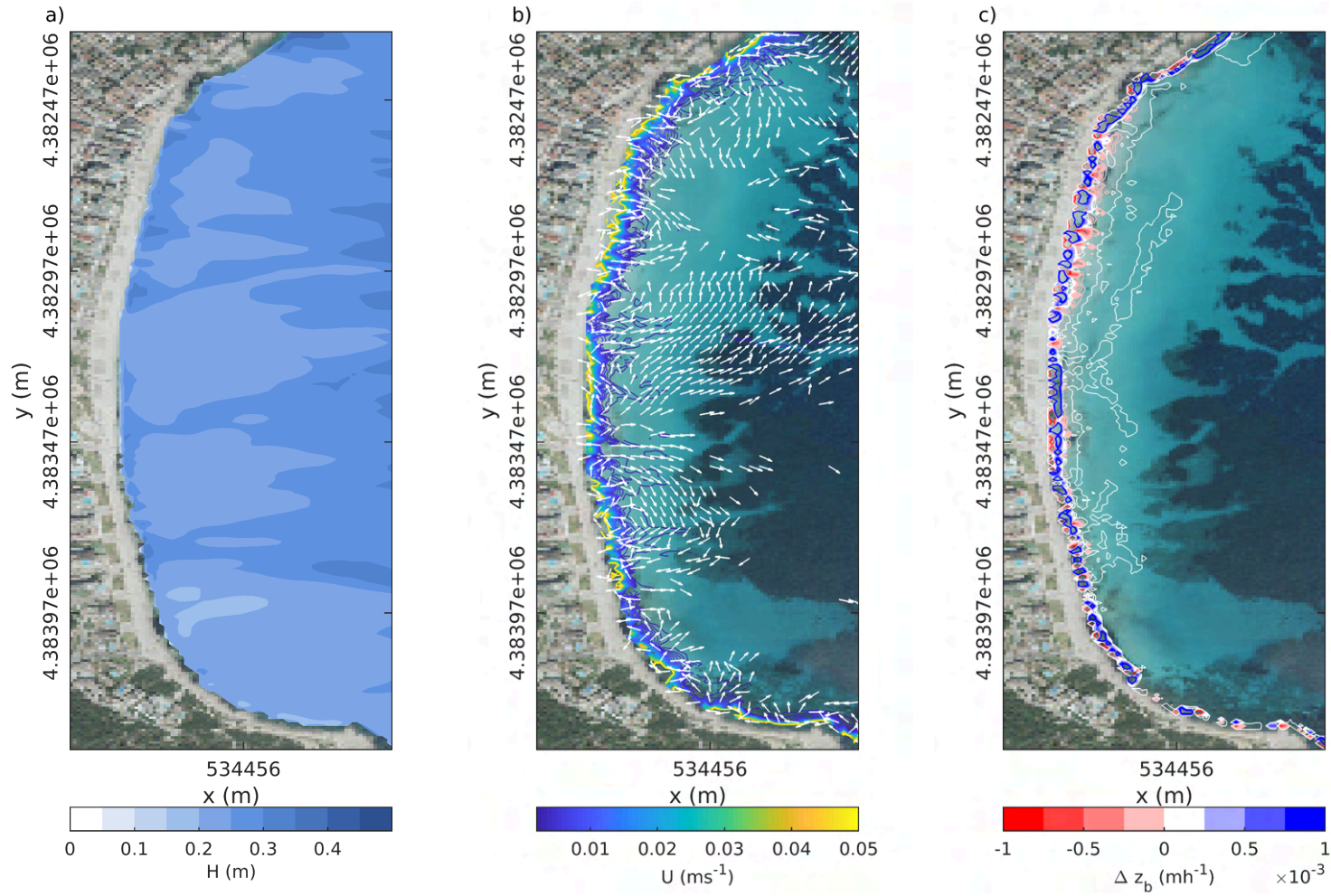


Figure 39. Mean autumn wave conditions at Cala Millor. a) Time averaged significant wave height H_s (m); b) Mean current field U (ms^{-1}) (arrows show the mean circulation patterns related to $U > 0.01 ms^{-1}$); c) time-averaged bottom changes Δz_b (mh^{-1}).

b) Morphodynamics under storm conditions

i) MEAN STORM CONDITIONS

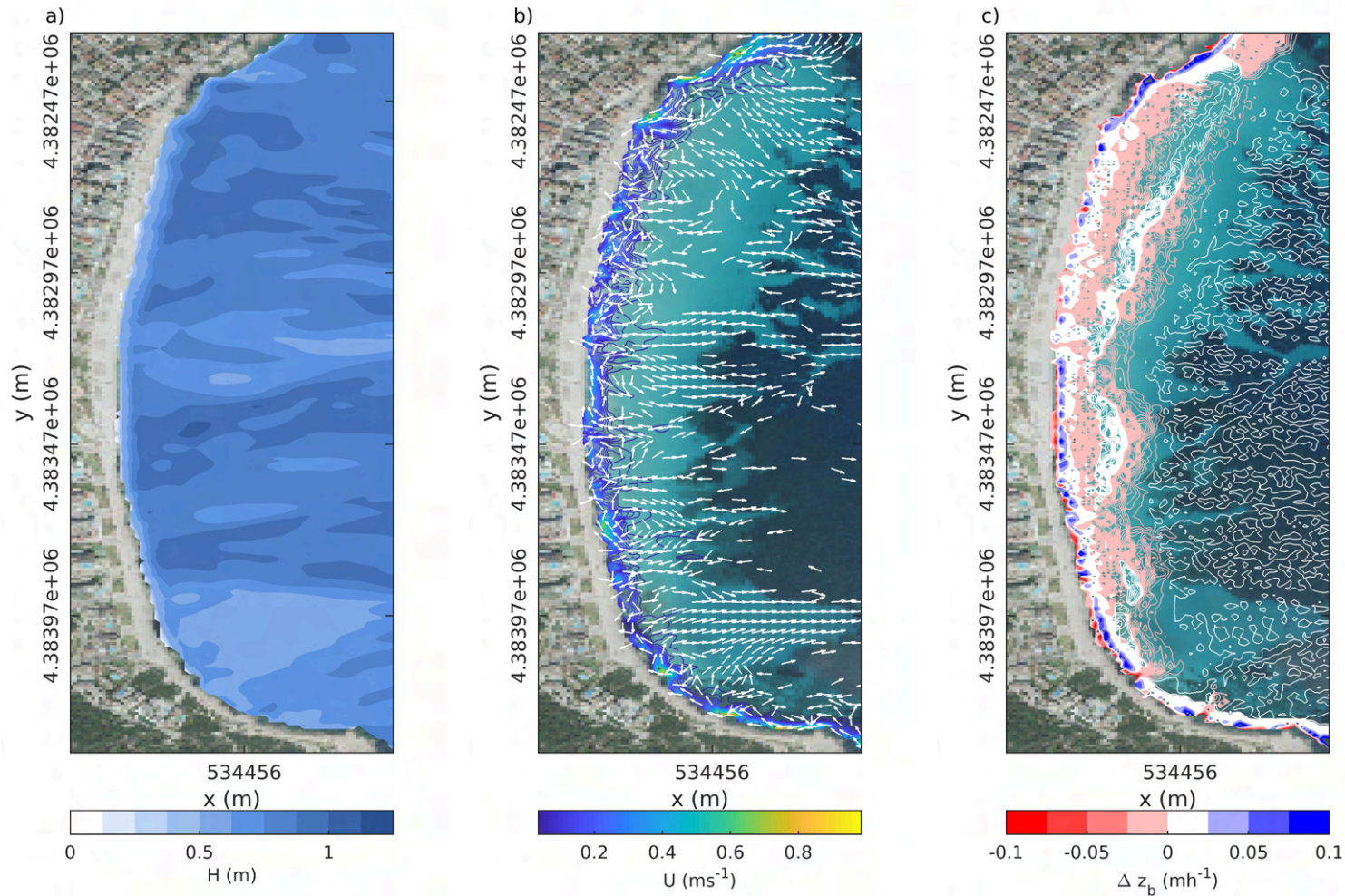


Figure 40. Mean storm conditions at Cala Millor. a) Time averaged significant wave height H_s (m); b) Mean current field U (ms^{-1}) (arrows show the mean circulation patterns related to $U > 0.02 ms^{-1}$); c) time-averaged bottom changes Δz_b (mh^{-1}).

ii) MEAN STORM CONDITIONS - NORTHERN COMPONENT

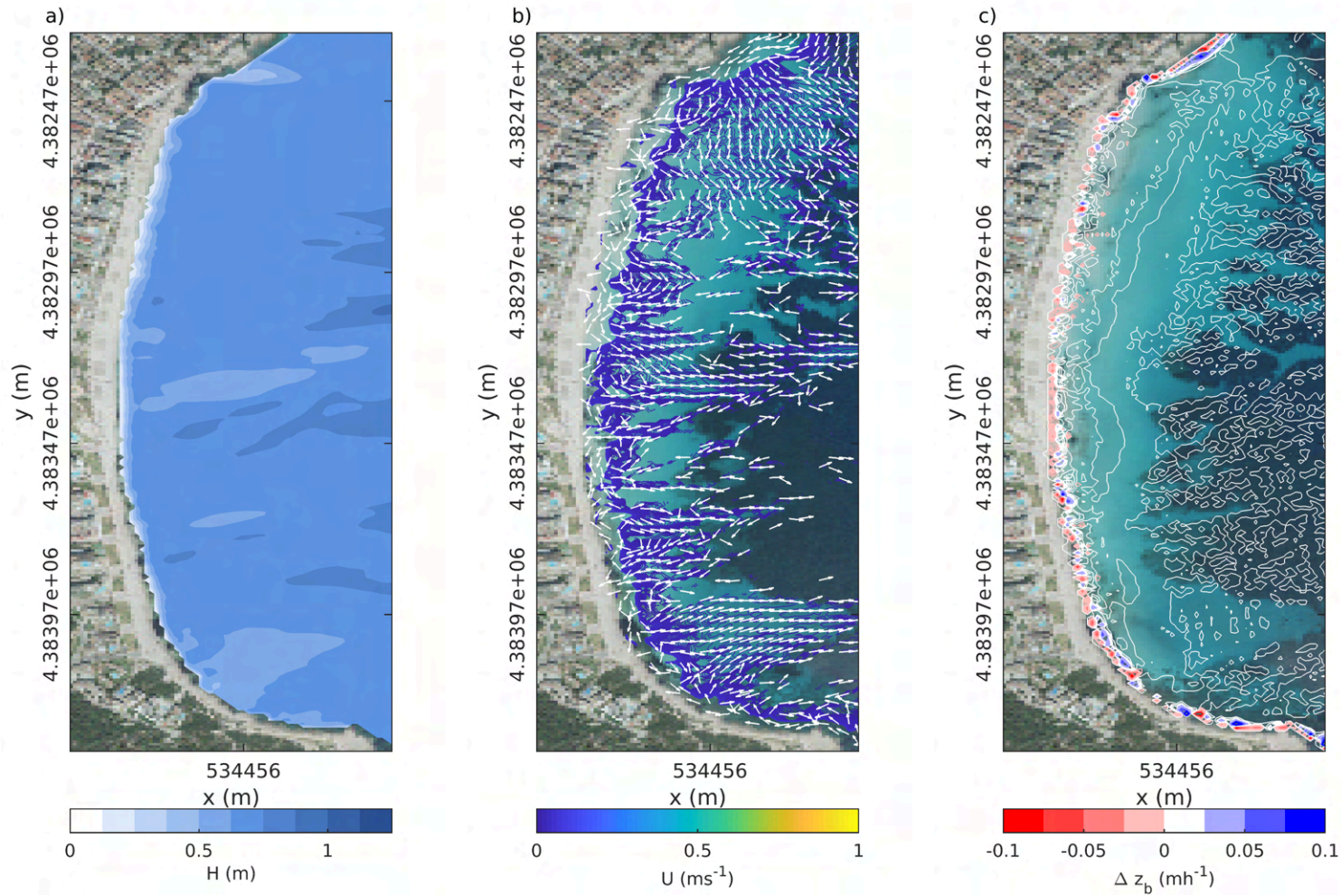


Figure 41. Mean northern component storm conditions at Cala Millor. a) Time averaged significant wave height H_s (m); b) Mean current field U (ms^{-1}) (arrows show the mean circulation patterns related to $U > 0.02 ms^{-1}$); c) time-averaged bottom changes Δz_b (mh^{-1}).

iii) MEAN STORM CONDITIONS - SOUTHERN COMPONENT

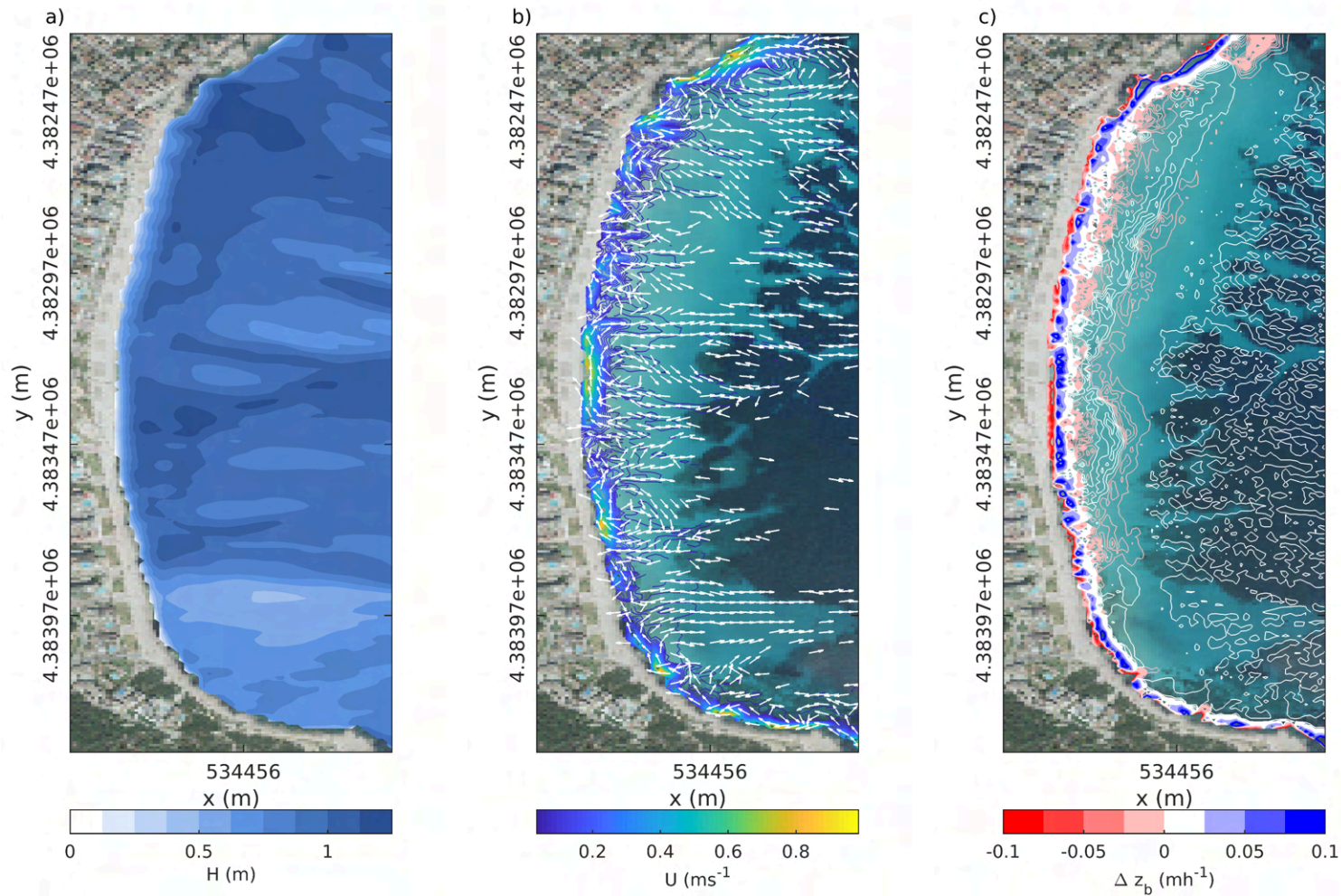


Figure 42. Mean southern component storm conditions at Cala Millor. a) Time averaged significant wave height H_s (m); b) Mean current field U (ms^{-1}) (arrows show the mean circulation patterns related to $U > 0.02 ms^{-1}$); c) time-averaged bottom changes Δz_b (mh^{-1}).

iv) WINTER MEAN STORM CONDITIONS

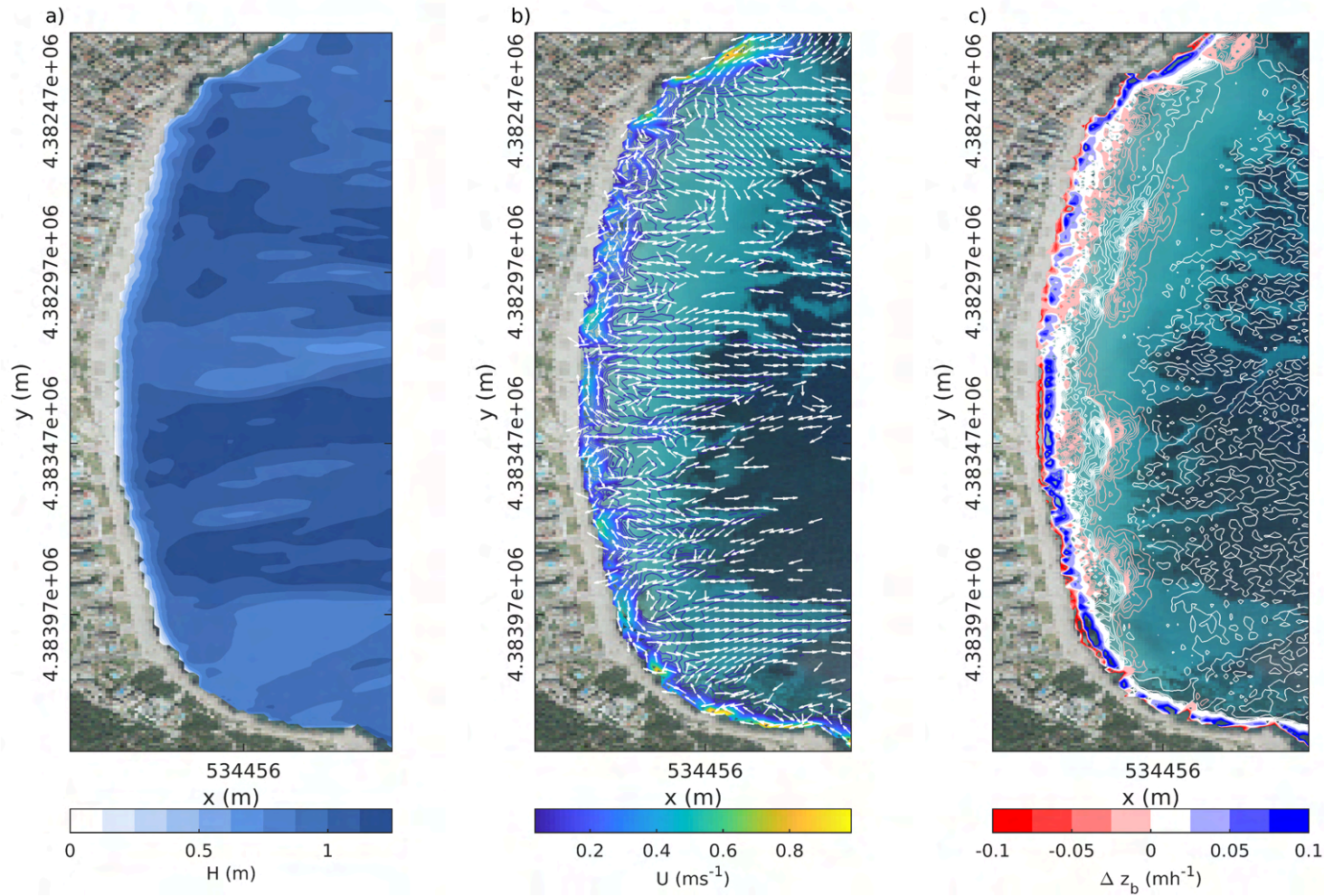


Figure 43. Mean winter storm conditions at Cala Millor. a) Time averaged significant wave height H_s (m); b) Mean current field U (ms^{-1}) (arrows show the mean circulation patterns related to $U > 0.02 \text{ ms}^{-1}$); c) time-averaged bottom changes Δz_b (mh^{-1}).

v) SPRING MEAN STORM CONDITIONS

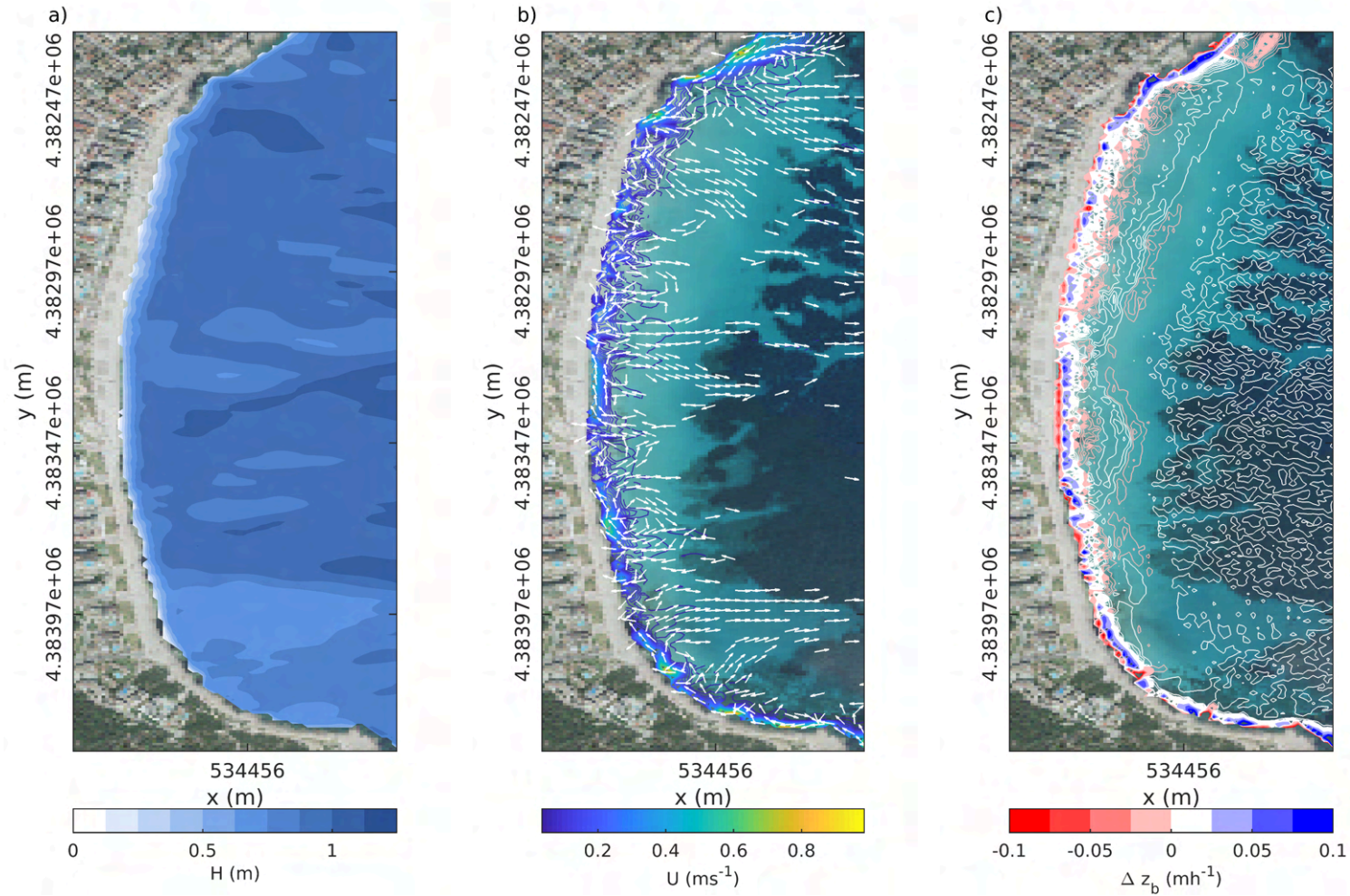


Figure 44. Mean spring storm conditions at Cala Millor. a) Time averaged significant wave height H_s (m); b) Mean current field U (ms^{-1}) (arrows show the mean circulation patterns related to $U > 0.02 ms^{-1}$); c) time-averaged bottom changes Δz_b (mh^{-1}).

vi) SPRING MEAN STORM CONDITIONS: NORTHERN COMPONENT

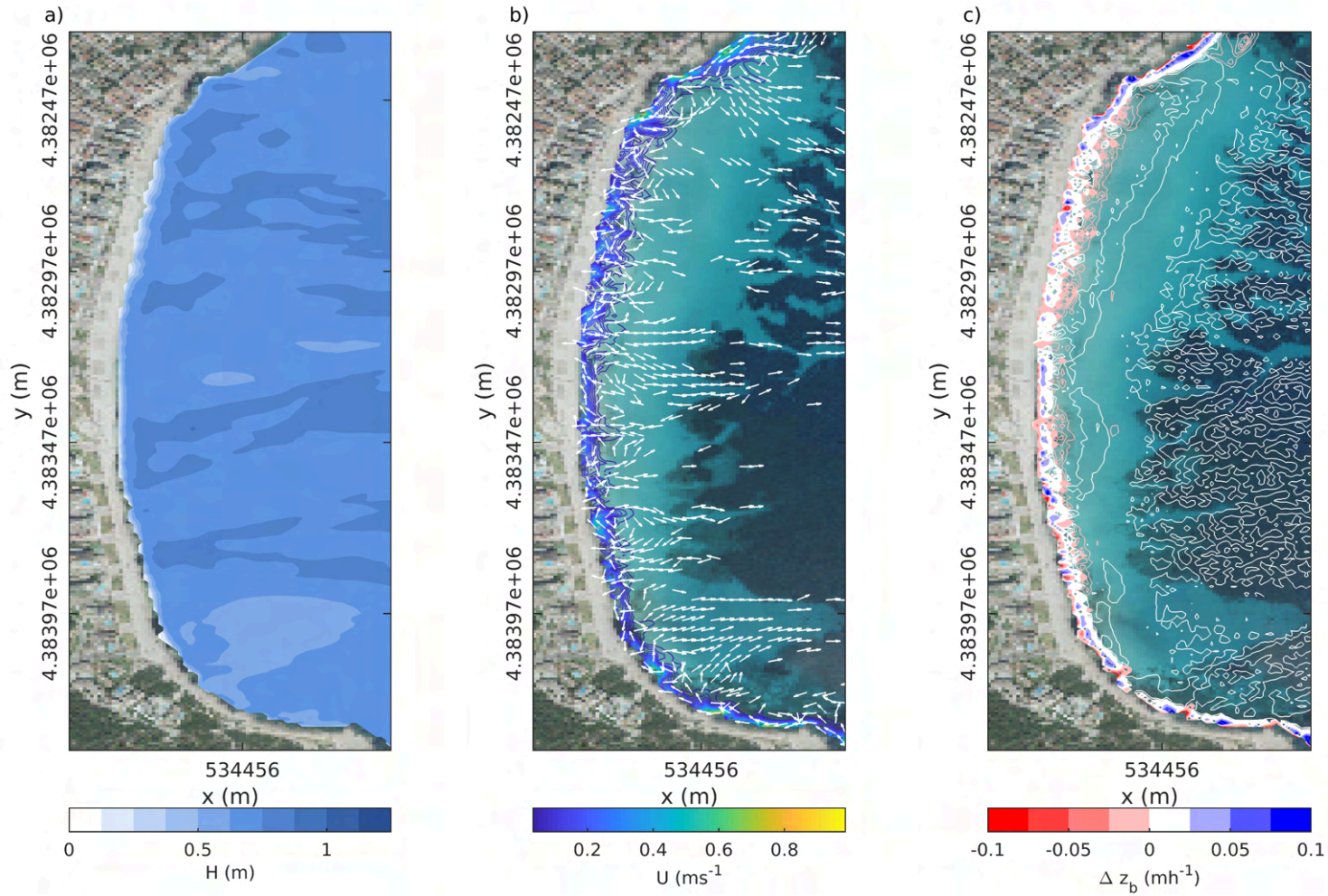


Figure 45. Mean northern component spring storm conditions at Cala Millor. a) Time averaged significant wave height H_s (m); b) Mean current field U (ms^{-1}) (arrows show the mean circulation patterns related to $U > 0.02 ms^{-1}$); c) time-averaged bottom changes Δz_b (mh^{-1}).

vii) SPRING MEAN STORM CONDITIONS: SOUTHERN COMPONENT

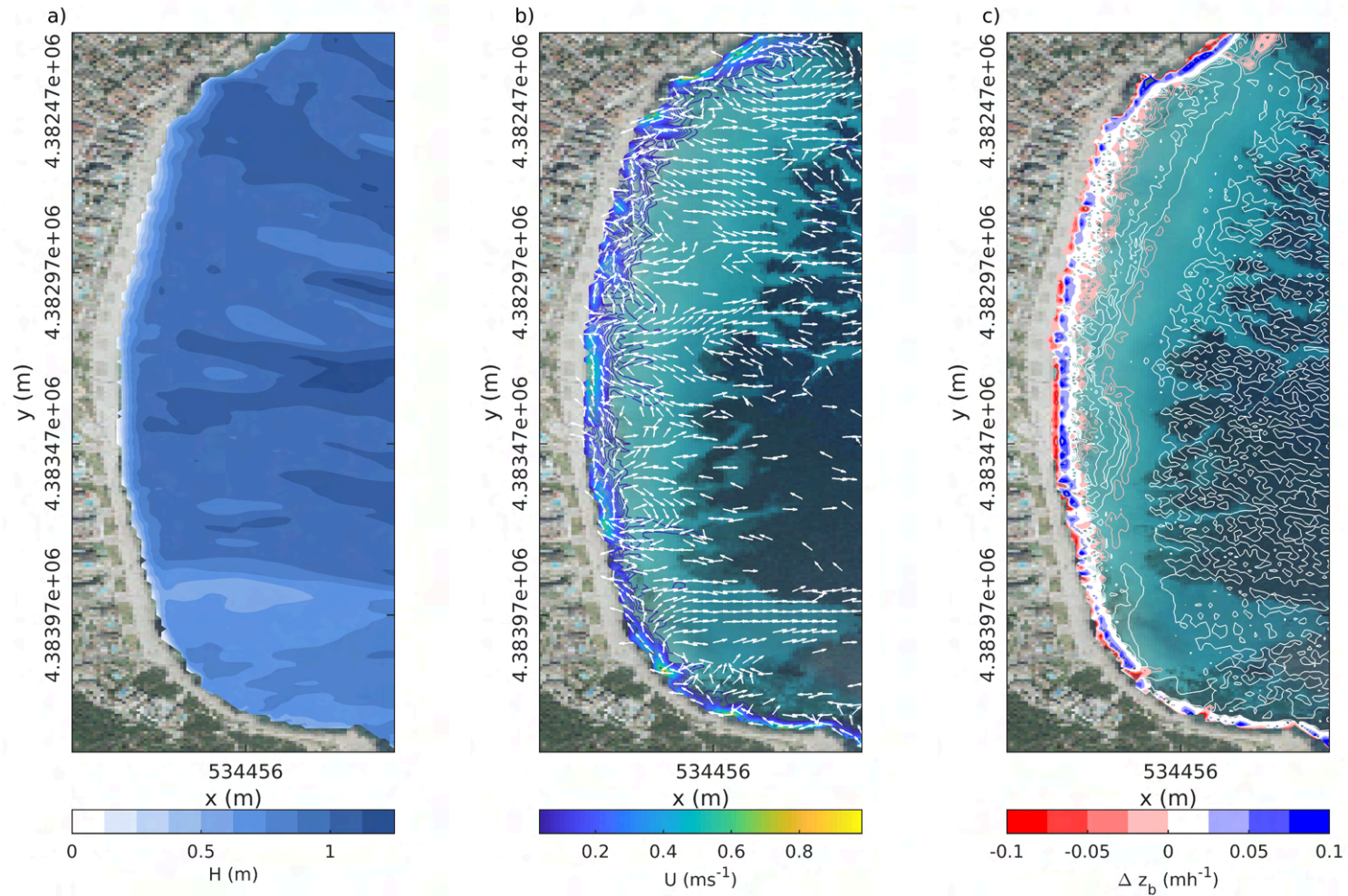


Figure 46. Mean southern component spring storm conditions at Cala Millor. a) Time averaged significant wave height H_s (m); b) Mean current field U (ms^{-1}) (arrows show the mean circulation patterns related to $U > 0.02 ms^{-1}$); c) time-averaged bottom changes Δz_b (mh^{-1}).

viii) SUMMER MEAN STORM CONDITIONS

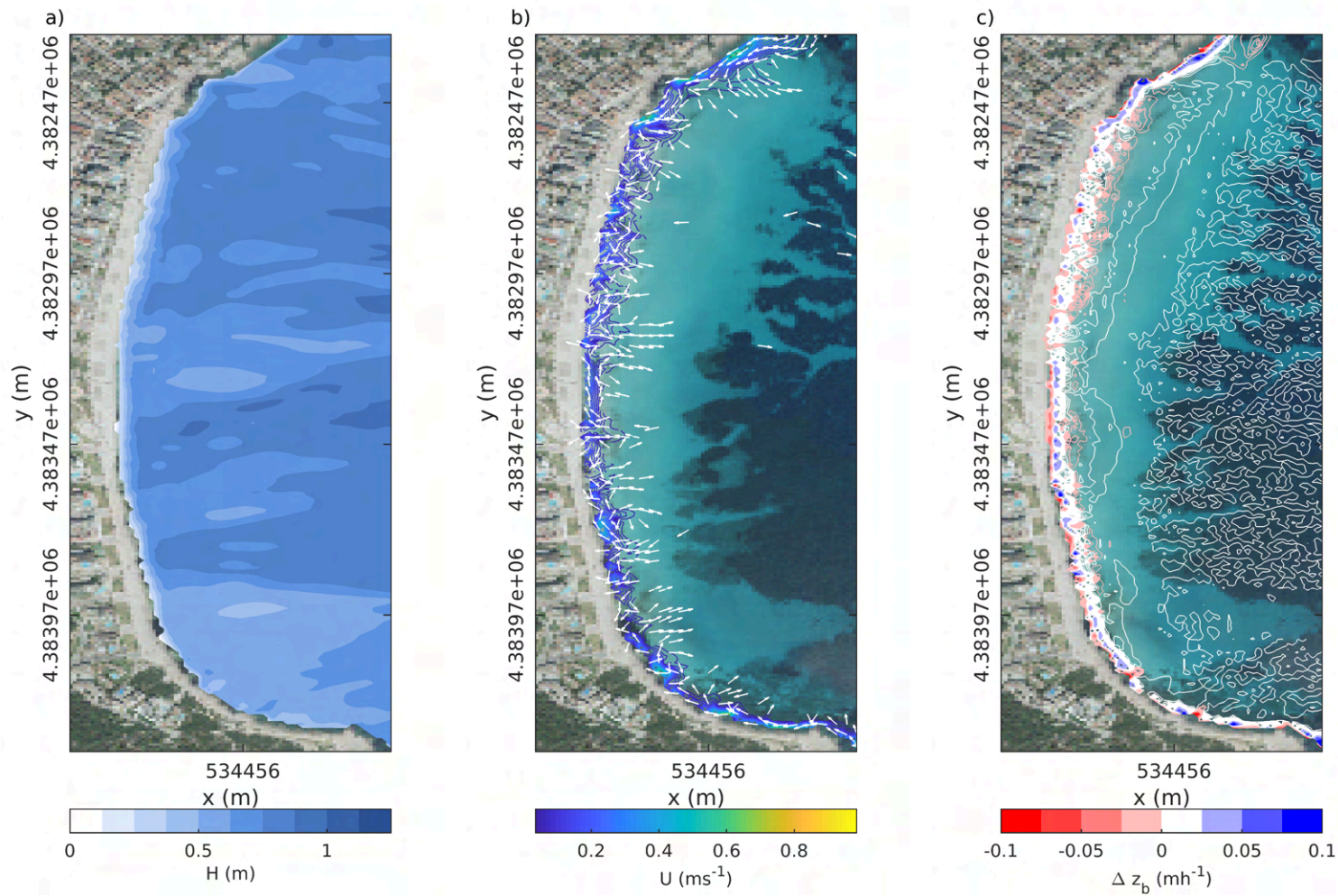


Figure 47. Mean summer storm conditions at Cala Millor. a) Time averaged significant wave height H_s (m); b) Mean current field U (ms^{-1}) (arrows show the mean circulation patterns related to $U > 0.02 ms^{-1}$); c) time-averaged bottom changes Δz_b (mh^{-1}).

ix) SUMMER MEAN STORM CONDITIONS - NORTHERN COMPONENT

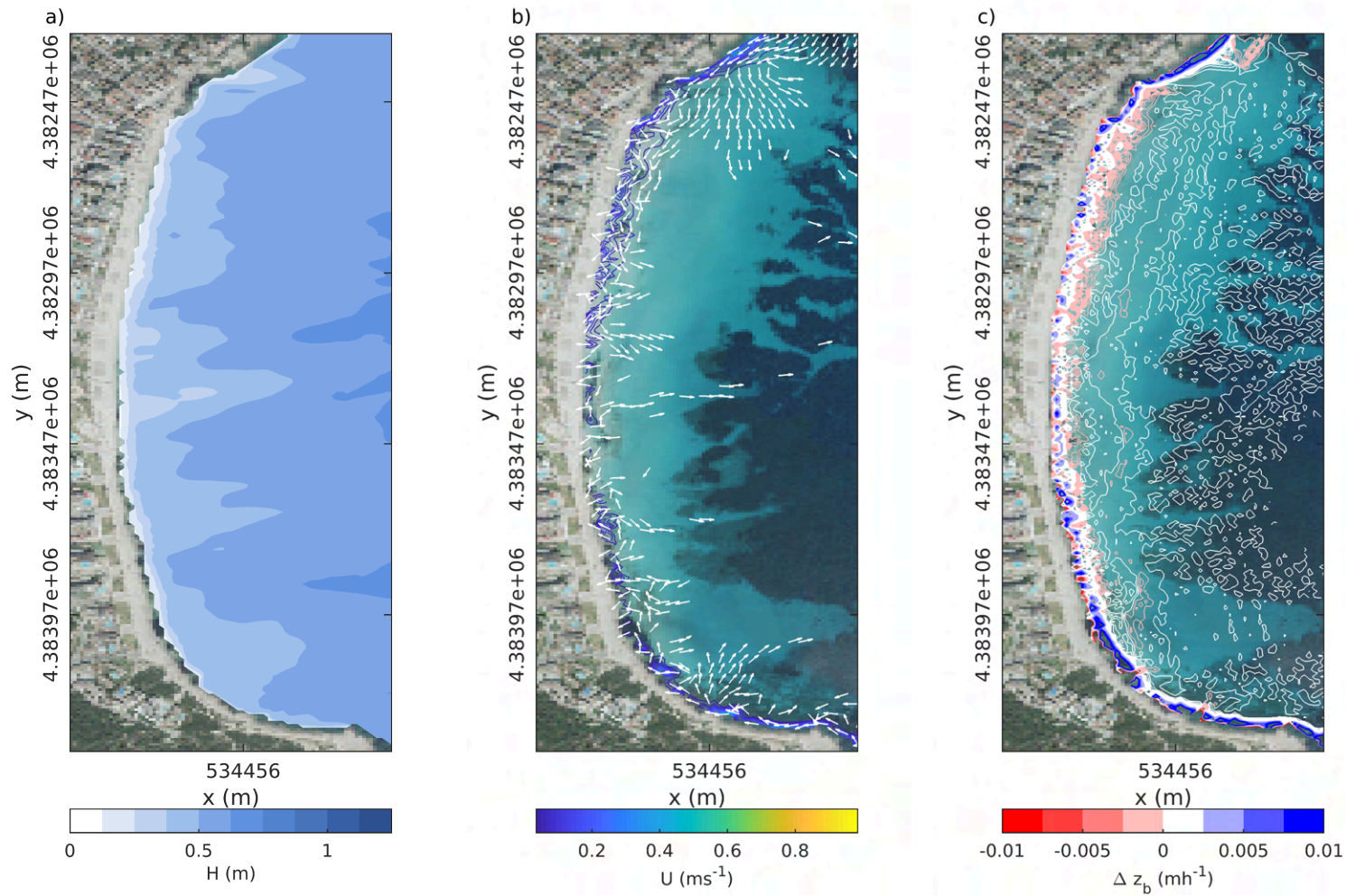


Figure 48. Mean northern component summer storm conditions at Cala Millor. a) Time averaged significant wave height H_s (m); b) Mean current field U (ms^{-1}) (arrows show the mean circulation patterns related to $U > 0.02 ms^{-1}$); c) time-averaged bottom changes Δz_b (mh^{-1}).

x) SUMMER MEAN STORM CONDITIONS - SOUTHERN COMPONENT

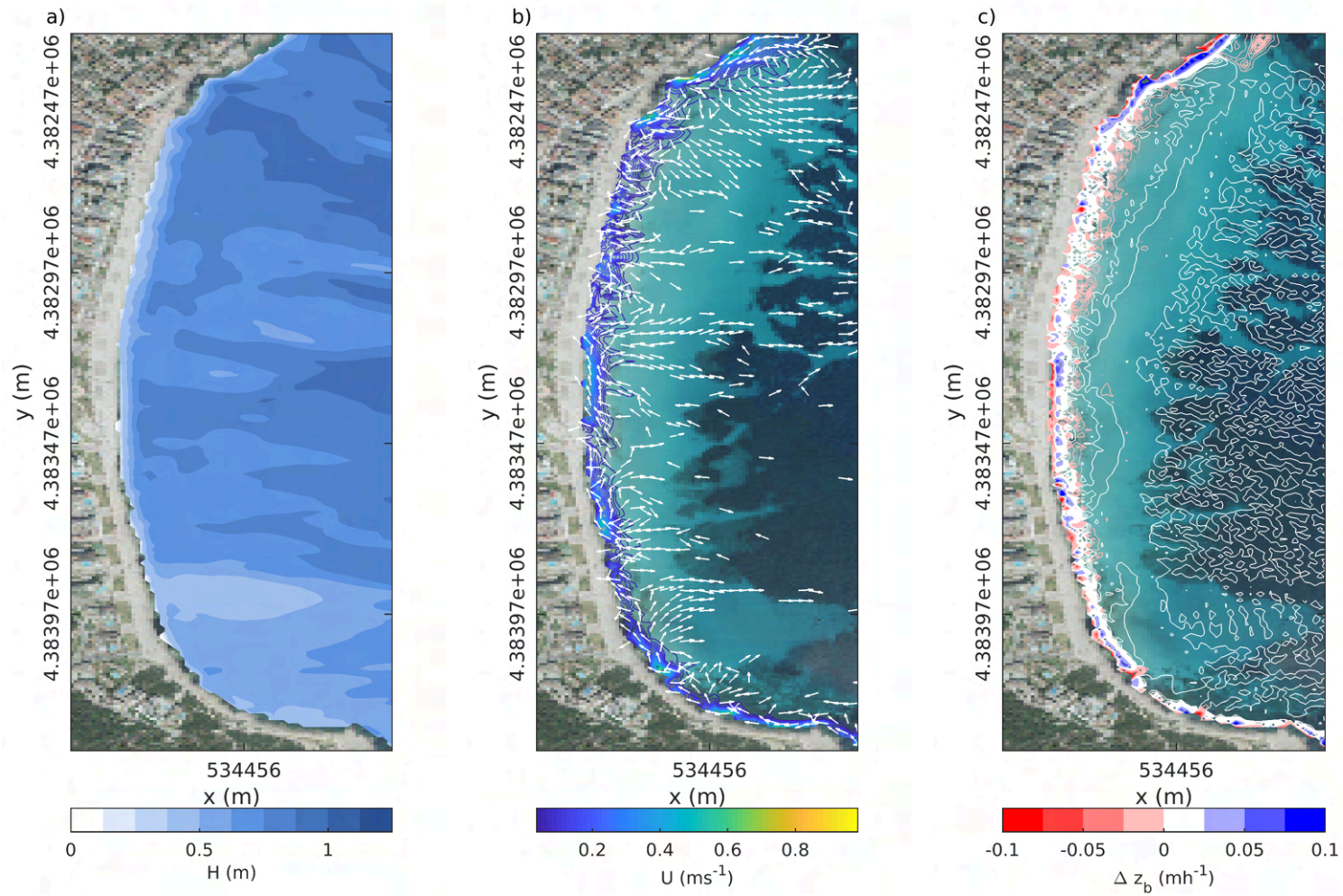


Figure 49. Mean southern component summer storm conditions at Cala Millor. a) Time averaged significant wave height H_s (m); b) Mean current field U (ms^{-1}) (arrows show the mean circulation patterns related to $U > 0.02 ms^{-1}$); c) time-averaged bottom changes Δz_b (mh^{-1}).

xi) AUTUMN MEAN STORM CONDITIONS

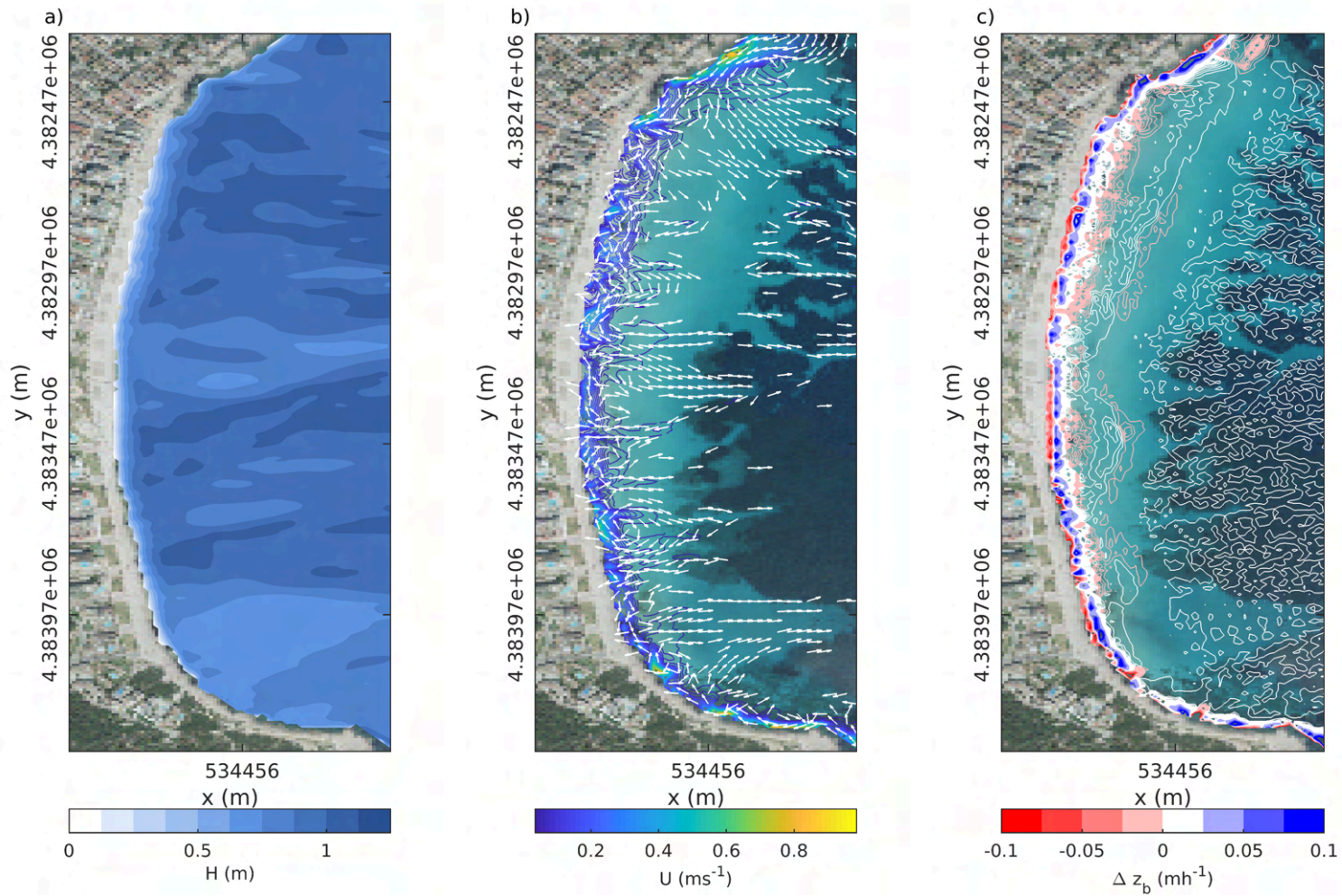


Figure 50. Mean autumn storm conditions at Cala Millor. a) Time averaged significant wave height H_s (m); b) Mean current field U (ms^{-1}) (arrows show the mean circulation patterns related to $U > 0.02 ms^{-1}$); c) time-averaged bottom changes Δz_b (mh^{-1}).

2.1.2.6. Conceptual model

The beach model is outlined following the results from the mean and storm wave conditions described in the previous sections of this document.

Following the data provided by the AWAC at Cala Millor the mean wave climate at Cala Millor is 0.5 m with a wave period of 6.2 s and a direction from the ESE (100.3°) (Table 6 and Fig. 35). This mean wave conditions are very similar for the different seasons being slightly smoother during summer with milder wave heights and shorter periods. As waves propagate towards the coast, waves are transformed by refraction, diffraction, reflection, dissipation and bottom viscous effects that modify the wave fronts in the direction of propagation.

Cala Millor is well exposed to waves from the first and second quadrant (waves from the NE to the SE) and only the orographic ends that shelter the bay provide some protection. Swells from the NNE, are reduced by the diffraction from Cap des Pinar at the northern end of the bay. For the mean wave climate the waves are not completely diffracted reaching the shallow part of Cala Millor beach with wave heights below 0.10 m. Waves breaking generate mild currents (with magnitude below $1 \text{ cm}\cdot\text{s}^{-1}$), mainly parallel to the planform with a moderate capacity to mobilize sand outside the breaking zone. During mild conditions, the southern and northern sides of the beach present a submerged sandbar 200 m from the shoreline and between 2 and 3 m depth, being the beach mainly dissipative in the central part. Beach width during mean conditions is wider. Even though for mean conditions currents are weak there are longshore currents in the north part of the beach directed southwards and in the southern part of the beach northwards with multiple cells in the central part of the beach (Fig. 51).

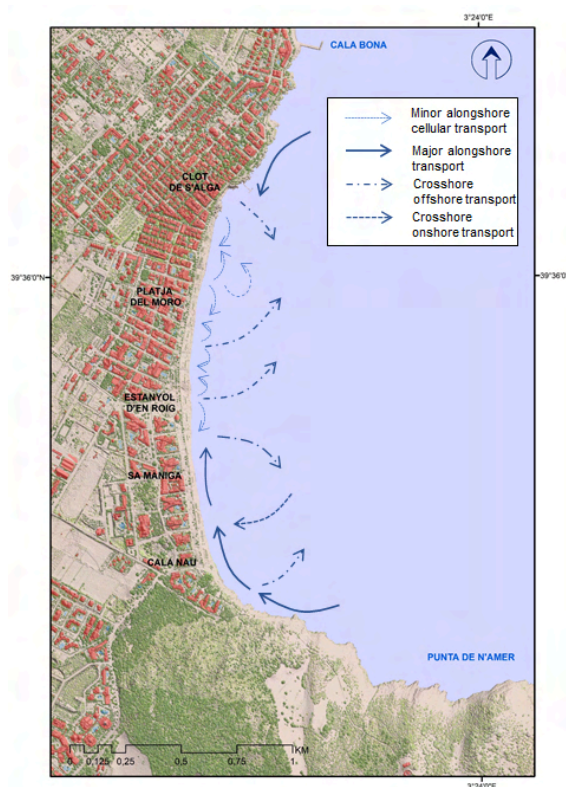


Figure 51. Schematic circulation for mean conditions at Cala Millor.

Swells from NE, ENE, E and SSE directions directly affect Cala Millor beach, so as they refract little during propagation. NE waves, which are the most frequent and energetic in deep waters, induce currents towards the S at the northern part of Cala Millor and several cells in the central section with outflowing currents. In the southern part currents are directed northwards (Fig. 52, left).

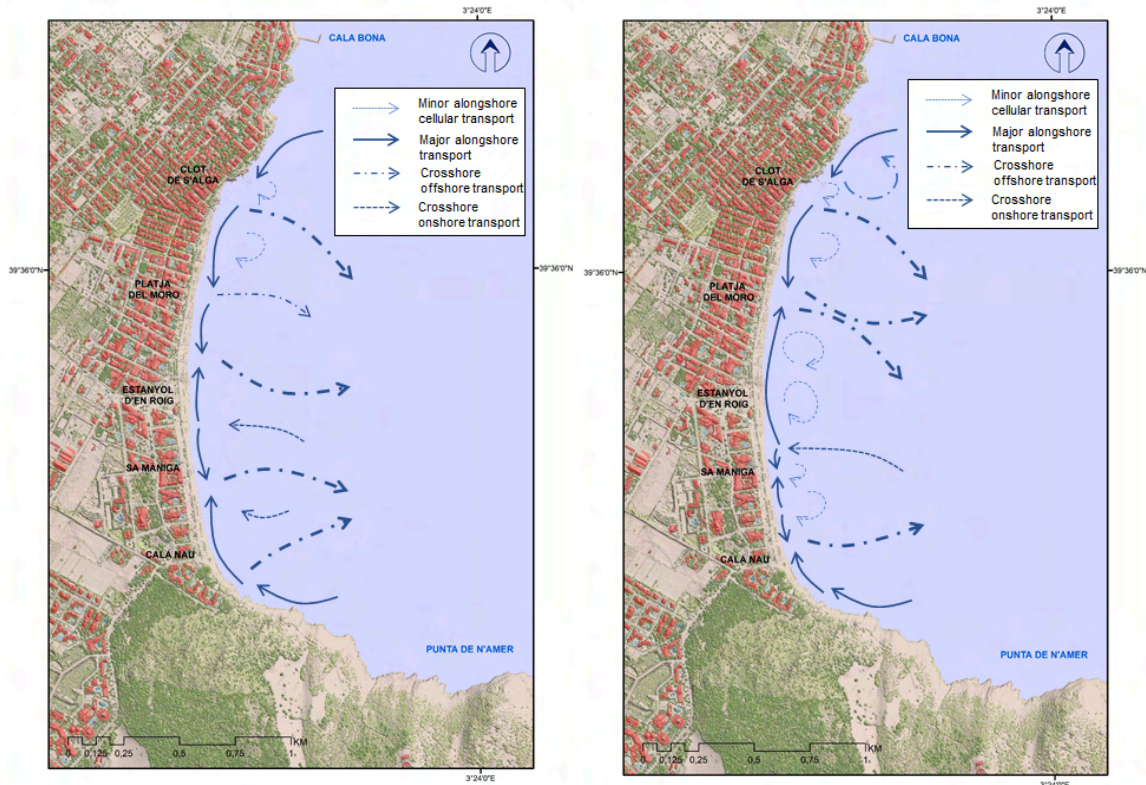


Figure 52. Schematic circulation for storm NE (left) and ESE (right) conditions at Cala Millor.

For ESE waves (Fig. 52, right), a well defined southward current is observed along the north part of the beach. On the other hand, SE waves do not influence the southern end of the beach, but they generate south to north currents from the central portion to the northern end of the beach with several cells in the central and southern part. Currents of $20 \text{ cm} \cdot \text{s}^{-1}$ (Fig. 40, 41 and 42) transport the sediment generating a longshore bar parallel to the coast at depths between 2 and 3 m. Cala Millor is bounded by Cap Pinar in the north and Punta de n'Amer in the south thus deep water waves from NNE to SSE represent well the main behaviour of the beach system. From Fig. 41, it can be observed that deep water waves with a NNE component are highly modified by the *Posidonia* meadow, which highly reduces the energy of the waves. NNE waves are the dominant regime and the most energetic at deep waters during winter and summer. However, during winter waves are more energetic than in summer and therefore higher wave-induced currents are generated in winter with larger morphological changes.

Waves from the East (Fig. 53) impact directly in Cala Millor beach directly being the shoaling by depth and *Posidonia* meadow the actors acting on the loss of energy in the wave fronts. In these cases, strong rip currents are generated in the central part of the beach, while at the northern part there is a southwards current and in the southern part northwards.

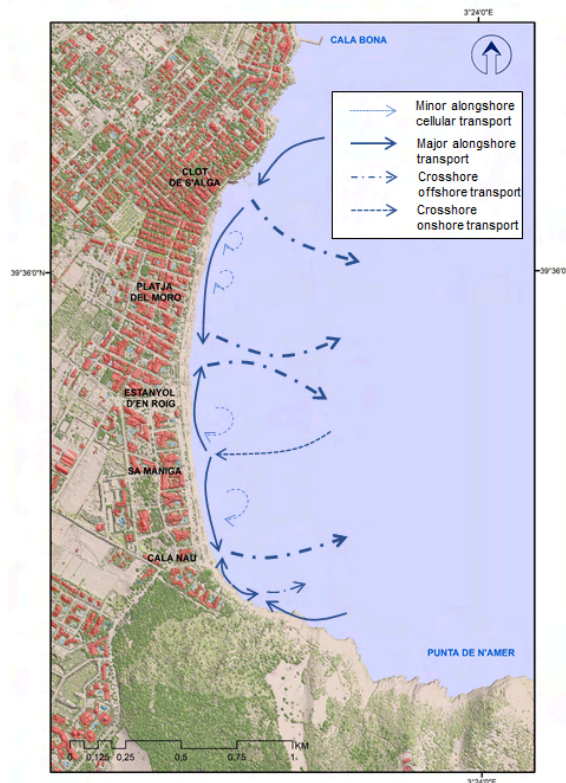


Figure 53. Schematic circulation for East storms conditions at Cala Millor.

2.1.3. Hazard Assessment Physical Dimension

The hazard assessment of coastal flooding has been developed through modelling different scenarios and time-horizons, taking into account factors such as sea level rise, storm surge, wave action, and *Posidonia oceanica* meadow evolution to predict extent of flooding.

2.1.3.1. Model setup

Model setup in terms of computational domain, grid, bottom and lateral boundary conditions are the same as stated in Section 2.1.4.

2.1.3.2. Sea-level Scenarios and time-horizons

Forcing conditions in terms of sea level and time-dependent wave and surges forcing are determined by the combination of sea-level projections stated in Section 1.1 and the extreme storms computed in Section 1.2 for the RCP-4.5 and RCP-8.5 scenarios and the 2030, 2050 and 2100 time-horizons (Table 8). A total amount of 55 simulations and resulting flooding maps considering the three confidence intervals (min, mean, max) for each RCP scenario and time horizon: for RCP-4.5 we have 9 permanent flooding (Pf) maps, 9 extreme flooding maps considering *P. oceanica* invariant (Ef_P0); 9 extreme flooding maps considering *P. oceanica* variant (Ef_Pt); ídem for RCP-8.5; and an extra map for the simulation of an extreme flooding for the current state (Ef_P0).

IPCC Sc	Forcing	Current(2023)	2030	2050	2100
RCP-4.5	Sea level		PERMANENT (Pf)	PERMANENT (Pf)	PERMANENT (Pf)
	Sea level + wave and storm surge T100	EXTREME (Ef_PO)	EXTREME (Ef_PO)	EXTREME (Ef_PO)	EXTREME (Ef_PO)
	Sea level + wave and storm surge T100 Corresponding <i>P. oceanica</i> meadow		EXTREME (Ef_Pt)	EXTREME (Ef_Pt)	EXTREME (Ef_Pt)
RCP-8.5	Sea-level		PERMANENT (Pf)	PERMANENT (Pf)	PERMANENT (Pf)
	Sealevel + wave and storm surge T100		EXTREME (Ef_PO)	EXTREME (Ef_PO)	EXTREME (Ef_PO)
	Sea level + wave and storm surge T100 Corresponding <i>P. oceanica</i> meadow		EXTREME (Ef_Pt)	EXTREME (Ef_Pt)	EXTREME (Ef_Pt)

Table 8. Summary of simulations and resulting flooding events for Cala Millor.

Considering the interannual fluctuations in sea level, and recognizing that the sea level provided by the AWAC represents variations from a reference level rather than an absolute value, the current sea level from the Porto Cristo tide gauge (SOCIB) is used as the baseline (2023 averaged sea-level). To this baseline, the average interannual variation from the previously described sea level analysis is first added. Subsequently, the projected sea level rise for each RCP scenario and time horizon is incorporated, using the 0.05, 0.5, and 0.95 quantiles (Table 9).

	RCP 4.5 η_t (m)			RCP 8.5 η_t (m)		
	2030	2050	2100	2030	2050	2100
Current sea-level η_0	0.27					
Average seasonal variation η_s	0.34					
Projected SLR η_{RCP}	0.12 (0.03,0.23)	0.24 (0.09,0.42)	0.59 (0.26,1.07)	0.12 (0.04,0.22)	0.26 (0.11,0.45)	0.81 (0.45,1.31)

Table 9. Sea-level forcing components considered on simulations for Cala Millor.

2.1.3.3. Wave forcing

The model is forced at the offshore boundary using the synthetic storm derived from the multivariate analysis detailed in Section 1.2. This storm corresponds to the T100 event, characterized by wave heights and surges of a duration of 88 h (Fig. 54). To focus on the maximum inundation level and reduce computational demands, the model is run for the 5 intermediate hours of the storm, capturing its peak. Model warm-up is achieved by running waves for at least 1 hour prior to the analysis, ensuring initial stabilization. Wave direction is set to 90° (E) during the storm.

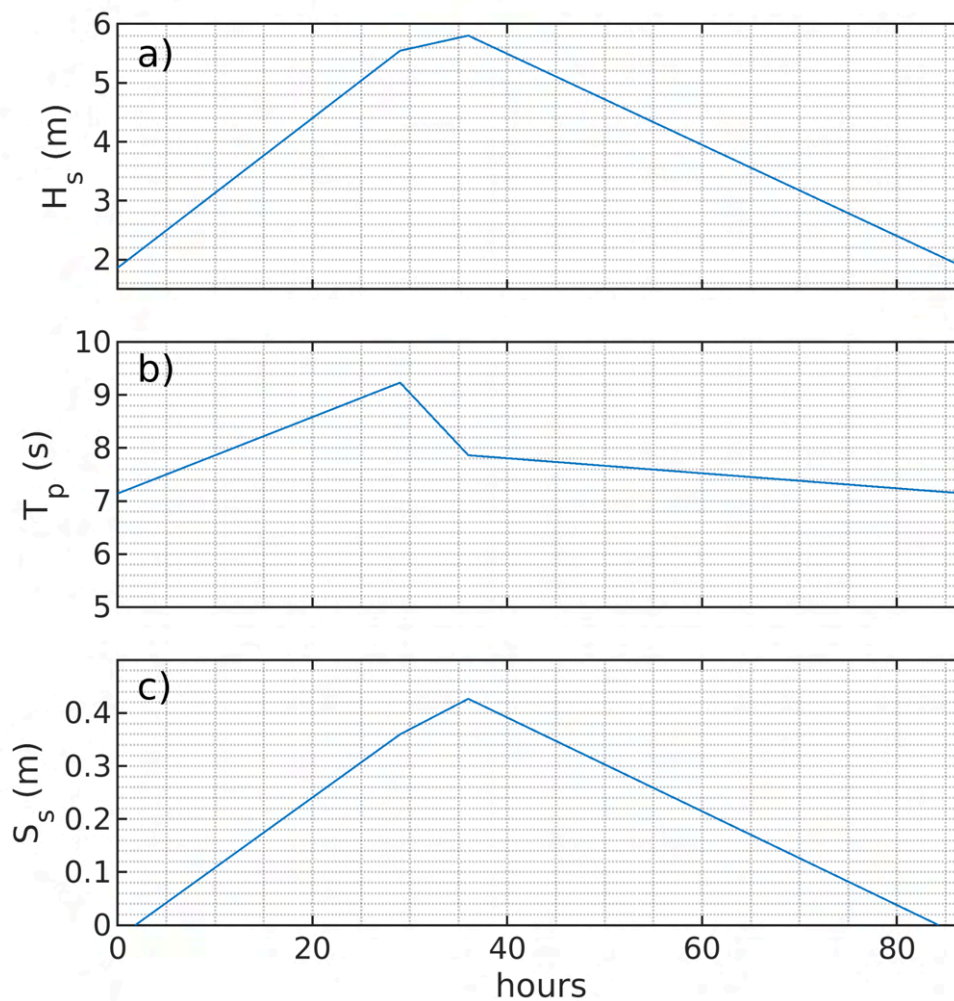


Figure 54. Synthetic reference storm of T100 for Cala Millor: a) Significant wave height; b) Peak period and c) Storm surge.

2.1.3.4. *Posidonia oceanica* meadow conditions

In addition to the hydrodynamic forcing, two types of simulations are performed by considering: i) no changes in *P. oceanica* meadow, and ii) changes in *P. oceanica* extent and characteristics (detailed in Section 4.3). *P. oceanica* meadow characteristics for the types of runs and time horizons are summarized in Table 9.

RCP scenario	Time-horizon	N (#/m ²)	α_h	b_v	C_d (-)
No changes		589	0.8	0.026	0.08
RCP-4.5	2030	314	0.8	0.026	0.08
	2050	77	0.8	0.026	0.08
	2100	-	-	-	-
RCP-8.5	2030	305	0.8	0.026	0.08
	2050	69	0.8	0.026	0.08
	2100	-	-	-	-

Table 9. *Posidonia oceanica* characteristics considered on numerical modelling at Cala Millor.

Since data regarding the evolution of *P. oceanica* leaves width and length considering the different IPCC RCP scenarios and time-horizons are not available, α_h , b_v and C_d are considered invariants for all the simulations and set to the values from the experiment of Infantes *et al.*, (2012) and from model calibration (Fernandez-Mora *et al.*, 2024; Fernández-Mora *et al.*, 2025, submitted; Fernández-Mora *et al.*, 2025, in prep.).

In order to summarize the impacts of the physical dimension, Table 10 lists the surface area of current emerging land that appears flooded for the different climatic scenarios, and the expected beach width.

RCP scenario	Time-horizon	Pf (m ²)	Ef (Po) (m ²)	Ef (Pt) (m ²)	Beach width (m)
-	2024	-	71,400	-	32.75
RCP4.5	2030	4,900 (2,800; 8,075)	78,500 (74,500; 83,500)	75,100 (72,000; 79,600)	26.1 (24.08; 27.6)
	2050	8,375 (4,025; 14,700)	83,700 (78,500; 91,800)	87,400 (78,200; 101,900)	23.91 (19.78; 26.71)
	2100	19,300 (8,975; 31,700)	112,500 (86,800; 205,100)	117,200 (101,500; 240,500)	16.84 (9.16; 23.51)
RCP8.5	2030	4,900 (2,925; 8,075)	78,200 (71,400; 82,400)	74,700 (69,800; 77,400)	26.1 (24.08; 27.49)
	2050	8,975 (4,550; 15,750)	82,600 (79,400; 94,300)	91,500 (81,000; 98,400)	23.51 (19.10; 26.33)
	2100	24,425 (15,750; 43,900)	145,700 (100,800; 723,600)	155,100 (101,200; 190,850 ⁷)	13.61 (1.69; 19.1)

Table 10. Flooded surface in m² from 2024's emerged part in the different climatic scenarios and for the three confidence intervals (min, mean, max). The flooded maps considered are "Permanent flooding (Pf)"; "Extreme flooding with *Posidonia oceanica* of current state (Ef-Po)"; "Extreme flooding with *Posidonia oceanica* dependent on the scenario (Ef-Pt)". Finally the average value of the beach width in m.

⁷ Corresponding to the flood-prone area in the first time step of the storm for RCP85 P95. The storm simulations result in the complete flooding of the computational area.

PHYSICAL DIMENSION ABSTRACT

- Cala Millor beach is a microtidal, semi-enclosed beach, predominantly influenced by waves. In terms of modal morphodynamics, it can be classified as an intermediate beach, with sediment sources primarily consisting of biogenic carbonate sands.
- The planform of the beach is slightly concave, characterised by regular sandy bottoms, although rocky features emerge in the central sector (s'Estanyol d'en Roig) and in the southern section (Sa Màniga-Cala Nau), particularly in the shallowest areas or along the coastline itself. At depths greater than 5 metres, an extensive meadow of *Posidonia oceanica* is present, within which a network of paleochannels can be observed.
- Nearshore is characterized by the presence of crescentic and parallel bars, quite dynamic and variable over time. Most intense changes in shoreline and sediments transport related to sand bar dynamics occur in the northern and central sector of the beach (Platja del Moro - Estanyol d'en Roig) and expands from shoreline to 3 m in depth.
- The average wave climate at Cala Millor displays pronounced seasonality. During autumn and winter, significant wave heights typically range from 0.5 to 0.7 m, gradually diminishing through spring and reaching an average height of 0.3 m in summer. This seasonal pattern adds to the sea level seasonal cycle. In addition, wave periods are larger during winter months, transitioning to very short waves in summer, reflecting calmer sea conditions. The predominant wave direction varies slightly seasonally, generally shifting between E-ENE and E-ESE, which may influence local sediment transport and coastal morphology throughout the year.
- Energetic wave periods at Cala Millor are observed predominantly during winter and autumn months, when both maximum and extreme values occur. Storm events are rare during the summer period. When analyzing extreme events, defined by the 99th percentile of wave height, these are most frequently observed in mid-autumn and late winter. In terms of wave direction, winter storms display a distinct E-NE component, whereas spring storms are more variable, with a mix of E-NE and E-SE directions, the latter being predominant. Autumn storms, on the other hand, show a broader range of directions. There is no clear signal of the frequency and duration of storms in the long term, although longer series are necessary to analyze this in more detail based on larger observational data sets.
- In terms of sediment balance, a slight overall sediment deficit is observed ($-0.14 \text{ m}^3/\text{m}^2$) within the context of topo-bathymetric three-dimensional changes. However, considering the limitations of the topo-bathymetric surveys, along with the recorded episodes of positive sediment balance, it is reasonable to infer that much of the sediment exiting the monitored area is not lost, but rather remains in adjacent regions (either near Punta de n'Amer or in front of Cala Bona). Depending on wave characteristics and direction, this sediment may eventually return to the study area. Notably, between 2021 and 2022, the final sediment balance indicated an influx of $52,000 \text{ m}^3$ of sediment into the control area.
- There is a sequence of positive and negative sediment balance episodes. Although this time series is arguably one of the most comprehensive for any beach in the western Mediterranean, it does not yet allow us to draw definitive conclusions about the existence of significant temporal patterns or the specific forces responsible for these changes. However, it is evident that sediment balance dynamics involve transfers between different hydrodynamic zones of the beach. When the dry beach experiences sediment loss, accumulation tends to occur in the surf and shoaling zones, whereas when sediment is lost from these zones, the dry beach tends to recover. This cross-shore dynamic reflects an uneven response to the impacts of extreme

events, which typically transport large volumes of sediment to depths greater than 2 m in a short time frame. For sediment to be transported back to shore, however, less energetic and more persistent forces are required, which are not always present in the study area. Additionally the system of paleochannels beneath the beach plays a role in its dynamics. In successive bathymetric surveys, the geometry of these paleochannels appears more or less pronounced, depending on the sediment covering them, further influencing the beach's morphodynamics.

- Shoreline and dry beach width variability at Cala Millor are important, because the sand bars dynamics and changes in sediment mass budgets related to energetic storms. Changes backwards and seaward around 20 m, also on a daily basis, are not unusual.
- On a larger time scale, the historic beach width still remains above the reference natural conditions exhibited in aerial photographs from 1956. When the beach still has a healthy coastal dune ridge to compensate for the erosive action of the most energetic storms. Historically the dry beach has experienced 6 sand nourishments. The last one in 2002 in order to compensate for the impact of the 2001 extreme event, that receded the beach to lower value in terms of mean beach width, slightly below the 1956 reference. From 2008 and taking into account the maximum width attended after the last nourishment, the dry mean beach width is receding, specially in the southern sector of the beach where rock reefs crops out because the combined action of storm wave impact, urban pluvials draining on the beach and the interactions with the promenade wall that don't follow the natural plan view geometry of the beach.
- High spatio-temporal resolution data collected from the Cala Millor beach monitoring station from 2011 to 2023 reveal that there is a general decreasing trend in dry beach width. Although the dry beach width still is larger than the 1956 natural conditions references, and in the time series it can be observed some positive variations representing an increase in mean beach width. Spatially, the central area of the beach remains wider than the other areas. The southern area that presents rock outcrops, has a smaller width and it is controlled by rocks. The northern area presents larger variability, with width varying over time, and particularly from 2018 to 2023. Spatio-temporal analyses highlight that this variability is mainly controlled by the annual sea-level cycle, the seasonal wave climate, specific storms, and there is a peak of lower frequencies (2.5 yr) that could be related to climatic cycles, although the current timeseries length need to be larger to conclude this.
- Mean wave and storm-extreme conditions have been modelled to obtain a conceptual model on beach behavior. For the mean wave climate the waves are not completely diffracted reaching the shallow part of Cala Millor beach with wave heights below 0.10 m. Waves breaking generate mild currents (with magnitude below $1 \text{ cm}\cdot\text{s}^{-1}$), mainly parallel to the planform with a moderate capacity to mobilize sand outside the breaking zone. During mild conditions, the southern and northern sides of the beach present a submerged sandbar 200 m from the shoreline and between 2 and 3 m depth, being the beach mainly dissipative in the central part. Beach width during mean conditions is wider. Even though for mean conditions currents are weak there are longshore currents in the north part of the beach directed southwards and in the southern part of the beach northwards with multiple cells in the central part of the beach.
- Swells from NE, ENE, E and SSE directions directly affect Cala Millor beach, so as they refract little during propagation. NE waves, which are the most frequent and energetic in deep waters, induce currents towards the S at the northern part of Cala Millor and several cells in the central section with outflowing currents. In the southern part currents are directed northwards. For ESE waves, a well defined southwards current is observed along the north part of the beach.

On the other hand, SE waves do not influence the southern end of the beach, but they generate northward currents from the central portion to the northern end of the beach with several cells in the central and southern part. Currents of $20 \text{ cm}\cdot\text{s}^{-1}$ transports the sediment generating a longshore bar parallel to the coast at depths between 2 and 3 m. Waves from the East impact directly in Cala Millor beach directly being the shoaling by depth and *Posidonia* meadow the actors acting on the loss of energy in the wave fronts. In these cases, strong rip currents are generated in the central part of the beach, while at the northern part there is a southwards current and in the southern part northwards.

- The hazard assessment of coastal flooding has been developed through modelling different scenarios and time-horizons, taking into account factors such as sea-level rise, storm surge, wave action, and *Posidonia oceanica* meadow evolution to predict extent of flooding. For the IPCC scenario RCP4.5 in 2030 the area affected by permanent sea level flooding will range from $\sim 2,800 \text{ m}^2$ to $8,075 \text{ m}^2$, and the area affected by temporary storm flooding from $\sim 72,000 \text{ m}^2$ to $83,500 \text{ m}^2$; in 2050 the area affected by permanent sea level flooding will range from $\sim 4,025 \text{ m}^2$ to $14,700 \text{ m}^2$, and the area affected by temporary storm flooding from $\sim 78,200 \text{ m}^2$ to $101,900 \text{ m}^2$, and for the 2100 scenario the area affected by permanent sea level flooding will range from $\sim 8,975 \text{ m}^2$ to $31,700 \text{ m}^2$, and the area affected by temporary storm flooding from $\sim 86,800 \text{ m}^2$ to $240,500 \text{ m}^2$. For the IPCC scenario RCP8.5 in 2030 the area affected by permanent sea level flooding will range from $\sim 2,925 \text{ m}^2$ to $8,075 \text{ m}^2$, and the area affected by temporary storm flooding from $\sim 69,800 \text{ m}^2$ to $82,400 \text{ m}^2$; in 2050 the area affected by permanent sea level flooding will range from $\sim 4,550 \text{ m}^2$ to $15,750 \text{ m}^2$, and the area affected by temporary storm flooding from $\sim 79,400 \text{ m}^2$ to $98,400 \text{ m}^2$, and for the 2100 scenario the area affected by permanent sea level flooding will range from $\sim 15,750 \text{ m}^2$ to $43,900 \text{ m}^2$, and the area affected by temporary storm flooding from $\sim 100,800 \text{ m}^2$ to $723,600 \text{ m}^2$.
- Considering the ecosystemic services of the beach, especially those related to recreation, beach mean width is expected to be reduced for the IPCC scenario RCP4.5 in 2030 by $\sim 20.32\%$ in average compared to its current state, and an average reduction of $\sim 27\%$ and $\sim 48.57\%$ in 2050 and 2100 respectively. In relative terms and considering now the less favourable scenario (RCP8.5), this represents a dry beach loss between 16.05% and 26.47% in 2030, between 19.59% and 41.69% in 2050, and between 41.69% and the 94.84% in 2100.

2.2. Environmental Dimension

The environmental risk analysis of Cala Millor beach focused on two key ecosystems: the *Posidonia oceanica* meadow and the coastal dune system, as well as the impacts associated to these ecosystems related to sea level rise, the permanent and temporal coastal flooding and water, and rise in sea-water temperature. Various aspects of their evolution and current state have been evaluated, including:

Analysis of the Environmental Elements of Cala Millor

1) Evolution and Current State of the Coastal dune system

- Historical Changes of the Coastal dune system: Analysis of variations in shape, size, and location over time.
- Current State of the Coastal dune system: Assessment of its present configuration, including the presence of mobile or stabilized dunes, anthropogenic paths, size, and vegetation composition.

2) *Posidonia oceanica* meadow

- Meadow Upper limit
- Levels of burial and growth
- Current status: Density and meadow lower limit
- Future projections for *Posidonia oceanica* meadows

3) Environmental Risk Assessment

- Vulnerability of the coastal dune system
- Resilience of the *Posidonia oceanica* meadow

The methodology applied in each analysis is detailed in the following sections, along with the corresponding results.

2.2.1 Coastal dune system

Although the dune system expanded previously along the municipalities of Sant Llorenç des Cardassar and Son Servera, it is now entirely situated within the municipality of Sant Llorenç des Cardassar. This dune system is part of the typical Mediterranean coastal landscape, where coastal dunes play a crucial role in protecting the shoreline from erosion and in conserving biodiversity (Roig-Munar *et al.*, 2019). In Mallorca, dunes are generally found in transitional zones between the sandy beach and the inland, where the accumulation of sand is favored by wind dynamics and the presence of stabilizing vegetation, such as *Ammophila arenaria* and *Elymus farctus*.

The dunes of Mallorca are particularly important due to their role in protecting coastal ecosystems and their capacity to serve as natural barriers against storms and erosion. These formations have a complex structure, consisting of both mobile dunes, formed by the action of the wind, and stabilized dunes, which have been fixed by vegetation. Dune vegetation also plays a key role in preventing sand displacement and promoting the formation of new deposits.

The Cala Millor dune, like many others on the island, has been influenced by both natural and human factors (vid. Garcia & Servera, 2003). Tourist activities and urbanization in the surrounding

area have altered its structure and function, resulting in changes to its size, location, and vegetation composition.

This analysis will examine the historical evolution of the dune, assessing variations in its shape, size, and location over time, as well as its current state, considering factors such as the presence of mobile or stabilized dunes, anthropogenic pathways, its size, and vegetation composition.

2.2.1.1 Historical changes of the Dune

The analysis of the evolution of the dune system in Cala Millor has been conducted using images derived from orthophotos of the National Aerial Orthophotography Plan (PNOA), available in the spatial data catalogue of the Cartographic and Geographic Institute of the Balearic Islands (ICGIB) and the Collection of Maps and Historical Aerial Photography of the University of the Balearic Islands. These orthophotos include both modern digital images and scanned aerial photographs from historical flights over the Balearic Islands, spanning from 1956 to the present. The images enable the identification of changes in the shape and extent of the dune system, highlighting the dynamics of growth, erosion, and stabilisation in response to natural processes and human activities.

The resolution of older orthophotos imposes limitations on the analyses that can be performed, restricting them to general parameters such as area and perimeter, which remain discernible even in low-resolution images. Although measurements of length and width are available, these data are subject to greater uncertainty due to the limited resolution of historical imagery. Other parameters, such as vegetation types or the distinction between mobile and stabilised dunes, cannot be reliably identified or classified from these older images.

The accuracy of area and perimeter measurements is closely tied to pixel size. For example, the orthophotos from 1956 were originally captured in analogue format using aircraft-mounted aerial cameras. These photographs were later digitised, resulting in orthophotos with relatively low resolution, typically in the range of 1 m/pixel or more. At this resolution, a single pixel can encompass substantial variability over small areas, introducing uncertainty into the measurements. By comparison, modern PNOA orthophotos feature much higher resolutions, typically 0.25 m/pixel, enabling detailed analyses of smaller features such as dune contours, specific vegetation patterns, and even human infrastructure.

Despite the limitations of older orthophotos, the combination of historical and contemporary imagery provides an invaluable tool for assessing long-term changes in the dune system and understanding its interactions with urban development in Cala Millor.

Below, we examine orthophotos from 1956, 1973, 1981, 1990, and 2024 (Fig. 55), allowing for a comparison of the significant changes in the dune system and the notable reduction in dune area.

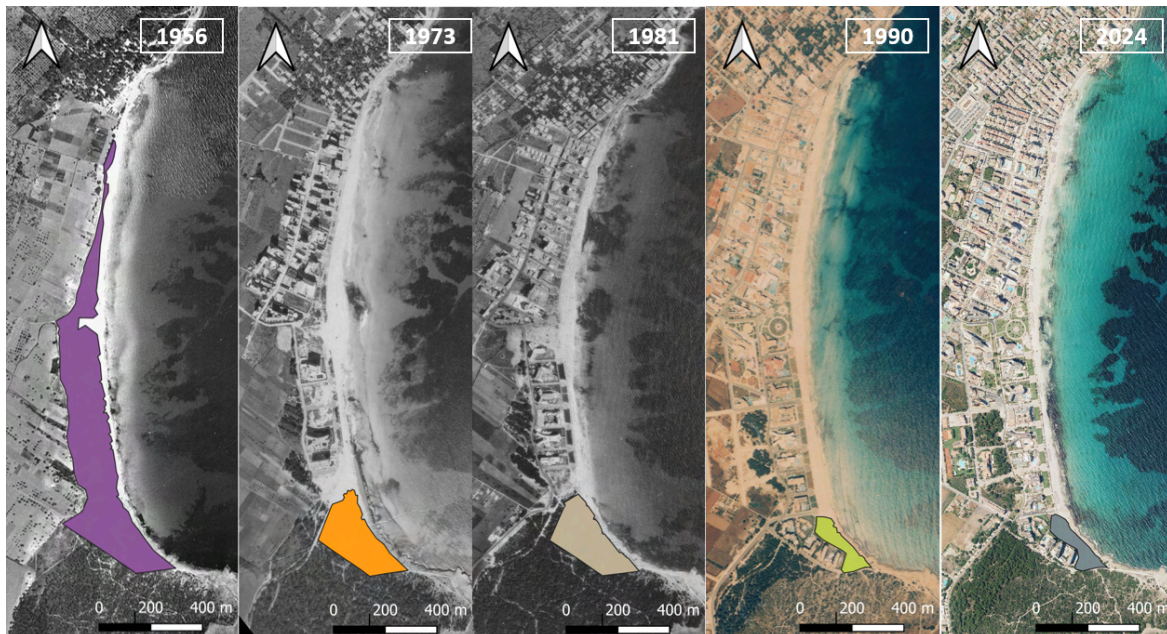


Figure 55. Cala Millor coastal dune system extension evolution, 1956-2024.

In 1956, the Cala Millor coastal dune sector directly related to the beach covered an area of 18.8 ha (187,965 m²), forming a well-preserved dune system that provided significant ecological and functional benefits (Fig. 55). These dunes acted as natural barriers against coastal erosion, helping to stabilize sediments and offering protection against storms and extreme waves. They also served as habitats for a unique biodiversity characteristic of coastal systems. At this time, the dune was intact and free of urbanization, allowing natural processes (such as wind-driven sediment transport) to maintain the ecosystem's balance.

Between 1956 and 1973, the analysis of the aerial photography reveals a drastic loss of the dune's area, reducing it from 18.8 ha (187,965 m²) to only 5.1 ha (51,293 m²), a reduction of 73%, or 13.7 ha (136,672 m²). This decline coincided with the explosion of tourism and the onset of massive urbanization in Cala Millor, particularly with the construction of hotels and other infrastructure along the beachfront. The occupation of the dune system not only led to the direct loss of its surface area, but also drastically altered the sedimentary dynamics of the environment. The destruction of the dune system disrupted the natural cycle of sand storage and regeneration, making the beach more vulnerable to erosion, increasing exposure to storms, and altering local biodiversity.

Between 1973 and 1981, the dune area decreased from 5.1 ha (51,293 m²) to 4.9 ha (48,935 m²), a loss of 2,357 m² (4.6%). Although the rate of loss slowed, urbanization continued to expand, further limiting the natural dynamics of the ecosystem.

Between 1981 and 1990, the dune experienced another drastic loss, shrinking from 4.9 ha (48,935 m²) to just 1.6 ha (15,892 m²), a cumulative loss of 91% of the dune system surface compared to its original extent.

The most recent images, covering the period between 1997 and 2024, show that the dune system's area has remained stable at around 1.5 ha (15,051 m²). This stability is partly due to the fact that most of the dune area had already been developed, leaving only a small remnant of the

original system and because the urban protection associated with the declaration as a Natural Area of Special Interest (ANEI) already obtained in 1985 and consolidated by the law *Llei d'Espais Naturals i de Règim Urbanístic de les Àrees d'Especial Protecció de les Illes Balears* (LEN, 30 January 1991), as well as by subsequent environmental protection figures linked to the Habitat Directive of the European Union and its inclusion as a Special Conservation Area (ZEC, Decree 17/2023 de 20 de març, BOIB 36, 21.03.2023 that approves the management plan for the unit of the Nature network, Costa de Llevant, where Punta de n'Amer is included).

The aerial image and orthophoto comparison (Fig. 55) illustrates this evolution, showing how the dune transformed from a large, continuous system in 1956 to increasingly smaller fragments surrounded by infrastructure in the following years. Fig. 56 summarizes these changes quantitatively, highlighting the drastic reduction in dune area during the first decades and its stabilization at minimal levels over the last two decades.

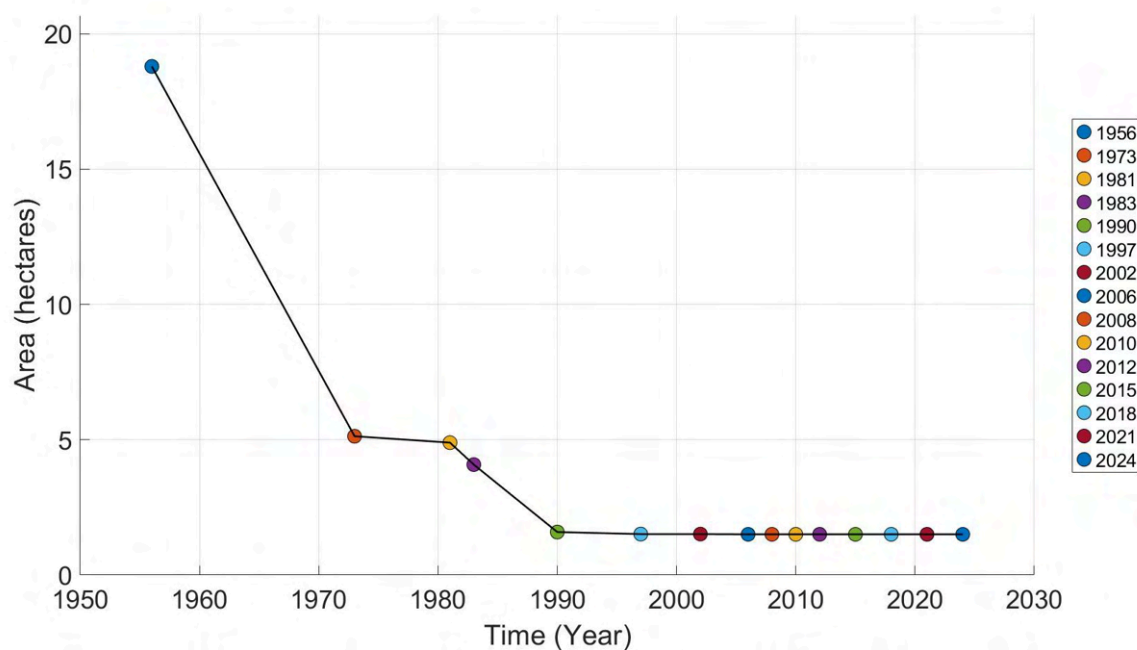


Figure 56. Area occupied by dune system in Cala Millor from 1950 to 2024.

The disappearance of a large part of the Cala Millor dune system has had significant environmental and functional implications. By the end of the 1960s, when the basic infrastructure for the development of the s'Estanyol - Sa Màniga sector and the construction of the promenade commenced, significant volumes of sand were either relocated to the beach or used as construction aggregate. Of the once extensive dune cordon that had enclosed the beach, only a 15,892 m² section remained at the transition from Sa Màniga to Punta de n'Amer. This area was further diminished between 1990 and 2000 with the development of the final hotel facilities along the seafront. Therefore, the loss of sediment retention has increased the risk of erosion and sand loss on the dry beach, directly impacting the coastline. In addition, the removal of the dune ridge has reduced natural protection against storms, making nearby infrastructure more vulnerable. A substantial key ecosystem has been lost. Finally, the eolian sand feeding of the dune system that remains on the Punta de n'Amer has been disrupted, leading to paralysis of the natural processes inherent to dune systems and to a decline in the biodiversity associated, which also means a reduction in the ecosystem services of this habitat.

2.2.1.2 Current state of the coastal dune

The current coastal dune system of Cala Millor has lost over 99% of its original extent since 1956, now reduced to a small fraction of its initial size (Fig. 57). This ecosystem, currently highly degraded, is surrounded by urbanisation and disconnected from the beach and sediment supply natural dynamics that once maintained its functional balance. Today, the system reflects not only the ecological characteristics of the Mediterranean environment but also the significant alterations caused by anthropogenic modifications over recent decades.



Figure 57. Dunes directly related with the beach system at Cala Millor existing at december de 2024.

The coastal dune system comprises three main components: the mobile dune, the stabilised dune, and the areas impacted by human interventions, such as roads and pathways, which fragment the ecosystem and exacerbate its degradation.

The mobile dune is the most dynamic and exposed part of the dune system, situated closest to the coast and directly influenced by the action of waves and wind. In this area, sand remains in constant motion, creating an unstable environment that hinders the establishment of vegetation. Nevertheless, certain highly adapted pioneer species manage to colonize these areas, playing a critical role in the initial stabilization of sediments.

On the other hand, the stabilised dune is located further inland, in an area where conditions are more stable, allowing for the development of denser and more diverse vegetation. This part of the system is dominated by species such as *Pinus halepensis*, along with an undergrowth characteristic of the Mediterranean region. These plants not only contribute to soil stabilisation but also play a crucial role in supporting the biodiversity of the ecosystem. In this area, the sandy soil begins to blend with organic matter, creating more favourable conditions for the growth of

woody plants and perennial grasses. The increased stability provided by the vegetation cover serves as an effective barrier against wind and sand transport, strengthening the ecosystem's resistance to erosion.

The increasing tourist and urban pressure on the coast of Cala Millor has led to significant alterations in the dune system. Anthropogenic modifications include the creation of roads and paths to facilitate pedestrian access, recreational use of the dunes, and the continuous trampling of vegetation. These activities have a detrimental impact on the ecosystem, compacting the soil, destroying vegetation cover, and reducing the dune's ability to regenerate naturally. In modified areas, vegetation tends to disappear, leaving the sandy substrate exposed to erosion. Furthermore, fragmentation caused by roads reduces the ecological connectivity of the system, hindering the recovery of both mobile and stabilised dunes.

To distinguish the different components of the Cala Millor dune system, we utilised the 2024 orthophoto from the Cartographic and Geographic Institute of the Balearic Islands (ICGIB) (ICGIBB) catalogue, which features a resolution of 0.25 metres per pixel, allowing for precise identification of the boundaries of each section. Additionally, a field visit to Cala Millor was conducted to verify and refine these boundaries on-site. During this visit, the various sections—mobile dune, stabilised dune, and anthropogenically modified areas—were carefully delineated (Fig. 58).

To further assess the vegetation within the dune system, on-site observations were carried out, complemented by photographs that documented and facilitated the classification of plant species present in each area.

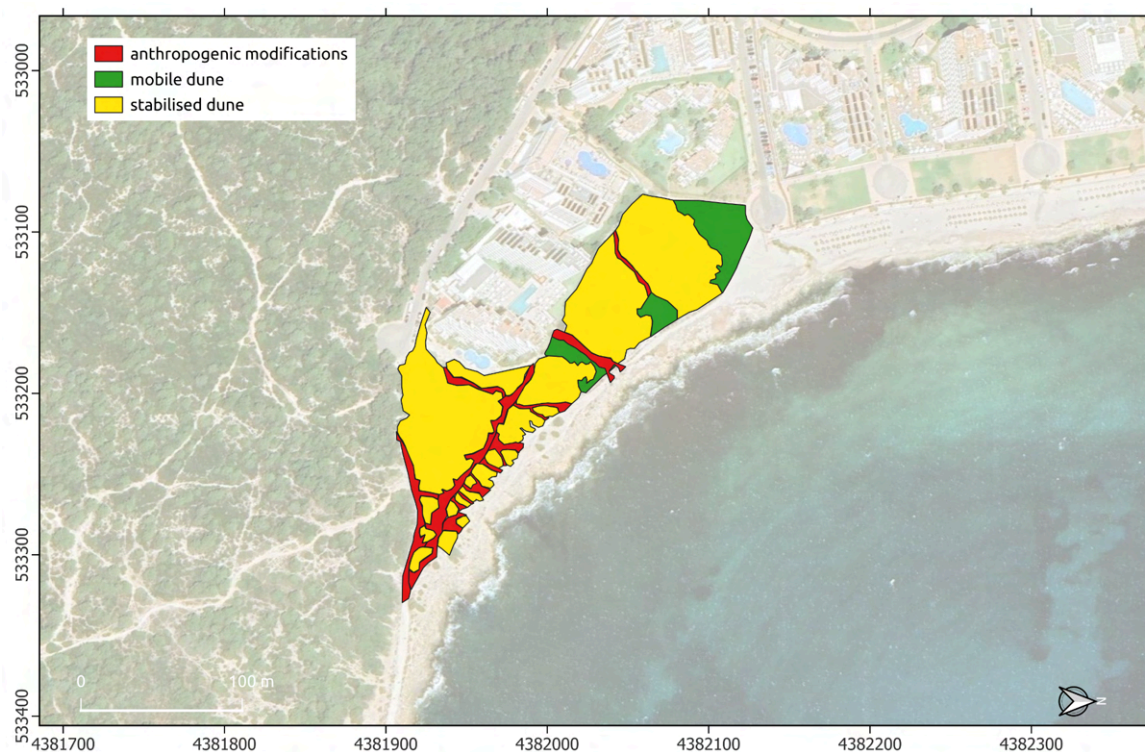


Figure 58. Delimitation of the actual dune system connected with the beach system at Cala Millor.

Based on these delineations, the extent of each component was calculated, being the stabilised dune the largest element in between de dune system components (Table 11):

Element	Area (Ha)	% Area
Mobile dune	0.20	14
Stabilised dune	1.15	76
Anthropogenic modifications	0.15	10

Table 11. Extension of dune typology and fragmentation corridors at Cala Millor coastal dune system.
Extension of each typology of the dune.

The vegetation of the Cala Millor dune system is characterised by a diverse array of species, each adapted to the unique ecological gradients of this environment. Field observations enabled the identification and classification of plants based on their location within the dune ecosystem: the mobile dune, the shrub-stabilised dune, and the dune fixed by pine forest (Fig. 59).

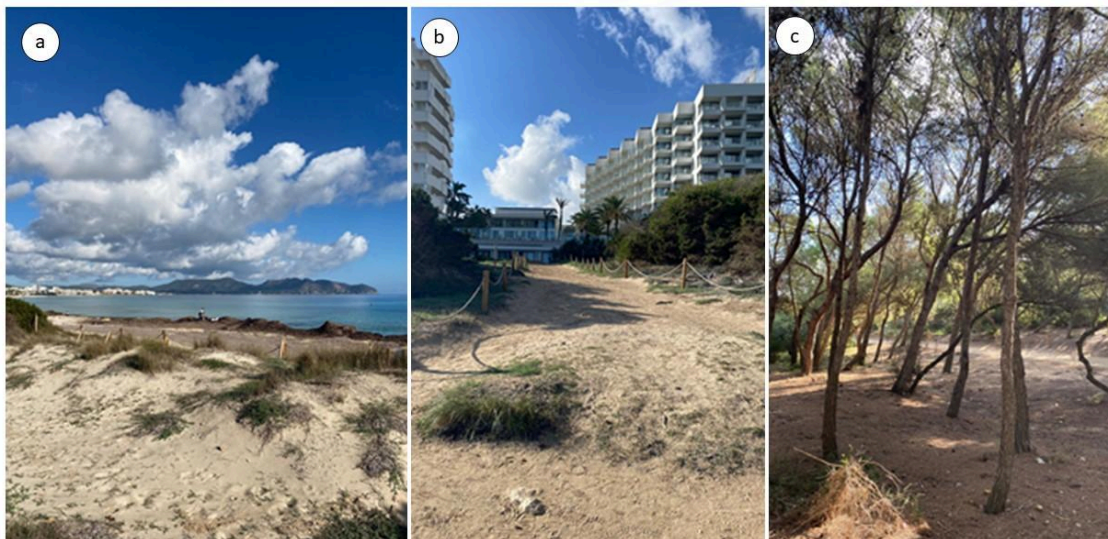


Figure 59. Dune typologies identified in Figure 58: a) Mobile dune; b) anthropized-disturbed dune , and c) Stabilised dune.

The mobile dune is sparsely vegetated, with plants specialised to withstand extreme conditions of salinity, wind, and the constant movement of sand. Among the species identified are *Eryngium maritimum*, *Pancratium maritimum*, and *Ammophila arenaria*. These plants are well adapted to nutrient-poor sandy soils and continuous exposure to waves and erosion. The shrub-stabilised dune exhibits a more stable environment, allowing for the growth of denser vegetation. This zone is dominated by shrubs such as *Erica multiflora*, *Cistus spp.*, *Juniperus oxycedrus*, and *Pistacia lentiscus*. These species play a crucial role in soil retention and contribute significantly to the biodiversity of the ecosystem.

In the innermost section of the dune system, pine forests dominated by *Pinus halepensis* serve as the primary vegetation. These forests are accompanied by an undergrowth that includes species such as *Chamaerops humilis*, reflecting the more developed and stable conditions of this zone. It is worth highlighting the presence of some ruderal and exotic species, associated with the degradation of the system or the invasion of plants from hotel gardens into the natural system.

Among the most striking and listed on the IUCN lists of invasive species in coastal dune systems: *Lantana camara* or *Carpobrotus edulis*.

2.2.2 *Posidonia oceanica* meadow

Posidonia oceanica meadows are key components of coastal ecosystems and sensitive receptors of various impacts, including eutrophication, reduced water clarity, erosion, and losses of coastal habitat and biodiversity (Martínez-Crego *et al.*, 2008). *P. oceanica* meadows are essential due to the wide range of ecosystem services they provide, such as carbon sequestration, nutrient cycling, coastal protection against erosion, and biodiversity enhancement (Jordà *et al.*, 2012). *P. oceanica* is a clonal marine angiosperm endemic to the Mediterranean, characterized by its extreme longevity, with individual shoots that can live for several decades, and very slow growth (1 cm/year) (Jordà *et al.*, 2012.). As a result, these meadows require centuries or even millennia to develop (Duarte, 1995; Kendrick *et al.*, 2005) and can experience declines due to small increases in mortality rates, leading to rapid vegetation loss. This has been observed throughout the Mediterranean where excess nutrient and organic inputs, along with mechanical impacts, have made these ecosystems highly vulnerable (Marbà & Duarte, 2010).

In recent decades, *P. oceanica* meadows have experienced significant decline due to various factors, including anthropogenic pressures, extreme storms impacts, and changes in sediment dynamics. The historical evolution of these meadows has been analyzed by focusing on changes in the upper limit, sediment burial, growth, and shoot density, using data collected between 1956 and 2024. These analyses were conducted using available data and orthophotos with resolutions suitable for meaningful comparisons.

2.2.2.1 Upper limit

The upper limit of the *Posidonia oceanica* meadow was analysed using historical orthophotos spanning the period from 1956 to 2024. These images were processed in a Geographic Information System (QGIS 3.38.2), where the meadow areas were visually identified and manually delineated. To evaluate its evolution, the 1956 coastline was employed as a consistent cartographic reference, enabling the identification of regression or progression trends in the meadow's position over time. This methodology has provided insights into how the distance of the meadow from the coast has changed over the decades.

The analysis of the upper limit was carried out digitising the corresponding areas in the orthophotos of 1956, 1973, 1984, 1989, 1997, 2008, 2012 and 2024. To ensure uniformity in the analysis, the 1956 coastline was used as a reference, on which the upper limits of each year were projected. Subsequently, lines were generated perpendicular to the coast every 50 m, covering the entire study area (Fig. 60). These lines made it possible to calculate the distances between the coastline and the upper limit of the meadow at each interval. The distances obtained for each year were averaged to represent the displacement of the upper limit with respect to the coastline.

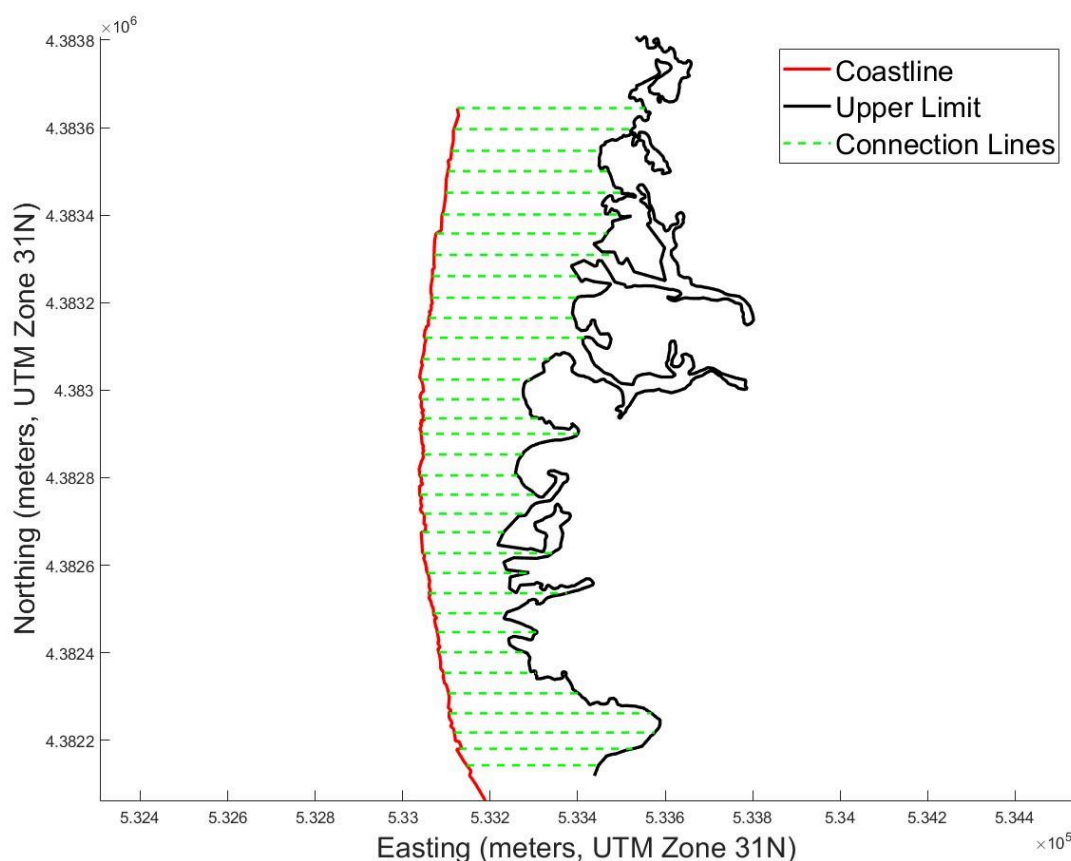


Figure 60. Example of calculation of the average distance to the upper limit of 2024

The results of average distances (in m) between the 1956 coastline and the upper limit of the meadow for each year analysed were as follows:

Year	<i>P. oceanica</i> upper limit average distance (m)
1956	398
1973	460
1984	443
1979	479
1997	426
2008	457
2015	468
2024	409

Table 12. Evolution of the average distance of the upper limit of the *P. oceanica* meadow relative to the 1956 coastline at Cala Millor.

In general, the results show moderate fluctuations in the position of the upper boundary of the meadow over time. Although the changes between years are not drastic, a certain trend of retreat can be identified between 1956 and 1989. The average distance of the upper boundary reaches its maximum value in 1989 (479 m), reflecting a regression of the meadow possibly influenced by factors such as coastal development or environmental changes. Subsequently, there is an alternation of retreat and advance, suggesting that local conditions or environmental pressures have fluctuated over time.

Comparing the initial 1956 values (398 m) with those of 2024 (409 m), the upper limit does not seem to have undergone a substantial change over the almost 70 years analysed. This could indicate a certain stability in the system, albeit with periods of temporal variations.

2.2.2.2 Levels of burial and growth

Burial refers to the progressive accumulation of sediment on the plant, particularly on the rhizome, which directly influences its structure and functionality. This natural process in marine ecosystems plays a key role in the dynamics of *Posidonia oceanica* meadows. Burial has notable implications for growth, as it triggers adaptive vertical growth through the elongation of rhizome internodes, allowing the plant to remain above the accumulated sediment and maintain access to the light required for photosynthesis.

However, excessive or persistent burial can become a significant stressor, impeding the plant's survival. While moderate burial can enhance system stability by shielding rhizomes and reducing erosion risks, excessive sediment accumulation can suffocate buried tissues, lower leaf density, and, in severe cases, compromise the meadow's overall integrity. Consequently, studying burial processes and the adaptive responses of *P. oceanica* is essential for understanding the resilience of these meadows in the face of environmental changes and anthropogenic pressures.

For the analysis of burial, the vertical growth of rhizomes was assessed. The length of internodes -defined as the sections of the rhizome between two consecutive growth points- was measured as a proxy for vertical growth. This length can vary depending on environmental factors, such as sedimentation levels and light availability. In the long-term analysis, data were collected from rhizome samples taken at specific intervals in Cala Millor (39.5959°N, 3.3724°E).

The analysis of the vertical growth of *Posidonia oceanica* reveals the evolution of its vertical growth rate (in mm/year) from 1975 to 2022 (Fig. 61), indicating a general decreasing trend. The linear regression analysis shows a coefficient of determination (R^2) of 0.47, suggesting a gradual reduction in the plant's vertical adaptive capacity over the decades. The highest growth rates were observed during the initial decades of the study, particularly in the 1980s, possibly due to sediment redistribution of the most important nourishment actions and the loss of dry beach as is noticed in Fig. 32. However, from 1990 onwards, a sustained decline in vertical growth becomes evident, although an increase in growth after 2001 nourishment is also noticeable (Fig. 32).

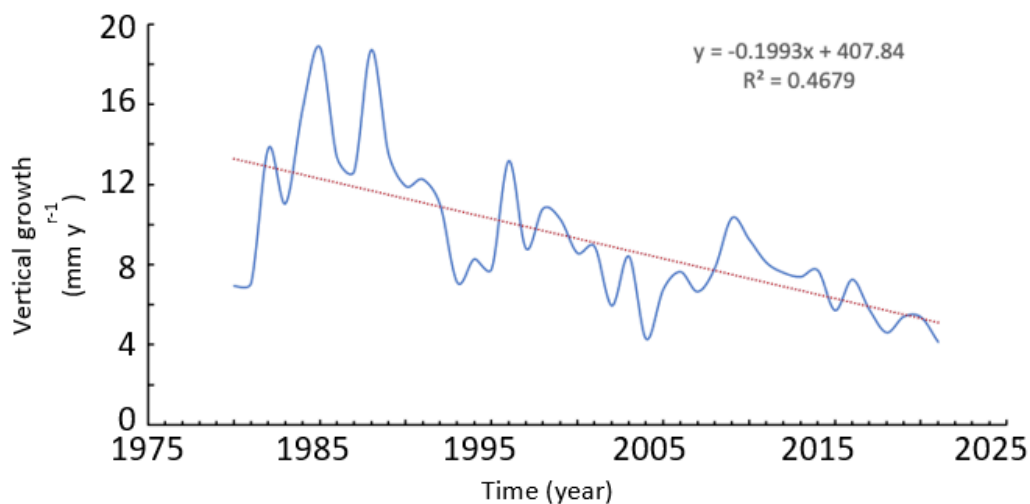


Figure 61. Evolution of the vertical growth rate of *Posidonia oceanica* rhizomes (1975-2022) in Cala Millor.

Internode length data also reveal significant variations in the response of rhizomes to burial (Fig. 62). Between 1975 and 1990, internode lengths were relatively high, with notable fluctuations. However, from the 1990s onward, a consistent decline in internode length is observed, reflecting a reduction in the elongation capacity of the rhizomes and, more broadly, a sustained decrease in the plant's adaptability to continuous burial.

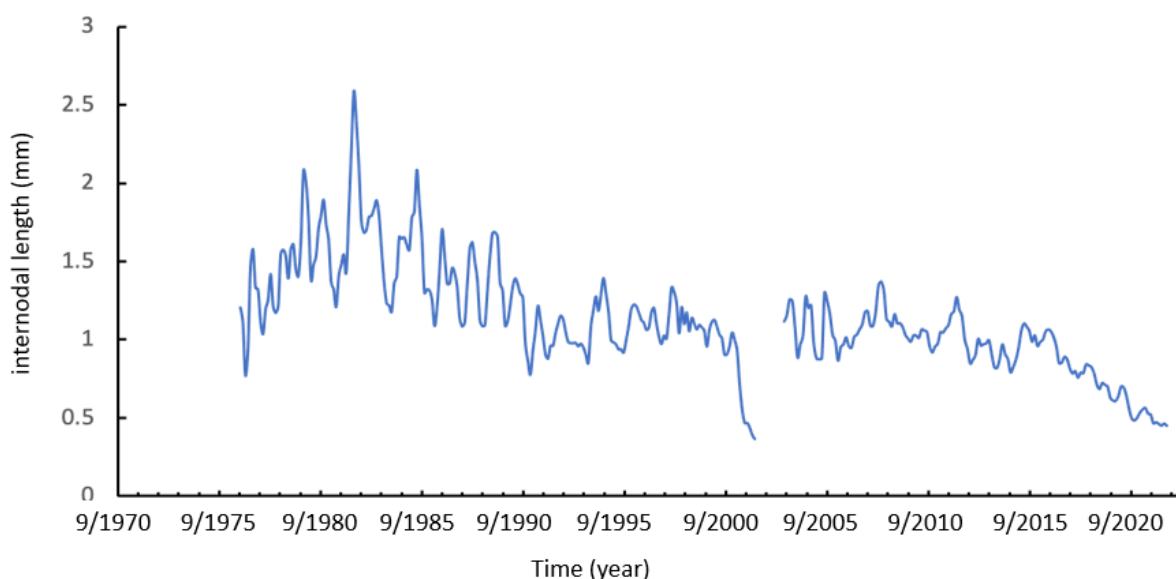


Figure 62. Temporal variation of internode length in *Posidonia oceanica* (1975-2022) in Cala Millor.

This downward trend in both vertical growth and internode length underscores a significant shift in environmental conditions, likely driven by more intense and persistent erosional processes that constrain the plant's ability to adapt. The sustained decline in vertical growth serves as evidence of the detrimental effects of excessive burial and erosion on the structure and functionality of the seagrass meadow. Moreover, this phenomenon suggests a potential structural weakening of the rhizomes, compromising their resilience to disturbances.

2.2.2.3 Current status

After analyzing the historical trends of *Posidonia oceanica* meadows, it is essential to focus on their current status using three descriptors: shoot density, the lower limit, and the upper limit.

The density of *P. oceanica* decreases with increasing depth, a pattern primarily associated with the reduction in light availability with bathymetry. This is due to the extinction coefficient of water, which quantifies the loss of light intensity as it passes through the water column. Consequently, as depth increases, the energy available to the plant diminishes. The lower limit represents the maximum depth at which *P. oceanica* is found and is similarly influenced by the extinction coefficient of water.

At greater depths, light limitation results in a progressive reduction in shoot density, as the plant struggles to sustain its metabolic and productive activities. In the deepest zones, where incident light is insufficient to meet the plant's minimum requirements, the lower limit of the meadow is reached. This threshold not only reflects the restrictions imposed by light but also the interaction with other environmental factors, such as sediment accumulation, substrate quality, and hydrodynamic conditions, all of which can influence the stability and persistence of the plant.

Analysis of these patterns, both in terms of density and lower limit, is essential to understand the current distribution of *Posidonia oceanica* meadows.

To calculate the density of the meadow, taking into account the decrease in density with depth, we applied an empirical formula that establishes the relationship between bathymetry and the density of *P. oceanica*. This formula allowed us to generate a detailed map illustrating the current distribution of meadow density, providing an accurate representation of the current state of this ecosystem (Zupo *et al.*, 2006):

$$Density = a - (b \times D_p)$$

where D_p is the water depth, and a and b empirical adimensional constants; being $a = 807$, and $b = 24$.

The bathymetric data for Cala Millor used in this study were obtained from the SOCIB Data Catalog, part of the Coastal Observing and Forecasting System of the Balearic Islands. This catalog facilitates the search, visualization, and download of oceanographic data collected by SOCIB's observation facilities. The data for Cala Millor, which include systematic and sustained measurements of beach morphology and nearshore waves, were collected from 20 May 2011 to 26 October 2020 and are accessible through the SOCIB Data Catalog (Fernandez-Mora *et al.*, 2023).

The bathymetric data used for the bay were sourced from the bionomic mapping campaign conducted by Tecnoambiente during 2019-2020 on the island of Mallorca. This campaign employed Side Scan Sonar (SBL) to gather detailed information about the seabed, particularly in areas with seagrass meadows. The resolution of the Side Scan Sonar data was approximately 0.2 m, enabling precise differentiation of seabed types and accurate delineation of their boundaries. These data were further complemented by additional sampling methods, including transects with remotely operated vehicles (ROVs), direct observations by diving, and towed video recordings, ensuring high accuracy in the mapping of underwater habitats (Fig. 63).

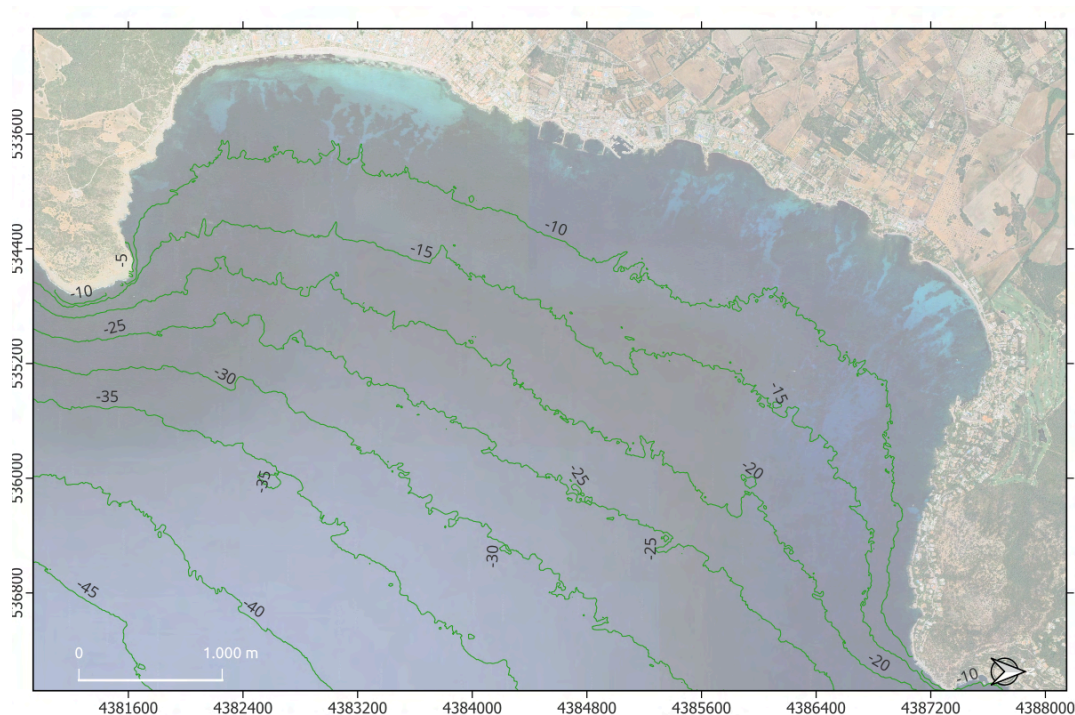


Figure 63. Bathymetric Mapping of the Bay of Cala Millor by Tecnoambiente (2019-2020)

Once the bathymetric data were obtained, the current densities of *P. oceanica* were calculated and used to create a density map, which serves as a baseline reference for future simulations (Fig. 64).

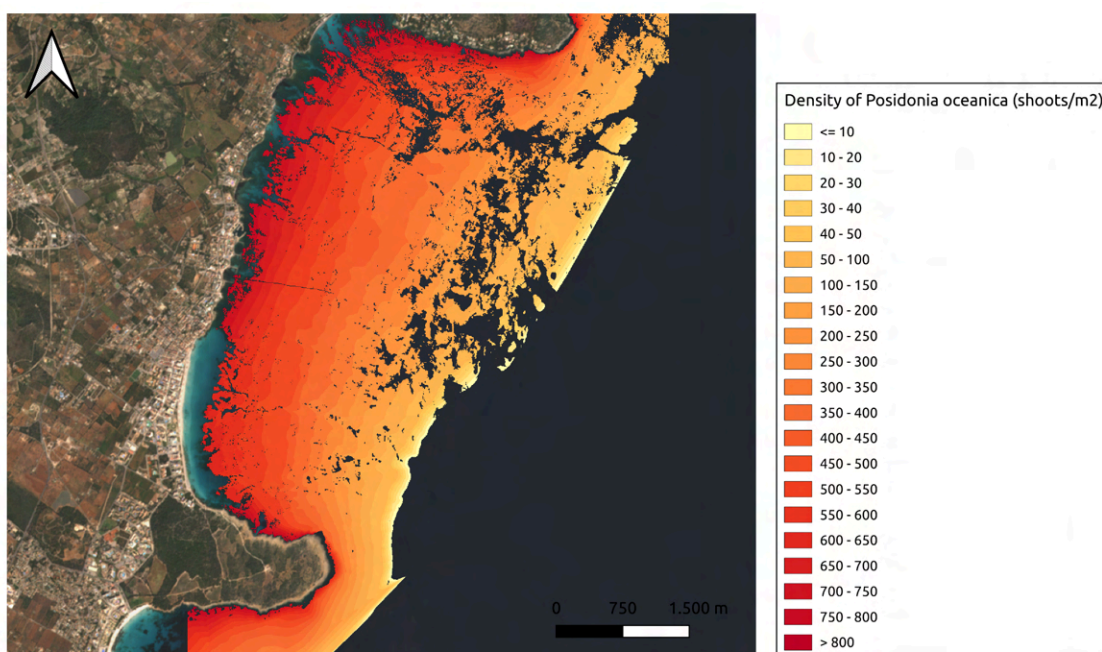


Figure 64. Map of density of *Posidonia oceanica* (shoots/m²) in Cala Millor. Current state

2.2.2.4 Future projections for *Posidonia oceanica* meadows

Posidonia oceanica is highly sensitive to seawater warming, which affects shoot survival and increases mortality rates in natural populations (Duarte, 2002). The average maximum summer seawater temperature in the Mediterranean has already risen, and climate model projections predict that temperatures in the Mediterranean region will continue to increase, leading to significant negative impacts on *P. oceanica* meadows (Jordà et al., 2012).

To assess the vulnerability of *P. oceanica*, shoot density (shoots/m²) has been identified as an effective descriptor of long-term temporal variations in meadow condition (Mazzella & Buia, 1989). Consequently, we examined the future density trajectories of these meadows under the RCP-4.5 and RCP-8.5 emission scenarios. Initially, we estimated the current shoot density in the Cala Millor area and then projected future densities for the years 2030, 2050, and 2100.

To assess the health of *P. oceanica* meadows and determine the associated risks, we will calculate future densities based on the current density. The density of *P. oceanica* is a critical indicator of marine ecosystem health, reflecting the meadow's ability to withstand disturbances and sustain its ecological functions.

To model the evolution of density over time, we calculated density trajectories using the following exponential function (Jordà et al., 2012):

$$N(t) = N_0 e^{t(R-M)}$$

where N_0 is the initial density, t (in years) is the time elapsed between density observations, R is the recruitment rate of shoots, and M is the mortality rate of shoots. Recruitment (R) is determined from an average of in situ data collected in Cala Millor over the past 20 years, providing a value that reflects realistic conditions. The recruitment value is 0.076 shoots year⁻¹, and has been used as a constant throughout the simulations.

The mortality rate (M) is closely related to the annual maximum temperature (T_{max}), with significant increases in *P. oceanica* shoot mortality observed at temperatures above 28°C. Annual mortality is estimated using the empirical linear relationship adjusted for temperature (Marbà & Duarte, 2010):

$$M(T_{max}) = -0.674 + (0.028 T_{max})$$

The projections of maximum sea surface temperatures in the Balearic Archipelago for the years 2024–2100 were obtained from computational models developed under the CMIP6 framework. To ensure the highest possible representativeness and accuracy, 29 climate models were used (see Table 2) under two greenhouse gas emission scenarios, RCP-4.5 and RCP-8.5. Averages were taken across these models to mitigate potential biases and provide a more robust and reliable estimate of the projected temperatures (Fig. 65 and 66; Table 13 and 14).

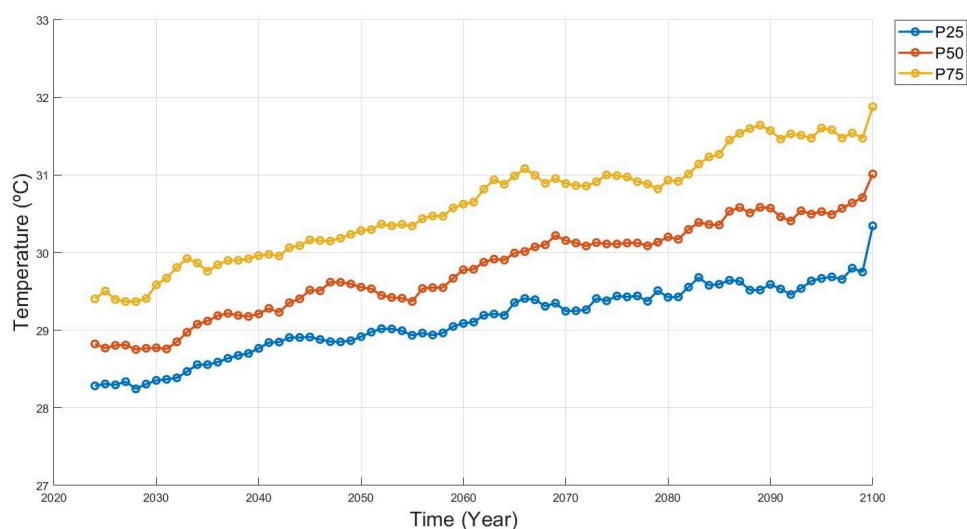


Figure 65. Projections of annual maximum sea surface temperature (°C) for the period 2024-2100 under scenario RCP-4.5, based on 29 climate models. The values represent the 25th (P25, blue line), 50th (P50, red line), and 75th (P75, yellow line) percentiles of the simulations.

Percentil	Minimum	Maximum
P25	28.01 °C	30.35 °C
P50	28.59 °C	31.01 °C
P75	29.17 °C	31.93 °C

Table 13. Projected range of minimum and maximum values of maximum sea surface temperature for the 25th, 50th, and 75th percentiles during the period 2024-2100 under scenario RCP-4.5.

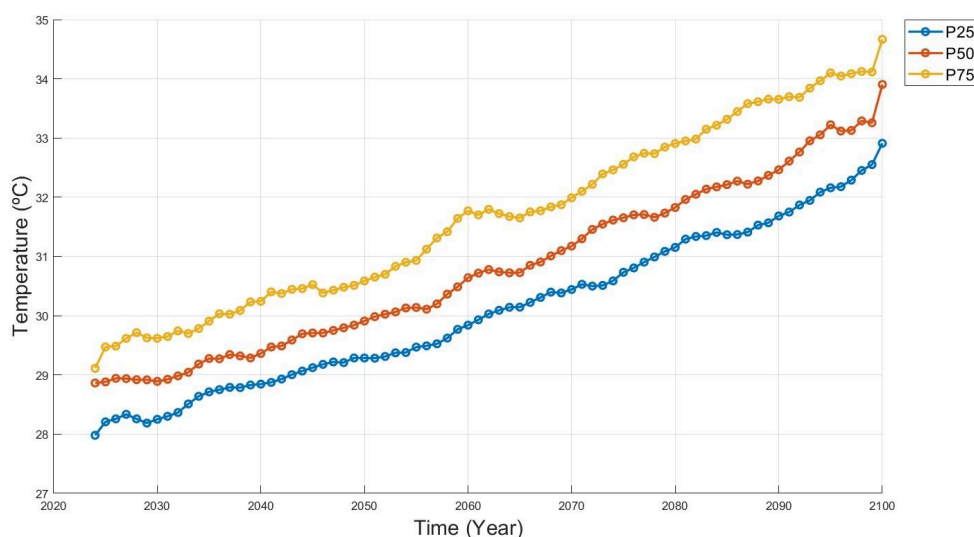


Figure 66. Projections of annual maximum sea surface temperature (°C) for the period 2024-2100 under scenario RCP 8.5, based on 29 climate models. The values represent the 25th (P25, blue line), 50th (P50, red line), and 75th (P75, yellow line) percentiles of the simulations.

Percentil	Minimum	Maximum
P25	27.92 °C	32.91 °C
P50	28.71 °C	33.90 °C
P75	29.11 °C	34.67 °C

Table 14. Projected range of minimum and maximum values of maximum sea surface temperature for the 25th, 50th, and 75th percentiles during the period 2024-2100 under scenario RCP 8.5.

To enhance the precision and robustness of our projections, we decided to represent the 25th, 50th, and 75th percentiles of the projected maximum temperatures. This approach captures a broader range of climatic variability, thereby avoiding reliance on a single mean value that might not adequately reflect the inherent uncertainty of climate models. By employing these percentiles, we generated three future density trajectories for each climate scenario (RCP-4.5 and RCP-8.5), allowing for a more detailed assessment of the potential impact of climate change on *P. oceanica* meadows. Values highlight the extreme temperature expected for each percentile, providing a clear reference for the variations across different projected scenarios (Table 14).

For air temperature Table 3 presents the values expected for each percentile, providing a clear reference for the variations across different projected scenarios that will be further used for the socioeconomic dimension in the next section.

For the future projections under the RCP-4.5 and RCP-8.5 scenarios, the mortality rates of *P. oceanica* were calculated for each reference year using the previously described formula. This annual calculation of mortality, combined with constant recruitment, allowed us to generate maps showing how *P. oceanica* meadows will evolve by 2030, 2050, and 2100. This provides a crucial tool for future planning and conservation efforts (Fig. 67 and 68).

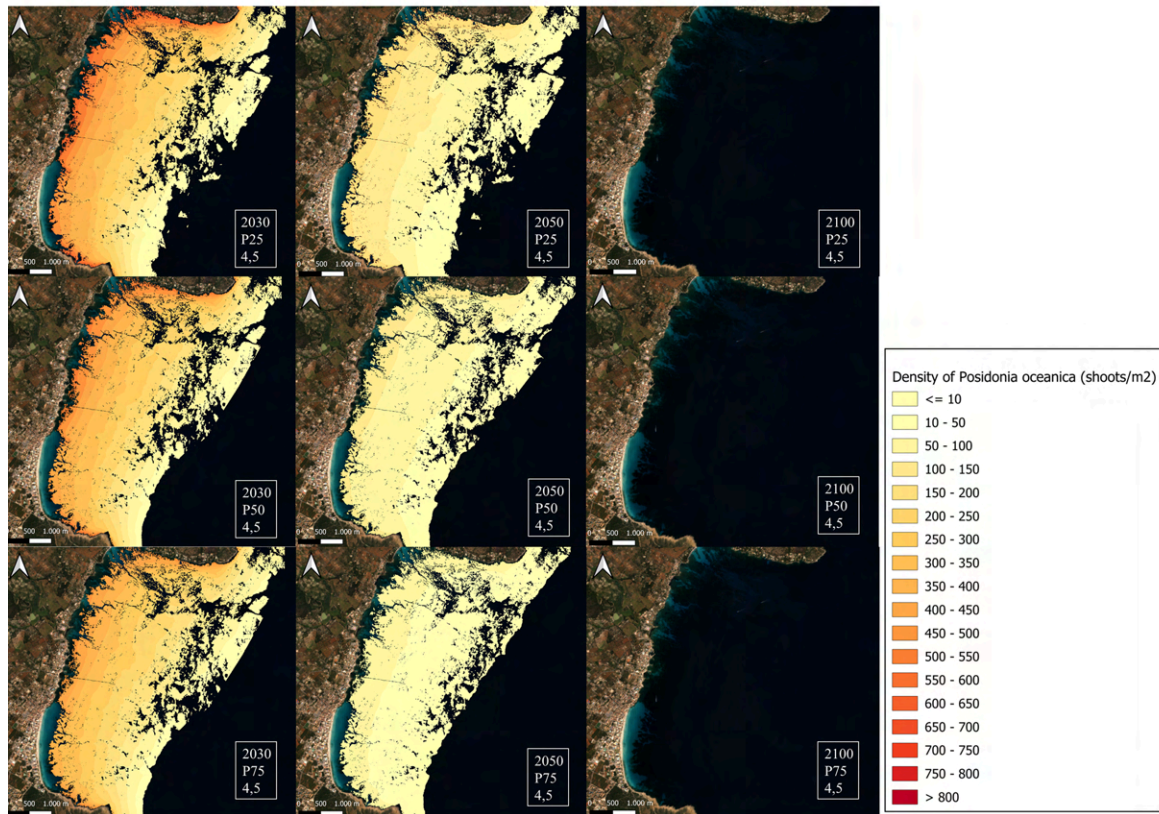


Figure 67. Projections of *P. oceanica* density (shoots/m²) under RCP 4.5 scenario for 2030, 2050 and 2100 (left, center and right). First row: percentile 25%. Medium row: percentile 50. Bottom row: percentile 75.

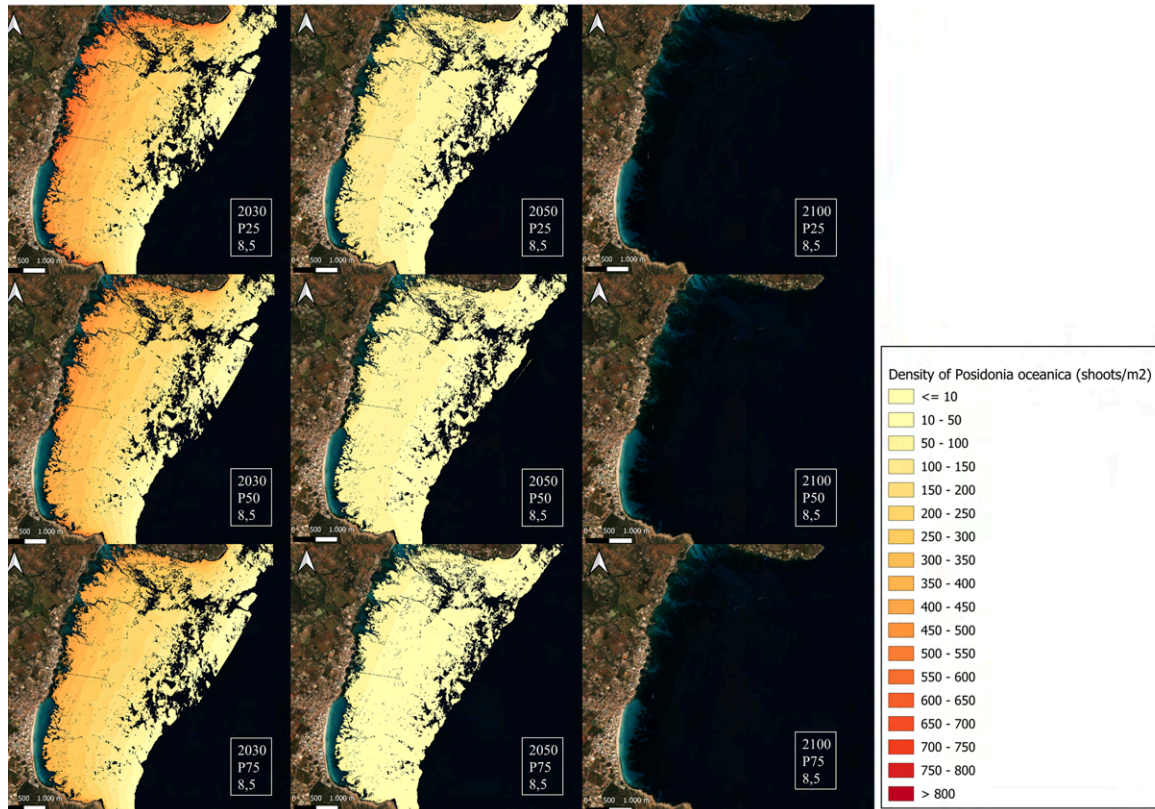


Figure 66. Projections of *P. oceanica* density (shoots/m²) under RCP 8.5 scenario for 2030, 2050 and 2100 (left, center and right). First row: percentile 25%. Medium row: percentile 50%. Bottom row: percentile 75%

ENVIRONMENTAL DIMENSION ABSTRACT

- The current coastal dune system of Cala Millor has lost over 99% of its original extent since 1956, now reduced to a small fraction of its initial size. This ecosystem, currently highly degraded, is surrounded by urbanisation and disconnected from the beach and sediment supply natural dynamics that once maintained its functional balance. Today, the system reflects not only the ecological characteristics of the Mediterranean environment but also the significant alterations caused by anthropogenic modifications over recent decades.
- The mobile dune is the most dynamic and exposed part of the dune system, situated closest to the coast and directly influenced by the action of waves and wind. In this area, sand remains in constant motion, creating an unstable environment that hinders the establishment of vegetation.
- *Posidonia oceanica* upper limit shows moderate fluctuations in the position of the upper boundary of the meadow over time. Although the changes between years are not drastic, a certain trend of retreat can be identified between 1956 and 1989. Upper limit comparison between 1956 and 2024 (398 m and 409 m respectively) shows that the upper limit has not undergone a substantial change over the last 70 years indicating a stability in the system, albeit presenting periods with some fluctuations.
- *Posidonia oceanica* vertical growth shows a gradual reduction in the plant's vertical adaptive capacity over the decades probably as a consequence of the several nourishment actuations performed in the beach system.
- For both RCP scenarios *Posidonia oceanica* density presents a large decline in the three percentiles (25, 75 and 75%) for 2050 with respect to the current state. This decline is notably higher at lower depths changing from the 600 plants/m² present today to densities around 200 plants/m². In both sceneries, due to the sea water temperature increase *Posidonia oceanica* totally will disappear from Cala Millor in 2100 for both RCP-4.5 and RCP-8.5, in all percentiles analyzed (25, 50 and 75).

2.3. Socio-Economic Dimension

The hazard assessment for the economic dimension of Cala Millor beach has been developed following the methodology outlined in D3.2. To estimate the economic value of the area and the loss of value due to the risk of climate change under different RCP scenarios and time horizons, the following analyses have been conducted:

- Definition of the general context of tourist flows worldwide under climate change scenarios.
- Characterization of the economic activities of Cala Millor by cadastral parcels.
- Assessment of the Cala Millor zone of the cadastral parcels based on the activities developed in each of them (Residential, Commercial, tourist accommodation).
- Evaluation of the impact of the rise in temperature and the loss of beach surface on tourist demand: Exposure and adaptation.

The methodology applied in each analysis is summarized in the following sections, along with the respective results.

2.3.1. The Worldwide context

The economic assessment of risks in the area of Cala Millor generated by the consequences of climate change focuses on the local tourist activity and considers a dual context. Firstly, the deterioration of natural attractions and changing climatic conditions are expected to impact tourist demand in Cala Millor, similar to other Mediterranean destinations. This effect on demand is comparable to other similar areas, and its quantification can be derived from existing literature ([Amelung *et al.*, 2007](#); [Amelung and Viner, 2006](#); [Bujosa and Rosselló, 2013](#); [Hamilton *et al.*, 2005a and 2005b](#); [Hein *et al.*, 2007](#); [Lise and Tol, 2002](#); [Maddison, 2001](#); [Matei *et al.*, 2023](#); [Moreno and Amelung, 2009](#); [Rosselló and Santana-Gallego, 2014](#)).

In this context it is recognized that the increase in temperatures will be associated with a change in the feeling of comfort. Thus, based on [Mieczkowski's \(1985\)](#) proposal to create a comfort index based on different climate indicators (temperature, wind, hours of sunshine...), different scenarios have been estimated that consider the projections of these climate variables and the comfort temperature desired by tourists. In general, these projections show a loss of comfort in the case of Spain ([Amelung *et al.*, 2007](#)) and in the specific case of the coasts of Mallorca ([Moreno and Amelung, 2009](#)). When quantifying the impact on demand, most studies ([Hamilton *et al.*, 2005a and 2005b](#); [Rosselló and Santana-Gallego, 2014](#)) talk about a drop in the international market share of almost a percentage point of the Spanish market against an eventual warming of the global temperature. Projections for national tourism also show a redistribution of domestic tourism from the warmer areas of the south-east towards the north of the peninsula ([Bujosa and Rosselló, 2013](#); [Bujosa *et al.*, 2015](#); [Priego *et al.*, 2015](#)). However, it is worth saying that all these studies show a great dependence of tourism on other factors (such as, for example, income), so the future evolution of tourism depends on the future evolution of these as well factors and not only climate change.

Consequently, despite the negative consequences on tourism demand predicted by all these studies, it should be noted that climate change is a long-term process. Therefore, to obtain a

reliable prediction of tourism demand, the rest of the determinants should be taken into account and not just the climate. In this sense, traditionally, population and income levels have been the main factors that have been pointed out by the literature as driving the demand for international tourism (Rosselló-Nadal and Santana-Gallego, 2022). Thus, if we consider that these determinants have an increasing tendency at a global level (UNWTO, 2011), when they are incorporated into the demand models together with the climate predictions, it is obtained that the demand projections are no longer so catastrophic, showing that the climate, although it plays a significant role when explaining the world tourist flows, is still a secondary factor behind economic and population growth. In this line Hamilton *et al.* (2005a) already confirm this idea by showing how a very marginal change in the market share of countries is obtained by incorporating temperature after having previously incorporated population and economic growth.

2.3.2. Characterization of the economic activities of Cala Millor by cadastral parcels

Conducting a comprehensive economic assessment of the Cala Millor area involves defining smaller geographical zones to differentiate between the direct economic losses resulting from areas affected by rising sea levels and the indirect losses caused by beach erosion, also driven by sea level rise and/or the increase in temperatures. To undertake this issue, we use data from the Spanish cadastre, which is the analytical census of real estate property of the Spanish central government. This analytical census aims to locate, describe, and record the physical characteristics of each real estate property to detect the intrinsic particularities that define it both materially and specifically. The Spanish cadastre identifies real estate properties with two types of codes:

- 14-digit codes. These are codes that refer to the plot, a unit of geographic surface and are used as units of value potentially affected by floods or other effects of climate change. Different properties, businesses, and common areas can be located on each plot. See Figure 39 for an overview of these plots in our area of analysis.
- 20-digit codes. The minimum value units used to calculate, by aggregation, the value of the cadastral plot (14 digits). These references refer to houses, flats, commercial premises, tourist apartments, warehouses, parking areas, etc. existing in each cadastral plot.

To study the effect of climate change on the economy of the area being analyzed we compute the economic value of each 20-digit cadastral reference, and by aggregation, the value of each 14-digit cadastral reference (cadastral plot) (Fig. 67). From the economic valuation of each cadastral plot, we will be able to detect the direct effect of climate change on specific plots of the geographical area being analyzed, depending on the results of the physical dimensions, specifically on the identification of any plot that cannot be further used due to the climate change (i.e., floodings).

To assign an economic value to each of the 20-digit cadastral references, the following classification is considered:

1. Hotels and other tourism accommodations, and commerce.

2. Housing and other real estate properties.

Businesses in the analyzed area are mainly in the hospitality (e.g., hotels and tourist apartments) and commerce (e.g., shops, bars and restaurants) industries. The economic value generated by businesses depends on the cash flows generated by these businesses (Brealey *et al.*, 2023; Ross *et al.*, 2022) while the economic value of housing and other real estate properties depends on the dynamics of the real estate market (e.g., the quality of the materials and the specific characteristics of each neighborhood). The Spanish cadastre provides a value of each real estate property based on the dynamics of the real estate market, although it is computed mainly for taxation purposes, and it is generally considered a conservative valuation. Therefore, for housing and other real estate properties not used to develop business activities, we will measure their economic value with the value provided by the Spanish cadastre.

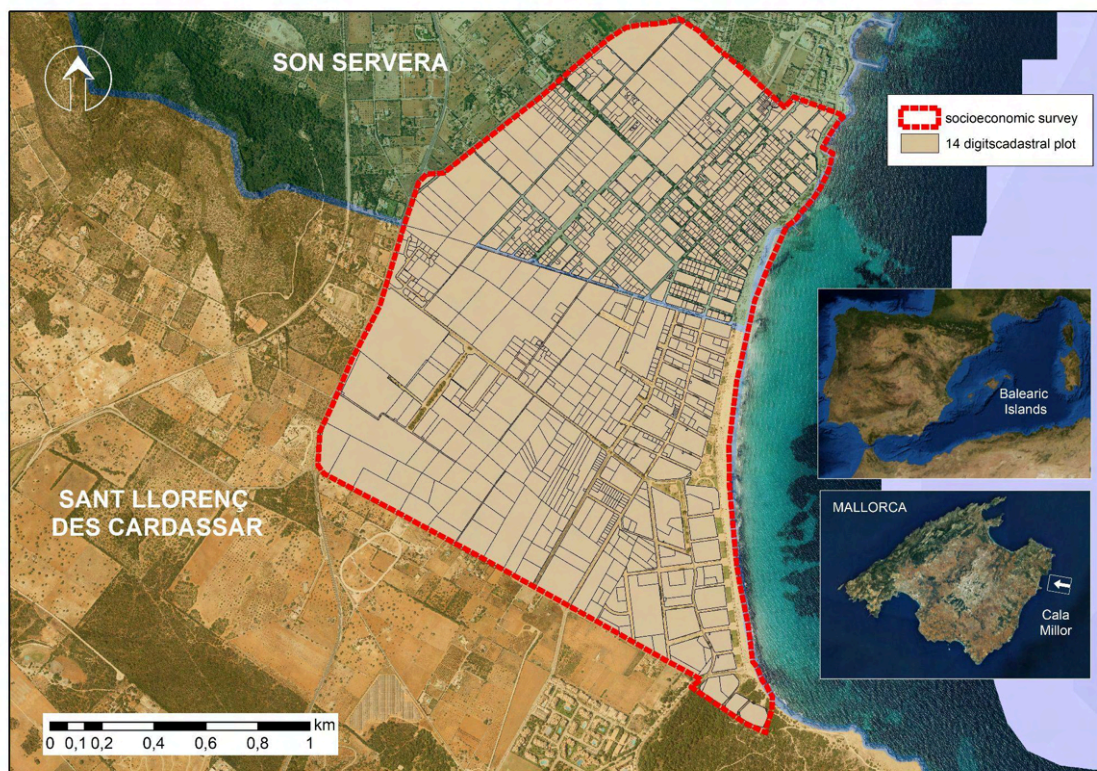


Figure 67. 14-digit cadastral parcels cadastral plots in in Cala Millor socioeconomic survey.

2.3.3. Valuation of cadastral parcels

To compute the economic value of real estate properties in the context of the 20-digit cadastral references used to develop business activities (hospitality and commerce) we will compute its market value as the present value of all the cash flows these businesses are expected to generate in the future for all their stakeholders, which are their owners, workers, suppliers, and any other agent receiving cash flows from the businesses (e.g., taxes paid to the local government). Therefore, we compute the economic value of businesses from an economic and social point of view.

Given that revenues generated by the businesses are the source of cash flows paid to all the stakeholders, we will compute the market value of each 20-digit cadastral reference used by business activities as the present value of the revenues generated in this cadastral reference. Therefore, for businesses, we estimate the expected revenues generated in each 20-digit cadastral reference and then we compute its present value. This market value encompasses the market value of each 20-digit cadastral reference for all the stakeholders of the business activities developed there, therefore providing an economic and a social dimension to the value we are computing.

For this valuation methodology use publicly available information to approximate the revenues generated by business activities in each 20-digit cadastral reference. In the case of hotels and other accommodation businesses, we use data from the Balearic Institute of Statistics (IBESTAT), the regional government office of statistics, while for commerce we use public data on rental prices to proxy the capacity to generate revenues and accounting data that is also publicly available

2.3.3.1. Hotels and other tourism accommodations

To identify hotel establishments in the Cala Millor area, on the one hand, we obtain data on hotels and other tourism accommodations from the open-access database of the regional government (<https://catalegdades.caib.cat/>). This database includes different establishment magnitudes, like category (from one to 5 stars in the case of hotels, and from one to 4 keys in the case of apartments) and number of rooms/apartments. On the other hand, we use the regional government statistics agency (<https://ibestat.es/>) to obtain data to estimate the revenues of these tourism accommodations. This agency provides survey data about prices and the occupancy ratio of tourism accommodations, although more details are provided for hotels than for apartments.

Additionally, for hotel establishments, IBESTAT provides the overall average daily rate (per room) per month and municipality (Son Servera and Sant Llorenç), without information per category. The average daily rates per hotel category (one to 5 stars) are provided for the island. This data is used to extrapolate the hotel average daily rates in Sant Llorenç and Son Servera per category. The total amount per room allows us to estimate the total annual revenues of each of the analyzed hotels. For this computation, we use hotel category, number of rooms, and the specific location of each hotel (municipality). For our analysis, we use the total revenues in 2023 as the expected revenues in future years if no climate change occurs. This provides us a conservative approximation of the total revenues of each hotel since we only considered the average daily rate, and therefore we do not consider any additional expenses in the hotel not included on this rate.

For apartments, IBESTAT provides average daily rates per month at the regional level (Balearic Islands), and occupancy rates per month and municipality. However, no data on occupancy rates is provided for Son Servera, and therefore we use the occupancy rates provided for Sant Llorenç in Son Servera also. Additionally, IBESTAT does not provide average daily rates per category in the case of apartments. Therefore, the average daily rates for apartments in Son Servera and Sant Llorenç are adjusted to obtain the rates per category of apartments. For this adjustment the 4 key apartments assimilated to 4 star hotels, and equivalently for 3, 2, and 1 key apartments

As a result of these computations, we obtain the total revenues per apartment of different categories, which allows us to compute the total revenues of each apartment business in 2023. As in the case of hotels, we will use the total revenues in 2023 as the expected revenues in future years if no climate change occurs.

2.3.3.2. Commerce

To identify commercial activities, we use data from the Spanish cadastre and geo-localize each real estate property (at 20-digit cadastral reference level) dedicated to commerce activities in our area of analysis. In this database, we may identify different characteristics of each real estate property, such as its primary use and the total area of land and of any building. In the analyzed area most of the businesses are in the tourism and hospitality industry (hotels, bars, restaurants, shops, etc.).

For all real estate properties used for business, except hotels and apartments for tourists, we compute the total meters of the building and estimate annual revenues according to the rent price per square meter paid in similar businesses. This implies two steps. In the first step, we estimate the market rent price that could be paid for each real estate property dedicated to businesses in our area of analysis. In the second step, we estimate the standard relation between revenues and rent prices paid in similar real estate properties dedicated to businesses. The logic is that in equilibrium rent prices of real estate properties are adjusted to the expected revenue capacity of the businesses developed there.

For the first step, we proxy the rent each real estate property dedicated to businesses would pay by the information obtained from the announcements found in IDEALISTA (<https://www.idealista.com/>), which is a very large real estate agency in Spain. To this end, we divide the area of analysis into 4 zones according to their proximity to the town's commercial center. We consider all the real estate properties dedicated to businesses available on Idealista (August 5 and 6 of 2024) in similar and close tourist towns from Cala Millor. Specifically, we consider "Puerto de Pollença, Puerto de Alcudia, Can Picafort, Cala Ratjada, Canyamel, Cala Millor, Cala Bona, Sa Coma, S'Illet, Porto Cristo, Cala d'Or, Porto Petro".

In each announcement, there is the price per month asked and the number of square meters of the real estate property on rent. In some cases, the owners ask for a down payment in addition to the price per month. In such cases, we compute a homogenized price per month and square meter by adding the equivalent portion of the down payment as if it was paid per month and square meter for 10 years, dividing the down payment by the number of months in ten years times the square meters of the property ($12 \text{ months} \times 10 \text{ years} \times \text{square meters}$). Then we compute the average homogenized price per month and square meter in each commercial zone. We use this average to proxy the year rental price per square meter in each commercial zone in Cala Millor. Finally, we multiply this price by the square meters of each property (20-digit cadastral reference) to estimate the annual rental price that each business would pay according to the current expectations of future revenues for businesses in the area.

For the second step, we use data from SABI of Bureau Van Dijk, which provides accounting data of all Spanish firms elaborating and registering their accounting data in the central government archive for accounting information (Registro). We consider data from retail firms, bars, and restaurants in all the municipalities where we collected data on real estate rentals from

IDEALISTA⁸. Specifically, “Alcudia, Pollença, Santa Margalida, Capdepera, Son Servera, Sant Llorenç, Manacor, and Felanitx”. In the SABI database, there is accounting data of 873 firms developing these activities in these municipalities. We obtain their total revenues and Other Operating Expenditures for the last year available (generally 2022). Some of these firms (33) are close to bankruptcy since their revenues are not sufficient to pay Other Operating Expenses, and therefore their rentals (included in Other Operating Expenses) are not a good proxy of their capacity to generate revenues (their managers overestimated their capacity to generate revenues). Using the remaining firms (840), on average we obtain that total revenues are 4.8 times Other Operating Revenues.

Assuming that the whole amount of Other Operating Expenditures are real estate rentals we obtain a conservative estimation of the total expected revenues generated by all real estate properties dedicated to businesses (except hotels and apartments) by multiplying the market real estate rental price per square meter by the square meters of the property and by the 4.8 factor.

2.3.3.3. Market value of the economic activity

We compute the market value of the economic activity generated by businesses located in our area (including hotels and apartments) as the present value of their expected revenues in the future (e.g., Ross, Westerfield, and Jordan, 2022). We assume that future years’ revenues will be as in 2023. Our baseline computation assumes that no climate change happens. In such a case, we do not know how long the economic activity in the area analyzed would last. Then, one possibility is to assume it lasts forever. However, we choose a more conservative valuation strategy which is to assume the 2023 revenues for the next 50 years and replace the revenues of the remaining years with the real estate value of these businesses at the end of these 50 years (as if those businesses were running for 50 years and then closed and the real estate sold). As a proxy of the value of the real estate of these businesses in 50 years, we use the current real estate values provided by the Spanish cadastre, which computes these values mainly for taxation purposes and generates a conservative valuation. This real estate valuation is based on the dynamics of the real estate market. In sum, the value of the economic activity developed by businesses located on each property (20-digit cadastral reference) is computed as follows:

$$Value\ of\ Economic\ Activity_i = \sum_{t=1}^n \frac{Revenues_{it}}{(1+r)^t} + \frac{Revenues_{i,20}}{(1+r)^{20}}$$

Where *Revenues* are the revenues of the economic activity developed in property *i* in year *t*, and the *Residual Value* of the economic activity developed in property *i* in year 50 is proxied as the current real estate value provided by the Spanish cadastre for this property *i*.

The discount interest rate *r* to compute the present value of revenues is the expected return that in equilibrium compensates investors for the risks of the businesses where they invest. We compute this expected return using the Capital Asset Pricing Model (CAPM) introduced simultaneously by Treynor (1962), Sharpe (1964), Lintner (1965), and Mossin (1966), based on the portfolio theory (Markowitz, 1952 and 1999). This is a standard method to compute the discount interest rate to estimate the market value of businesses (e.g., Brealey et al., 2023). For the valuation of the economic activity developed in our area of analysis, we compute the equilibrium

⁸ <https://www.idealista.com/>

market return that compensates for the type of risks of the economic activity developed in the area, which is mainly related to tourism.

According to the CAPM model, the equilibrium expected return of assets (business) depends on the return of risk-free assets and a risk premium rewarding the risks of the specific economic activity being analyzed. This risk premium is a function of the market risk premium and the systematic risk of the asset to be valued. Systematic risk is the portion of risk that cannot be eliminated by diversification and may be computed from stock market data as the covariance between the returns of the asset being analyzed and the returns of the stock market index divided by the variance of the returns of the stock market index. This measure is commonly known as Beta. Since the businesses developed in our area of analysis are not listed on stock markets, we proxy their systematic risk with the systematic risk of Spanish-listed corporations operating in the tourism and hospitality industry.

The interest rate on the European Central Bank's main refinancing operations (updated in September 2024, 3.65%) is used to proxy the return of risk-free assets. We proxy the systematic risk of the businesses in our area of analysis as the average of the systematic risk (Beta parameter using the IBEX-35 to compute the stock market index return calculated from the stock returns over the last five years) of the two major Spanish hotel companies (Minor Hotels Europe & America S.A. – previously known as NH Hotel Group S.A. - and Meliá Hotels International S.A.) and the two largest technological operators of the tourism and hospitality industry (Amadeus IT Group SA, and Edreams Odigeo S.A) listed on the Spanish Stock Exchange. These four companies are subject to the risks of the tourism and hospitality sector, similar to the tourism and hospitality businesses located in Cala Millor, which represent the vast majority of businesses in this area. The systematic risk measure used in our valuation amounts to 1.287 (average of the Beta parameter of Minor – 1.240 -, Meliá – 1.359 -, Amadeus – 1.247 - and Edreams – 1.303 -). This measure indicates that the tourism companies have a systematic risk higher than the market average (IBEX-35). Regarding the market risk premium (expected return for the market – IBEX 35 -, less the return on risk-free assets), we use the estimation by [Fernández et al. \(2023\)](#) for Spain (6.6%), which is consistent with the forecasts of [Damodaran \(2023\)](#) for the US (5.98%) and other European countries of similar characteristics than Spain (i.e., Italy, 7.21%).

Below we show how the CAPM model generates the market equilibrium return we use to compute the market value of the businesses in our area of analysis:

$$E(r_j) = r_f + \beta_j(\text{Market risk premium}) = 3.65\% + 1.287 * 6.6\% = 12.14\%$$

On the other hand, the Bank of Spain foresees a decreasing annual inflation, from 3% in 2024 and 2% in 2025, to up to 1.8% in 2026. To obtain a prudent valuation, an annual inflation of 2% is assumed during the valuation period. Thus, a nominal return of 12.14% per year translates into a return of 9.95% in real terms – at constant prices - ($(1+r_{\text{Nominal}})=(1+r_{\text{Real}})*(1+\text{Expected Inflation})$).

The forecasts made for future revenues above are at constant prices (expecting the same revenues as in 2023 in future years) although in nominal terms all prices are expected to rise by an average of 2% each year. Therefore, we use a discount rate of 9.95% (in real terms) to compute the present value of revenues at constant prices, which is the market value of the economic activity developed in Cala Millor.

2.3.4. Risk Assessment

Once the economic value of the 14-digit cadastral parcels has been estimated, the assessment of the direct effects of the risk of climate change, that is, due to the flooding of lands due to rising sea levels or areas of influence, could be very direct and consists of calculating the parcels flooded or affected by a higher probability of flood risk. In this context, regarding direct effects, it is assumed that parcels subject to permanent flooding become entirely unusable and lose their full value since the owners lose control once they become permanently flooded, even legally. Conversely, parcels impacted by temporary flooding, provided the events have a long return period, retain their current value since their owners have the capacity and the incentives to maintain their economic value. Therefore, it is assumed that the economic value of urban areas subject to permanent flooding will have no adaptability. In contrast, areas experiencing only temporary flooding, provided such events have relatively long return periods are expected to adapt fully and relatively quickly.

The effects of climate change on the Cala Millor area will not only be determined by the direct effects but also by the indirect effects, which means that tourists in Cala Millor in areas not directly affected by rising sea levels will see their level of satisfaction reduced by the loss of beach surface area and by the increase in temperatures. In this sense, the value of the urbanized area is conditioned by the risk of climate change due to exposure to higher temperatures and the potential loss of beach surface, which can reduce tourist demand in the area and consequently the economic value of the activities developed there. For indirect assessment, it is assumed that adaptability will be negligible unless measures out of the capabilities of their owners, such as beach regeneration, are implemented. To establish what the effect of the loss of beach and increase of temperature on demand may be and, consequently, to be able to assess this decrease in economic terms and due to the impossibility of simulating real situations or scenarios in which tourists face beach losses or increases in temperature, this project has opted to survey tourists directly to assess a temperature increase and the loss of the beach surface.

To carry out the surveys, the opportunity was taken to include two questions in a survey that was being developed within the framework of the project and which aimed to assess the perception of tourists on the impacts and risks of climate change in Cala Millor ([Pericás-Palou et al., 2024a](#)). A total of 385 surveys were carried out between April 8 and June 26 2024 in the tourist offices located in strategic transit areas in Cala Millor. The survey analyzed tourists' opinions and attitudes on climate change, the impact on ecosystems, individual action, beach use and preferences on possible adaptation measures for the management of ecosystem services. With special interest for the economic valuation, tourists were interviewed about whether a temperature increase of +4°C and a 50% loss of beach would affect their intention to return to the area using a five-points Likert Scale. To translate the results of the surveys into terms of demand, we define the conversion factor as:

$$Conversion\ Factor = \sum_{r=1}^5 L_r \cdot P_r$$

Where L is the probability associated with each one of the values of the Likert Scale ($r=\{1, 2, 3, 4$ and $5\}$, where 1 refers that it would not affect you or very little and 5 means that it would affect you a lot), and P the percentage of the tourists that have answered each item in the Likert Scale. For our case study, Likert scale values in relation to the probability of visiting the destination take

the following form: If the surveyed tourist has answered that she is not affected by the reduction of the beach or a 4°C increase in temperature (1 on the Likert scale), the probability that she would choose the destination in the case of the reduction of the beach surface or a 4°C increase in temperature would be equal to 1 ($L=1$); while in the case that she would be very affected (5 on the Likert scale) the probability that she would choose the destination would be equal to 0 ($L=0$). For the rest of the values of the Likert scale we assume linear distribution, thus, $L=0.75$ when Likert Scale is 2; $L=0.5$ when Likert Scale is 3; $L=0.25$ when Likert Scale is 4. In this way, on the one hand, we can check that if all the tourists, hypothetically, had answered 1 on the Likert scale (A 50% reduction in beach or a 4°C increase in temperature would have very little effect on them when it comes to returning to the destination) then the conversion factor would be equal to 1, and we interpret that their decision to visit Cala Millor would not change in case the analyzed potential effects of climate change happened (effects on beach area and temperature). On the other hand, if all the tourists had answered 5 (A 50% reduction in beach or a 4°C increase in temperature would have a great effect on them when it comes to making the decision to return to Cala Millor) then the conversion factor would be equal to 0, and we interpret they would not come to Cala Millor with a probability of 100%. Similarly, we interpret the probability they would come to Cala Millor as 75% if the Likert Scale is 2, and equivalently with the other values of the Likert Scale. Therefore, for the case of temperature increase (+4°C), the conversion factor obtained is 0.48 while for the case of beach loss (50%) it is 0.42. Given the high relationship between the answers to both questions. The rest of the scenarios are projected from this one.

In this way, based on the data found for the physical dimension in relation to the loss of beach surface area of Cala Millor and the temperature for each of the predicted scenarios (vid. Sections 1 and 2), the percentages of beach surface area that are maintained and the increase in temperature with respect to current conditions are shown in [Table 15](#).

		Width of remaining beach compared to the present (%)			Temperature Increase (°C)		
		Min	Mean	Max	P25	P50	P75
RCP4.5	2030	84.3%	79.7%	73.5%	0.21	-0.11	-0.19
	2050	81.6%	73.0%	60.4%	1.37	0.94	0.64
	2100	71.8%	51.4%	28.0%	1.20	1.90	1.77
RCP8.5	2030	83.9%	79.7%	73.5%	-0.63	0.24	0.63
	2050	80.4%	71.8%	58.3%	0.83	1.29	1.42
	2100	58.3%	41.5%	5.2%	4.58	4.64	4.71

Table 15. Projected beach width of minimum and maximum values and temperature increase for the 25th, 50th, and 75th percentiles during the period 2024-2100 under scenarios RCP4.5 and RCP8.5

From the data on the percentages of beach surface that remain, the increase in temperature compared to current conditions and the responses declared by tourists, it is possible to estimate

the percentage of demand that remains in each of the scenarios, assuming proportionality in relation to the scenario proposed. The results of the estimates appear in [Table 16](#).

		Width of remaining beach compared to the present (%)			Temperature Increase (%)		
		Min	Mean	Max	P25	P50	P75
RCP4.5	2030	70.6%	66.7%	61.6%	97.5%	101.3%	102.3%
	2050	68.3%	61.1%	50.6%	83.7%	88.8%	92.4%
	2100	60.1%	43.1%	23.4%	85.7%	77.3%	78.9%
RCP8.5	2030	70.3%	66.7%	61.6%	107.5%	97.1%	92.5%
	2050	67.4%	60.1%	48.8%	90.1%	84.6%	83.1%
	2100	48.8%	34.8%	4.3%	45.4%	44.6%	43.8%

Table 16. *Percentage of demand that remains during the period 2024-2100 under scenarios RCP4.5 and RCP8.5 at Cala Millor.*

As clearly shown in [Table 17](#), the effects on demand caused by the loss of beach are more significant than those resulting from the increase in temperature for each of the scenarios considered. That is why the loss of demand considered as a reference for making the indirect assessment is generally that which corresponds to the loss of beach. In this way, Table 23 shows the economic losses for each of the climate change scenarios considered, taking into account that the total economic value of the area is estimated at 2,673,486 thousand euros. It is important to note that the loss in value for the best-case scenario is a 25% drop, while the worst-case scenario is an 83% drop.

Regarding temporary flooding affecting cadastral parcels, the results of physical impact analyses indicate that all cases exhibit return periods exceeding 100 years. Consequently, it is assumed that such flooding has no impact on the economic value of the plots, owing to the full adaptive capacity of both residential and commercial values. Since the physical impact of flooding does not permanently affect any cadastral parcels, the economic assessment of climate change risk in Cala Millor is primarily determined by its indirect impacts. The results indicate that this assessment is driven by the reduction in beach surface area, as the impact of rising temperatures results in only minor decreases in demand. This impacts the value of sales in commercial and accommodation establishments. Consequently, the effect of beach reduction on the value of non-commercial properties is not considered, as it is unclear whether a smaller beach area negatively impacts property values. This is because reduced tourist saturation could potentially offset any loss in value.

		Lost Value in thousand euros (in percentage)		
		Min/P25	Mean/P50	Max/P75
RCP4.5	2030	672,280 (25.1%)	765,009 (28.6%)	880,919 (33.0%)
	2050	741,826 (27.7%)	904,101 (33.8%)	1,135,922 (42.5%)
	2100	927,283 (34.7%)	1,321,379 (49.4%)	1,785,021 (66.8%)
RCP8.5	2030	695,462 (26.0%)	765,009 (28.6%)	1,112,740 (41.6%)
	2050	765,009 (28.6%)	927,283 (34.7%)	1,275,015 (47.7%)
	2100	1,182,287 (44.2%)	1,506,836 (56.4%)	2,225,481 (83.2%)

Table 17. Projected Lost economic value in thousand euros and in percentage during the period 2024-2100 under scenarios RCP4.5 and RCP8.5

The key point of the overall valuation methodology is that economic values are derived from very detailed geographical units (cadastral parcels), enabling the integration of data from physical and environmental dimensions. This approach allows for the creation of value maps (shown in “Deliverable 3.5 of the LifeAdaptCalaMillor project”) based on the scenarios and probabilities defined in these dimensions.

SOCIOECONOMIC DIMENSION ABSTRACT

- Global tourism demand models do not allow us to predict a substantial change in tourism demand that would affect the Cala Millor area. Local factors linked to rising temperatures and the loss of beach surface are what can determine the economic impact of climate change on Cala Millor.
- Cala Millor is a region whose economy depends on tourism. The number of rooms available, the high levels of seasonality and the type of commercial establishments are evidence of this situation.
- The total economic value of the Cala Millor area has been estimated at 2.673 billion euros. Rising temperatures, but especially the loss of beach surface area due to climate change, will lead to a loss in value of the area of between 25% and 83% depending on the scenario considered.

2.4. Urban Dimension: Compound flooding

2.4.1. Rationale

The climate change multirisk assessment for the LIFEAdaptCalaMillor project was designed to integrate physical, environmental, and socioeconomic dimensions. The primary impacts considered include rising atmospheric and water temperatures, as well as coastal flooding driven by sea-level rise and extreme wave storm events under various IPCC RCP scenarios.

The **urban dimension**, which encompasses the built environment and associated infrastructure within urban areas, plays a critical role in interactions with the coastal zone. Key elements such as roads, services, green spaces, and drainage systems are directly connected to the beach. Given that the urban dimension is addressed in **Work Package 4 (WP4)**, it is evident that a multi-level approach to assessing risks associated with flooding and temperature must include this dimension.

To incorporate this perspective into the multirisk assessment, three interconnected and crucial exposed elements have been identified, forming the foundation for determining climate change adaptation strategies: road types, land use, and the drainage system.

The **drainage system** in coastal urban areas serves as a direct link between the urban environment and the beach/sea system. The functionality of these systems is essential to ensure effective management of rainfall, prevent urban flooding and water pooling, and facilitate proper water discharge to the sea through well-designed outfalls. Effective drainage systems must account for climate change impacts, including variations in rainfall patterns and, more critically, challenges posed by **permanent flooding** from sea-level rise and **extreme flooding** caused by severe storms. These events can severely compromise the ability of drainage systems to manage water during peak events or persistent flooding conditions.

Rainfall in urban areas plays a critical role in amplifying the impact of coastal flooding, especially in regions prone to storms and rising sea levels. Urban landscapes, characterized by impermeable surfaces such as concrete and asphalt, limit natural water absorption, leading to rapid surface runoff. When heavy rainfall coincides with high tides or storm surges, the combined water volume can overwhelm drainage systems, exacerbating flood risks. This interaction is particularly relevant for coastal cities, where infrastructure resilience and effective stormwater management are essential to mitigate damage and protect communities from compounded flooding events.

Street ponding due to drainage system malfunctions leads to significant problems, including traffic disruptions, road damage, public health risks, economic losses, and emergency response delays. Flooded streets slow down vehicles, increase the risk of hydroplaning, and reduce visibility, making driving hazardous. Prolonged water exposure weakens asphalt, causes potholes, and can even lead to sinkholes by undermining road foundations. Stagnant water becomes a breeding ground for mosquitoes and bacteria, while sewage overflows contaminate the environment. Businesses suffer from reduced customer access, and frequent road repairs increase maintenance costs. Additionally, emergency vehicles face delays, and waterlogged streets pose electrical hazards. Preventing street ponding requires regular drainage maintenance,

improved urban planning with permeable surfaces, and advanced stormwater management technologies to enhance flood resilience.

To address this issue, an analysis has been conducted to evaluate the **compound flooding of sea-level rise, extreme wave storms, and rainfall** on the drainage systems in Cala Millor. The findings of this analysis have been integrated into the multi risk assessment to enhance the understanding of climate change impacts and inform adaptation measures.

This section outlines the **methodology** and **results** of the analysis of Cala Millor's beach drainage systems, to later address their vulnerability to climate change impacts and the implications for future resilience planning.

2.4.2. Compound Coastal And Rainfall Flooding Impacts On Drainage Systems

2.4.2.1. Data and methods

a) Exposed elements

The urban elements analyzed in this approach include critical infrastructures such as streets, roads, and the stormwater runoff drainage system, which together influence how water flows and accumulates during heavy rainfall and coastal flooding events. Specifically, the assessment focuses on how these elements interact to manage and direct stormwater, thereby reducing or exacerbating flood risks.

For Cala Millor beach, the data sources utilized are comprehensive and varied to ensure accurate modeling and analysis. These include:

- **Digital Elevation Model (DEM) at 2.5 m resolution** provided by the Spanish National Geographic Institute (IGN), offering detailed topographical information essential for understanding water flow dynamics.
- **Current and planned drainage system designs** for Cala Millor outline the existing infrastructure and proposed improvements aimed at enhancing flood mitigation capacity. However, regarding the existing drainage system at Cala Millor beach, 'as-built' data is unavailable, and the accessible information consists of a compilation of drainage system analyses and ongoing and planned projects. To develop the current analysis, and based on the data provided by the local authorities, a simplified model of the drainage system has been created, focusing on the most relevant components. The characteristics of pipes and junctions are derived from the available data and in-situ observations.
- **Field data from in-situ campaigns** documenting the precise locations of stormwater runoff drainage outlets at the beach, providing ground-truth information critical for validating models and identifying potential bottlenecks or vulnerabilities in the system.

This multi-source approach ensures a robust understanding of how urban and natural elements interact at Cala Millor, enabling more effective flood management strategies.

b) Flooding drivers

Two primary flooding drivers are considered in this assessment: **extreme storm waves and surges** and **rainfall processes**.

- a) Coastal Flooding:** The impact of coastal flooding on the drainage system is evaluated using the numerical modeling results of extreme storm waves and surges (T100) for the IPCC RCP4.5 and RCP8.5 scenarios (considering only the mean interval -P50-), projected for the years 2030, 2050, and 2100 of the Physical Dimension assessment (called as “Ef_Pt”).
- b) Rainfall:** To assess the drainage system's functionality under rainfall events, synthetic rainfall scenarios are designed based on the following assumptions:
- The methodology adheres to **Spanish Road Instruction 5.1-IC** of the road drainage system guidelines.
 - Maximum hourly rainfall intensities (I_m) are selected for return periods of T10, T25, and T100 following the instruction. Note that a first analysis of the in-situ meteorological data of SOCIB Coastal Station at Cala Millor has been developed to ensure that the **Intensity-Duration-Frequency curves** of the instruction are coherent with in situ data. In addition, from in-situ measurements, the mean rain duration has been determined and set to 6 h.
 - As rainfall pattern changes were not explicitly addressed in the project, a **no-variation scenario is assumed**, maintaining current rainfall patterns for all IPCC scenarios.⁹
 - Rainfall storms are modeled as triangular synthetic events, with peak intensity occurring during the first half of the storm-reflecting typical rainfall patterns characteristic of the Spanish Mediterranean coast.

These considerations ensure a comprehensive assessment of how both coastal and rainfall-induced flooding events may impact the drainage system under different climate scenarios.

Following the **Spanish Road Instruction 5.1-IC**, the design maximum hourly intensities for the study area and different return periods are:

	T5	T10	T25	T50	T100
I_{max} (mm/h)	143	150	156	159	162

Table 18. Maximum hourly rain intensity I_{max} (mm/h) for the selected return period (years).

The resulting synthetic storms are shown in Figure 72:

⁹ For further analysis, IPCC RCP considerations on rain intensity changes should be accounted for.

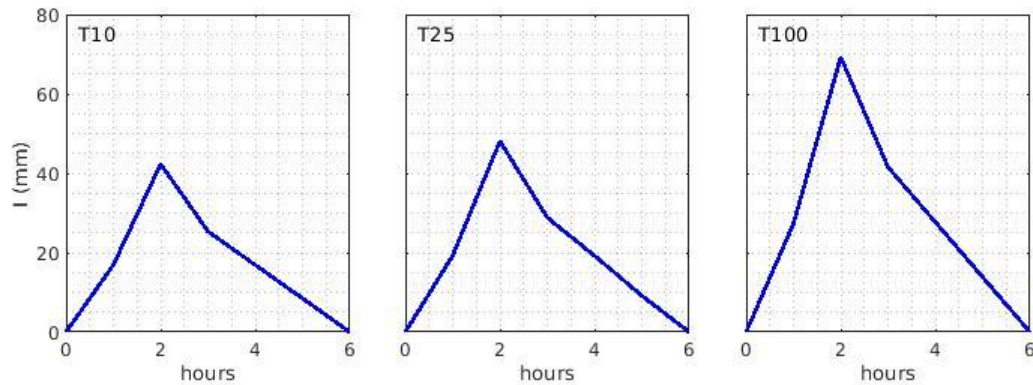


Figure 68. Synthetic triangular storms for T10, T25 and T100 following the Spanish Road instruction 5.1c.

2.4.2.2. Modelling StormWater Systems Functioning

a) Numerical Modelling

In order to assess the functioning of storm water drainage systems, the EPA SWMM (Huber,1985) model has been used. The EPA **Storm Water Management Model (SWMM)** is a numerical model widely used for analyzing urban drainage systems. Developed by the U.S. Environmental Protection Agency (EPA), SWMM evaluates the quantity and quality of runoff generated from precipitation events, incorporating the effects of various land uses, drainage networks, and control measures. It can simulate the behavior of stormwater and wastewater systems, including surface runoff, flow routing, LIDs, and pollutant transport, under a range of conditions and scenarios. Its flexibility allows users to model complex hydraulic and hydrological systems, making it invaluable for urban planning, flood risk assessment, and climate change adaptation strategies. By integrating inputs such as rainfall, land characteristics, and infrastructure design, SWMM provides actionable insights for managing stormwater sustainably and mitigating flood risks in urban environments.

b) Main Assumptions

For the current analysis, the following assumptions are made:

- Rainfall on buildings is directly transferred to the drainage system.
- Runoff coefficients are set as follows: 0.8 for roads, 0.6 for pedestrian areas, and 0.3 for vegetated areas. Catchment impermeability is set at 25% for low-density urban areas and 75% for medium-density urban areas.
- A Modified Horton approach is used to estimate rainfall runoff, with runoff from catchments directly transferred to the drainage system.
- The characteristics (drainage radius, DR) of each drainage segment are based on data provided by the presented projects. If no data is available, a minimum surface distance of 0.9 m and a nominal drainage diameter of 0.4 m are assumed.
- Junctions and outlets planned but not matching with in-situ field observations are disregarded. Additional conduits are added to compensate for these omitted outlets.
- The entire system is assumed to function by gravity, with no pumping systems considered due to a lack of necessary data.

- No Low Impact Development (LID) measures are considered in this approach due to the absence of relevant data.

This framework ensures the analysis is based on the best available data while addressing any gaps in information.

c) Model Setup

The simplified drainage system model covers the Sant Llorenç and Son Servera areas. Areas closer to the shoreline and beach are modeled in greater detail, while the outer areas are simplified to streamline the analysis and focus on key problem zones. Fig. 69 illustrates the drainage system used in the modeling process.

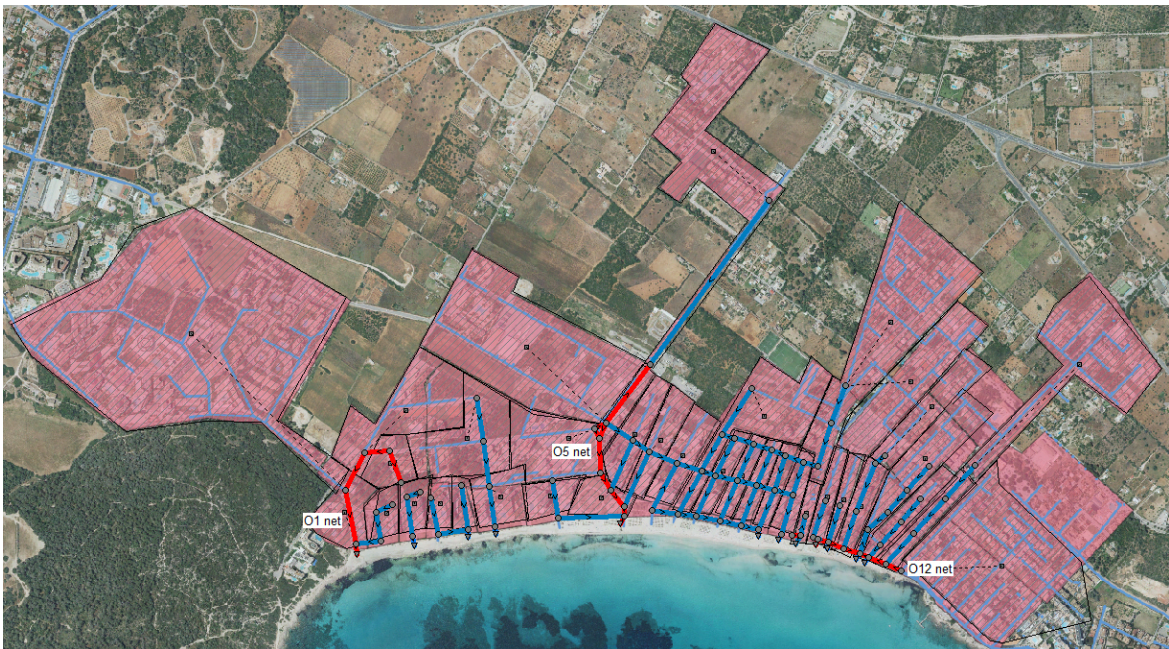


Figure 69. Simplified drainage system: Circles represent junctions, triangles denote outlets, and lines indicate conduits. Red lines stand for the net systems O1, O5 and O12.

For the different scenarios, rainfall is applied as a forcing factor, directly applied to the most elevated junction of each drainage segment considering also the corresponding affected area slope. Outlets are modeled with a fixed water level corresponding to the flooding observed at the beach location for each coastal flooding scenario. The urban area junctions impacted by coastal flooding are modeled with a constant input flow, based on the results from coastal flooding modelling. For each case, a 12-hour simulation was conducted, with the rainstorm occurring during the first 6 hours.

A total of 21 composed cases have been considered. Table 25 summarizes the combination of cases:

Coastal flooding case	Rain-fall case
Current state - Extreme storm	T10, T25, T100
RCP4.5 - 2030/2050/2100 - Extreme storm	T10, T25, T100
RCP4.5 - 2030/2050/2100 - Extreme storm	T10, T25, T100

Table 19. Simulations of the composed coastal and rainfall flooding on the drainage system.

2.4.3. Analysis of drainage system across different scenarios

The performance of the drainage system under various composite scenarios provides insights into the drainage nodes where the system may potentially fail to function correctly, leading to ponding.

Given the large number of simulations conducted, the following analysis focuses on the most significant cases to illustrate system performance:

1. **Current State without and with T100 Wave Storm:** Evaluating the system under the design rainstorm (T10) without wave storm conditions (design conditions) and assessing performance under wave storm conditions.
2. **Future Projections for 2030:** Analyzing system behavior under RCP-4.5 and RCP-8.5 scenarios with wave storm conditions, combined with the T25 rainstorm (upper limit of recommended design return period of the Spanish Road Instruction 5.1. C).
3. **Worst-Case Scenarios:** Examining the most critical conditions under RCP-4.5 and RCP-8.5.

For the following analysis, we will focus on three main separated nets in the full drainage system: the O1 net, located at the southern area of Cala Millor; the O5 system, that cover the drainage network of the central zone; and the O12 system, parallel to the coastline that captures the northern catchments. Figure X indicates the three net systems.

2.4.3.1. Current State wo/w T100 wave storm

For the current state, since the system has been designed for a T10 rainstorm with no boundary conditions at the beach outlets, although part of the system operates under pressure during 2.5 h, no flooding issues are observed in junctions (Fig. 70).

When the system is subjected to wave storm effects at the outlets (set as a fixed stage) and coastal water inflow at the affected nodes, certain sections of the drainage system become immediately pressurized. Analyzing the worst time step during the rainstorm reveals that most of the system operates under pressure (Fig. 71). Examining the behavior of the main drainage networks highlights key differences:

- **O1 Network:** Its worst state (2:20 h) is out of phase with the O5 and O12 networks (3:20 hrs). This discrepancy is clearly due to variations of catchments areas, the time of concentration of the respective catchments and the runoff duration. In this scenario, while the O1 network does not exhibit relevant flooding at any nodes, the O5 network experiences pressurization and flooding, particularly at nodes located in the central square.

- **O12 Network:** This network, which collects runoff from the upper catchments and runs parallel to the coastline, is fully pressurized. Partial flooding is expected in this nodes and even at the upstream tributary nets.

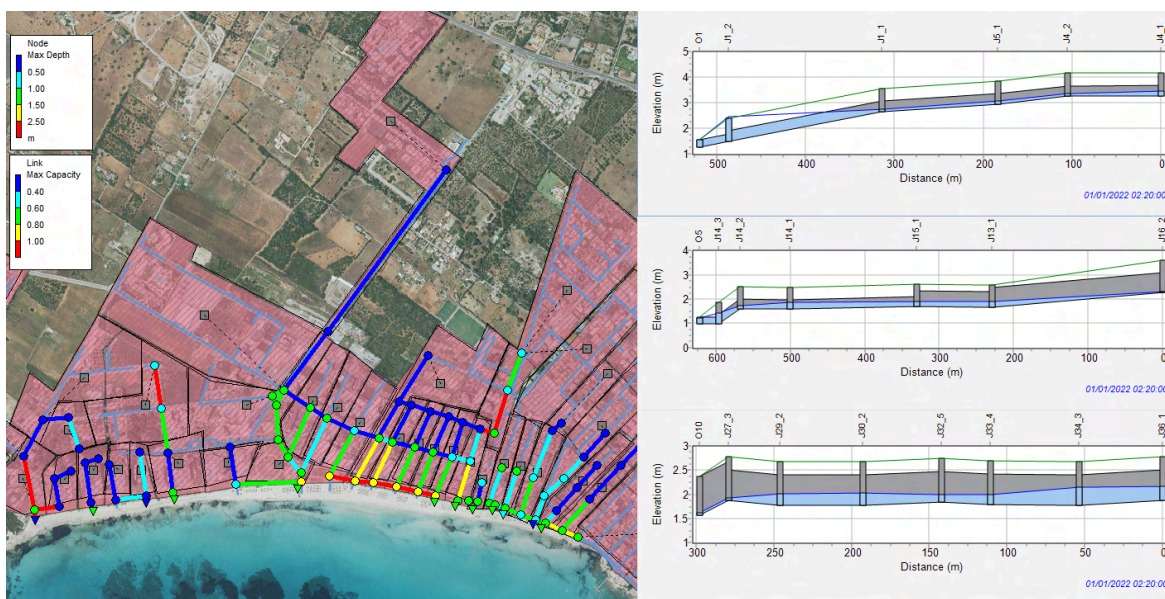


Figure 70. Left panel: Net system links capacity and junction water head (m) at first time-step (no rain-storm). Right panels: Water head along de O1, O5 and O12 nets at the first time-step.

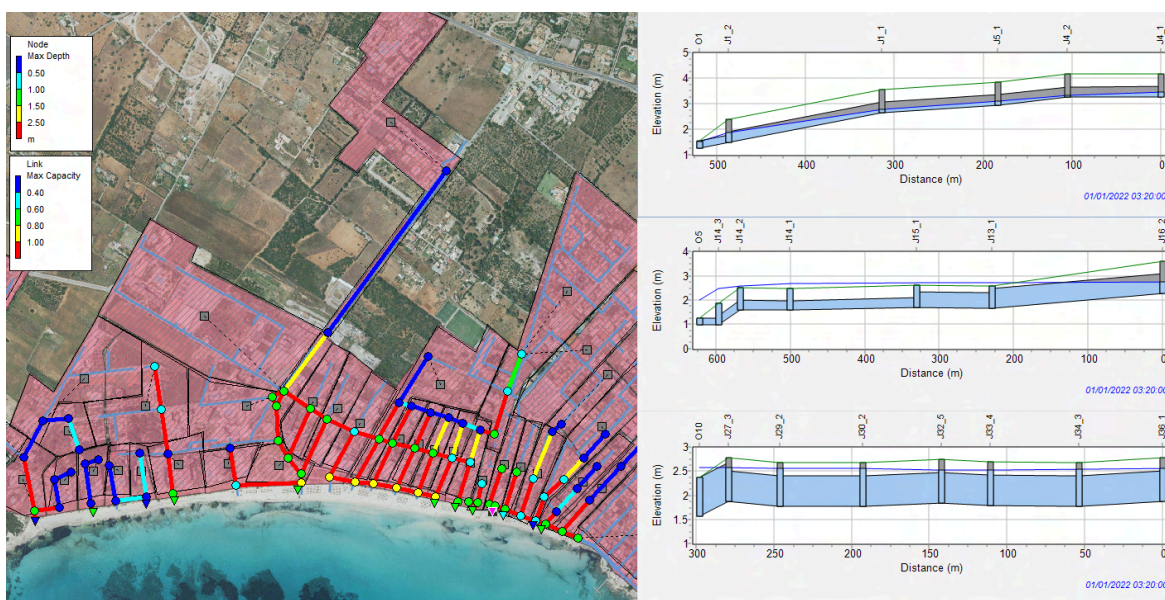


Figure 71. Left panel: Net system links capacity and junction water head (m) at 3:20 h elapsed time. Right panels: Water head along de O1, O5 and O12 nets at 3:20 hrs elapsed time.

2.4.3.2. Future Projections for 2030

On analyzing the drainage system under the RCP4.5 coastal flooding scenario for 2030, combined with the T25 rainstorm (Fig. 72), failures in flow capacity are observed in sections of the network

running longitudinally along the promenade. These failures persist for over three hours in the southern and central areas and exceed 12 hours in the northern section. In particular, the O12 network becomes overloaded due to direct sea level effects at the outlet, impacting upstream flows. Under this scenario, partial flooding is expected at nodes adjacent to the promenade, as well as at the southern roundabout, where maximum heads occur earlier than in the rest of the network. Flooding also extends to the upper nodes of the central plaza within the O5 system. The O12 network and its tributaries experience significant disruptions. Notably, during the rainstorm period, flow reversal is observed in some segments of the network.

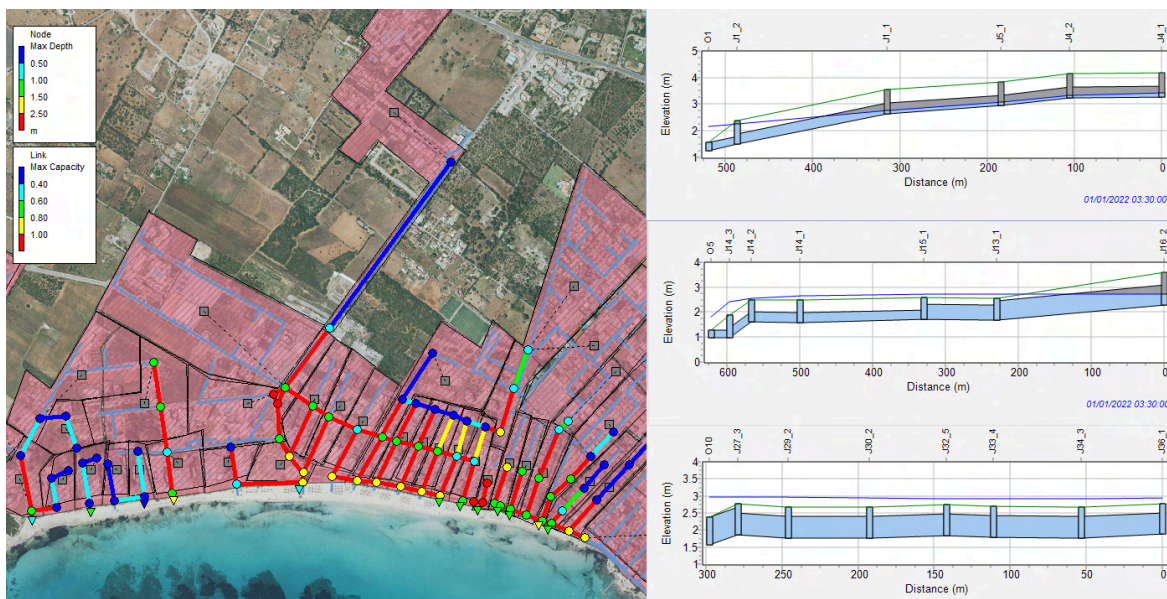


Figure 72. Drainage system status at 2030 for the RCP4.5 scenario. Left panel: Net system links capacity and junction water head (m) at 3:20 hrs elapsed time. Right panels: Water head along de O1, O5 and O12 nets at 3:20 hrs elapsed time.

A similar pattern emerges on analyzing the drainage behavior under the RCP8.5 scenario (Fig. 73), which exhibits higher water head values at the nodes and increased link capacity throughout the drainage system. Notably, the O1 network becomes fully pressurized, though no significant pounding effects are expected. However, coastal inundation at the outfalls of the O5 and O12 networks is observed from the initial stage, leading to upstream disruptions in the tributary networks, affecting link capacity and water depth at the nodes and generating flow reversal.

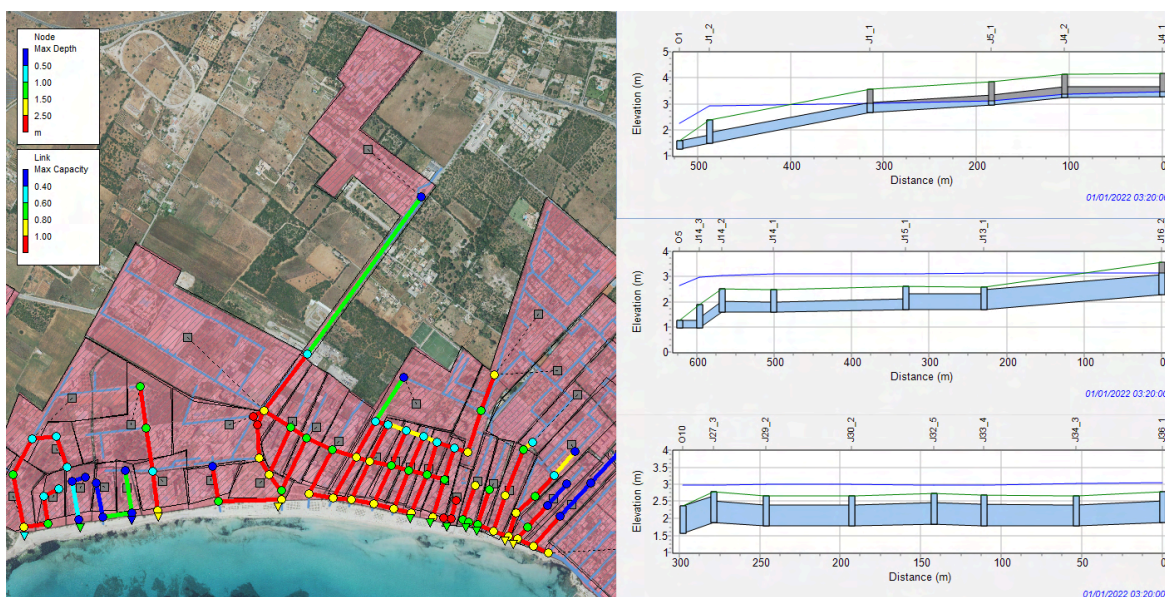


Figure 73. Drainage system status at 2030 for the RCP8.5 scenario. Left panel: Net system links capacity and junction water head (m) at 3:20 hrs elapsed time. Right panels: Water head along de O1, O5 and O12 nets at 3:20 hrs elapsed time.

2.4.3.3. Future projections for 2100

For the 2100 projections, under both the RCP4.5 and RCP8.5 scenarios (Fig. 74 and 75), the effects of sea level rise and extreme flooding on the system are evident, impacting most of the drainage network. Nodes adjacent to the promenade are affected, with partial flooding expected in these areas, particularly in the central and northern networks and their upper tributaries. The O1 network is also impacted.

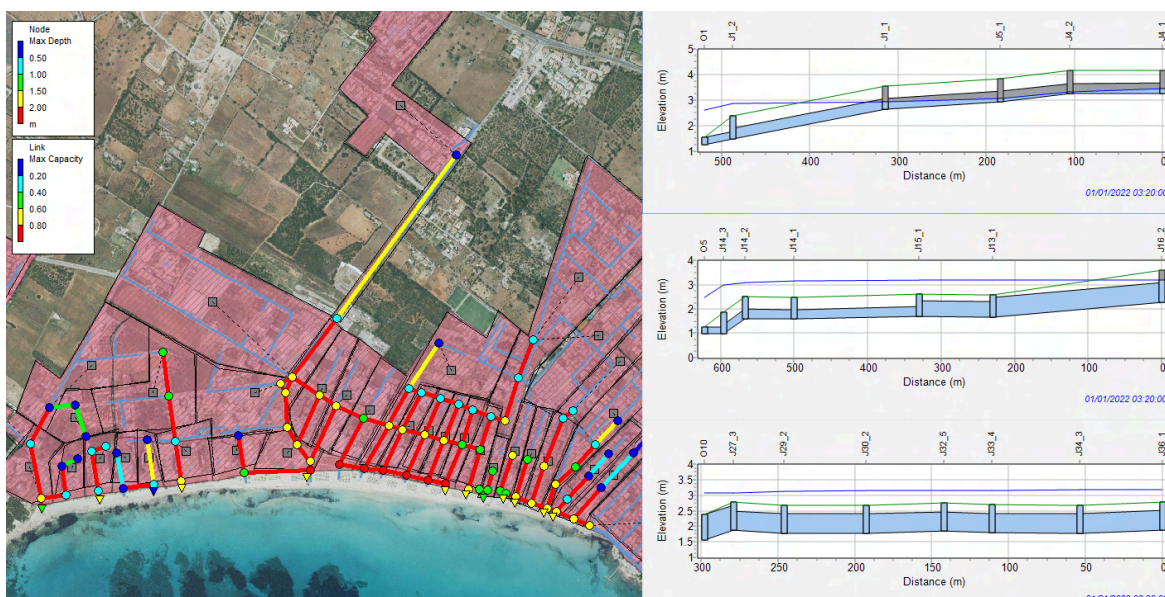


Figure 74. Drainage system status at 2100 for the RCP4.5 scenario. Left panel: Net system links capacity and junction water head (m) at 3:20 h elapsed time. Right panels: Water head along de O1, O5 and O12 nets at 3:20 h elapsed time.

Under the RCP8.5 scenario, the effects are more severe, with the entire network adjacent to the promenade being affected. Additionally, the upper tributary networks in the central and northern areas exhibit higher water head values at the nodes and increased link capacity.

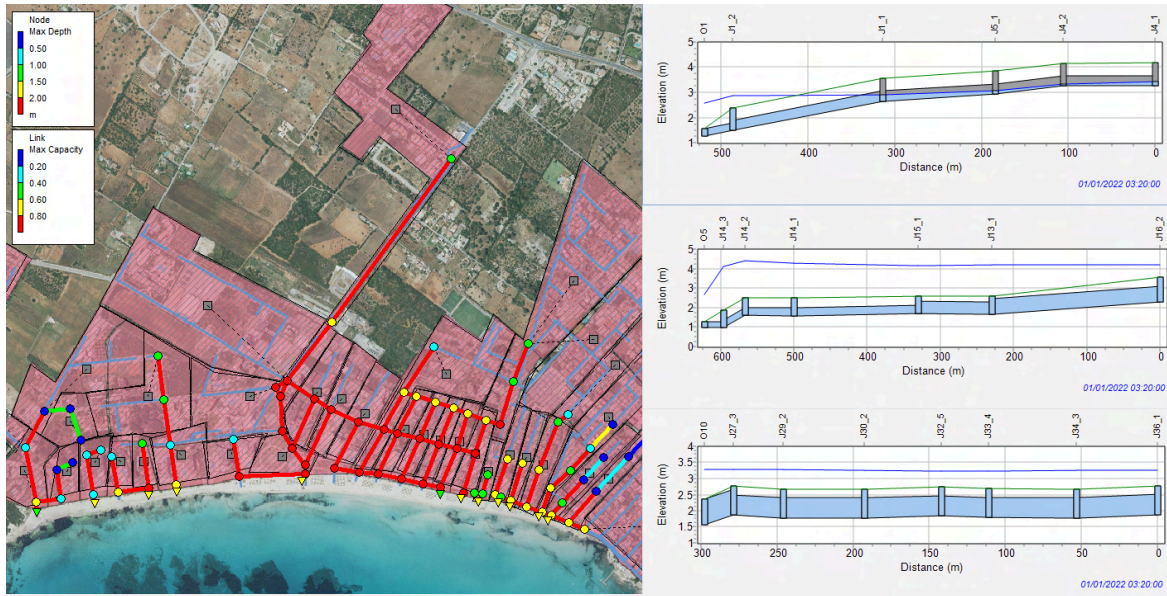


Figure 75. Drainage system status at 2100 for the RCP8.5 scenario. Left panel: Net system links capacity and junction water head (m) at 3:20 h elapsed time. Right panels: Water head along de O1, O5 and O12 nets at 3:20 h elapsed time.

2.4.4. Hazard assessment of compound flooding

For the calculation of composite flooding (coastal flooding combined with rainwater runoff), all scenarios have been considered for the T25 rainstorm. Based on the results for water head and flooding duration at nodes where ponding occurs, the flooding impact is estimated using a ponding depth threshold (set to 0.05 m) and the maximum reported head at the nodes. The normalized ponding is computed as:

$$H_n = \min(1, H_e/H_t)$$

where H_e is the effective water head at the nodes, and is computed as the water head above the node crown, and H_t is the head threshold for which it is considered that compound flooding is significant **and longer than 3 h. This threshold has been set to 2.0 m** considering model node flooding flow rates and ponding times. H_n values lower than 1 stand for low flooding and short ponding times. Since these results are generated at the junctions of the drainage system, the data have been spatially interpolated along the street network following the drainage system's path. This interpolation process ensures a continuous representation of the normalized ponding impact across the entire network, facilitating a more accurate assessment of flow distribution and hydraulic behavior. The interpolation method accounts for spatial variability and is designed to maintain consistency with the underlying drainage infrastructure, enabling better visualization and analysis of localized compound flooding conditions.

To summarize the compound flooding impact, the percent of the area (corresponding to the urban area containing and tributing to the drainage system) with $H_n > 0.75$ values along the study area has been computed (Table 20):

	Current	2030	2050	2100
RCP-4.5	4.1%	6.3%	17.3%	26.6%
RCP-8.5	—	7.4%	32.5%	59.7%

Table 20. % of area affected by compound flooding considering $H_n > 0.75$.

The compilation of the compound flooding hazard maps is presented in Section 3.3. The results highlight how the disruption of the drainage system primarily leads to compound flooding along the promenade, with varying degrees of severity depending on the scenario. The most affected areas are the central and northern sections, as well as the main plaza, across all scenarios. Additionally, these effects extend upstream into the second-row streets.

COMPOUND FLOODING ABSTRACT

- Coastal urban drainage systems are vital for managing rainfall and preventing urban flooding but are increasingly threatened by sea-level rise and extreme weather. A new dimension has been considered to assess how compounded effects of storms, rainfall, and sea-level rise impact drainage in Cala Millor to guide climate adaptation strategies.
- A simplified drainage system, reflecting the current state of Cala Millor, has been incorporated into the simulations. These simulations take into account the hazard results from Section 2.1.3 on sea-level rise and extreme coastal flooding, as well as the recommendations of the Spanish Road Instruction 5.1-IC.
- The current drainage system was designed to handle rainstorms with a return period of T10, without considering the effects of sea-level rise and wave storms on the system's outlets.
- Simulations indicate that when the system is subjected to rainstorms of T25 and coastal flooding caused by wave storms, it reaches capacity, causing disruptions along the promenade and central plaza under RCP4.5 and RCP8.5 scenarios by 2030. These disruptions could affect the upstream network, resulting in potential compound ponding in affected street areas.

3. IMPACT MAPS

This section presents the results of the hazard assessment methodology described earlier in this document. Impact maps illustrate the effects of hazards on both the natural and human systems. In Annex 2 there are links to a shared folder that contains all the resulting layers, and each subsection provides examples of various scenarios.

3.1. Flooding maps

The 55 flooding maps in asci format as it was defined in [Table 10](#) are available as Annex 2, as well as the derived layers with the flood water depth information. To simplify the visualization of these results, figures in .png format are also provided ([Annex 2](#)). Each of these figures combines the three interval scenarios (minimum, mean, and maximum) into a single hazard map. Some of them are shown here:

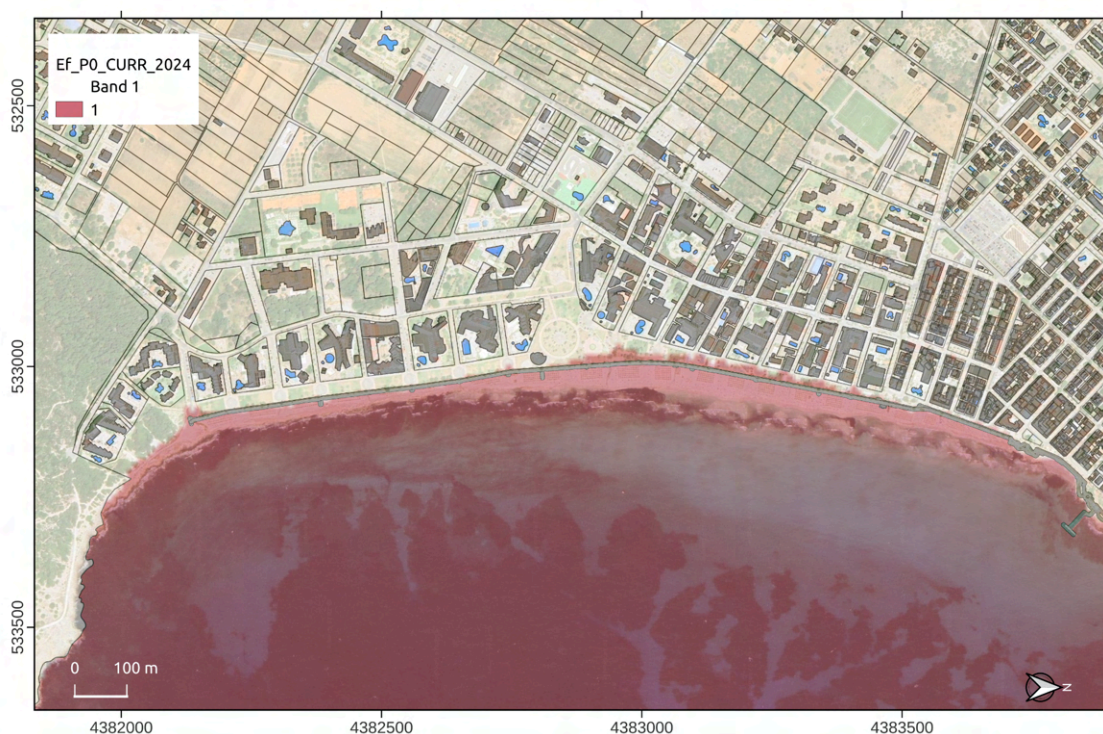


Figure 76. Current Extreme Flooding (Ef_P0) map (2024 year).

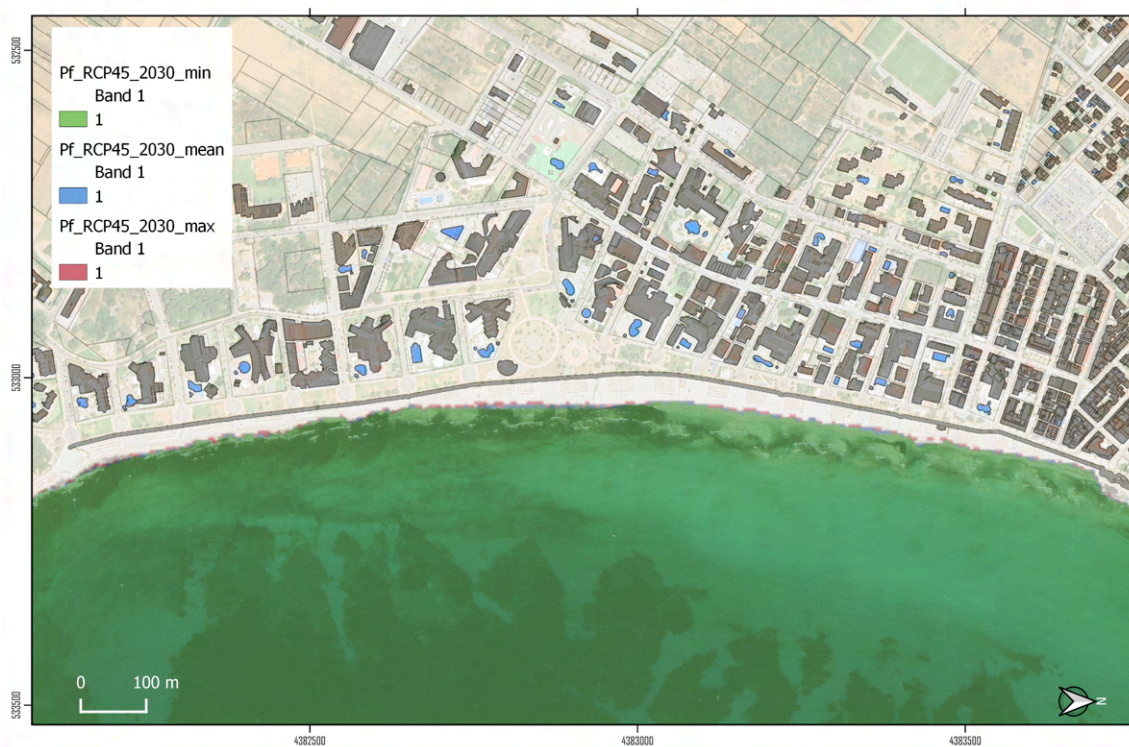


Figure 77. Permanent Flooding (Pf) map of RCP-4.5 and 2030 time horizon.

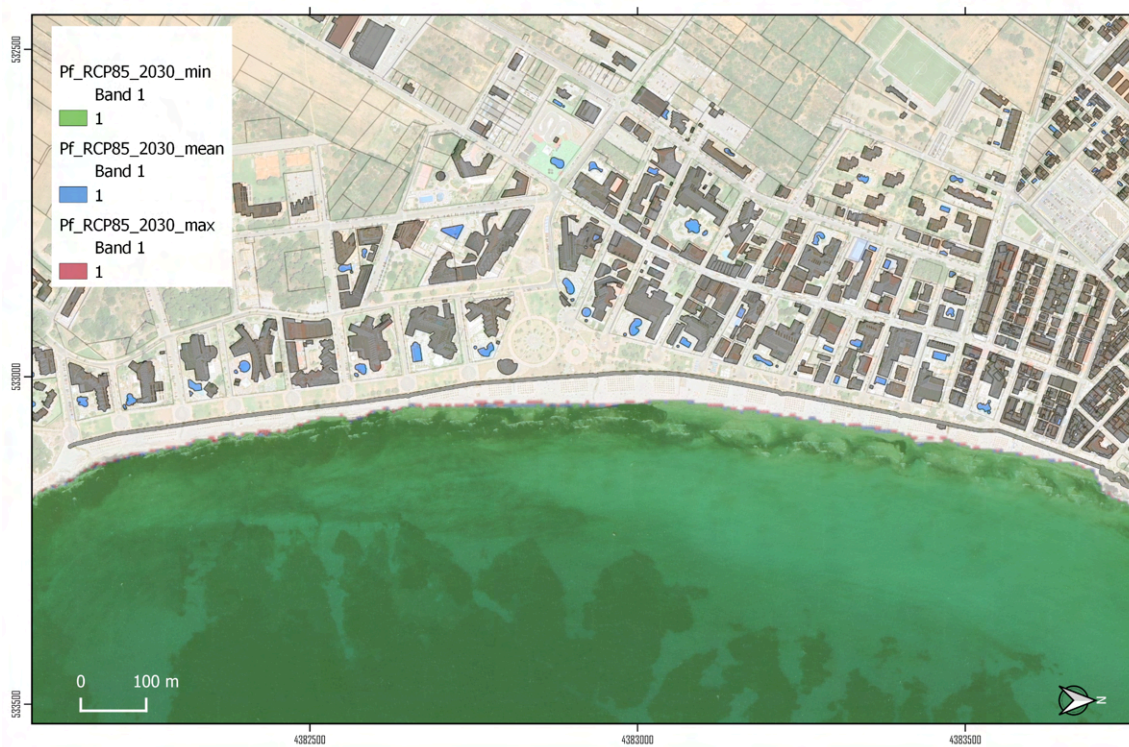


Figure 78. Permanent Flooding (Pf) map of RCP-8.5 and 2030 time horizon.

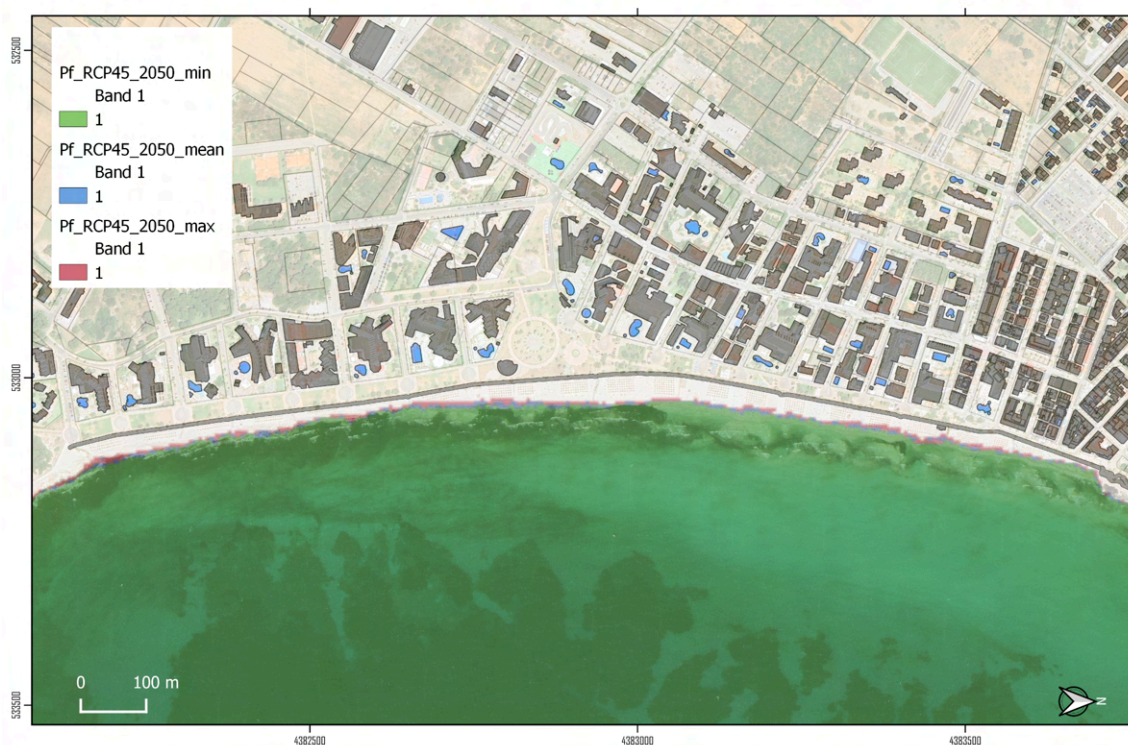


Figure 79. Permanent Flooding (Pf) map of RCP-4.5 and 2050 time horizon.



Figure 80. Permanent Flooding (Pf) map of RCP-8.5 and 2050 time horizon.

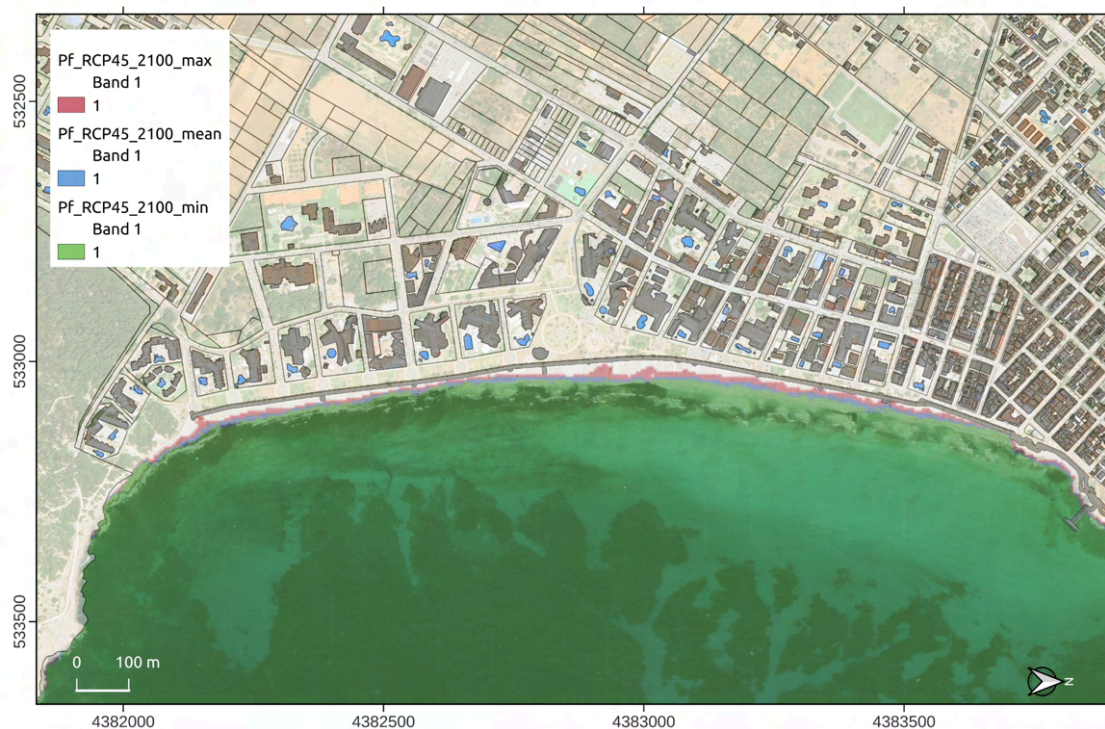


Figure 81. Permanent Flooding (Pf) map of RCP-4.5 and 2100 time horizon.



Figure 82. Permanent Flooding (Pf) map of RCP-8.5 and 2100 time horizon.



Figure 83. Extreme Flooding with Posidonia meadow invariant map (Ef_P0) for RCP-8.5 in 2030.



Figure 84. Extreme Flooding with Posidonia meadow invariant map (Ef_P0) for RCP-8.5 in 2050.



Figure 85. Extreme Flooding with Posidonia meadow invariant map (Ef_P0) for RCP-4.5 in 2100.



Figure 86. Extreme Flooding with Posidonia meadow invariant map (Ef_P0) for RCP-4.5 in 2100.

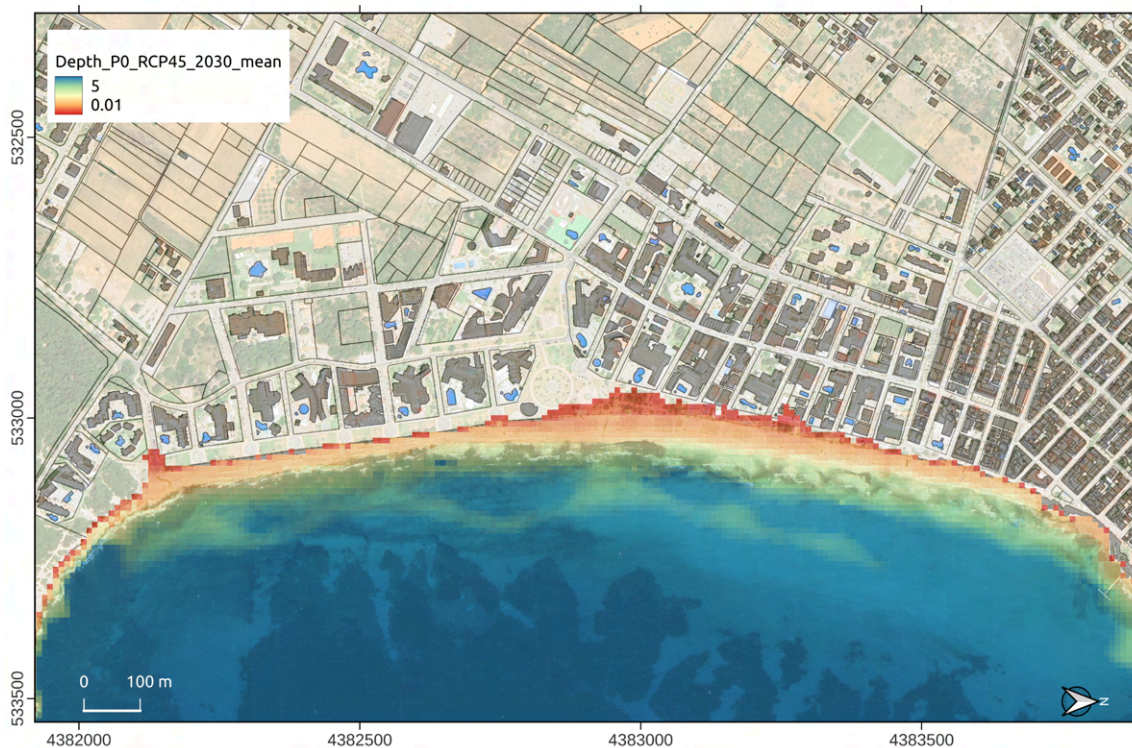


Figure 87. Water depth map in meters of the Ef_P0_RCP4.5_2030_mean flooding map.

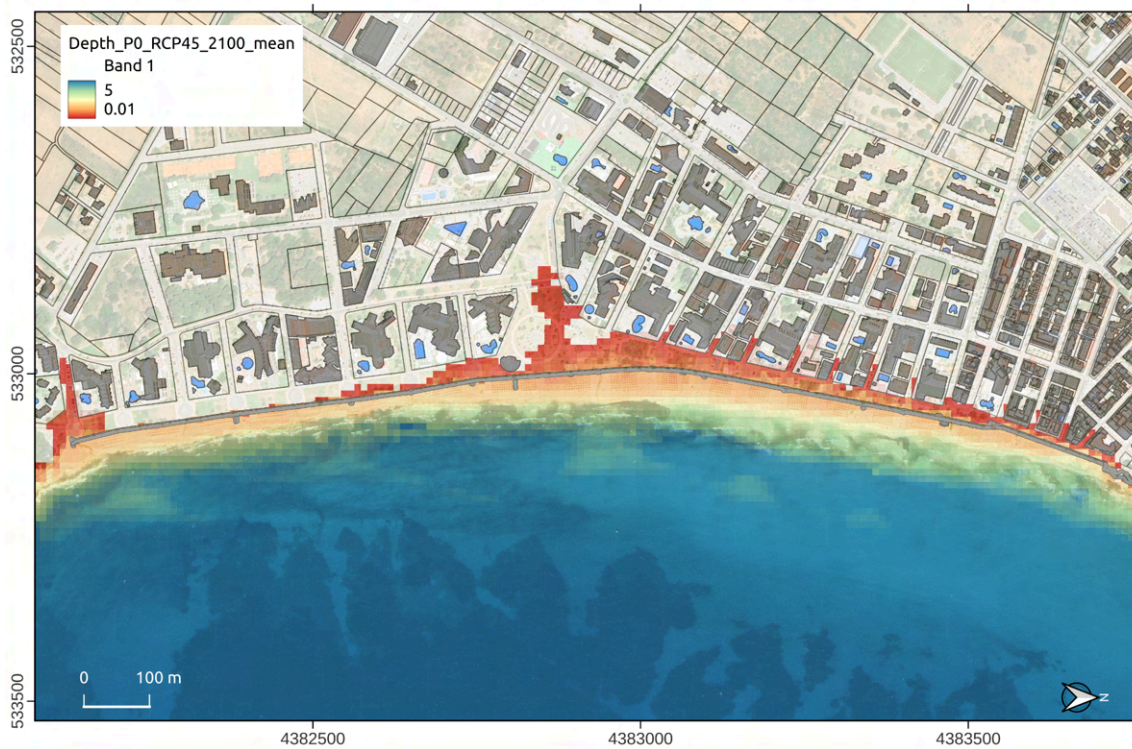


Figure 88. Water depth map in meters of the Ef_P0_RCP4.5_2100_mean flooding map.

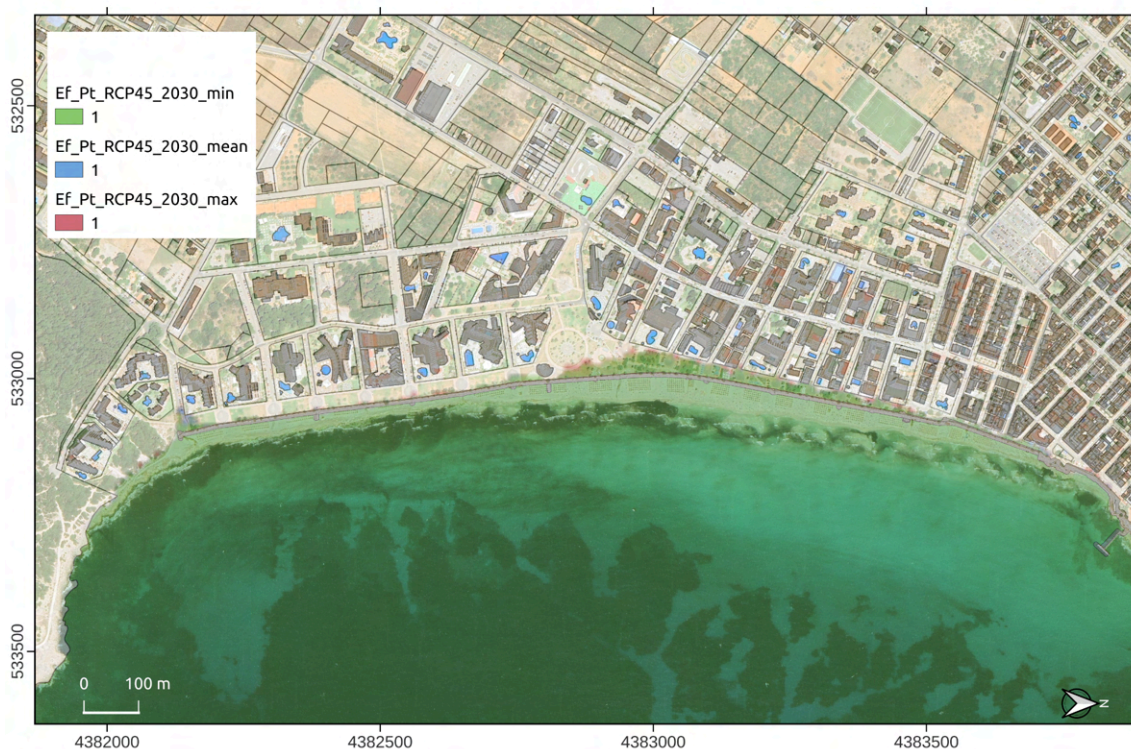


Figure 89. Extreme Flooding with Posidonia meadow dependent scenario (Ef_Pt) for RCP-4.5 in 2030.

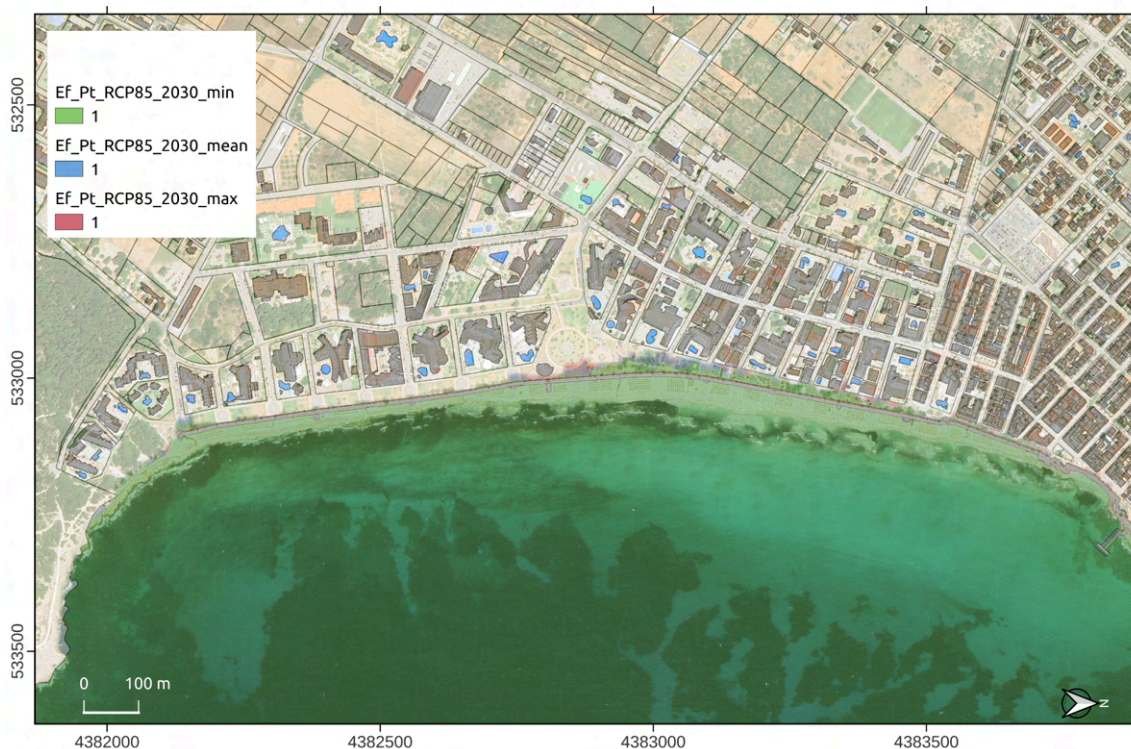


Figure 89. Extreme Flooding with Posidonia meadow dependent scenario (Ef_Pt) for RCP-8.5 in 2030.

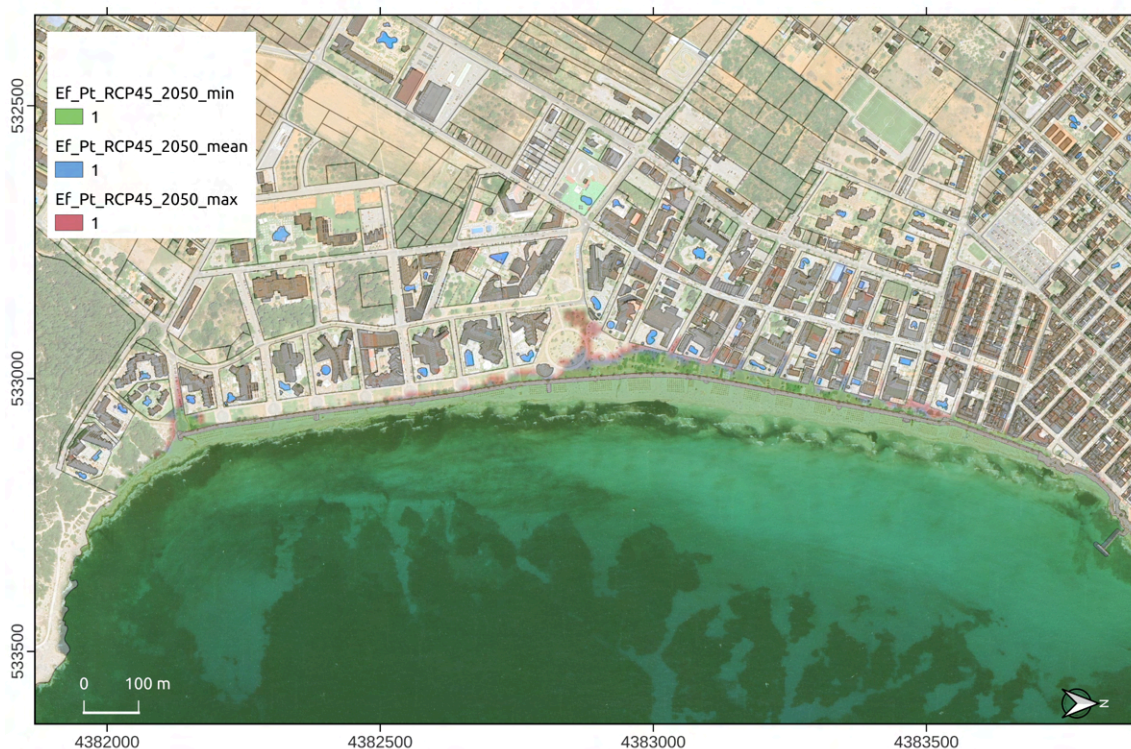


Figure 90. Extreme Flooding with Posidonia meadow dependent scenario (Ef_Pt) for RCP-4.5 in 2050.

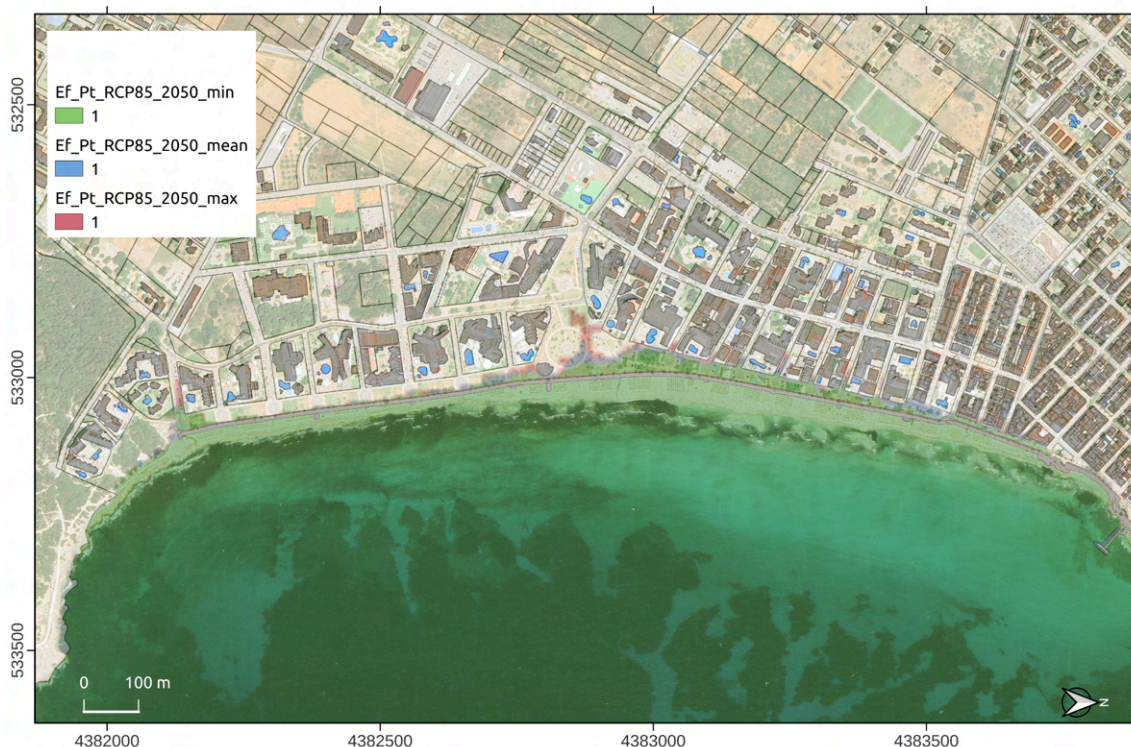


Figure 90. Extreme Flooding with Posidonia meadow dependent scenario (Ef_Pt) for RCP-8.5 in 2050.

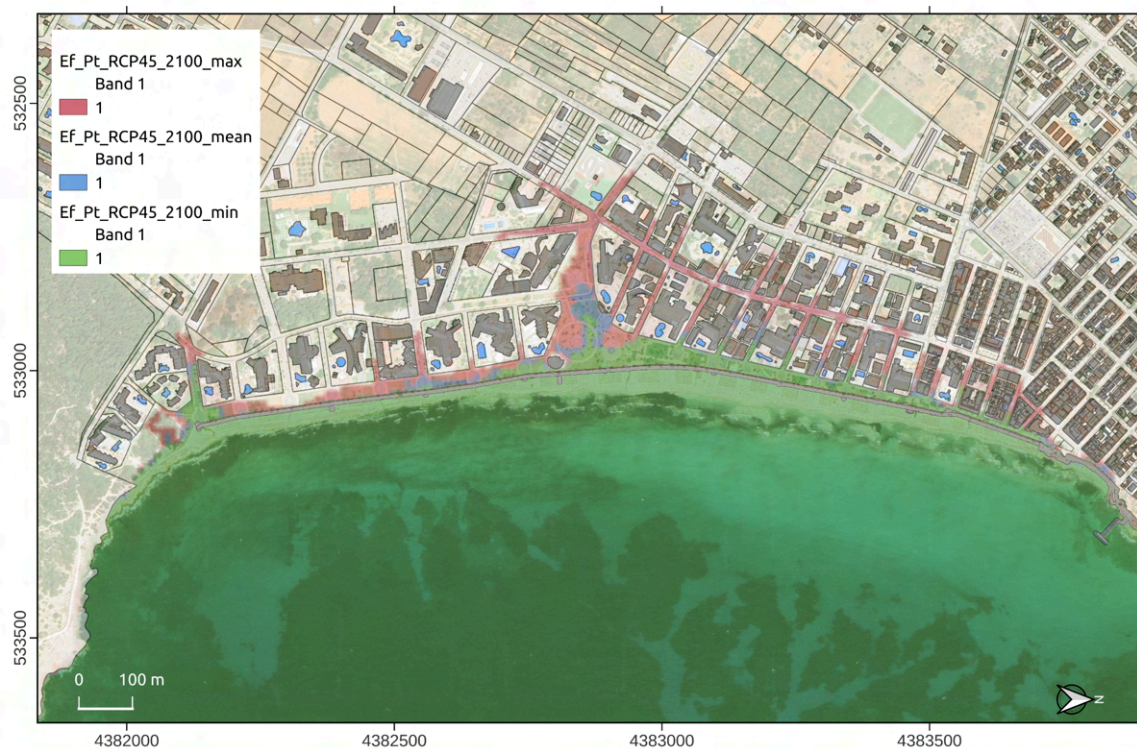


Figure 90. Extreme Flooding with Posidonia meadow dependent scenario (Ef_Pt) for RCP-4.5 in 2100.

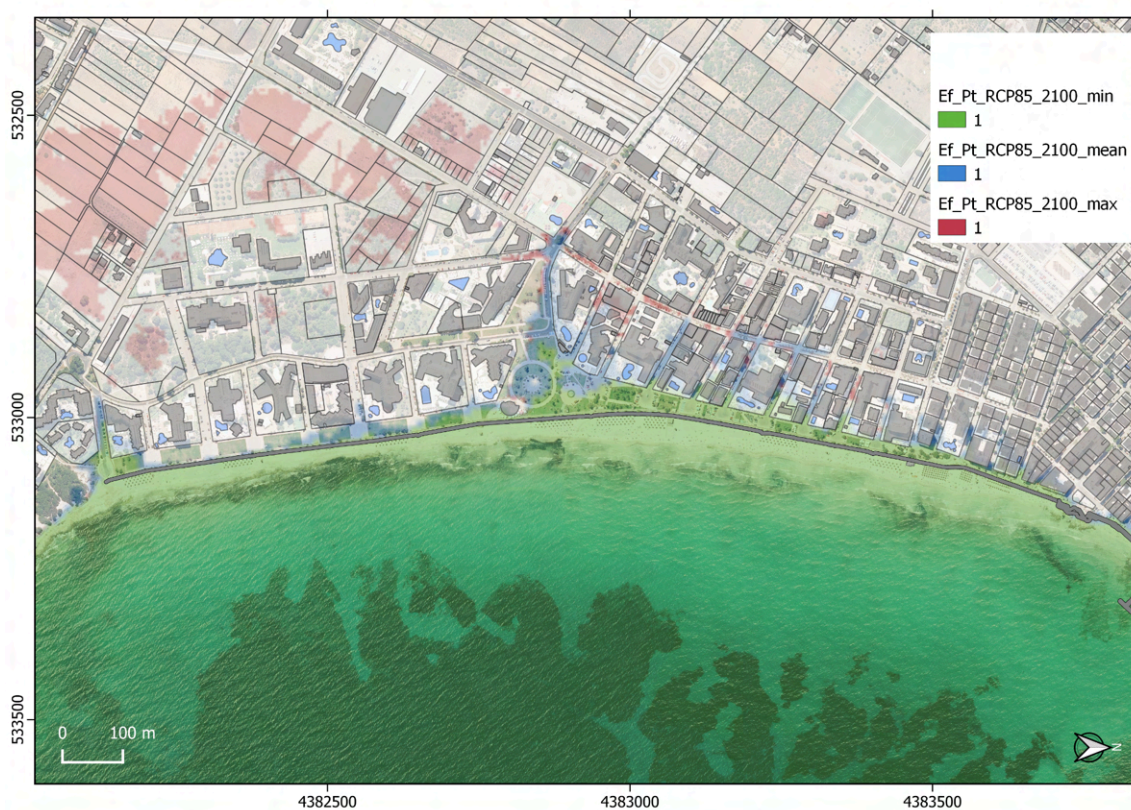


Figure 90. Extreme Flooding with Posidonia meadow dependent scenario (Ef_Pt) for RCP-8.5 in 2100.

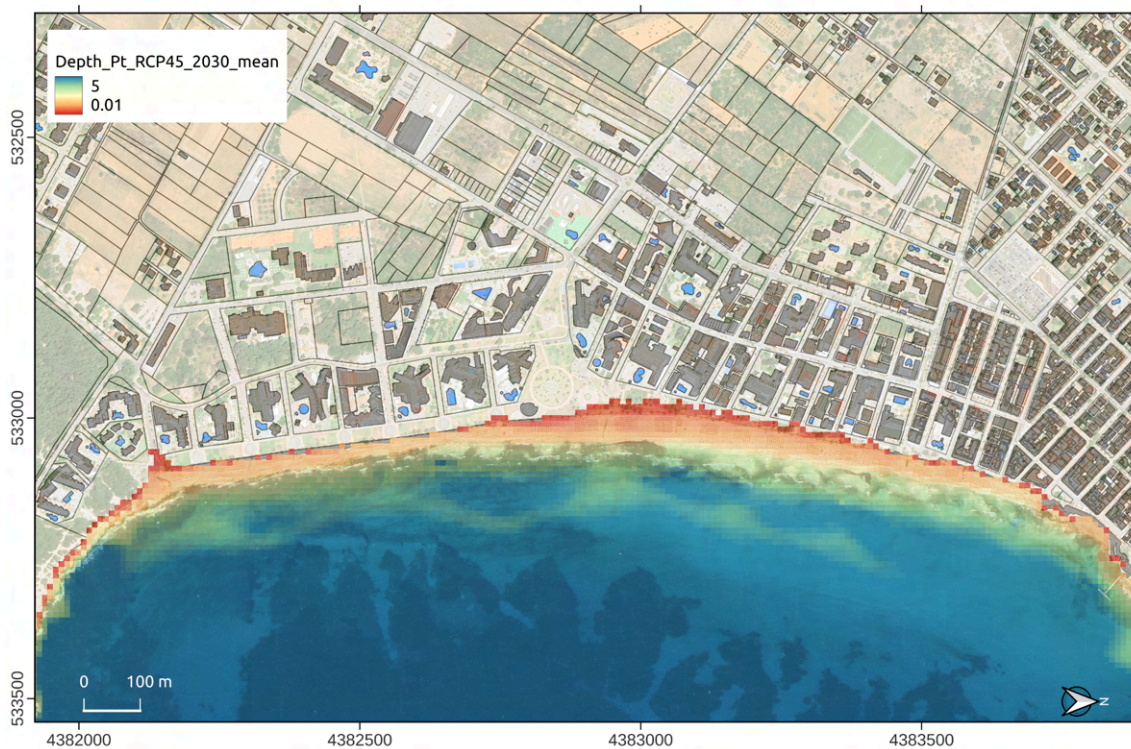


Figure 91. Water depth map in meters of the Ef_Pt_RCP4.5_2030_mean flooding map.

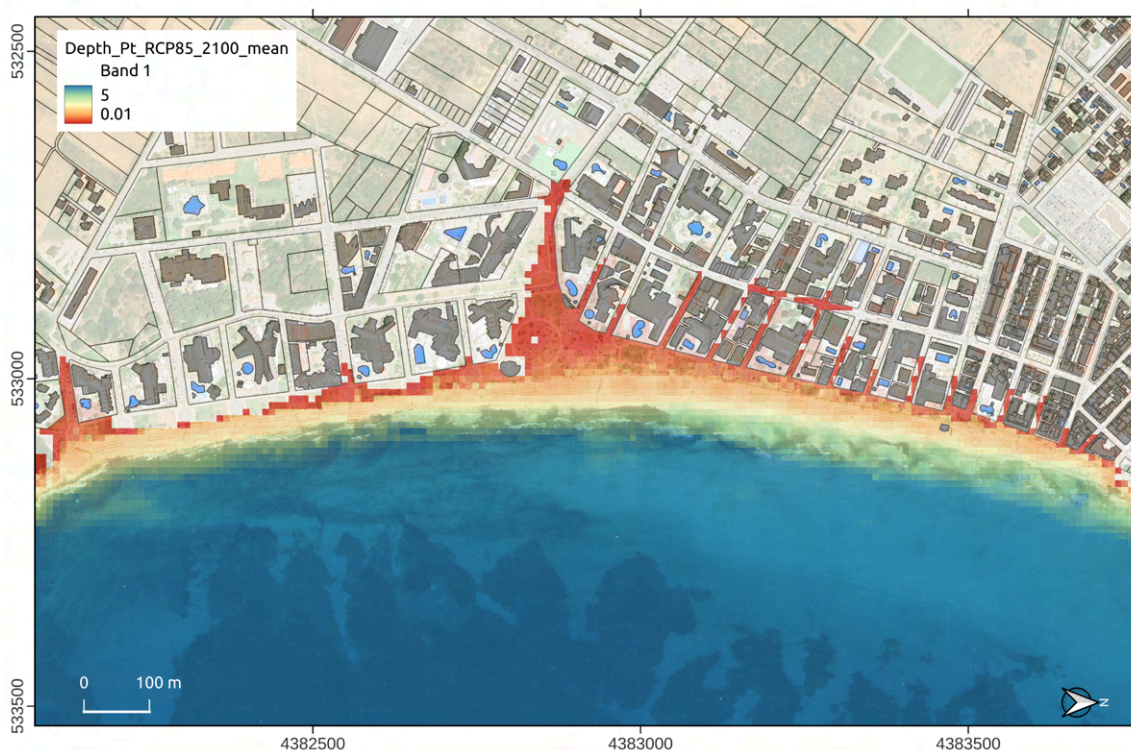


Figure 92. Water depth map in meters of the Ef_Pt_RCP8.5_2100_mean flooding map

3.2. *Posidonia oceanica* meadow shoot density impact maps

The impact of shoot density loss on *Posidonia oceanica* maps in asci format as it was defined in section 2.2.2.4 are available as [Annex 2](#). To simplify the visualization of these results, figures in .png format are also provided ([Annex 2](#)).

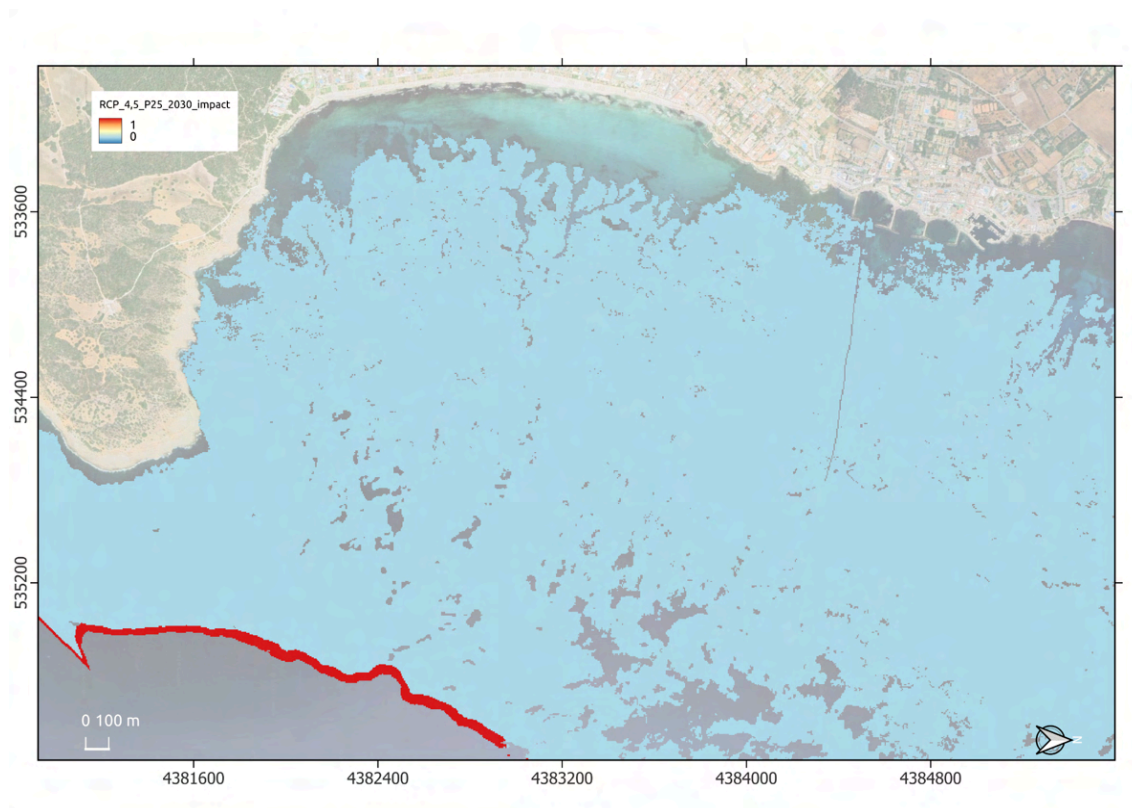


Figure 93. Impact of shoot density loss on *P. oceanica* meadow at the 25th percentile, RCP-4.5 (2030).

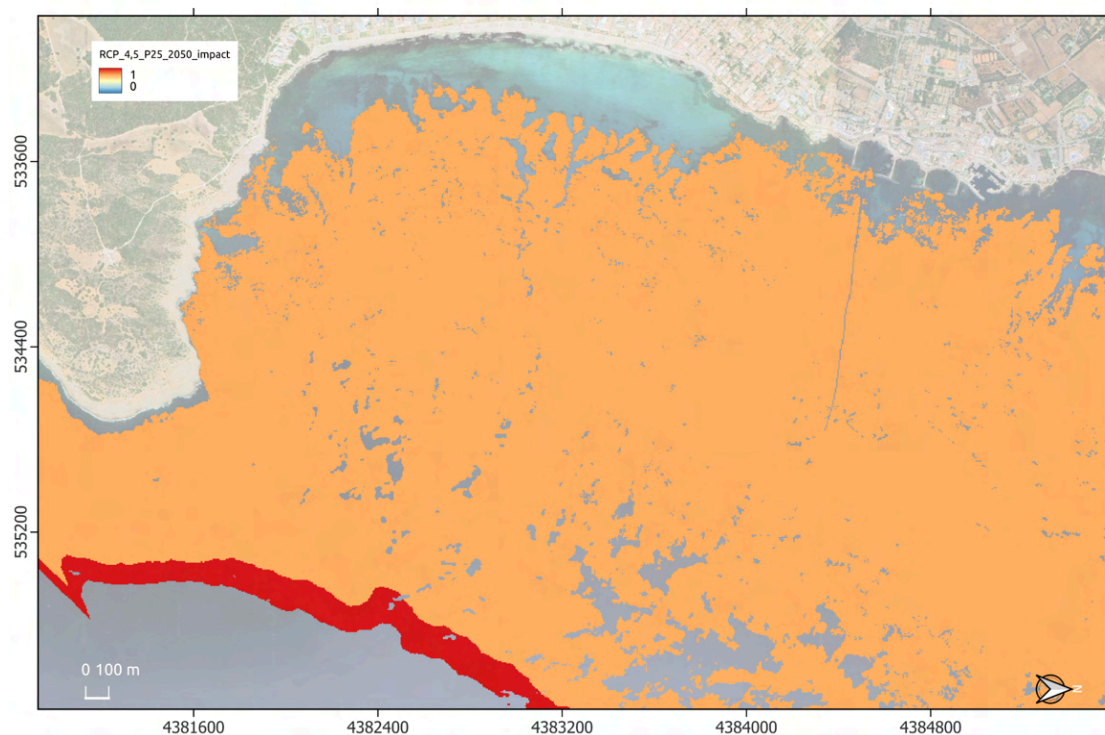


Figure 94. Impact of shoot density loss on *P. oceanica* meadow at the 25th percentile, RCP-4.5 (2050).

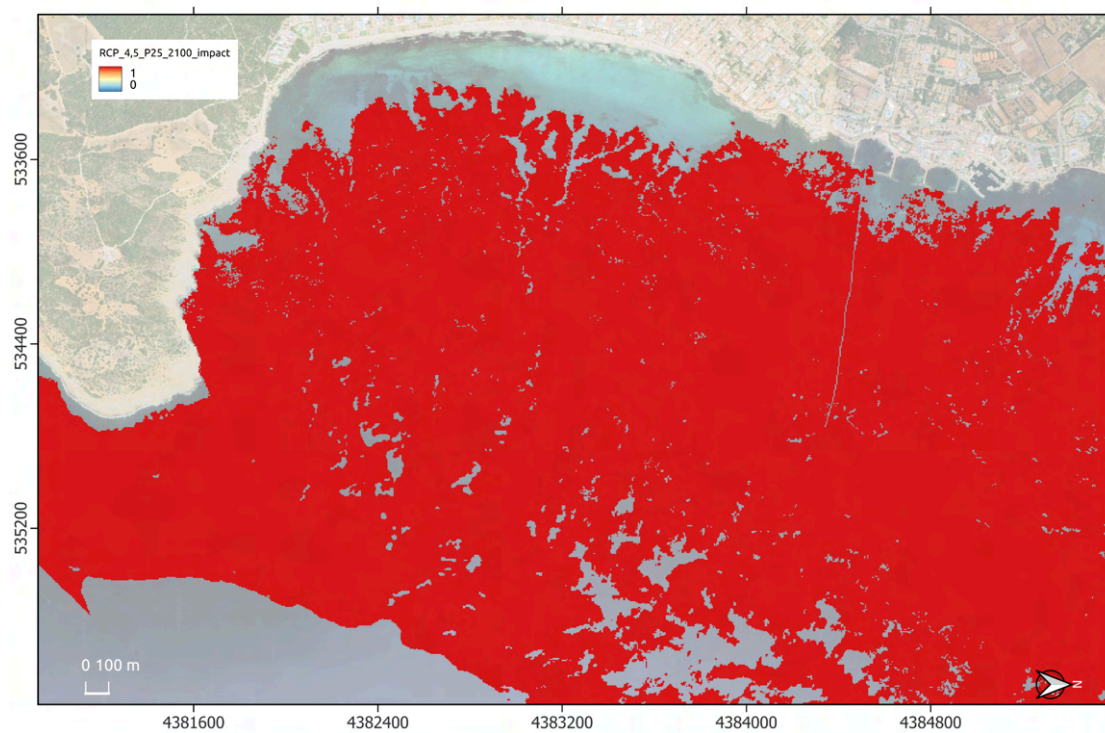


Figure 95. Impact of shoot density loss on *P. oceanica* meadow at the 25th percentile, RCP-4.5 (2050).

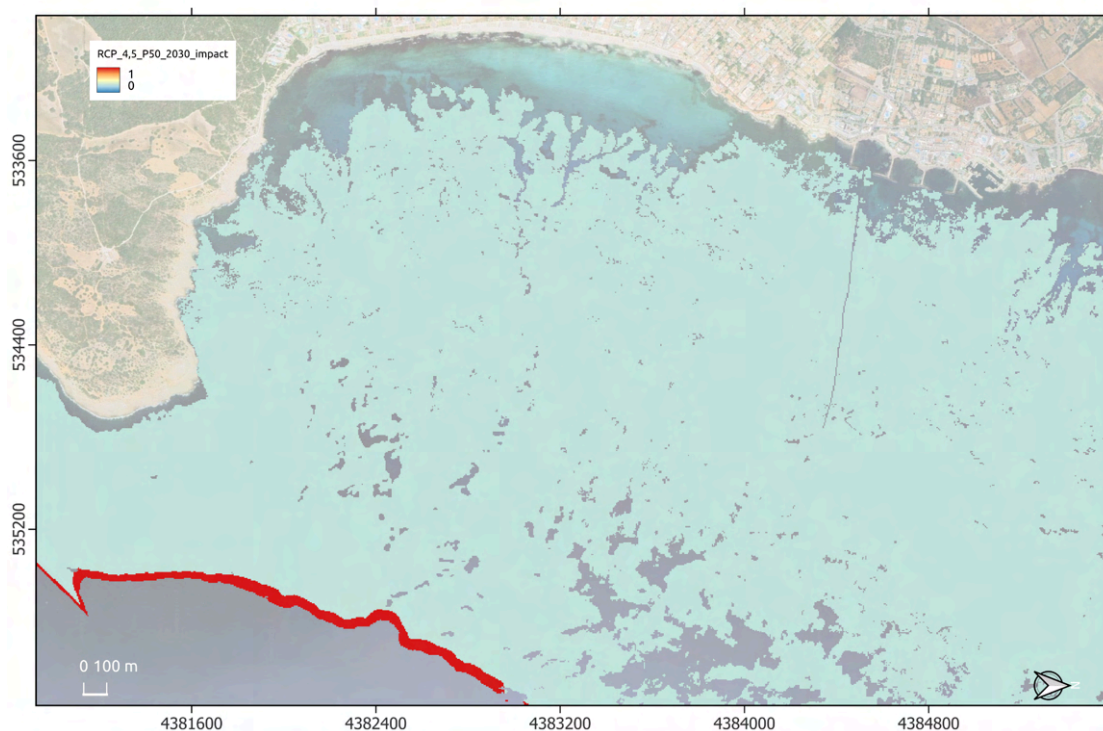


Figure 96. Impact of shoot density loss on *P. oceanica* meadow at the 50th percentile, RCP-4.5 (2030).

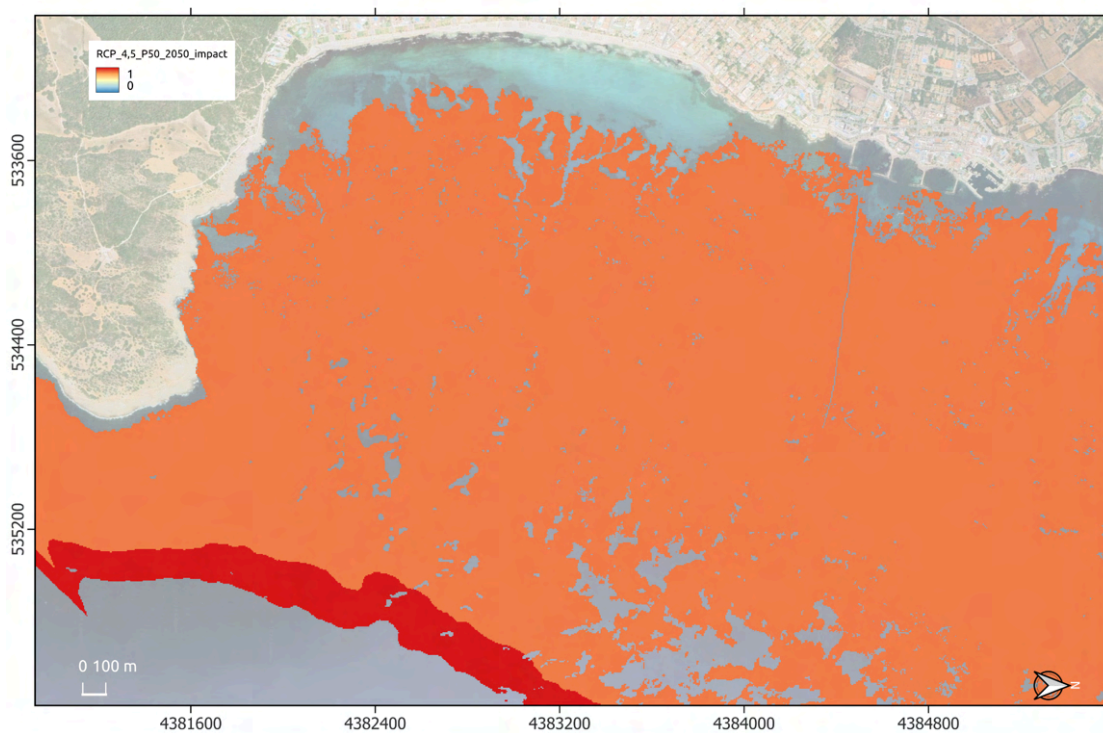


Figure 97. Impact of shoot density loss on *P. oceanica* meadow at the 50th percentile, RCP-4.5 (2050).

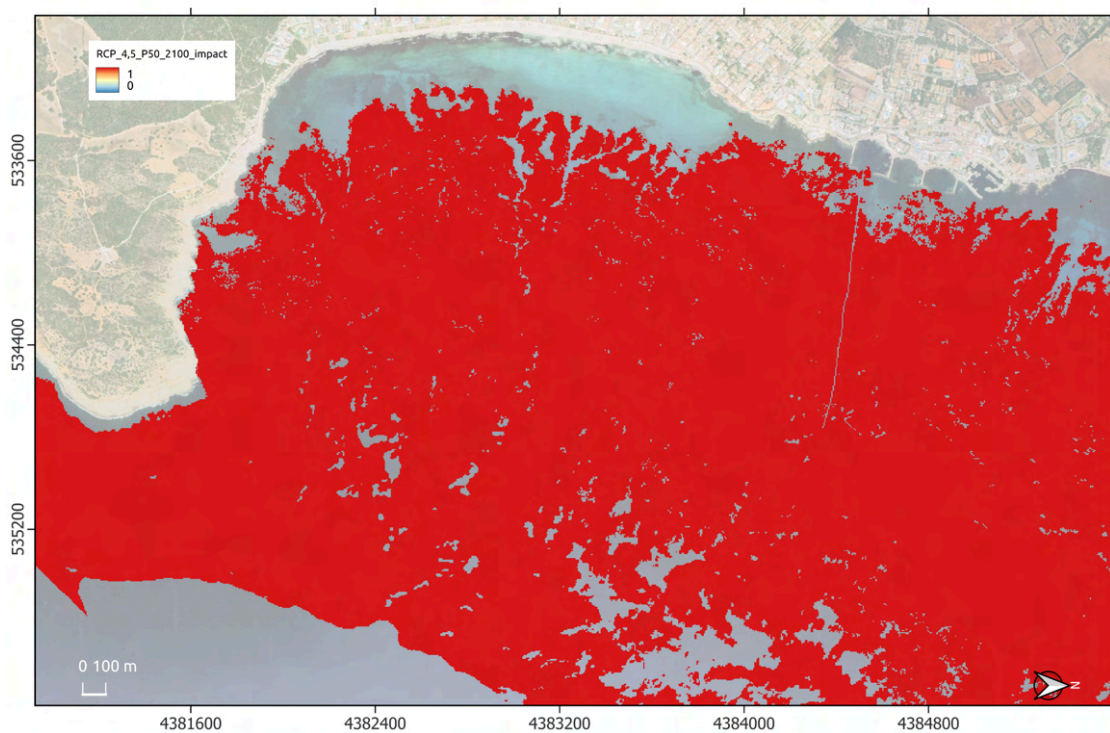


Figure 98. Impact of shoot density loss on *P. oceanica* meadow at the 50th percentile, RCP-4.5 (2100).

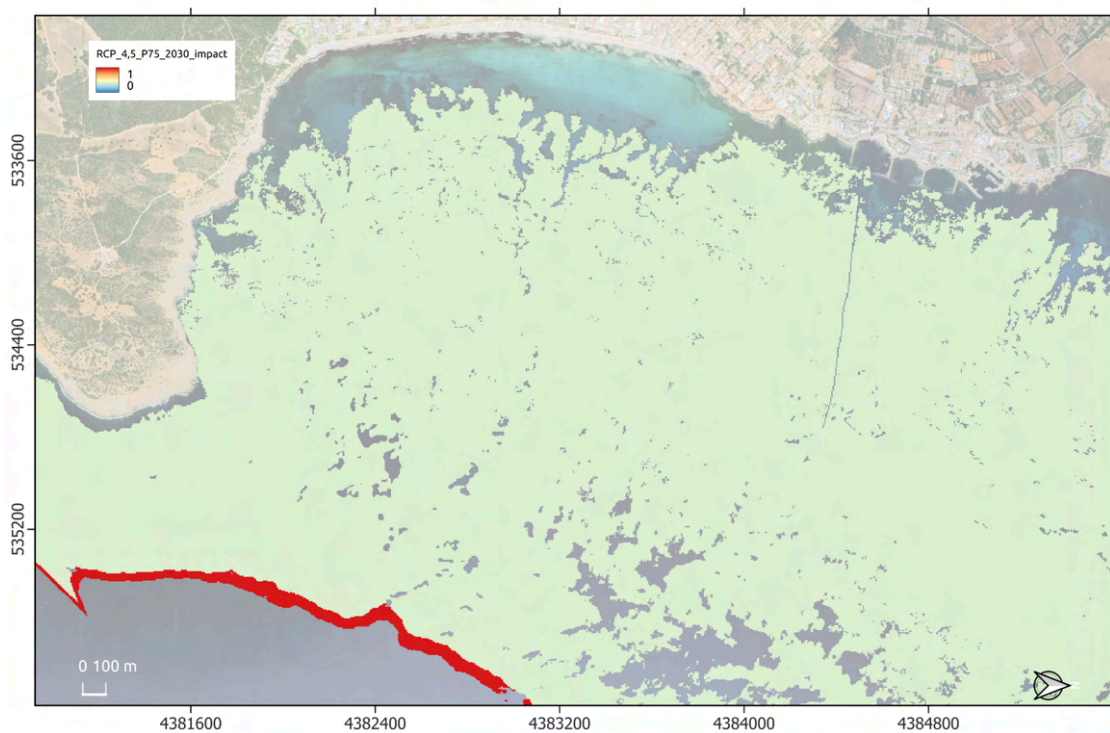


Figure 99. Impact of shoot density loss on *P. oceanica* meadow at the 75th percentile, RCP-4.5 (2030).

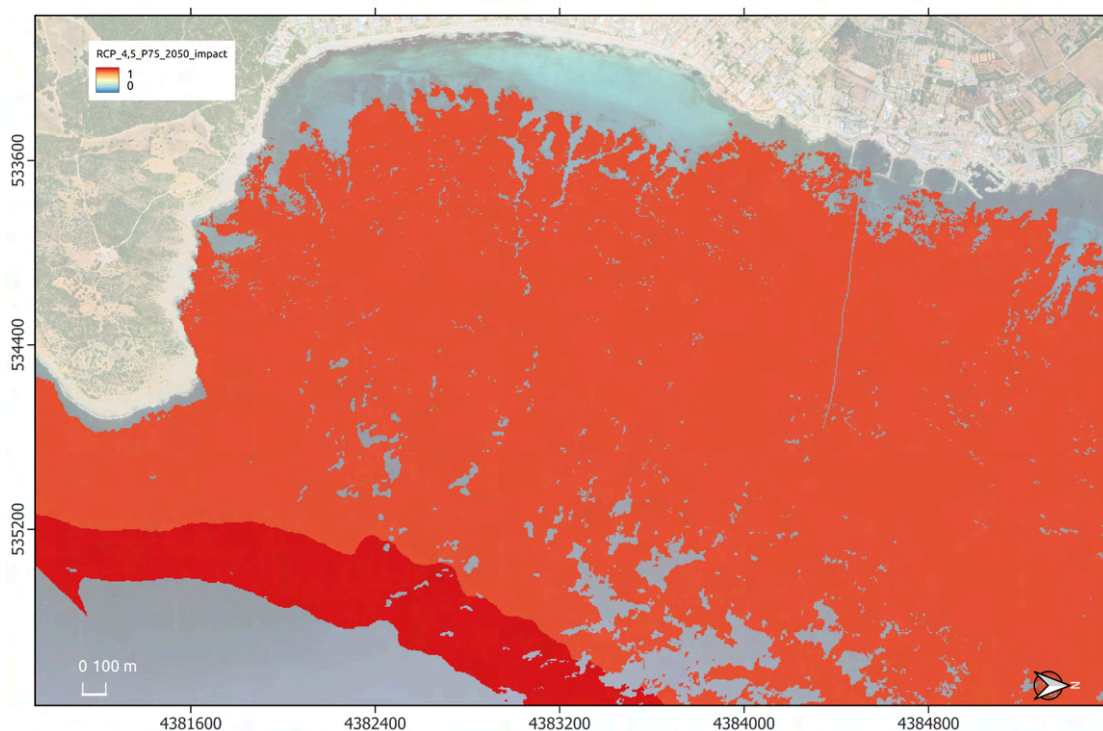


Figure 100. Impact of shoot density loss on *P. oceanica* meadow at the 75th percentile, RCP-4.5 (2050).

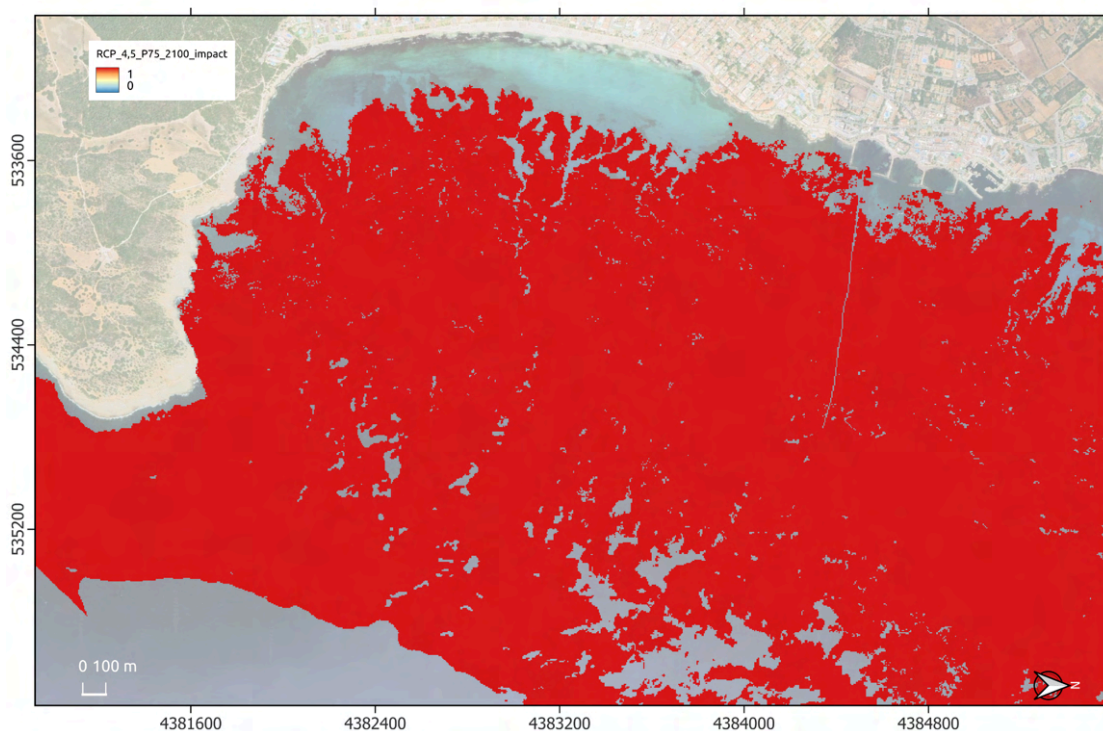


Figure 101. Impact of shoot density loss on *P. oceanica* meadow at the 75th percentile, RCP-4.5 (2100).

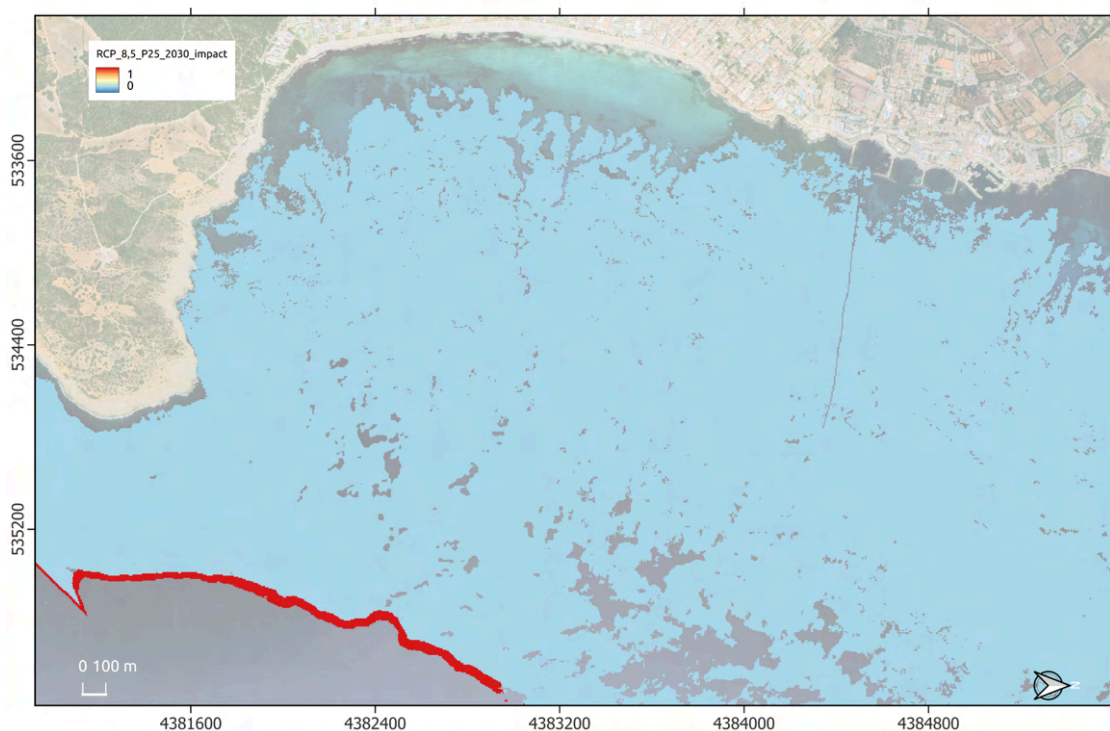


Figure 102. Impact of shoot density loss on *P. oceanica* meadow at the 25th percentile, RCP-8.5 (2030).

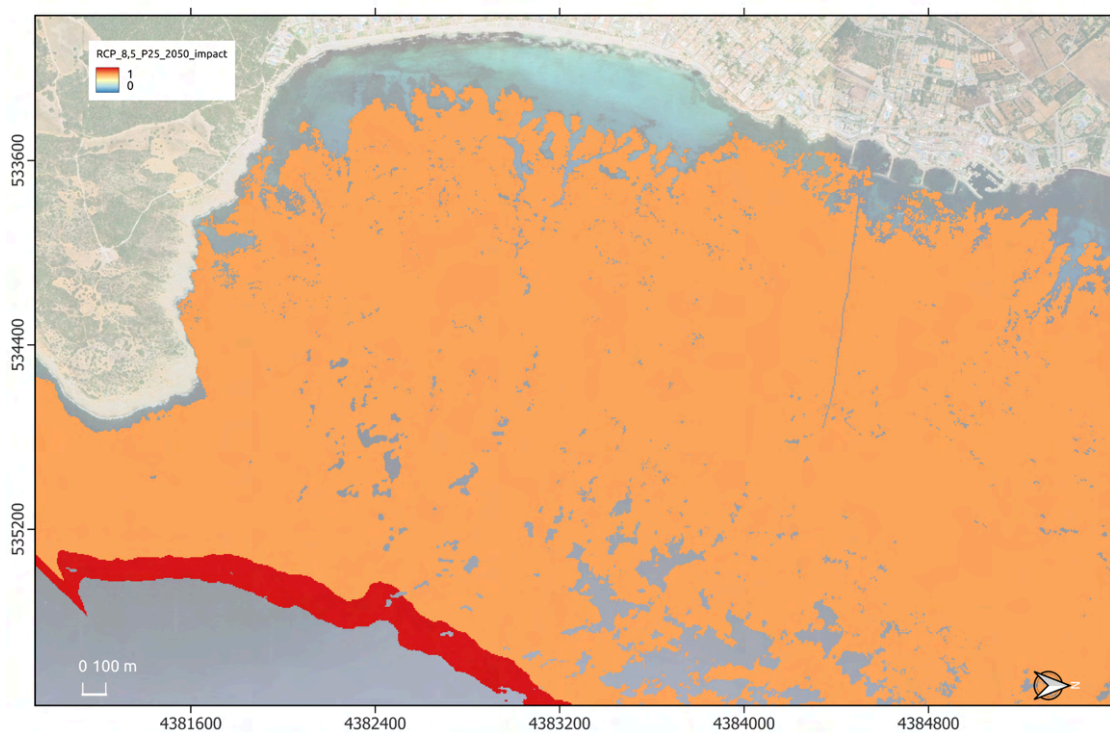


Figure 103. Impact of shoot density loss on *P. oceanica* meadow at the 25th percentile, RCP-8.5 (2050).

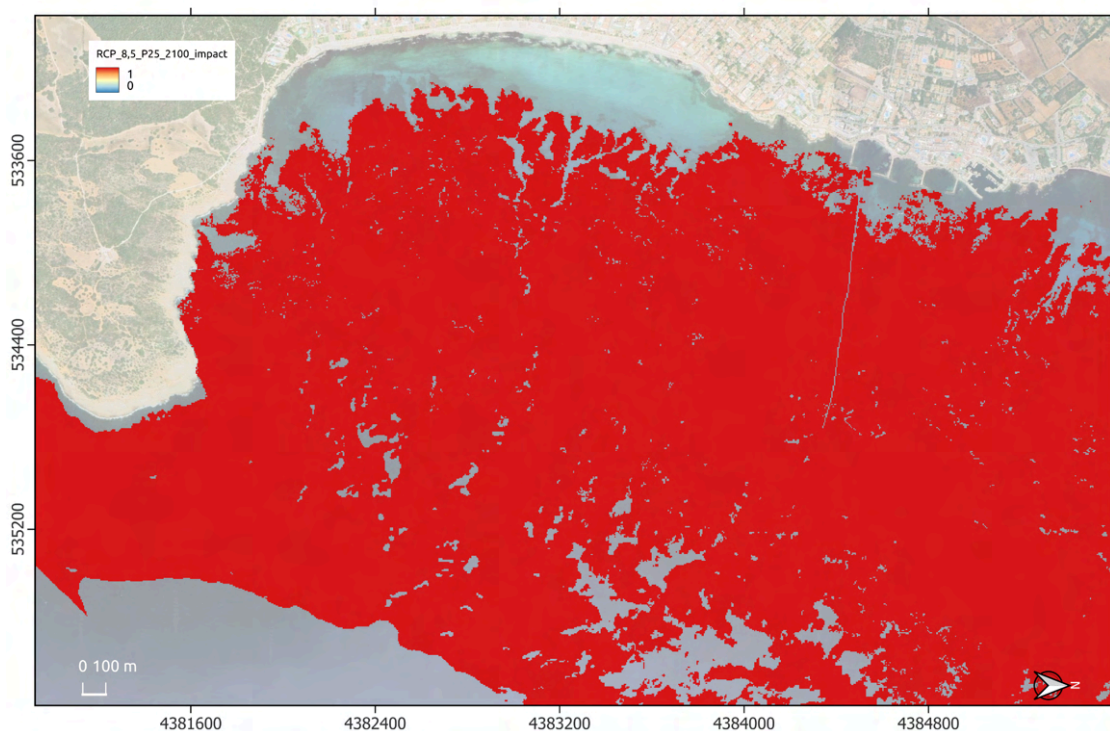


Figure 104. Impact of shoot density loss on *P. oceanica* meadow at the 25th percentile, RCP-8.5 (2100).

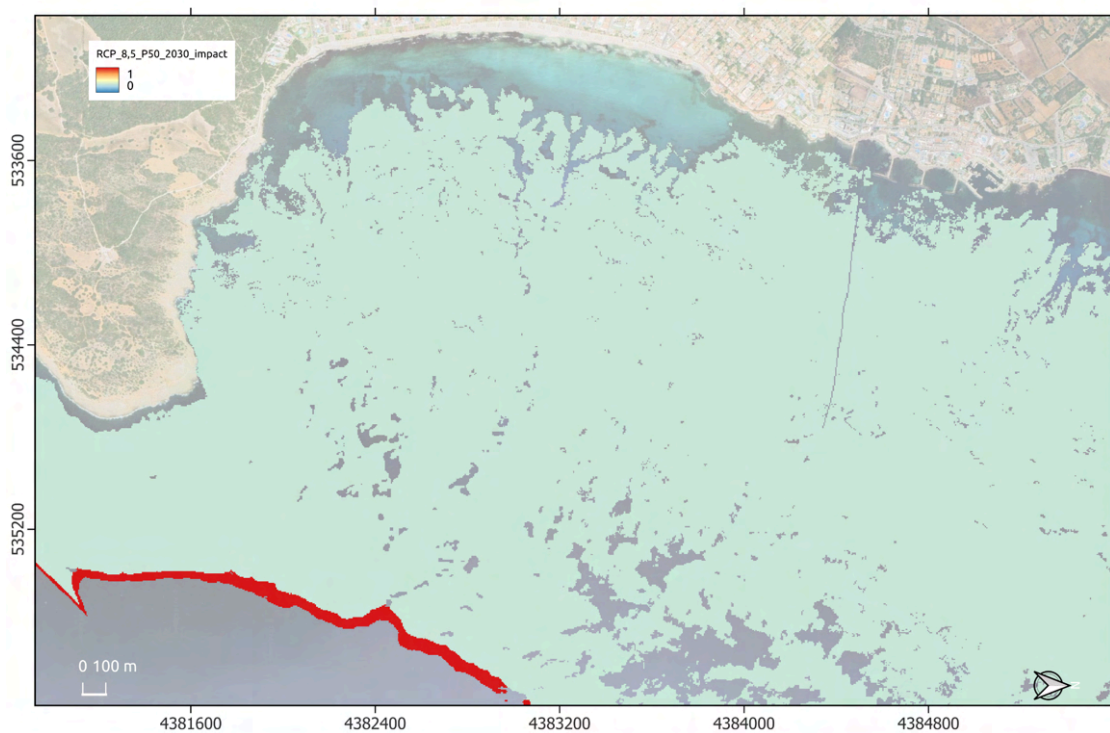


Figure 105. Impact of shoot density loss on *P. oceanica* meadow at the 50th percentile, RCP-8.5 (2030).

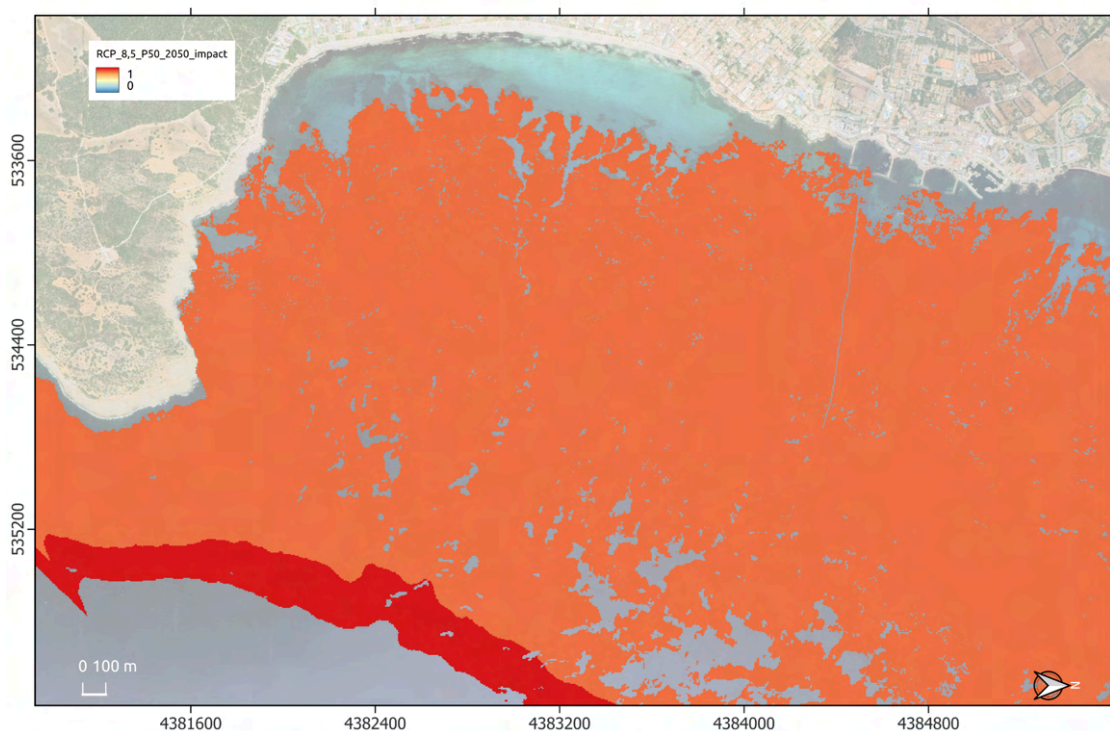


Figure 106. Impact of shoot density loss on *P. oceanica* meadow at the 50th percentile, RCP-8.5 (2050).

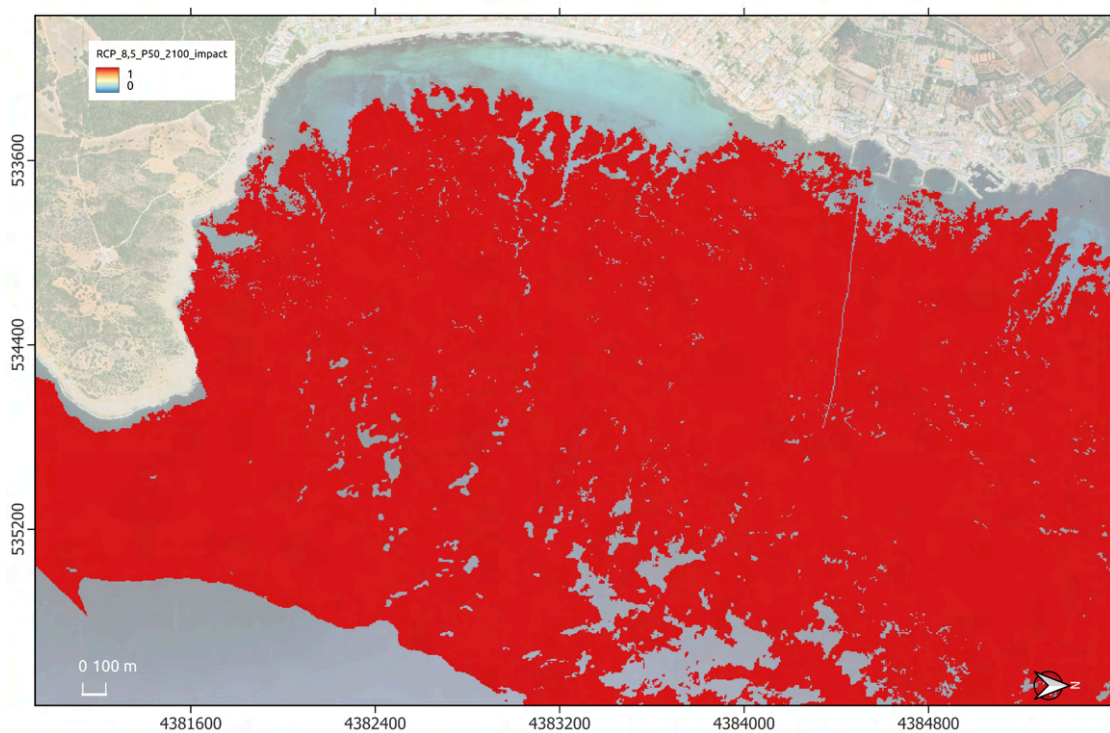


Figure 107. Impact of shoot density loss on *P. oceanica* meadow at the 50th percentile, RCP-8.5 (2100).

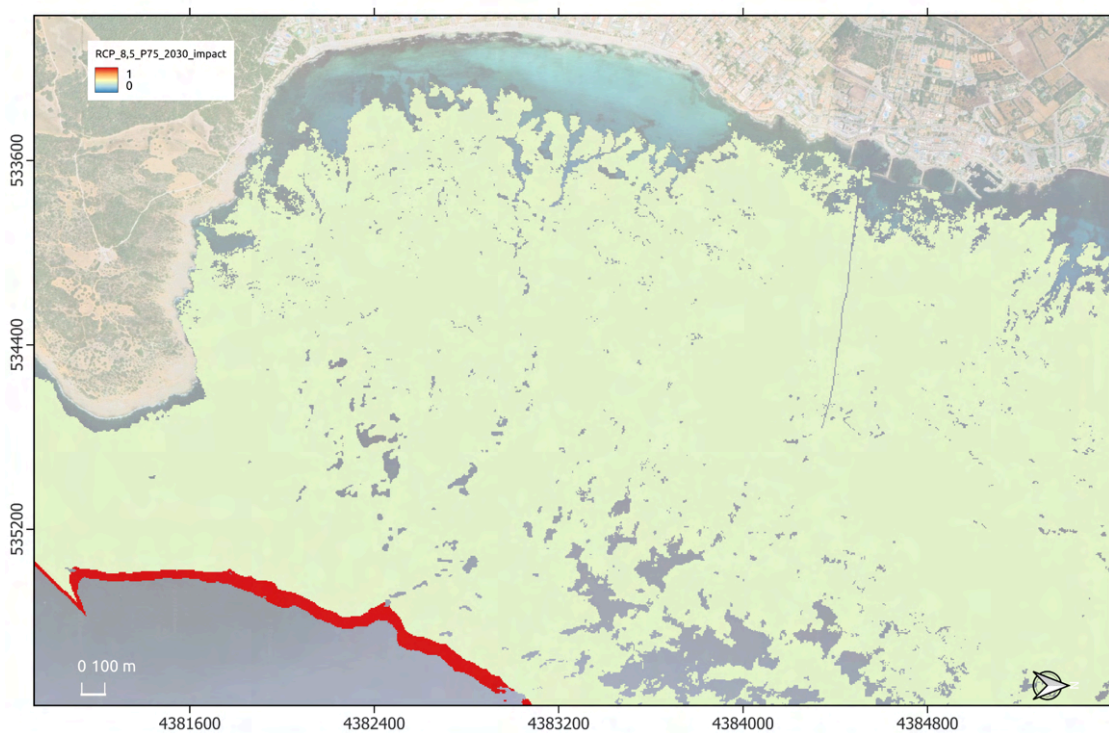


Figure 108. Impact of shoot density loss on *P. oceanica* meadow at the 75th percentile, RCP-8.5 (2030).

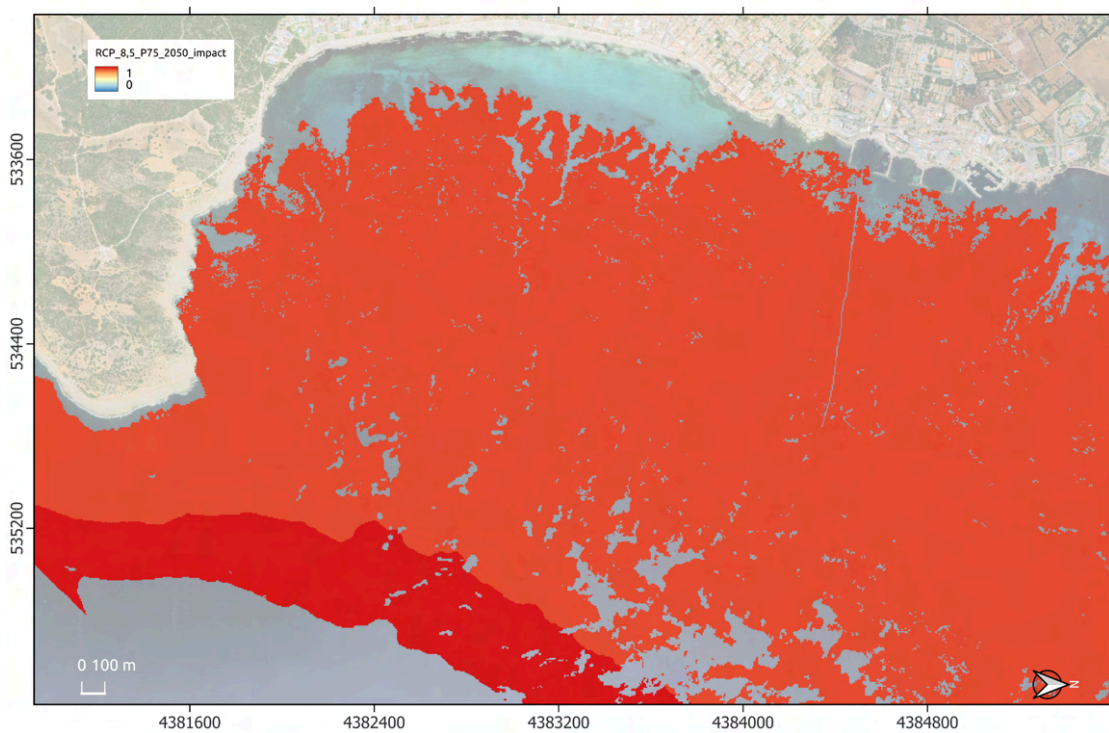


Figure 109. Impact of shoot density loss on *P. oceanica* meadow at the 75th percentile, RCP-8.5 (2050).

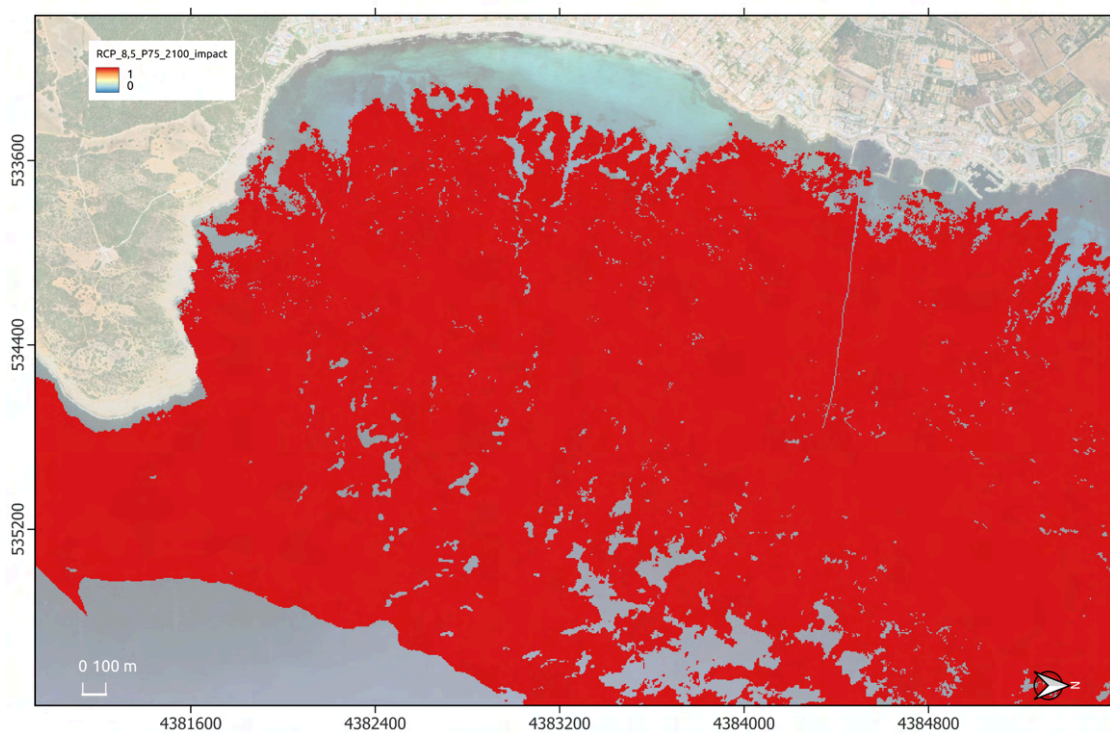


Figure 110. Impact of shoot density loss on *P. oceanica* meadow at the 75th percentile, RCP-8.5 (2100).

3.3. Coastal dune impact maps

The impact on coastal dune at Cala Millor in asci format as it was defined in section 2.2.2.3 are available as [Annex 2](#). To simplify the visualization of these results, figures in .png format are also provided ([Annex 2](#)).

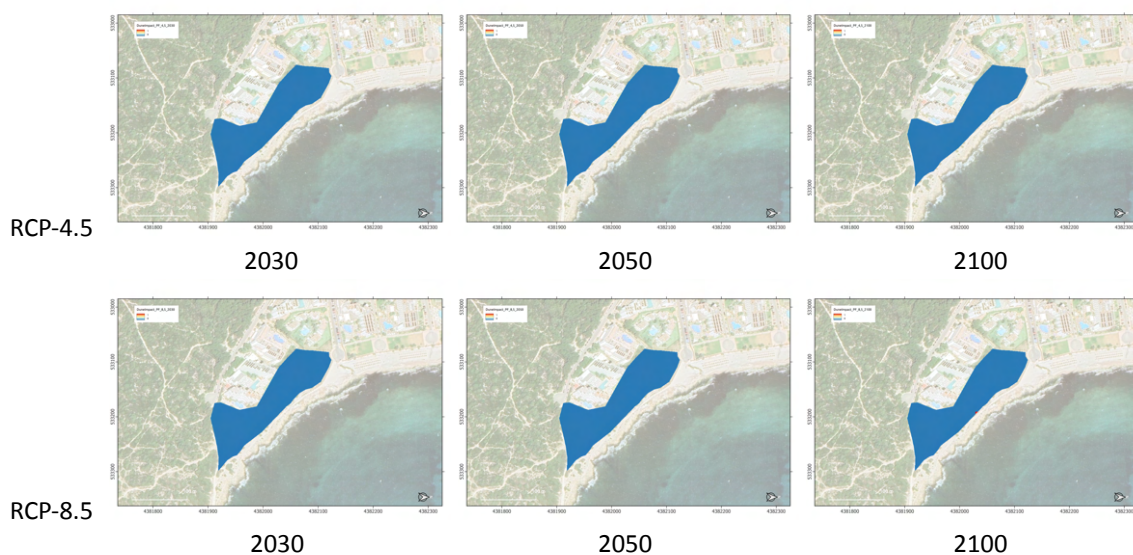


Figure 111. Impact on coastal dune system at Cala Millor by Permanent Flooding (Pf) map of RCP-4.5 and RCP-8.5, 2030, 20250 and 2100 time horizon (red denotes affection by permanent flooding).

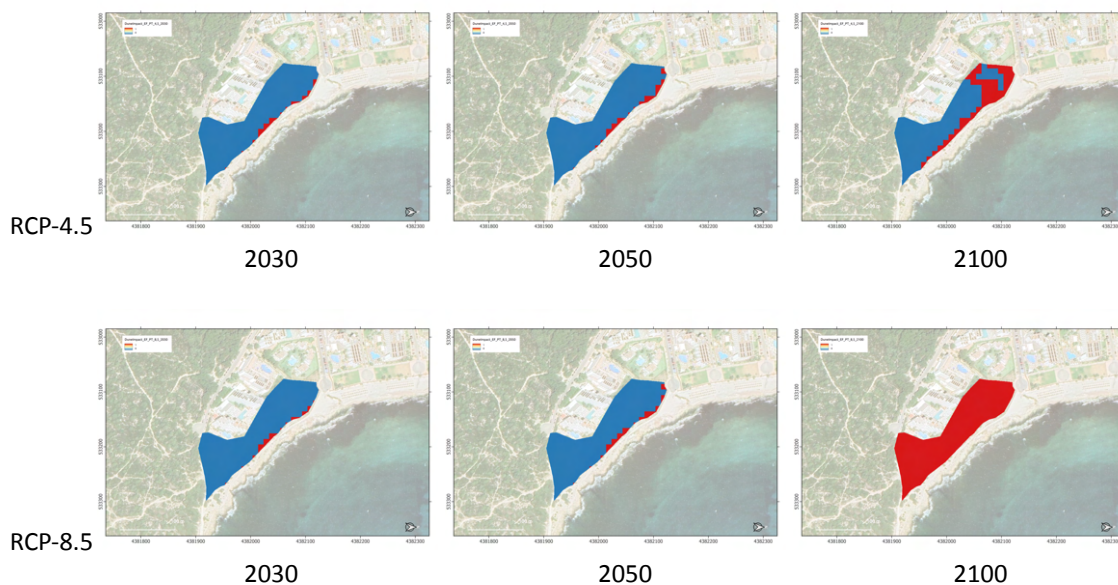


Figure 112. Impact on coastal dune system at Cala Millor by Permanent Flooding with Posidonia oceanica scenario (Pt) map of RCP-4.5 and RCP-8.5, 2030, 20250 and 2100 time horizon (red denotes affection by permanent flooding).

3.4. Compound flooding impact maps

The 7 drainage flooding maps (2030, 2050 and 2100 years for both RCP4.5 and RCP8.5 and current state) resulting from the composed analysis of coastal and rainfall flooding impacts on the drainage system are shown in this subsection. The tiff layers are available in the [Annex 2](#). The flooding layers are shown below:

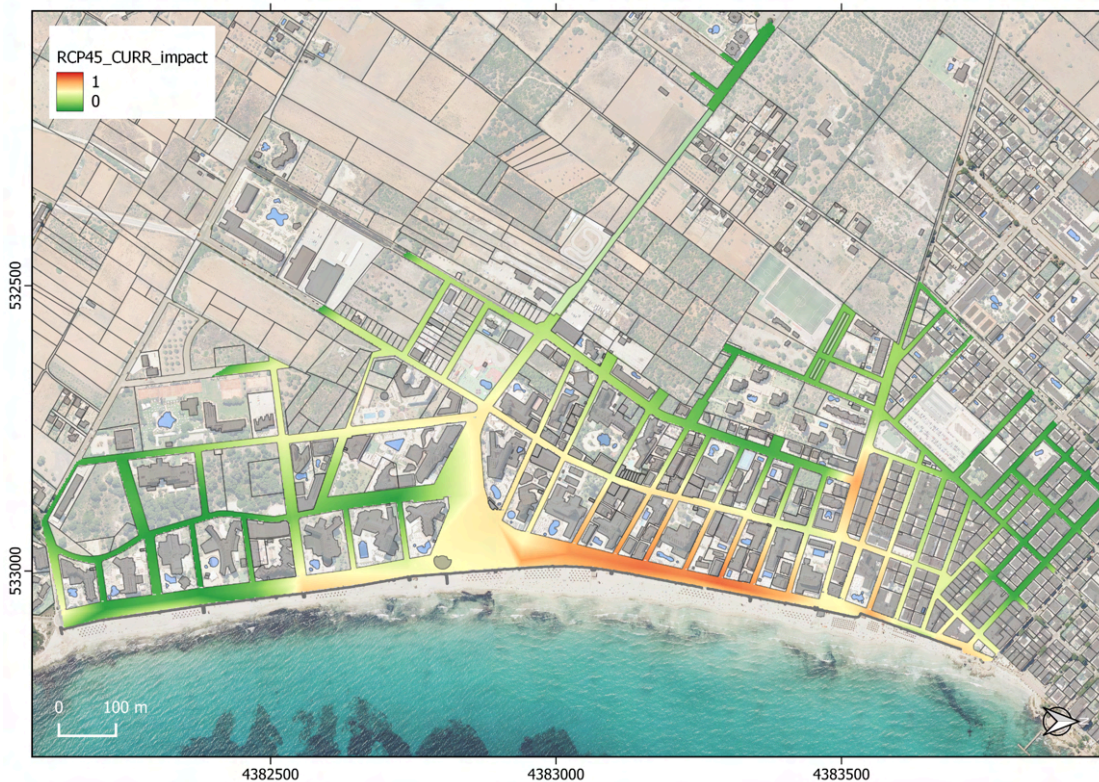


Figure 113. Drainage composed flooding map (2024).

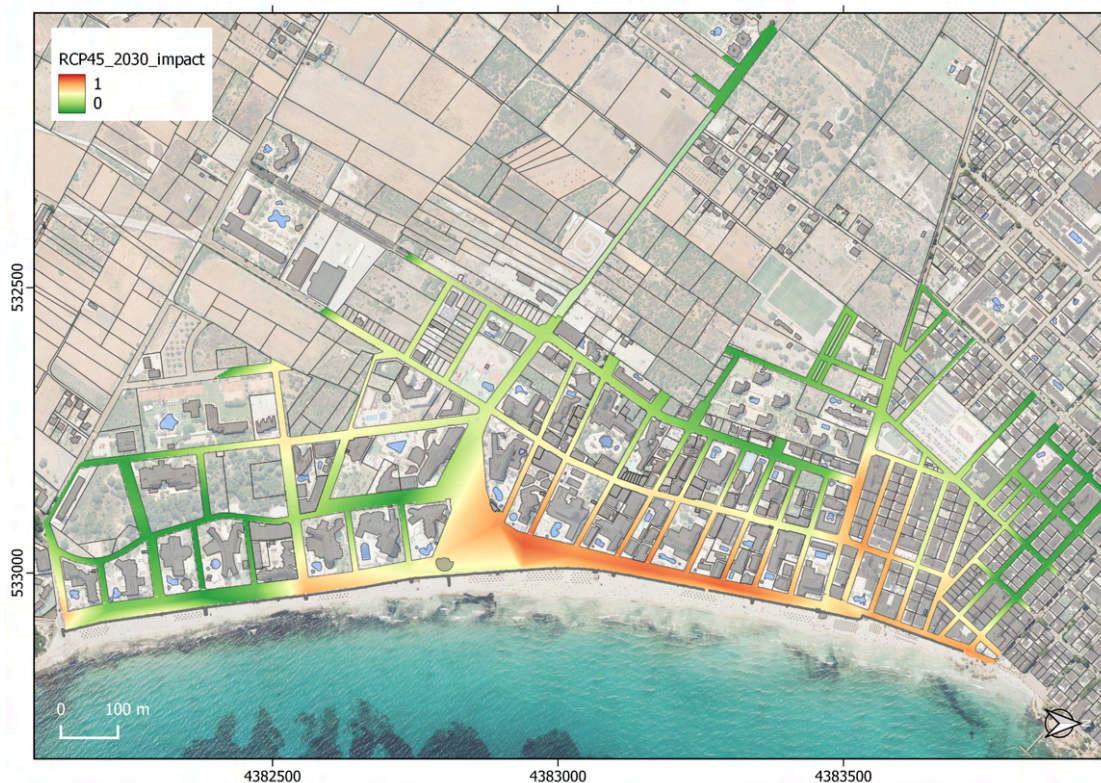


Figure 114. Drainage composed flooding for RCP-4.5 at 2030.

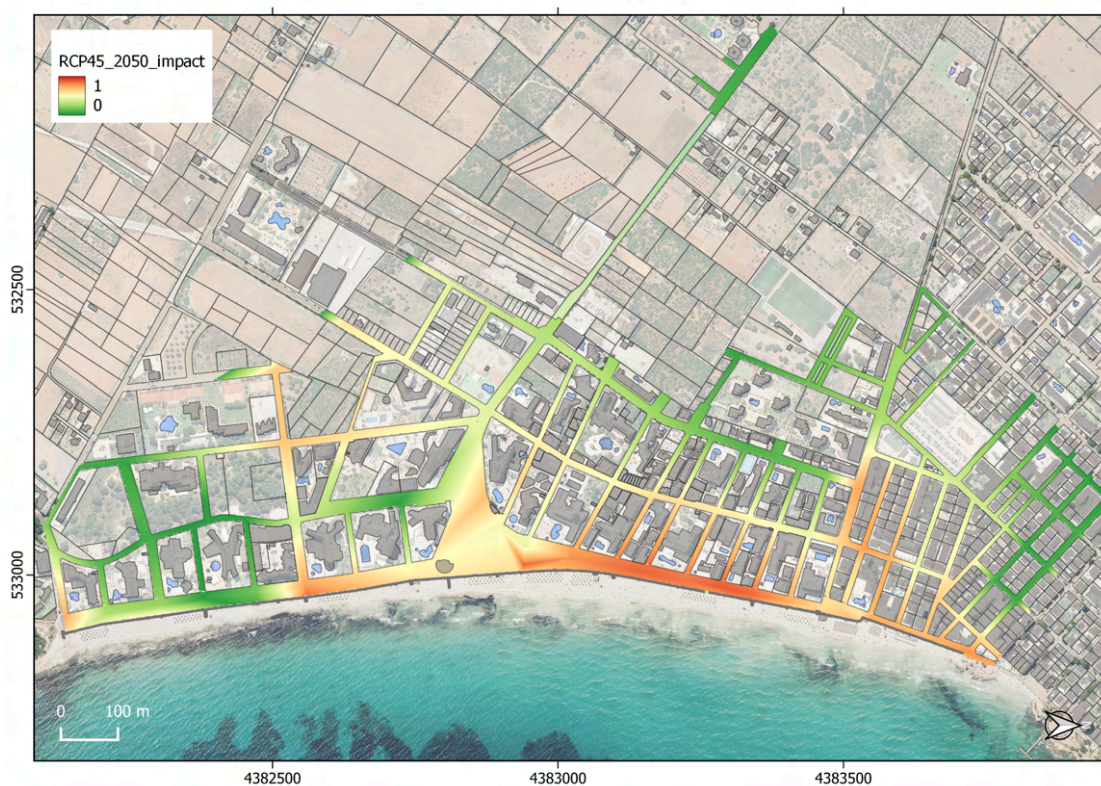


Figure 115. Drainage composed flooding for RCP-4.5 at 2050.

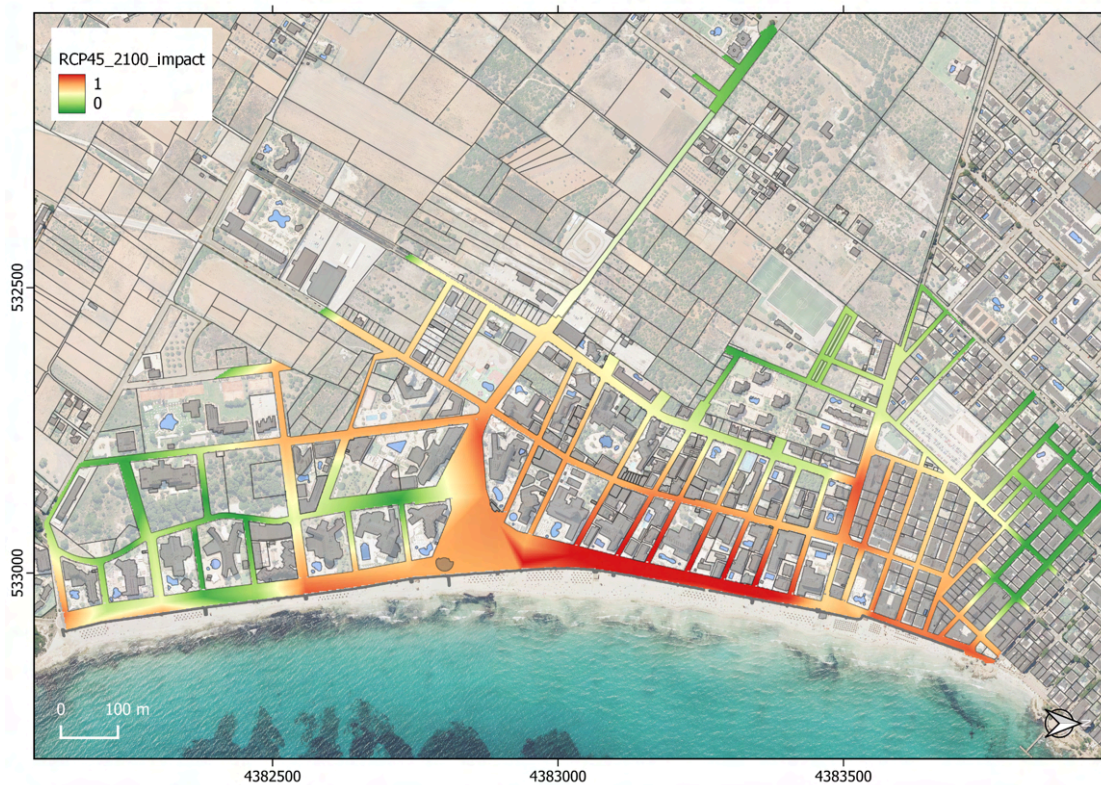


Figure 116. Drainage composed flooding for RCP-4.5 at 2100.

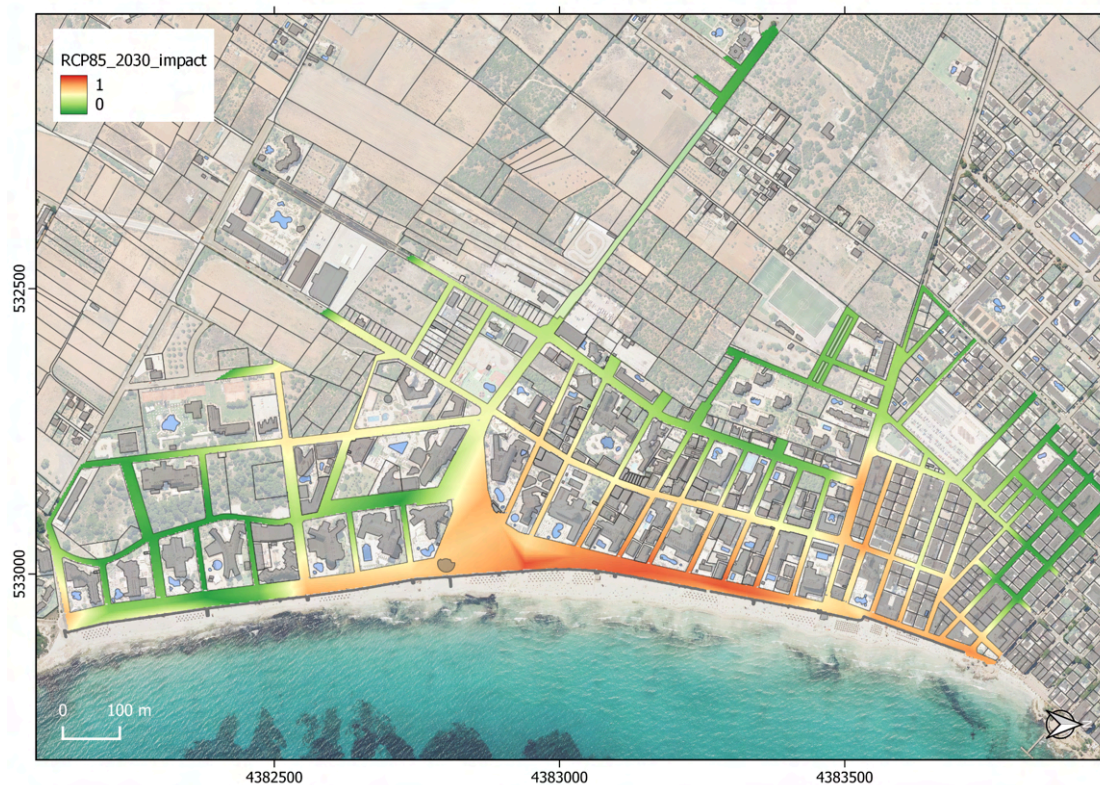


Figure 117. Drainage composed flooding for RCP-8.5 at 2030.

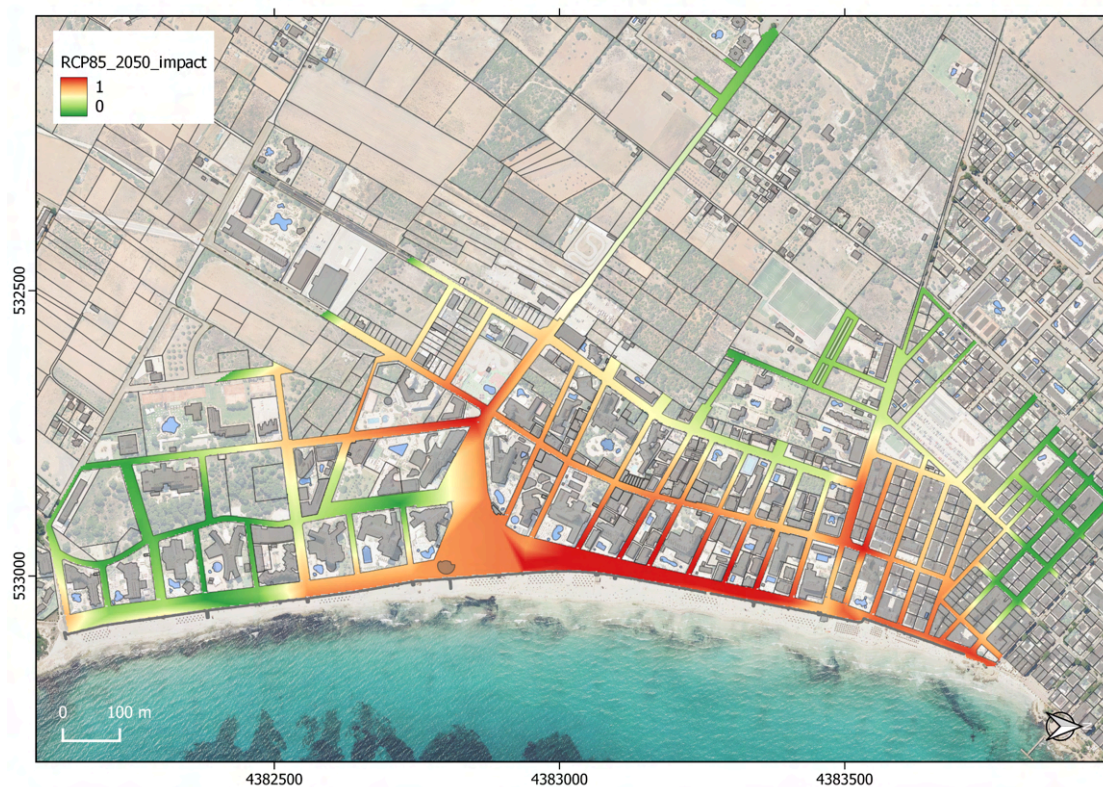


Figure 118. Drainage composed flooding for RCP-8.5 at 2050.

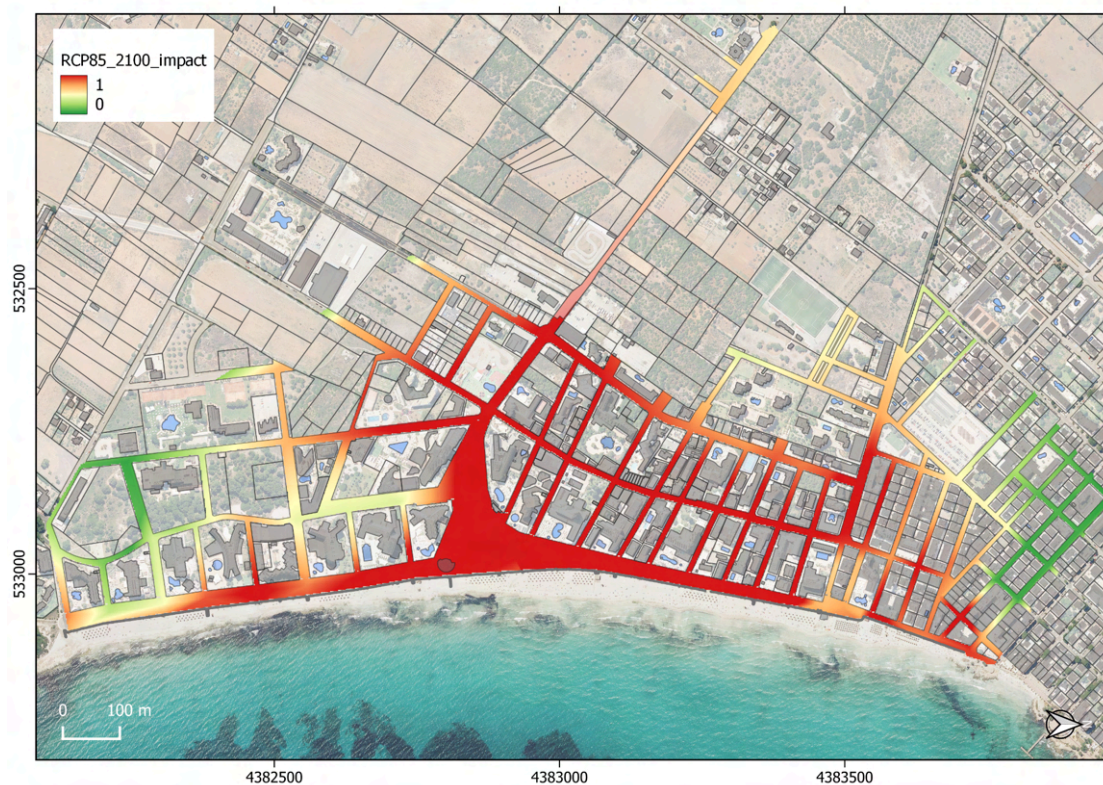


Figure 119. Drainage composed flooding for RCP-8.5 at 2100.

BIBLIOGRAPHY

- Alvarez-Ellacuria, A., Orfila, A., Gómez-Pujol, L., Simarro, G., Obregon, N. (2011). Decoupling spatial and temporal patterns in short-term beach shoreline response to wave climate. *Geomorphology*, 128: 199-209. DOI: 10.1016/j.geomorph.2011.01.008.
- Amelung, B., Viner, D. (2006). Mediterranean tourism: exploring the future with the tourism climatic index. *Journal of Sustainable Tourism*, 14(4): 349–366.
- Amelung, B., Nicholls, S., Viner, D. (2007). Implications of Global Climate Change for Tourism Flows and Seasonality. *Journal of Travel Research*, 45: 285-296.
- Berens, P. (2009). CircStat: A MATLAB Toolbox for Circular Statistics. *Journal of Statistical Software*, 31(10): 1–21. <https://doi.org/10.18637/jss.v031.i10>
- Brealey, R., Myers, S., Allen, F., Edmans, A. (2023). *Principles of Corporate Finance*, 14th Edition. McGraw-Hill.
- Bujosa, A., Rosselló, J. (2013). Climate change and summer mass tourism: the case of Spanish domestic tourism. *Climatic Change*, 117:363–375.
- Bujosa, A., Riera, A., Torres, C.M. (2015). Valuing tourism demand attributes to guide climate change adaptation measures efficiently: The case of the Spanish domestic travel market. *Tourism Management*, 47: 233-239.
- Calafat, F. M., Marcos, M. (2020). Probabilistic reanalysis of storm surge extremes in Europe. *Proceedings of the National Academy of Sciences*, 117(4): 1877-1883.
- Cañellas, B., Orfila, A., Mendez, F. J., Menendez, M., Gomez-Pujol, L., Tintore, J. (2007). Application of a POT model to estimate the extreme significant wave height levels around the Balearic Sea (Western Mediterranean). *Journal of Coastal Research, Special Issue*, 50: 329-333.
- Caruso, M. F., Marani, M. (2022). Extreme-coastal-water-level estimation and projection: a comparison of statistical methods. *Nat. Hazards Earth Syst. Sci.*, 22: 1109–1128, DOI: 10.5194/nhess-22-1109-2022.
- Codiga, D.L. (2011). *Unified Tidal Analysis and Prediction Using the UTide Matlab. Functions*. Technical Report 2011-01. Graduate School of Oceanography.
- Damodaran, A. (2023). *Equity Risk Premiums (ERP): Determinants, Estimation and Implications - The 2023 Edition*. <https://ssrn.com/abstract=4398884>. DOI: 10.2139/ssrn.4398884.
- De Michele, C., Salvadori, G., Passoni, G., Vezzoli, R. (2007). A multivariate model of sea storms using copulas. *Coastal Engineering*, 54(10): 734-751.
- Duo, E., Sanuy, M., Jimenez, J., & Ciavola, P. (2020). How good are symmetric triangular synthetic storms to represent real events for coastal hazard modelling. *Coastal Engineering*, 159: 103728.
- Duarte CM (1995) Submerged aquatic vegetation in relation to different nutrient regimes. *Ophelia*, 41, 87–112.

- Duarte CM (2002) The future of seagrass meadows. *Environmental Conservation*, 29, 192–206.
- Eyring, V., Bony, S., Meehl, G. A., Senior, C. A., Stevens, B., Stouffer, R. J., Taylor, K. E. (2016). Overview of the Coupled Model Intercomparison Project Phase 6 (CMIP6) experimental design and organization. *Geoscientific Model Development*, 9: 1937–1958. DOI: 10.5194/gmd-9-1937-2016.
- Fernández, P., Garcia de la Garza, D., and Fernández-Acín, J. (2023). *Survey: Market Risk Premium and Risk-Free Rate used for 80 countries in 2023* <https://ssrn.com/abstract=4407839> or <http://dx.doi.org/10.2139/ssrn.4407839>.
- Fernández-Mora, A., Criado-Sudau, F.F., Gómez-Pujol, L. et al. (2023). Ten years of morphodynamic data at a micro-tidal urban beach: Cala Millor (Western Mediterranean Sea). *Sci. Data*, 10: 301. <https://doi.org/10.1038/s41597-023-02210-2>.
- Fernández-Mora, A., Criado-Sudau, F., Sánchez-García, E., Soriano, J. and Prat-Bayarri, O. (2025) On wave energy dissipation along a seagrass field. In *Proceedings of Coastal Dynamics'25* (submitted).
- Fernández-Mora, A., Criado-Sudau, F., Sánchez-García, E., Soriano, J. and Calvete, D. Morphodynamics effects of extreme storms in urban beaches, (in prep.).
- Gaufres, P., Sabatier, F. (2005). *Extreme storm surges distributions at Marseilles. Proc. 7th Int. Conf. Mediterranean Coastal Environment, MEDCOAST 05*. In: E. Ozhan (Ed.), 25-29 Oct. 2005, Kusadasi, Turkey. Water Level Changes, Vol. 2, p. 1235-1246.
- Goda, Y. (1992). Uncertainty of design parameters from the viewpoint of extreme statistics. *J. Offshore. Mech. Arct.*, 114(2): 76-82.
- Gómez-Pujol, L., Orfila, A., Cañellas, B., Álvarez-Ellacuría, A., Méndez, F.J., Medina, R., Tintoré, J. (2007). Morphodynamic classification of sandy beaches in a low energetic marine environment. *Marine Geology*, 242: 235-246. DOI: 10.1016/j.margeo.2007.03.008.
- Gómez-Pujol, L., Orfila, A., Álvarez-Ellacuría, A., Tintoré, J. (2011). Controls on sediment dynamics and medium-term morphological change in a barred microtidal beach (Cala Millor, Mallorca, Western Mediterranean). *Geomorphology*, 132: 87-98. DOI: 10.1016/j.geomorph.2011.04.026.
- GOIB and IMEDEA, (2004). *Variabilidad y dinámica sedimentaria de las playas de Cala Millor y Cala Sant Vicenç*. ISBN 84-7632-913-X.
- Haddad, M., Hassani, H., Taibi, H. (2013). Sea level in the Mediterranean Sea: Seasonal adjustment and trend extraction within the framework of SSA. *Earth Science Informatics* 6, DOI: 10.1007/s12145-013-0114-6.
- Hamilton, J., Maddison, D., Tol, R.S.J. (2005a). The effects on climate change on international tourism. *Climate Research*, 29: 245–254.
- Hamilton, J., Maddison, D., Tol, R.S.J. (2005b). Climate change and international tourism: a simulation study. *Global Environmental Change*, 15: 253–266.
- Hein, L., Metzger, M., Moreno, A. (2009). Potential impacts of climate change on tourism; a case study for Spain. *Current Opinion in Environmental Sustainability*, 1: 170–178.

- Hersbach, H., Bell, B., Berrisford, P., et al. (2020). The ERA5 global reanalysis. *Q. J. R. Meteorol. Soc.*, 146: 1999–2049. DOI: 10.1002/qj.3803.
- IH Cantabria (2017). *Estudio de las condiciones actuales de la Playa de Cala Millor (Mallorca) y propuesta de líneas de actuación para su mejora durante el verano de 2017*. IH Cantabria, Universidad de Cantabria, Santander, 213 pp.
- Infantes, E., Orfila, A., Simarro, G., Terrados, J., Luhar, M., and Nepf, H. (2012). Effect of a seagrass (*Posidonia oceanica*) meadow on wave propagation. *Mar. Ecol. Prog. Ser.*, 456: 63-72. DOI: 10.3354/meps09754.
- Kendall, M. (1938) A New Measure of Rank Correlation. *Biometrika*, 30: 81-89. DOI: 10.1093/biomet/30.1-2.81.
- Jordà, G., Marbà, N., Duarte, C.M. (2012). Mediterranean seagrass vulnerable to regional climate warming. *Nature Climate Change*, 2(11): 821–824. DOI: 10.1038/nclimate1533.
- Lin-Ye, J., Garcia-Leon, M., Gracia, V., Sanchez-Arcilla, A. (2016). A multivariate statistical model of extreme events: An application to the Catalan coast. *Coastal Engineering*, 117: 138-156.
- Lintner, J. (1965). The valuation of risk assets and the selection of risky investments in stock portfolios and capital budgets. *Review of Economics and Statistics*, 47 (1): 13–37.
- Lira-Loarca, A., Cobos, M., Losada, M. Á., Baquerizo, A. (2020). Storm characterization and simulation for damage evolution models of maritime structures. *Coastal Engineering*, 156, 103620.
- Lise, W., Tol, R.S.J. (2002). Impact of climate on tourism demand. *Climatic Change*, 55: 429–449.
- Luque, P., Gómez-Pujol, L., Marcos, M., Orfila, A. (2021). Coastal Flooding in the Balearic Islands During the Twenty-First Century Caused by Sea-Level Rise and Extreme Events. *Frontiers in Marine Science*, 8: 676452. DOI: 10.3389/fmars.2021.676452.
- Kendrick, G. A., Marbà, N., Duarte, C. M. (2005). Modelling formation of complex topography by the seagrass *Posidonia oceanica*. *Estuarine, Coastal and Shelf Science*, 65(4), 717-725.
- Kopp, R. E., Horton, R. M., Little, C. M., Mitrovica, J. X., Oppenheimer, M., Rasmussen, D. J., et al. (2014). Probabilistic 21st and 22nd century sea level projections at a global network of tide-gauge sites. *Earth's Future*, 2: 383–406. DOI: 10.1002/2014EF000239
- Maddison, D. (2001). In search of warmer climates? the impact of climate change on flows of British tourists. *Climatic Change*, 49: 193–208.
- Marbà, N., Duarte, C., Díaz-Almela, E., Terrados, J., Álvarez, E., Martínez, R., Santiago, R., Gacía, E., Grau, A.M. (2005). Direct evidence of imbalance seagrass (*Posidonia oceanica*) shoot population dynamics in the Spanish Mediterranean. *Estuaries*, 28: 53-62. DOI: 10.1007/BF02732753.
- Marbà, N., Duarte, C. (2010). Mediterranean warming triggers seagrass (*Posidonia oceanica*) shoot mortality. *Global Change Biology*, 16: 2366-2375. DOI: 10.1111/j.1365-2486.2009.02130.x.
- Markowitz, H. M. (1999). The Early History of Portfolio Theory: 1600-1960. *Financial Analysts Journal*, 55: 5-16.

- Markowitz, H. M. (1952) Portfolio Selection. *Journal of Finance*, 7(1): 77–91.
- Martín-Hidalgo, M., Martín-Soldevilla, M.J., Negro, V., Aberturas, P., & López-Gutiérrez, J.S. (2014). Storm evolution characterization for analysing stone armour damage progression. *Coastal Engineering*, 85: 1-11.
- Martín Hidalgo, M. (2015). *Caracterización multivariada de los temporales para su aplicación en el dimensionamiento del manto principal*. Tesis (Doctoral), E.T.S.I. Caminos, Canales y Puertos (UPM). DOI: 10.20868/UPM.thesis.36262.
- Matei, N.A., García-León, D., Dosio, A., Batista e Silva, F., Ribeiro Barranco, R., Císcar Martínez, J.C. (2023). *Regional impact of climate change on European tourism demand*. Publications Office of the European Union, Luxembourg, DOI: 10.2760/899611, JRC131508.
- Martínez-Crego, B., Vergés, A., Alcoverro, T., & Romero, J. (2008). Selection of multiple seagrass indicators for environmental biomonitoring. *Marine Ecology Progress Series*, 361: 93-109.
- Mazzella, L., Scipione, M. B., & Buia, M. C. (1989). Spatio-temporal distribution of algal and animal communities in a *Posidonia oceanica* meadow. *Marine Ecology*, 10(2): 107-129.
- Menemenlis, D., Fukumori, I., Lee, T. (2007). Atlantic to Mediterranean Sea Level Difference Driven by Winds near Gibraltar Strait. *Journal of Physical Oceanography*, 37(2): 359-376. DOI: 10.1175/JPO3015.1
- Mieczkowski, Z. (1985). The tourism climatic index: a method of evaluating World climates for tourism. *Canadian Geographer*, 29: 220-233
- Ministerio de Fomento (2009). *ROM 1.0-09: Recomendaciones del diseño y ejecución de las obras de abrigo. Parte 1ª: Bases y factores para el proyecto, agentes climáticos*. Ministerio de Fomento.
- Morales-Márquez, V., Orfila, A., Simarro, G., Gómez-Pujol, L., Álvarez-Ellacuría, A., Conti, D., Galán, A., Osorio, A.F., Marcos, M. (2018). Numerical and remote techniques for operational beach management under storm group forcing. *Natural Hazards and Earth System Sciences*, 18, 3211–3223. DOI: 10.5194/nhess-18-3211-2018, 2018.
- Moreno, A., Amelung, B. (2009). Climate change and tourist comfort on Europe's beaches in summer: a reassessment. *Coastal Management*, 37: 550–568.
- Mossin, J. (1966). Equilibrium in a Capital Asset Market. *Econometrica*, 34 (4): 768–783.
- O'Neill, B. C., Tebaldi, C., van Vuuren, D. P., Eyring, V., Friedlingstein, P., Hurtt, G., Knutti, R., Kriegler, E., Lamarque, J.-F., Lowe, J., Meehl, G. A., Moss, R., Riahi, K., Sanderson, B. M. (2016). The Scenario Model Intercomparison Project (ScenarioMIP) for CMIP6. *Geoscientific Model Development*, 9, 3461–3482, <https://doi.org/10.5194/gmd-9-3461-2016>.
- Pawlowicz, R., Beardsley, B., Lentz, S. (2002). Classical tidal harmonic analysis including error estimates in MATLAB using T_TIDE. *Computers and Geosciences*, 28: 929-937.

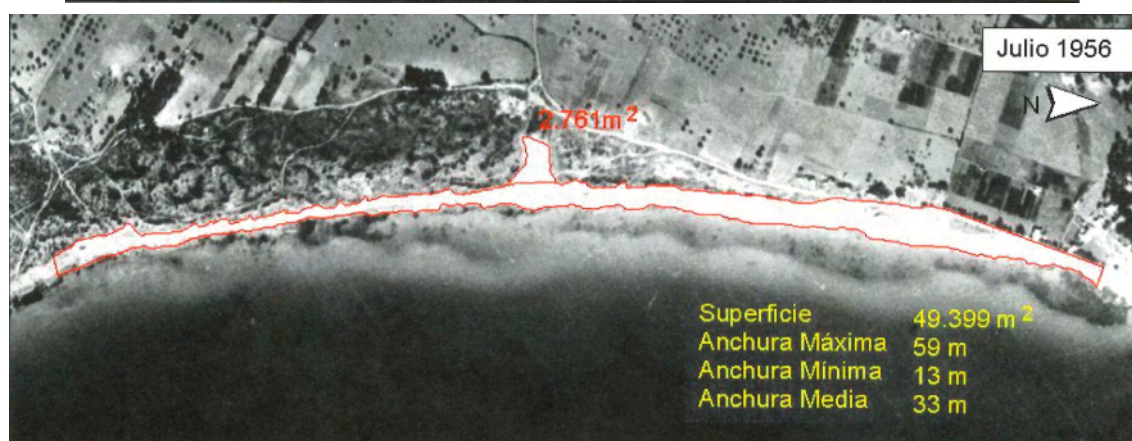
- Pericàs-Palou, A., Gómez, A.G., Bujosa, N., Gómez-Pujol, L. (2024). *Informe técnico Tarea 2.2.2. Understanding tourists*. WP2 Governance framework: Stakeholders & Citizens' engagement at Cala Millor. Proyecto LIFE AdaptCalaMillor. Palma, España. <https://acortar.link/tKy8HV>
- Priego, F.J., Rosselló, J., Santana-Gallego, M. (2015). The impact of climate change on domestic tourism: a gravity model for Spain. *Regional Environmental Change*, 15(2): 291-300.
- Roelvink, J., Reniers, A., van Dongeren, A., van Thiel de Vries, J., McCall, R., Lescinski, J. (2009). Modelling storm impacts on beaches, dunes and barrier islands. *Coastal Engineering*, 56: 133-1152.
- Roig-Munar, F.X., Martín, J.A., Pintó, J., Rodríguez-Perea, A., Gelabert, B. (2019). *Coastal Management in the Balearic Islands*. In: Morales, J.A. (Ed.) *The Spanish Coastal Systems. Dynamic Processes, Sediments and Management*: 765-788. Springer, Cham.
- Roland, A., Zhang, Y.J., Wang, H.V., Meng, Y., Teng, Y-C., Maderich, V., Brovchenko, I., Dutour-Sikiric, M., Zanke, U. (2012). A fully coupled 3D wave-current interaction model on unstructured grids. *J. Geophys. Res.*, 117, C00J33, doi:10.1029/2012JC007952.
- Ross, S., Westerfield, R., Jordan, B. (2022). *Fundamentals of Corporate Finance*. McGraw-Hill.
- Rosselló, J., Santana-Gallego, M. (2014). Recent trends in international tourist climate preferences: a revised picture for climatic change scenarios. *Climatic Change*, 124: 119–132.
- Rosselló-Nadal, J., Santana-Gallego, M. (2022). Gravity models for tourism demand modeling: Empirical review and Outlook. *Journal of Economic Surveys*, 36(5): 1358–1409.
- Sadegh, M., Ragno, E., AghaKouchak, A. (2017). Multivariate Copula Analysis Toolbox (MvCAT): Describing dependence and underlying uncertainty using a Bayesian framework, *Water Resour. Res.*: 53, 5166–5183, DOI: 10.1002/2016WR020242.
- Sadegh, M., Moftakhari, H., Gupta, H. V., Ragno, E., Mazdiyasni, O., Sanders, B., Matthew, R., AghaKouchak, A. (2018). Multihazard scenarios for analysis of compound extreme events. *Geophysical Research Letters*, 45: 5470–5480. DOI: 10.1029/2018GL077317
- Sharpe, W. F. (1964). Capital asset prices: A theory of market equilibrium under conditions of risk. *Journal of Finance*, 19 (3): 425–442.
- Soldevilla, M.J., Martín-Hidalgo, M., Negro, V., López-Gutiérrez, J.S., Aberturas, P. (2015). Improvement of theoretical storm characterization for different climate conditions. *Coastal Engineering*, 96: 71-80.
- Tebaldi, C., Debeire, K., Eyring, V., Fischer, E., Fyfe, J., Friedlingstein, P., Knutti, R., Lowe, J., O'Neill, B., Sanderson, B., van Vuuren, D., Riahi, K., Meinshausen, M., Nicholls, Z., Tokarska, K. B., Hurtt, G., Kriegler, E., Lamarque, J.-F., Meehl, G., Moss, R., Bauer, S. E., Boucher, O., Brovkin, V., Byun, Y.-H., Dix, M., Gualdi, S., Guo, H., John, J. G., Kharin, S., Kim, Y., Koshiro, T., Ma, L., Olivié, D., Panickal, S., Qiao, F., Rong, X., Rosenbloom, N., Schupfner, M., Séférian, R., Sellar, A., Semmler, T., Shi, X., Song, Z., Steger, C., Stouffer, R., Swart, N., Tachiiri, K., Tang, Q., Tatebe, H., Voldoire, A., Volodin, E., Wyser, K., Xin, X., Yang, S., Yu, Y., Ziehn, T. (2021). Climate model projections from the Scenario Model Intercomparison Project (ScenarioMIP) of CMIP6. *Earth Syst. Dynam.*, 12: 253–293. DOI: 10.5194/esd-12-253-2021.

- Tintoré, J., Medina, R., Gómez-Pujol, L., Orfila, A., Vizoso, G. (2009). Integrated and interdisciplinary scientific approach to coastal management. *Ocean and Coastal Management*, 52: 493-505. DOI: 10.1016/j.ocecoaman.2009.08.002.
- Treynor, J. L. (1962). *“Toward a Theory of Market Value of Risky Assets”*. Unpublished manuscript. A final version was published in 1999, in *Asset Pricing and Portfolio Performance: Models, Strategy and Performance Metrics*. Robert A. Korajczyk (editor) London: Risk Books, pp. 15–22.
- Toomey, T., Amores, A., Marcos, M., Orfila, A. (2022). Coastal sea levels and wind-waves in the Mediterranean Sea since 1950 from a high-resolution ocean reanalysis. *Frontiers in Marine Science*, 9: 991504. DOI: 10.3389/fmars.2022.991504.
- UNWTO (2011) *Tourism Towards 2030 / Global Overview*. UNWTO: Madrid.
- van Vuuren, D.P., Edmonds, J., Kainuma, M. *et al.* (2011) The representative concentration pathways: an overview. *Climatic Change* 109, 5 (2011). <https://doi.org/10.1007/s10584-011-0148-z>
- Walton, T.L. (2000). Distributions for storm surge extremes. *Ocean Engineering*, 27: 1279-1293.
- World Climate Research Programme (2020). CMIP Phase 6 (CMIP6): Overview CMIP6 Experimental Design and Organization. Available at: <https://www.wcrp-climate.org/wgcm-cmip/wgcm-cmip6> (Accessed: 30 July 2024).
- Zhang, Y., Ye, F., Stanev, E.V., Grashorn, S. (2016). Seamless cross-scale modeling with SCHISM. *Ocean Modelling*, 102: 64-81
- Zhang, Y., Baptista, A.M. (2008). SELFE: A semi-implicit Eulerian-Lagrangian finite-element model for cross-scale ocean circulation. *Ocean Modelling*, 21(3-4): 71-96.
- Zupo, V., Buia, M. C., Gambi, M. C., Lorenti, M., Procaccini, G. (2006). Temporal variations in the spatial distribution of shoot density in a *Posidonia oceanica* meadow and patterns of genetic diversity. *Marine Ecology*, 27(4): 328-338.

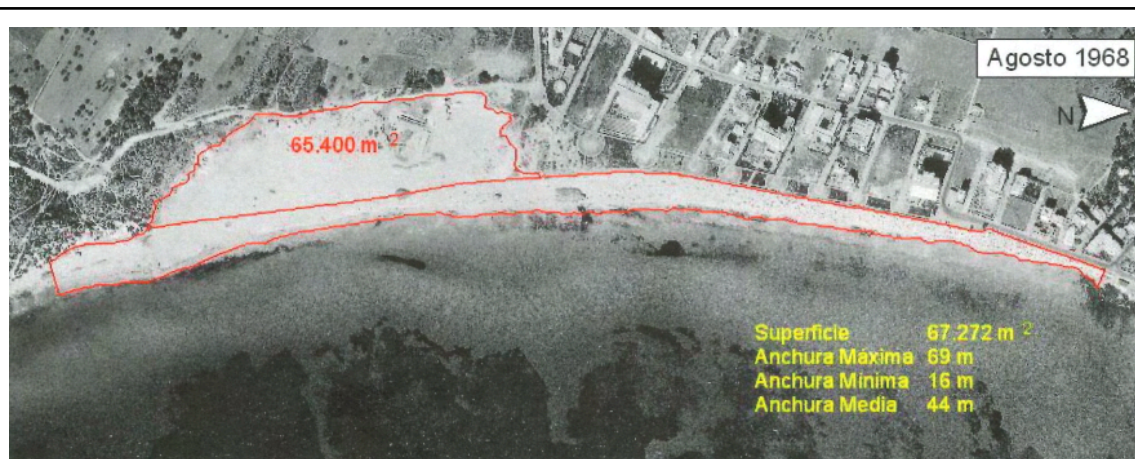
ANNEX 1. Historical photographs

Series of beach aerial photographs (modified from GOIB and IMEDEA, 2004):

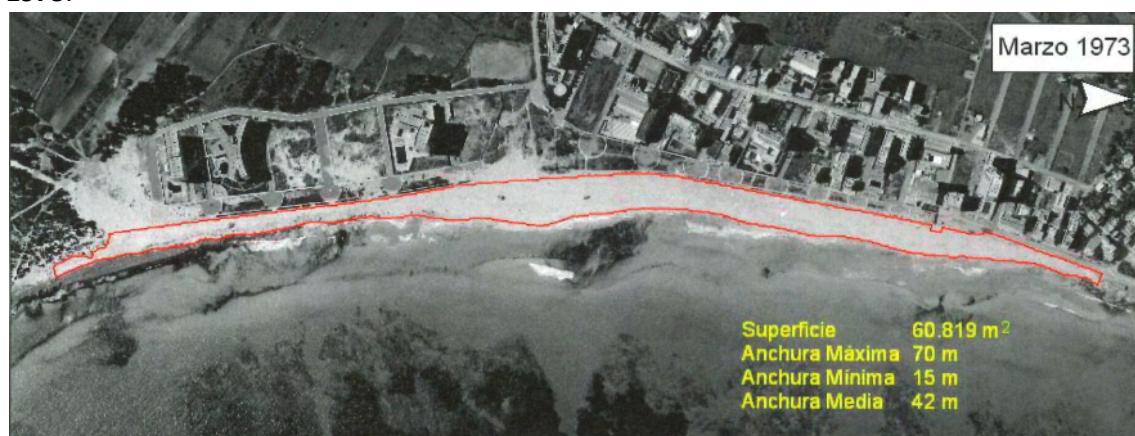
1956. Dune area located south of Cala Millor (Sa Mònica):



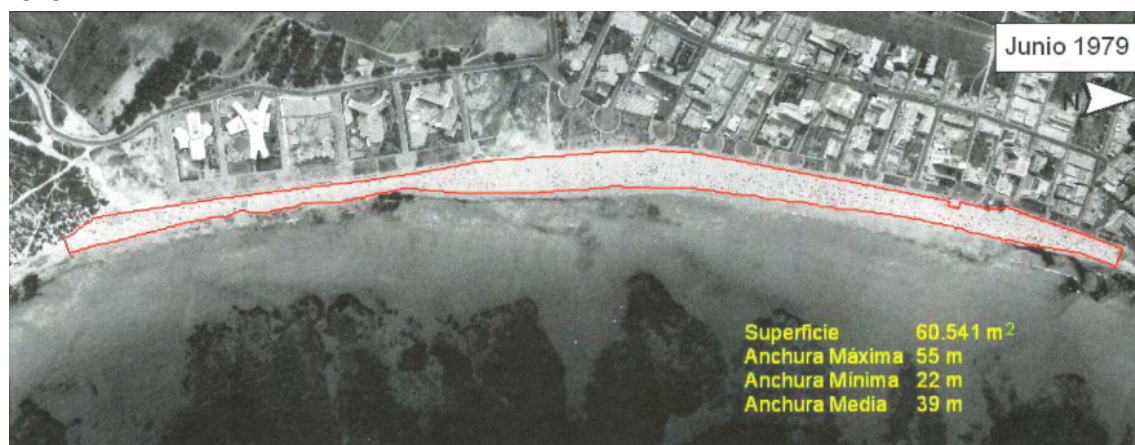
1968. Dismantling of the dune ridge of >65,400 m²:



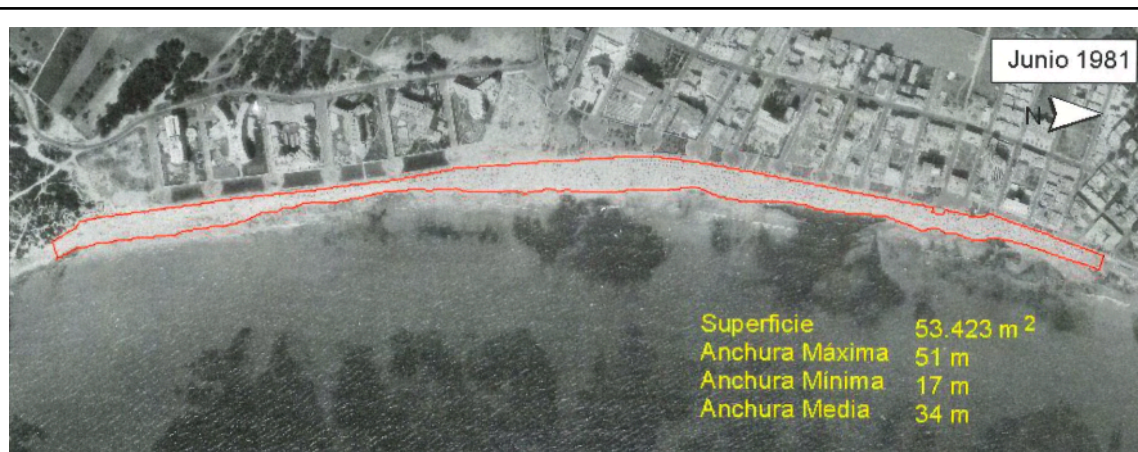
1973.



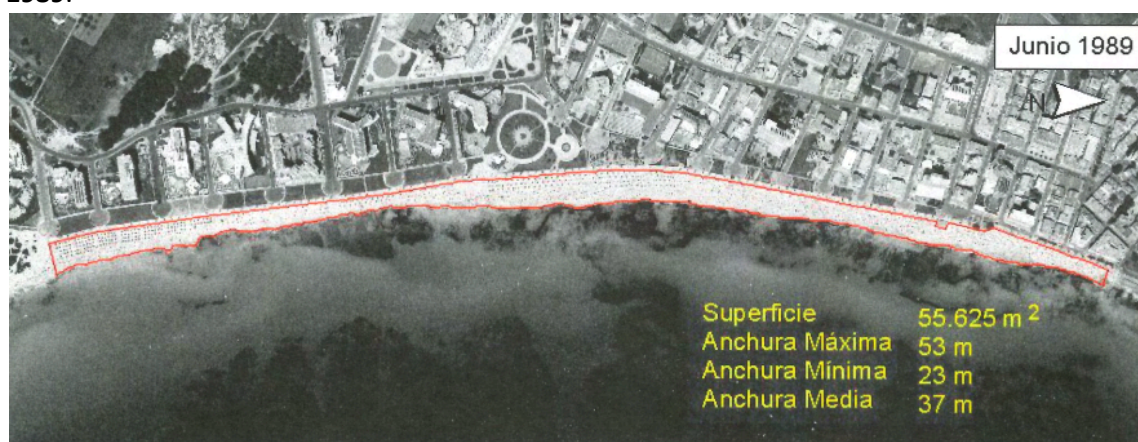
1979.



1981.



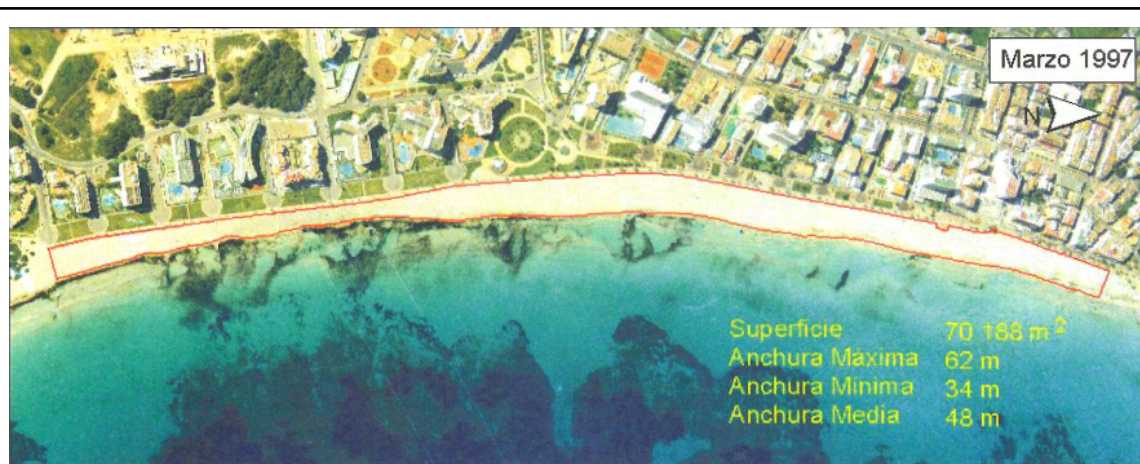
1989.



1995.



1997.



2001.



2002.

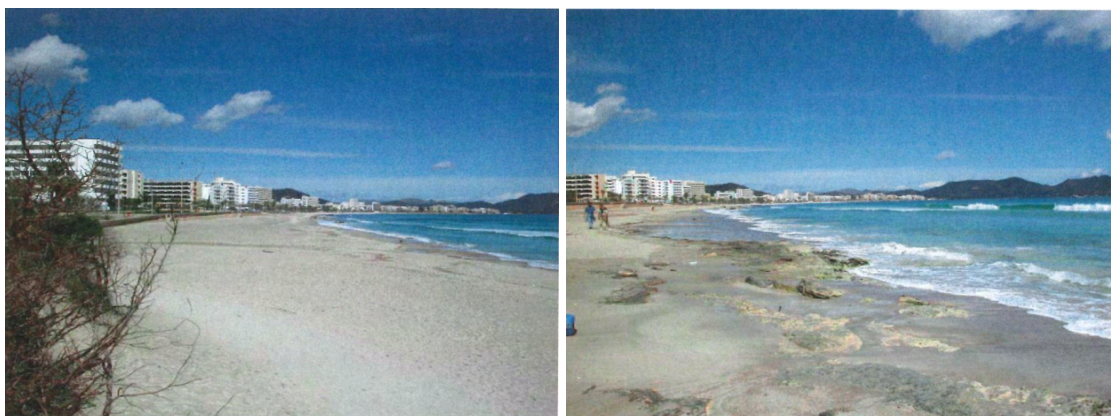


2004.



2004 May.

View of Cala Millor, from the south of Cala Nau in left photo and from the south of Sa Mònica, 2002:







Left photo: View of Cala Millor (Platja del Moro) from the north of the beach, 2002.

Right photo: View of 'Es Clot de s'Alga' pointing north, 2002:



ANNEX 2. Impact maps

The GIS datasets and PNG maps produced during WP3 are available for now upon request from the project coordinators at lifeadaptcalamillor@gmail.com. A list of these resources is provided in this annex:

-  MAPS Impact P. oceanica
-  MAPS Impact coastal dune
-  MAPS Impact flooding
-  MAPS Impact compound flooding (urban drainage system)